Ion-track technology based synthesis and characterization of gold and gold alloys nanowires and nanocones

Vom Fachbereich Material- und Geowissenschaften der Technischen Universität Darmstadt

zur Erklärung des akademischen Grades eines Doktors der Naturwissenschaften (Dr. rer. nat.) genehmigte

Dissertation von

Dipl. Ing. M.Sc. Loïc Burr

aus Colmar (Frankreich)

June 2016 - Darmstadt – D17

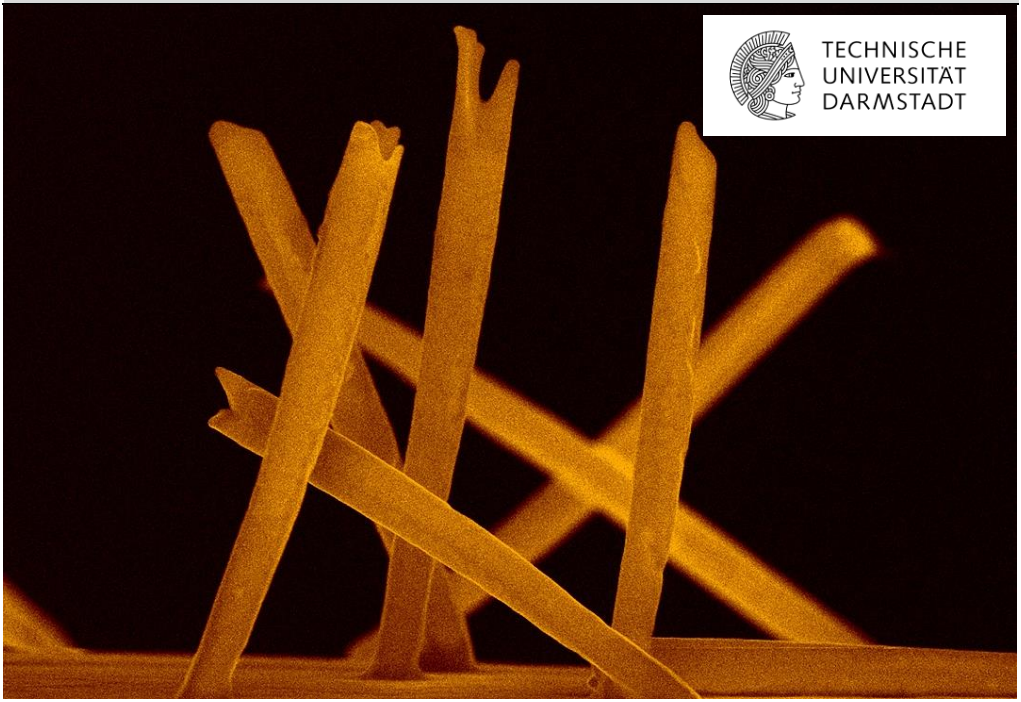

Ion-track technology based synthesis and characterization of gold and gold alloys nanowires and nanocones

genehmigte Disseration von Dipl. Ing. M.Sc. Loïc Burr aus Colmar (Frankreich)

1. Gutachten: Prof. Dr. Christina Trautmann

2. Gutachten: Prof. Dr. Ralph Krupke

Tag der Einreichung: 21.04.2016

Tag der mündlichen Prüfung: 21.04.2016

Darmstadt – 2016

D17

The work described in this thesis was carried out between November 2012 and June 2013 under the supervision of Prof. Dr. Trautmann at the Materials Research group of the GSI Helmholtz Centre for Heavy Ion Reseach, Plackstraße 1, D-64291 Darmstadt, Germany

Top cover image: colorized SEM image of Au nanowires standing on their Au backelectrode fabricated by electrodeposition in etched ion track templates as presented in this thesis

Back cover image: modified SEM image of Au nanocones with their caps overlaying a nanocone array

Erklärung zur Dissertation

Hiermit versichere ich, die vorliegende Dissertation ohne Hilfe Dritter und nur mit den angegebenen Quellen und Hilfsmitteln angefertigt zu haben. Alle Stellen, die aus den Quellen entnommen wurden, sind als solche kenntlich gemacht worden. Diese Arbeit hat in dieser oder ähnlicher Form noch keiner Prüfungsbehörde vorgelegen.

Darmstadt, den 19.04.2016

_____

(Loïc Burr)

Loïc Burr
Ion-track technology based synthesis and characterization of gold and gold alloys nanowires and nanocones

PhD Thesis, Technische Universität Darmstadt, Darmstadt, Germany

URN: urn:nbn:de:tuda-tuprints-55410
URI: http://tuprints.ulb.tu-darmstadt.de/id/eprint/5541

"Go back to work"

B.S.

Zusammenfassung

Metallische Nanostrukturen sind äußerst attraktiv für Anwendungen in Batterien, Solarzellen oder Arzneimitteln. In dieser Doktorarbeit wurden folgende Gold-Nanostrukturen durch elektrochemische Abscheidung in geätzten Ionenspurmembranen synthetisiert: (1) zylindrische Nanodrähte bestehend aus Gold oder Gold-Silber-Legierungen, (2) poröse, zylindrische Gold-Nanodrähte hergestellt durch selektives Auflösen des Silberanteils und (3) konische Gold-Nanodrähte (auch Nanokegel genannt).

Durch Kontrolle der Prozessparameter wurden zylindrische Nanodrähte unterschiedlicher Zusammensetzung (Au; $Au_{60}Ag_{40}$; $Au_{40}Ag_{60}$; Ag) und mit vorgegebenen Durchmessern abgeschieden. Für $Au_{40}Ag_{60}$-Nanodrähte führte chemisches Auflösen des Silbers zu porösen Au-Nanodrähten mit stark vergrößerter Oberfläche. Morphologie und Zusammensetzung dieser Strukturen wurden mit energiedispersiver Röntgenspektroskopie (EDX) und Transmissions-elektronmikroskopie (TEM) untersucht. Die Analyse der elementaren Zusammensetzung der Au-Ag-legierten Drähte gibt klare Hinweise auf Oberflächensegregation. $Au_{60}Ag_{40}$-Drähte zeigen ungleichmäßig goldreiche Oberflächen, $Au_{40}Ag_{60}$ Nanodrähte hingegen zeigen Silberanreicherungen. Nach der selektiven Auflösung des Silbers bestehen die porösen goldreichen Nanodrähte aus 5 bis 30 nm breiten Ligamenten. Diese porösen Nanodrähte könnten künftig als Sensoren benutzt werden. Hierfür müssen allerdings der elektrische und thermische Wiederstand ermittelt werden. Um diese Messungen zu ermöglichen, wurden geeignete Kontaktierungsverfahren für AuAg-Nanodrähten mittels Laserlithographie getestet.

Freistehende Gold-Nanokegel mit Mikrometer großen Basen und ca. 50 nm breiten Spitzen wurden elektrochemisch in Ionenspurmembranen mit asymmetrisch geätzten konischen Kanälen hergestellt. Stabile Nanokegel sind für Anwendungen interessant z.B. als hydrophobe Deckschicht oder als kalte Feldemitter. Die in dieser Arbeit hergestellten Gold-Nanokegel wurden

elektrochemisch von der Spitze zur Basis abgeschieden, um die mechanische Stabilität zu verbessern und einen soliden elektrischen und thermischen Kontakt zum Substrat sicherzustellen. Ein Test an geordneten Nanokegel-Arrays zeigt kalte Feldemission mit Feldüberhöhungen zwischen 200 und 1000 sowie maximalen Emissionsströmen zwischen 1 und 100 µA.

Die Ergebnisse diese Promotionsarbeit verdeutlichen die große Flexibilität und unterschiedlichen Möglichkeiten der Ionenspur-Nanotechnologie.

Abstract

Metallic nanostructures are attracting growing interest because of their potential application in various devices such as batteries, solar cells, or drug delivery systems. This thesis focuses on the synthesis and characterization of three different nanostructures: (1) solid cylindrical AuAg nanowires with controlled composition and size, fabricated by electrodeposition in etched ion-track membranes with cylindrical channels, (2) porous cylindrical Au nanowires attained by selective dealloying of AuAg nanowires, and (3) Au nanocones synthesized by electrodeposition in conical channels.

AuAg nanowires with controlled diameter and composition, namely Au, $Au_{40}Ag_{60}$, $Au_{60}Ag_{40}$, and Ag were synthesized and characterized. By dealloying these nanowires were converted into porous Au-based nanowires with diameters above and below 100 nm possessing an enhanced surface area. Surface morphology and composition of the nanostructures before and after dealloying were studied by means of high spatial resolution energy-dispersive X-ray spectroscopy (EDX) in a high-resolution transmission electron microscope (TEM). The results demonstrate surface segregation effects in solid AuAg nanowires that strongly vary with the initial composition. Surface segregation occurs on a time scale of days (< 3 days) independently of the wire dimensions. After dealloying of $Au_{40}Ag_{60}$ nanowires, the porous nanowires have a silver content below 10% and ligament size from 5 to 30 nm. Solid and porous wires are particularly attractive for future applications, e.g., in sensorics. The characterization of such small nanostructures regarding, e.g. electrical transport properties, requires suitable contacts. Special designs to contact nanowires by laser lithography as well as by using pre-patterned templates were developed.

Gold nanocones with sharp tips down to 50 nm diameter and several microns large bases were fabricated. Given by this special geometry, the nanostructures exhibit a high mechanical stability and are freestanding with an aspect ratio of 500 and above. Stable gold nanocone arrays are attractive for a large range of

applications including field emission and as coating for hydrophobic surfaces. In this work, the standard wire deposition process from base to tip was inverted in order to improve the electrical and thermal contact of the nanocones to the substrate. After selective removal of the template, 30 µm long gold nanocones with ~ 50 nm sharp tips were freestanding and vertically aligned. Such structures are highly tunable in terms of cone dimensions and number density. The field emission properties of patterned nanocone arrays, investigated in collaboration with the Bergische Universität Wuppertal, exhibit field enhancement factors between 200 and 1000 as well as a maximum emission current ranging from ~ 1 to 100 µA.

The results presented in this thesis emphasize the variety of possibilities that ion-track technology offers in order to tailor dimensions and characteristics of nanostructures.

Résumé

L'intérêt croissant pour les nanotechnologies et plus particulièrement les nanostructures métalliques provient des besoins de nouveaux développements technologiques dans le domaine des batteries, des panneaux solaires ou en médecine. Cette thèse aborde la fabrication et la caractérisation de trois différentes structures à base d'or: (1) des nano-fils en alliage or et argent (AuAg), (2) des nano-fils poreux obtenus par la dissolution sélective de l'argent contenu dans des fils AuAg, et (3) des nano-cônes en or. Ces structures ont été synthétisées par électrodéposition dans des pores calibrés de membranes polymères. Elles ont été obtenues par révélation chimique des traces latentes laissées dans le matériau après irradiation par des ions lourds accélérés (plus connus sous le nom anglais « ion-track technology »).

Cette technique permet de contrôler précisément le diamètre et la composition des nano-fils d'alliage or-argent. La dissolution de l'argent contenu dans des fils de composition $Au_{40}Ag_{60}$ par corrosion sélective rend possible l'obtention de nano-fils poreux. L'évolution de la morphologie et de la composition de ces nano-fils a été étudiée par microscopie électronique en transmission couplée à une analyse dispersive en énergie (EDX) avant et après traitement corrosif. Avant la dissolution de l'argent, les nano-fils sont cylindriques, mais leur composition n'est pas homogène. Une ségrégation de surface se produit au bout de quelques jours (< 3 jours). Les nano-fils de composition $Au_{60}Ag_{40}$ voient leur surface enrichie en or et, à l'inverse, celle des fils $Au_{40}Ag_{60}$ s'enrichie en argent. Après le traitement corrosif, seuls les fils comportant le plus d'argent ($Au_{40}Ag_{60}$) permettent la fabrication de nano-fils poreux, donnant lieu à une augmentation de leur surface. De tels fils sont particulièrement intéressants pour le développement de détecteurs ultra-sensibles. A cette fin, leurs propriétés électriques et thermiques doivent être caractérisées. En vue de la prochaine évaluation de ces propriétés, des nano-fils ont été connectés électriquement par un procédé de photolithographie laser.

Des nano-cônes, dont la pointe présente un diamètre inférieur à 50 nm, ont été fabriqués grâce à des membranes poreuses révélées chimiquement de manière asymétrique. D'une base de quelques micromètres de large, ces nano-cônes sont mécaniquement très stables. Ces structures autoportantes atteignent des rapports d'aspect supérieurs à 500. Elles peuvent être utilisées pour fabriquer des surfaces super-hydrophobes et autonettoyantes, ou servir de cathodes à émission électronique par effet de champs. Pour ces travaux, les cônes ont été synthétisés par électrodéposition dans une membrane poreuse depuis la pointe vers la base, grâce à une électrode sacrificielle. Cette déposition inversée permet de contrôler précisément la densité et la dimension des cônes. L'émission par effet de champs de réseaux de nano-cônes parallèles a été mesurée en collaboration avec la Bergische Universität de Wuppertal. Nous avons obtenus des facteurs d'amélioration de l'émission entre 200 et 1000, ainsi que des claquages sous vide à des courants entre 1 et 100 µA.

Les résultats présentés dans cette thèse soulignent la flexibilité et la performance de l'« ion-track technology » pour la fabrication de nanostructures métalliques.

Table of contents

INTRODUCTION

1. Nanotechnology: infinitely small, such a big topic

The race to miniaturization has been initiated by computer science and its increasing need of calculation power. According to Moore's law, the transistor density on a silicon chip should double every two years.[1] This demand led to the fabrication of smaller and smaller components, reaching nowadays dimensions in the nanometer scale (1 nm = 10^{-9} m). At the same time, in parallel to the technological drive for miniaturization, new properties different from those of the bulk were predicted and experimentally observed for nanomaterials generating a wildely increasing interest.[2–7]

Thus, for example, when the size of the particles is comparable to the electron Fermi wavelength, electronic energy levels start to quantize, i.e. to exhibit discrete values which significantly differs from the "continuous" energy bands in bulk materials. In addition, the number of surface atoms with low coordination numbers becomes more dominant, providing an additional way to modify and tailor the electron distribution and transport in nanoparticles. Consequently, all the material properties depending on the electronic energy levels such as thermal, electrical, spectroscopic, or chemical properties of these finite systems are expected to differ from those of bulk. These effects are also experimentally observable; for example, spherical gold nanoparticles with diameter of ~ 30 nm are red and not shiny deep yellow (gold) as the bulk.[8]

For the fabrication of nanostructures, i.e. structures with at least one dimension below 100 nm, two complementary ways are available: top-down and bottom-up approaches. Top-down processes start from bulk solid from which nanostructures are shaped out. Optical lithography is the most common top-down approach. It is extensively used in the electronic industry to fabricate silicon based transistors because it allows parallel production and controlled integration into systems.[9] The

bottom-up approach consists of assembling small building blocks (i.e. atoms, molecules, particles) to shape nanostructures. Bottom-up techniques such as nanoparticle self-assembly [10,11] provide higher throughput but on cost of size distribution control. Hybride methods combining top-down and bottom-up approaches such as the template method have also been developed and are attractive for their high flexibility and the possibility of direct integration into devices.

Nano-objects are attractive for a wide range of applications such as catalysis, optics, energy production and storage, sensors, chemical and biochemical assays, medicine, gene and drug targeting as well as nanoelectronics and nanodevices.[1,2,4,5,7,12–15] As a consequence of the broad variety of potential applications and the very fast progress of nanotechnologies, nanomaterials attract attention of manufacterers, economists, politicians and the general public. Though a large number of nanodevices are already commercialized such as components of computer central processing units (CPU),[16] nanoscience remains a relatively young science where new fabrication routes, concepts for devices and possible applications are constantly being unveiled.

According to C.N.R. Rao et al.,[2] "the immediate objectives of the science and technology of nanomaterials are: (1) to fully master the synthesis of isolated nanostructures (building blocks) and their assemblies with the desired properties, (2) to explore and establish nanodevice concepts and systems architectures, (3) to generate new classes of high performance materials, (4) to connect nanoscience to molecular electronics and biology, and (5) to improve known tools while discovering better tools of investigation of nanostructures."

2. Gold: a rich material

Symbol of wealth, gold has been fascinating humans since ages. Mostly supplied through mining and recycling, it is a malleable rare noble metal that is not affected

by dirt or corrosion.[5–7] For millenaries, its major uses were jewellery and monetary assets.

Because of its inherent physical and chemical properties (Table V-1), gold is being increasingly utilized for advanced technological applications. Initially of interest because of its high electrical and thermal conductivity as well as a strong corrosion resistance, gold was mostly employed in electronics and electrical engineering.

Table V-1: Principal physical properties of gold extracted from [17–21]

Atomic number (Z)	79
Electronic configuration	$[Xe]4f^{14}5d^{10}6s^{1}$
Atomic mass (M)	196.97 g·mol^{-1}
Atomic radius (r_A)	0.1442 nm
Unit cell	Face centered cubic
Lattice parameter	0.40781 nm
First ionisation energy	890 kJ·mol^{-1}
Standard potential Au/Au^+ (E^0)	+1.691 V
Electronegativity	2.4
Electron mean free path (λ)	$\geq$ 40 nm
Melting temperature	1064.43 °C
Density at 20 °C (d)	19.32 g·cm^{-3}
Electrical resistivity at 0°C (ρ)	2.06×10^{-6} Ω·cm
Thermal conductivity at 0 °C (κ)	3.14 W·cm^{-1}·K^{-1}

More recently, gold and gold alloys have been used in chemical industry as catalysts. In addition, the extended gold-thiol chemistry developed in the past decades render this material attractive for both materials science and biochemistry. However, due to the high price of the raw material, gold for technological purposes is sustainable only for high added value technologies.

3. Nanoscale gold: a perfect match

Nanostructuring of gold is being used since antic ages. Egyptians and chinese were already using colloidal gold (Au nanoparticles in solution) as colorant for ceramics or glasses millenaries ago. The Lycurgus Cup, dated from the 4th to 5th

century before Christus and exposed at the British Museum, is one of the most famous examples.[7,22] Cathedrals from the middle ages are another glaring example of the use of nanoparticles of gold and other materials to fabricate multicolored rosette windows. These peculiar optical properties originate from surface plasmon resonances in gold nanoparticles. In the presence of an electromagnetic field (i.e. incident light), the electrons of the nanoparticles oscillate. In the case where the electron oscillations coincide with the incident light frequency, resonances lead to strong absorption of that precise wavelength, giving rise to coloring of the media. These properties depend not only on the size of the nanoparticles but also on their shape, interparticle distances as well as their surrounding medium.[3,23]

Other effects observable for gold nanoparticles are intimately linked to the relative increase of surface atoms with low coordination number. Haruta et al. demonstated that nanostructured gold, in opposition to bulk, is chemically extremely active and can serve as catalyst.[24,25] With the decrease in particle size, the total number of atoms in each particle also drastically diminishes, impacting the quantum properties of gold. Through quantification of the energy levels, gold undergoes a size-induced metal-insulator transition. This results in a pronounced modification of the physical properties such as the electrical conductivity.[26] The mechanical properties of Au are also affected, and increasing attention has been given to the mechanical properties of nanoporous gold that can reach and overpass the theoretical yield strength of gold.[27–30] Gold nanoparticles are also priviledged tools for interacting with biological media such as cells with their small dimensions and their tunable surface chemistry.[7,12,31–33] The promises of these novel properties are reflected in the extensive number of published scientific articles (> 69.000 in the Web of Science Core data base , topic keyword “gold nanoparticles” on the 10/03/2016).

To tailor the properties of gold at the nanoscale, scientists have been trying to shape gold in a very large variety of nanostructures. As listed by Chanana et al. in the Encyclopedia of Nanotechnology,[3] nanoparticles can be sorted in two major

categories. Isotropic gold nanoparticles include spheres as well as shells. On the other hand, anisotropic gold nanoparticles comprehend nanorods, nanowires, nanoplates and polyhedrons (or facetted nanoparticles). Amongst the numerous strategies to fabricate gold nanostructures, the most commonly used processes are chemical reduction of Au salts in solution and seeding growth. Both steps are assisted by ligand chemistry for the control of size distribution, anisotropy, and self assembling of the particles. M. Daniel and D. Astruc reviewed[7] many other chemical and physical methods developed to fabricate gold nanoparticles. However, for some applications, specific arrangement/assembly of nanoparticles are required to have representative impact (i.e. catalysis, surface enhanced Raman spectroscopy (SERS)).

Furthermore, nanostructured gold can also be synthesized with various surface morphology under the form of nanoporous gold films and nanoporous gold particles. Two main fabrication routes coexist. (1) Galvanic replacement, mostly used to form hollow particles, requires sacrificial elements. The latest is made of a less noble metal and serves as template. It is then oxidized whereas the noble element is reduced and plates its surface.[34] (2) The dealloying process consists in the selective dissolution of the less noble metal of an alloy.[35] Porous gold can be directly synthesized as macroscopic self sustaining systems and direct intergration in devices or systems can be achieved using templated fabrication,[36] nanoimprinting,[37,38] or being designed with lithographic tools.[39,40]

Gold nanostructures are nowadays of particular interest for almost every advanced research and technological fields, including energy storage, energy harvesting, chemistry, catalysis, medicine, drug delivery, cancer therapy, biological sensing, electronics, welding, optics and many others. At this point, two important domains of application have been selected to reflect the pluridisciplinarity of nanoscale gold. Healthcare is one of the major human concern and gold nanoparticles wil play there an important role. Examples include the use of gold nanoparticles (e.g. nanocages), with chemically functionalised surface to selectively target cancer cells, in order to convey drugs and release

them in the intended cells.[31,41] Similar cancer selective gold nanoparticles can also be employed to kill the cancer cells by heat resulting from the exitation of surface plasmon resonance with specific wavelengths.[42] Gold nanoparticles can serve as contrast agent for imaging in cells and in vivo.[43] Therefore, they can operate as sensors, vehicles and even treatment using the specific optical absorption and typical gold-thiol chemistry of gold nanoparticles. A second hot topic is related to environmental issues and the increasing determination to act against global warming. Again, the potential of gold nanoparticles is broad. They can be employed for the treatment of exhaust gas, as shown by M. Haruta with their extreme catalytic activity for the oxidation of carbon monoxide.[24] Green technologies such as fuel cells may also profit from the activity and high surface of nanoporous gold.[44–46]

Despite the obvious qualities of the gold nanoparticles, many challenges remain to both synthesize and better understand the behaviour/properties of the resulting nanoparticles. For exemple, the electrical and thermal propeties of nanostructured gold is not well known and is strongly dependant on the environment and the shape of the particles. The mechanical stability nanostructures with high aspect ratio is low and requires improvement for application.

4. This work

The present work mainly focuses on the synthesis and characterization of three specific types of gold nanostructures, namely AuAg alloy nanowires, porous gold nanowires (PAuNWs), and gold nanocones (AuNCs). This thesis aims providing advanced understanding on the synthesis of these structures as well as their properties, fundamental for their succesful application in sensorics or field emission.

Both structures are fabricated by electrodeposition in etched ion-track templates. This technique consists in: (1) irradiating polymer foils with swift heavy ions; (2) chemically etching of the damaged tracks to obtain nanochannels of controlled

size and shape; and (3) electrodepositing the material in the nanochannels that serve as templates. By developing and optimizing these three main steps, it is thus possible to fabricate high aspect ratio particles with controlled geometry, length, diameter, composition and crystallinity. More details on this technique are presented in Chapter I.

The second part of this work presents the fabrication and characterization of PAuNWs that combine the advantages of both porous gold and nanowires. Due to their extremely large surface, such nanoporous nanowire systems are very attractive for different applications in optics,[47] catalysis,[48] and chemical,[49] and biological[50] sensing, for example as antennae for surface enhanced Raman spectroscopy.[51] In addition, porous gold is of particular interest for fundamental research. As a matter of fact, it already served as model system for corrosion studies,[52] but corrosion in nano-objects or transport phenomena in porous material still require investigations. PAuNWs thus constitute an excellent platform to study these effects, which are relevant for example for their application in sensorics. The PAuNWs are synthesized by electrodeposition of Au−Ag alloy (named in the rest of the thesis as "AuAg") into the cylindrical channels of etched ion-track membranes. In addition, dealloying (selective dissolution of Ag) allows tailoring size and morphology of the porous nanostructures. The fabrication of porous Au nanowires by single-bath electrodeposition of AuAg alloy in templates and subsequent dealloying was first demonstrated by Searson et al.[53–55] Past studies focused on the influence of the initial AuAg wire composition. The dealloying parameters on the resulting porosity was investigated in most cases for wire diameters larger than 200 nm.[49,53–58] This work presents the fabrication of porous nanowires with diameters below 100 nm. Taking advantages of the recent improvements in scanning transmission electron microscopy (STEM) as well as energy dispersive X-ray (EDX) detectors, characteristic properties of the nanowires such as the morphology, crystallinity, or composition are investigated. These analyses reveal the presence of surface effects such as surface segregation that had not been considered until now. To study the electrical and thermal properties of these porous nanostructures, a specific lithography process is

developed. Finally, upcoming transport measurements of porous gold and ultrathin nanostructures will be discussed.

The third part of this thesis is dedicated to gold nanocones. Because of their geometry, cones combine microscopic and nanoscopic dimensions in one structure. While the large base of the cone provides enhanced mechanical stability, the small tip with typical dimensions below 100 nm yields a high aspect ratio and attractive "nano" properties to the cone. In comparison to cylindrical nanowires, nanocones also present improved electrical and thermal contact to the support. Therefore, such cones are very attractive for a wide range of applications in various fields. AuNCs, as Au nanowires, can be used as nanoelectrode to probe chemical electrolyte [59,60] or to apply a potential directly to a living cell. Chemically functionalized gold cone arrays could also mimic the surface of lotus leaves and provide hydrophobic properties as well as self-cleaning properties to transparent surfaces. Taking profit of the optical properties of gold nanoparticles, gold nanocones may also serve as optical antenna or bases for SERS sensors.[61–63] Mounted on a cantilever, single gold nanocones may be used as scanning probe tip for atomic force microscopes. The optical properties of such a tip allow near-field enhanced scanning optical microscopy probes to resolve ultra-fine topographical details.[63] In this work, the suitability of AuNCs with high aspect ratio for field emission related applications is investigated. As a matter of fact, arrays of nanocones can serve as cold cathodes for various applications, such as switchable X-ray tubes,[64–67] powerful mm-wave and terahertz amplifiers,[68,69] mass spectrometers, vacuum sensors,[70] highly efficient light sources,[71] or high-resolution electron microscopes.[72,73] AuNCs are obtained by electrodeposition in assymetric channels of etched ion-track membranes. The synthesis process presented in this work, based on the electrodeposition of gold from the tip to the base of the channel, enables the production of freestanding vertically alligned nanocones with tunable geometry and density. It is noted that the synthesis process has been redesigned in this work in order to provide enhanced mechanical stability and contact to the substrate. Field emission from gold nanocones in a two electrode configuration is exposed in the third section of this thesis. Difficulties

and limitations of these measurement are also discussed. Finally, a proof of concept for the direct synthesis of conical emitter in a triode configuration is shown.

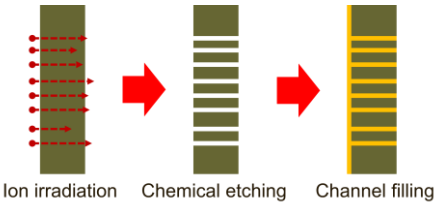

Chapter I

Fundaments of the synthesis of Au nanostructures by the template method

In this work, Au nanostructures are synthesized by electrodeposition in etched ion-track templates. This method is also generally known as the template method and is introduced in this first section. Then, the fabrication of polymer templates by heavy ion irradiation and chemical etching is explained. Next, the basics of metal electrodeposition and more precisely gold and gold alloys are described. The dealloying technique employed to fabricate porous nanowires is then presented. Finally, the various experimental techniques used for the characterization of the nanostructures are discussed.

1. The template method

As its name suggests, the template method consists in the use of a template or cast to shape a material during its fabrication process. This principle is commonly used since thousands years for the patterning and/or reproduction of tools and artefacts including swords, jewelry, or walls. In nanoscience, it has been applied for the

first time by Possin [74] and was further developed at GSI [75–79] and by others.[80–83] The template method consists of three major steps, namely: (1) template fabrication, (2) material deposition in the channels of the template and (3) removal of the template (optional). For the fabrication of nanowires, electrodeposition into the pores of AAO [80] or etched ion-track membranes [74,81] was developed in the 1990s to synthesize nanowires of controlled dimensions, composition, and crystallinity.

Porous alumina templates, often named anodized aluminum oxide (AAO) membranes are fabricated by anodic oxidation of aluminum in acidic solution.[84,85] AAO membranes can be fabricated with controllable channel diameters but their density is determined by their arrangement.[86] One of the major advantages of AAO membranes is the possibility to obtain hexagonally packed parallel channels using self-organization process through double anodization and that allows reaching very high channel densities (10^8 to 10^{12} channels·cm^{-2}).[87] Nevertheless, this technique has little flexibility to modify the channel shape and does not allow easy fabrication of nanostructures other than nanowires, nanorods, or nanotubes. In addition, the removal of the template is often performed using NaOH solution, thus deteriorating non-noble metal wires.

Etched ion-track templates are fabricated by irradiating foils such as mica/silica glass or polymer foils with swift heavy ions.[74,88] The tracks resulting from the passage of the ions are then selectively chemically etched and enlarged converting them into open channels. Thus, the major advantage of etched ion-track membranes relies on its high flexibility. Since each ion produces an etchable track, the channel density can be adjusted. Typical channel densities are between 1 and 10^{10} per cm^2. The upper limit is given by the mechanical stability of the irradiated membranes as well as the overlapping of the channels after etching. The channel shape and diameter is tailored during the etching process. The major drawback of this technique is the necessity of using large ion accelerators. The random distribution of the nanochannels and the limited channel densities achievable can also be a limitation for some applications.

Etched ion-track membranes are commercially available (e.g. Whatman, Sterlitech, Oxyphen, etc.) with limited membrane thicknesses, channel densities, and channel diameters. In order to have direct control over the channel geometry and density, all etched ion-track membranes used for this work were fabricated at the GSI Helmholtz Center in Darmstadt. Usually, membranes irradiated at GSI have stochastic distribution of channels. However ordered patterns can be obtained using a microprobe.[89,90] In addition, by controlling both the irradiation and the etching step, complex structures such as interconnected network of nanochannels or conical nanochannels can be fabricated.[91]

Additional techniques to fabricate templates such as self-assembled di-block copolymers,[92] laser induced self-organization of polyethylene terephthalate (PET),[93] monolayer photonic crystal,[94] interference lithography[95] or electron-beam lithography (EBL)[43,96] have also been reported in the literature. Other nanoporous materials have also been used as templates such as zeolites, aerogels, carbon nanotubes arrays or bio-molecules like DNA as discussed by A. Huczko.[97] Besides the direct use of templates, various techniques can be used for the fabrication of Au nanostructures such as nanoimprint lithography,[37,38] nanotransfer printing,[98] full wafer stencil lithography,[99] ultrasound-assisted interfacial synthesis,[100] electron-beam lithography (EBL) and, focused ion beam (FIB) etching.[40,43,101]

To synthesize metallic nanostructures in the above-mentioned templates, the most common techniques are sputtering (mostly for the lithographic techniques where structures with low aspect ratio, e.g. wires, are deposited from the side), electroless deposition, and electrochemical deposition. In literature also the deposition of material in templates by melt pressing,[102] sol-gel or chemical vapor deposition is reported by Hulteen and Martin.[82] New developments in the atomic layer deposition (ALD) technique and its precursors already allow the conformal deposition of oxides such as Al_2O_3, TiO_2, and SiO_2 [103,104] and is very promising for metal coating of porous templates.

Depending on the application, the template removal may be required. In all cases, the choice of the template is crucial. When the template has to withstand high thermal or aggressive chemical environments (e.g. for applications in electronics), highly resistant polymers such as polyimide (PI) have to be used. Other factors such as thermal expansion coefficient, channel roughness, outgassing, mechanical, and electrical performances, as well as the ease of integration in operating systems have to be considered. Template removal is easily achieved for polymers (e.g. polycarbonate (PC) or polyethylene terephthalate (PET)) with an appropriate organic solvent or acid/base bath. Special attention has to be addressed during the membrane dissolution step not to damage the nanostructures, e.g. due to solvent induced swelling of the polymer or due to capillary forces. Another technique to remove the template and/or template residues is oxygen plasma etching.[105–108]

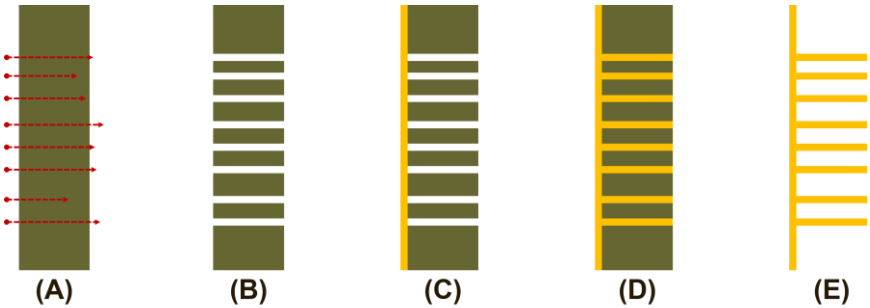

Figure I-1: Schematic of the five steps involved in the synthesis of Au based nanostructures using the template method. (A) Swift heavy ion irradiation of the PC foil, (B) selective chemical etching of the ion-tracks, (C) sputtering of an electrical contact layer, (D) electrodeposition of material in the template, and (E) dissolution of the template

In the following chapter, the fabrication of Au based nanostructures generated by electrochemical deposition of Au and Au alloys in etched ion-track PC templates is presented. Figure I-1 illustrates the five major steps of this technique. First, a thin polymer foil is irradiated with swift heavy ions (Figure I-1A). By selective chemical etching of the ion tracks open channels are formed (Figure I-1B). An electrical contact is sputter coated onto one side of the porous membrane (Figure

I-1C). Au or AuAg is then electrochemically deposited in the nanochannels (Figure I-1D) and if needed the polymer matrix is removed in a suitable solvent (Figure I-1E).

2. Fabrication of etched ion-track templates

In this section, the fabrication of etched ion-track membranes with two different channel geometries, namely cylindrical and conical is presented. The process consists in two major steps, namely the heavy ion irradiation of polymer foils and the selective etching of the ion-tracks.

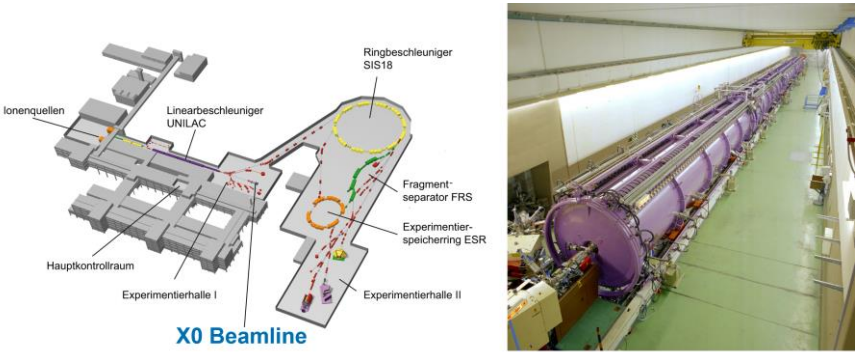

Figure I-2: Schematic representation of the GSI accelerator facility (left) and photography of the universal linear accelerator (UNILAC) of GSI (right).[109] *Irradiation of the PC foils is performed at the UNILAC beamline X0 (blue label)*

2.1. Heavy ion irradiation of polycarbonate

Polycarbonate (PC) foils were irradiated with swift heavy ions with a specific energy of 11.1 MeV/nucleon (≈ 10% of speed of light) at the universal linear accelerator (UNILAC) of GSI. The irradiations were performed in vacuum using the remote control sample exchange system available at the X0 beamline (Figure I-2). When passing through matter, the swift heavy ions lose energy. The energy deposited per unit path length is called the energy loss. It corresponds to the

energy accumulated by the target dE/dx and is defined as the sum of the **electronic** and the nuclear energy losses:

$$\frac{dE}{dx} = \left(\frac{dE}{dx}\right)_e + \left(\frac{dE}{dx}\right)_n \qquad (I\text{-}1)$$

The nuclear energy losses correspond to elastic collisions between the nucleus of the projectile and the atoms of the target. They result in billiard-like displacements of target atoms and lead to the formation of interstitial vacancies and other defects. This stopping process only occurs at very low ion velocities (≤100 keV/nucleon), close to the stopping range of the ion projectile.

At high velocities, accelerated ions predominantly interact with the electrons of the target atoms. The moving ions are stripped of part of their orbital electron and gain a net positive charge Z^*, also called the effective charge. Z^* is empirically defined as:

$$Z^* = Z\left(1 - e^{-\frac{130\beta}{Z^{\frac{2}{3}}}}\right) \qquad (I\text{-}2)$$

with β being the speed of the ions relative to the speed of light, and Z the atomic number of the accelerated ions. For ions at relativistic energies, all electrons are stripped off, $Z^* \approx Z$ and the energy losses are dominated by the electrical force between the ion and the electrons from target atoms. These so-called electronic energy losses are given by the Bethe-Bloch formula:

$$\left(\frac{dE}{dx}\right)_e = \frac{4\pi N Z_t Z^{*2} e^4}{mv^2}\left[\ln\left(\frac{2mv^2}{I}\right) - \beta^2 - \delta - U\right] \qquad (I\text{-}3)$$

N	=	density of target atoms
Z_t	=	atomic number of target atoms
e	=	electron charge
m	=	electron mass
v	=	speed of the projectile
I	=	ionization energy of the target atoms
δ	=	relativistic correction factor
U	=	low velocity correction factor

The consequences of the electronic energy losses are either to excite target electrons to higher energy levels or to eject them from their orbital. Such **ionization** processes result in the emission of energetic electrons also called delta rays, which can further ionize and excite atoms over large radial distance from the central ion path. This **electron cascade** around the ion path can lead to the formation of ion-tracks. Since $(dE/dx)_e$ scales with $(Z^*)^2$, the energy deposition of heavy projectiles is significantly larger than low-Z projectiles.[110]

Several models have been proposed to clarify the formation of ions tracks.[111,112] The Coulomb-explosion model suggests that the ion tracks result from intense ionization and excitation along the ion path, which leads to electrostatic repulsion of the ionized target atoms in the track. The thermal-spike model assumes a strong temperature increase due to the energy deposited by energetic ions.

Polymers are in general very sensitive to radiations and easily register ion-tracks due to the irreversible damaging of the polymer structure. In agreement with simulations, several studies conducted in the past decades prove that the passage of swift heavy ions results in a cylindrical damage zone of a several nanometers of diameter.[113] Damages to aromatic polymers (e.g. PET, PC) induced by swift heavy irradiation mainly results in the modification of the structure and of the chemical composition of the polymer. Dehaye and al. showed that the irradiation damages depend on the stopping power of the ion, i.e. on the energy of the ion and its atomic number, consistently with the Bethe-Bloch equation (I-3).[114] With the use of Au ions at a specific energy of 11.1-11.4 MeV/nucleon, the fast and high energy deposition is expected to be able to **alter any type of chemical bond**.[115,116] However, the main-chain scission may occur favorably in the chemical group with the weakest bonds: the carbonate group.[114] Other consequences of electronic excitation and radicals' formation are the outgassing of volatile fragments such as CO, CO_2, CH_4 and C_2H_2, crosslinking, and formation of unsaturated bonds such as alkynes that were observed by means of Fourier Transform Infrared spectroscopy (FTIR) and Mass Spectrometry (MS).[114,117–119]

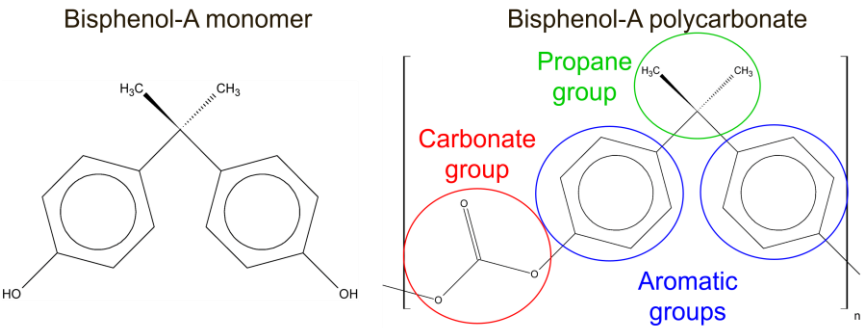

Figure I-3: Molecular structure of Bisphenol-A polycarbonate used for template fabrication and corresponding Bisphenol-A monomer

Polycarbonates are polymers consisting of organic functional groups (monomer) linked together by carbonate groups. Easily etched in basic solutions and easily dissolved in organic solvents such as dichloromethane, *Bisphenol-A* polycarbonates are ideal polymers for the fabrication of templates. Generally synthesized from the starting monomer 2,2-Bis(4-hydroxyphenyl)propane (well-known under the name Bisphenol-A), these polycarbonates entail 3 main functional chemical groups represented in Figure I-3, namely carbonate, alkane and aromatic groups. In the present work, different types of commercially available polycarbonate foils were used: Makrofol N/KG (Bayer) and Pokalon 462, 470 and N032 (LOFO). Because their chemical structures are identical, their properties are similar and the two polymers differ only in the applied synthesis process and in the contained additives. The two polymers can easily be identified by their color, yellow for Makrofol and translucent for LOFO foils.

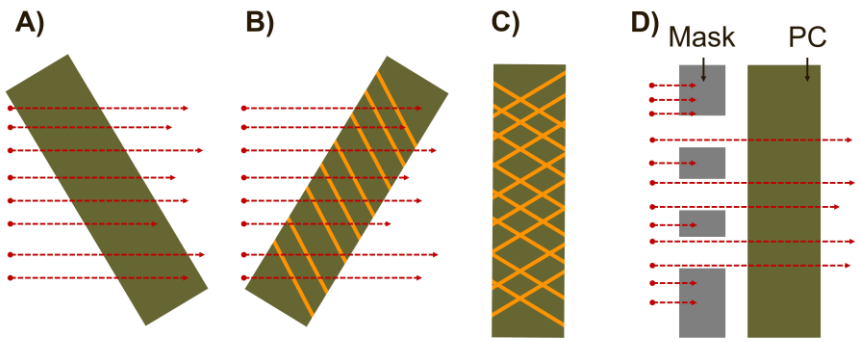

Figure I-4: Schematic of irradiation of under tilted beam incidence for networks production (A, B, and C) and patterned irradiation using a mask (D)

The projected range of Au ions at energy of 11.1 MeV/nucleon in polycarbonates is about 150 µm according to SRIM simulations.[120] For irradiation, stacks of foils with a total thickness below 110 µm were prepared in order to benefit from a rather homogeneous energy deposition within the foils of a stack. When the ion passes through the foil, it follows a straight line. Thus, the tracks are parallel oriented. It should be emphasized that each individual swift heavy ion undergoes electronic stopping. Therefore, each **individual swift heavy ion** passing through the PC foils creates one **individual linear ion-track**. It is thus possible to adapt the track density by controlling the ion fluence. Additionally, the beam incidence angle can be varied. By irradiating a polymer foil under different orientations (Figure I-4A and B), it is possible to create a network of cross-linked ion tracks (Figure I-4C). This technique has been used for the fabrication of nanowire networks.[78,121] The track distribution can also be patterned using an irradiation mask in front of the polymer as shown in Figure I-4D. This process is used in this work to fabricate patch arrays of nanocones and is presented in chapter IV and V.

After swift heavy ion irradiation and prior to track etching, the irradiated polycarbonate foils are illuminated with ultra-violet (UV) light (30 W, T-30M, Vilbert Lourmat) for 1 hour on each side. UV treatment is known to narrow the pore diameter distribution after etching.[122] Virk et al.[117] demonstrated in their UV-Visible (UV-Vis) analysis that pristine polycarbonate is transparent to UV

whereas ion-irradiated polycarbonate absorbs. Therefore, UV treatment mostly affects the tracks but not the non-irradiated polymer (so called bulk polymer or matrix). By selective **photo-degradation** of the damaged polymer in the ion tracks, the track etch rate increases compared to the bulk etch rate.[113,123–125]

Advanced studies of ion tracks by conductommetric measurements on PET and PC by P. Apel et al. show that the ion tracks are constituted of two zones with different etching behaviors.[126–128] On the one hand, the severely damaged track core is very sensitive to sodium hydroxide (NaOH) and has an etching rate much higher than the bulk. On the other hand, the track halo formed around the track core by the electron cascade. In PET, a halo region was identified, where the etching rate was lower than the bulk etching rate probably due to cross-linking. This halo is a ring ranging up to several hundreds of nanometers around the track core.

2.2. Chemical etching

The second step for the fabrication of the etched ion-track templates is the selective chemical etching that converts ion tracks in the polycarbonate foils into open nanochannels. By careful selection of the etching geometry, etching solution, etching time and etching additives, the geometry and size of the channel are controlled. The basics of the etching process and the experimental conditions used for the present work are presented.

2.2.1. Etching rate

Given the severe radiation damages produced along the ion trajectory, ion tracks have a different etching rate than the bulk polymer. The **track etching rate** v_t is defined as the etching rate along the track while the **bulk etching rate** v_b is defined as the etching rate of pristine material. PC being an amorphous polymer, v_b is isotropic by definition. The **radial etching rate** v_r is defined as the nanochannels' enlarging etching rate, perpendicular to the track direction. The parameter of interest for template application is the final diameter of the nanochannels $\emptyset_c$ which is defined by $\emptyset_c = v_r * t$.

These three different etching rates are schematically represented in Figure I-5.

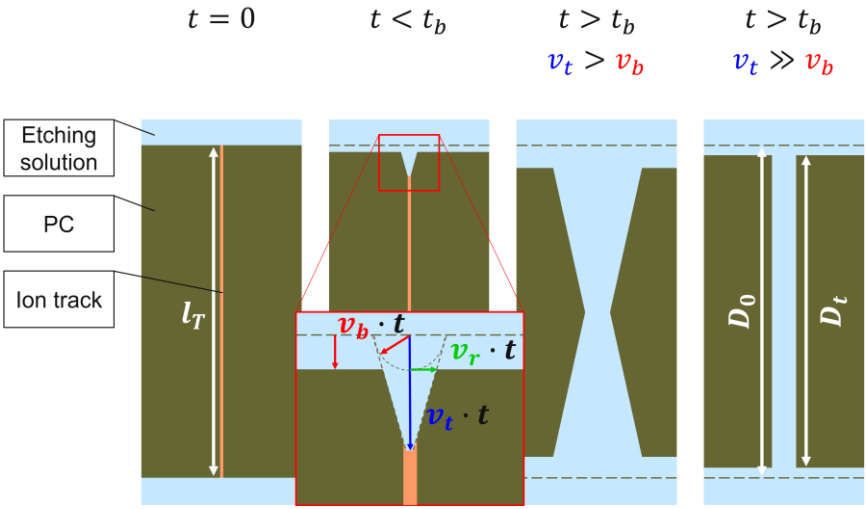

Figure I-5: Schematic representation of the track etching at different etching times with respect to the breakthrough time t_b and with various ratio of the bulk vs. track etching rate

The formation of a nanochannel by etching is characterized by its breakthrough time t_b, which corresponds to the time necessary for the complete etching of a track thus creating a continuous channel from one side of the PC foil to the other. By definition, in isotropic etching conditions, the track etching rate can be determined by measuring the channel breakthrough time t_b and the initial track length $l_T(t = 0)$.

$$v_t = \frac{l_T(t = 0)}{2 * t_b} \qquad (I\text{-}4)$$

The initial track length is equivalent to the initial PC foil thickness D_0. Under the same etching conditions, the bulk etching rate is defined as:

$$v_b = \frac{D_0 - D_t}{2 * t} \qquad (I\text{-}5)$$

with $D_t = l_T(t)$ being the PC foil thickness after etching and t the etching time.

The norm of the radial etching rate $v_r(z,r)$ is directly dependent on v_t and v_b. On the one hand, the channel can enlarge only if the track core is already etched and filled with etchant (dependence on z, position along the track: $z = v_t * t$). On the other hand, the radial etching rate is not constant but varies as a function of the etched radius and consequently with time. In fact, at the beginning of the etching, the radial etching rate is equal to the track etching rate, because etching occurs preferentially in the highly damaged track core. This very high initial radial etching rate also justifies that the minimum channel diameter achievable is about 10 nm in 10 µm thick PC membranes and larger for thicker foils. For long etching times, the damaged tracks are completely etched away and the channels continue to enlarge at the bulk etching rate. Therefore:

$$\lim_{t\to 0}(v_r) = v_t \qquad (I\text{-}6)$$

and

$$\lim_{t\to \infty}(v_r) = v_b \qquad (I\text{-}7)$$

As mentioned in section 2.1, several works report experimental curves of the etching rate vs. pore radius in various polymers as a function of the energy deposited by the ion. [126,127,129–132]

In most cases, the radial etching rate vs. pore radius curves have the following shape:

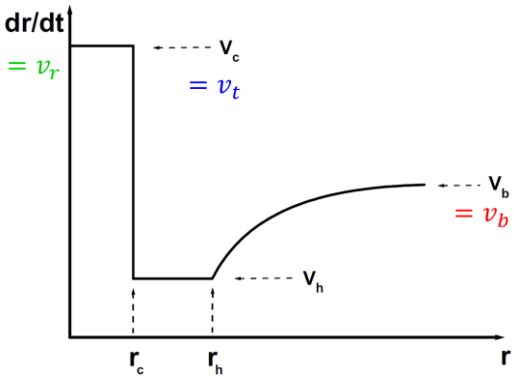

Figure I-6: Schematic model of radial etching rate of ion tracks, Reproduction with permission of Elsevier[*132]

Other studies evidenced the influence of many other parameters on the radial etching rate such as the track density, etchant concentration, temperature, or concentration of etching products in the etchant. [122,133]

Because v_r is intimately related to v_t and v_b, it is possible to monitor the geometry of the pore by tailoring the v_t/v_b ratio. Experimentally, the etching rates are mostly adjusted by controlling the etching solution (concentration, temperature). The etching of PC results from the action of hydroxide ions (HO^-) present in basic aqueous solutions. Standard etching solutions are based on aqueous sodium hydroxide solutions (NaOH). Changing the NaOH concentration modifies both v_t and v_b; higher concentrations lead to higher etching rates. On the contrary, adding organic solvent (i.e. methanol (MeOH) or ethanol) to dilute NaOH aqueous solution results in a larger decrease of the track etching rate than

[*] Reprinted from *Nuclear Instruments and Methods in Physics Research Section B: Beam Interactions with Materials and Atoms*, 236, Zhu, Z.; Maekawa, Y.; Liu, Q.; Yoshida, M., Influence of UV light illumination on latent track structure in PET, 61-67, Copyright (2005), with permission from Elsevier.

the bulk etching rate. In the present work, methanol (MeOH) was used to tailor the v_t/v_b ratio and thus tune the geometrical shape of the pores.

The channel geometries resulting from two different v_t/v_b ratio, namely biconical and cylindrical are shown in Figure I-5 and will be discussed in the following paragraphs.

2.2.2. Cylindrical etching: $v_t \gg v_b$

In the case where the bulk etching rate is negligible compared to the track etching rate, the etching along the track prevails and rapidly heads to the breakthrough. The resulting channel is quasi cylindrical and has a very small diameter (smallest diameter achievable is 10-15 nm [134]). Continuation of the etching after breakthrough leads to homogeneous enlarging of the nanochannels at the radial etching rate. By controlling the etching time, it is thus possible to adapt the diameter of the **cylindrical nanochannels**. By plotting the nanochannels diameter vs. etching time, it is thus possible to deduce v_r.

In this work, cylindrical nanochannels etching was performed by dipping the irradiated PC foils in 2M NaOH aqueous solution at 50 °C for defined times. A direct relation between the diameter of nanowires electrodeposited in the nanochannels and the etching time in **isotropic etching** conditions will be discussed in Chapter II.

2.2.3. Conical etching: $v_t > v_b$

In the case where the bulk etching rate is only slightly smaller than the track etching rate, track etching and channel widening occur simultaneously. This results in non-cylindrical channels. If the etching is performed under symmetric conditions, i.e. etching from both sides of the membrane, the resulting nanochannels are biconical as shown in Figure I-5. **Conical nanochannels** can be obtained by asymmetric etching,[135] where only one side of the PC foil is exposed the etching solution and on the other side to a stopping solution (e.g. water).

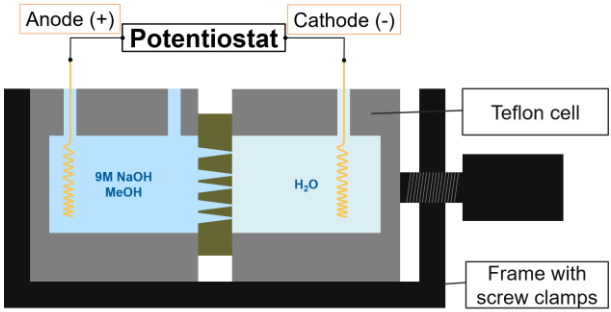

Figure I-7: Scheme of experimental setup used for asymmetric etching and fabrication of conical channels

In this work, conical channels were experimentally obtained by **asymmetric etching** geometry. An etching solution of 9M NaOH:MeOH (typically 40:60 volume ratio) was used on one side of the foil while a water stopping bath was placed on the other side (*chemical stopping*). In addition, a voltage of 1V was applied between two Au coil electrodes to monitor the breakthrough of the pores and to repel the etching HO^- anions from the small opening of the channel (*electrical stopping*). Figure I-7 schematically represents the setup used for asymmetric etching. The temperature was regulated by a heating plate and kept at 30 °C during the etching process.

3. Electrodeposition of Au and AuAg alloys

The aim of this section is to introduce the concept of electrodeposition, to present the electrodeposition setup and conditions, as well as the various electrolytes used for the electrodeposition of Au and AuAg in the channels of PC membranes.

3.1. Basics of electrochemical deposition

When a metal M is immersed in a solution containing ions of the same metal M^{n+}, the potential difference between the two media leads to metal ion exchange between the solid and the electrolyte. Some ions from the metal lattice enter the solution while some ions from the solution crystallize in the lattice.

At dynamic equilibrium, with no external contribution, this exchange can be summarized by:

$$M^{n+} + ne \rightleftharpoons M \qquad (I\text{-}8)$$

The reaction from left to right is called reduction and consumes electrons whereas the reverse reaction is named oxidation. At **dynamic equilibrium**, with no external contribution, the metal-solution interface is not polarized. Therefore, the current generated by the reduction reaction (cathodic current) and the current resulting from the oxidation reaction (anodic current) are equivalent. The equilibrium potential of the reaction (I-8) is defined by the **Nernst equation**:

$$E_{eq} = E° + \frac{RT}{nF} \ln \frac{a_{M^{n+}}}{a_M} \qquad (I\text{-}9)$$

with $E°$ being the standard potential, R the gas constant, T the absolute temperature, n the number of electrons involved in the reaction (I-8) and F the Faraday constant (96485 C). $a_{M^{n+}}$ and a_M refer to the activities of M^{n+} and M respectively. For a solid metal M, the activity is $a_M = 1$. The activity of the ionic species $a_{M^{n+}}$ is proportional to the ion concentration and defined by:

$$a_{M^{n+}} = \gamma C_{M^{n+}} \qquad (I\text{-}10)$$

with γ being the activity coefficient of M^{n+} and $C_{M^{n+}}$ its concentration. The activity coefficient γ depends on the concentration of all ions present in the solution.

To polarize the interface region, a second electrode immersed in the same solution is necessary. The two electrodes system combined with the electrolyte form an **electrochemical cell** and each individual electrode is a half-cell. Therefore, each half-cell has an equilibrium potential (defined by Nernst equation) and they are equivalent if the two electrodes are made of the same metal. When an external potential E is applied between the two electrodes, a current I flows in between them and their potentials defer from E_{eq}. These half-cell potentials shifts are

called overpotentials. The cell potential is then equivalent to the sum of the two half-cell potentials added to the potential drop resulting from the resistance of the electrolyte:

$$E = \eta_c - \eta_a + I * \mho \qquad (I\text{-}11)$$

with η_c being the cathodic overpotential, positive by definition, η_a the anodic overpotential, negative by definition, I the current flowing through the cell and $\mho$ the electrolyte resistance.

The **cell overpotential** η is defined as the potential difference between equilibrium cell potential in open circuit conditions $E_{o.c.}$ and the cell potential under **external load** $\boldsymbol{E}$.

$$\eta = E - E_{o.c.} \qquad (I\text{-}12)$$

The electrochemical deposition or electrodeposition of a metal is based on the application of a potential between two electrodes immersed in the same electrolyte. At an appropriate cell overpotential, the polarization of the two metal-electrolyte interfaces leads to the deposition of mater at the cathode by reduction of the metal ions and oxidation at the anode (dissolution of the metal anode, oxygen evolution). At a given overpotential η, hindrances from the overall cell reaction have to be considered. Therefore, each reaction step, namely, the *charge transfer* across the double layer (activation), the *mass transport* (i.e. diffusion), the *chemical reaction* and the *crystallization*, may influence the total current resulting from an applied η. The slowest process is usually considered as the limiting process, which determines the overall cell reaction rate, and is named the **rate-determining step** (RdS). The RdS depends on the cell overpotential. Figure I-8 shows general current-potential curves exhibiting charge transfer RdS at low potential and mass transport RdS at high potential.

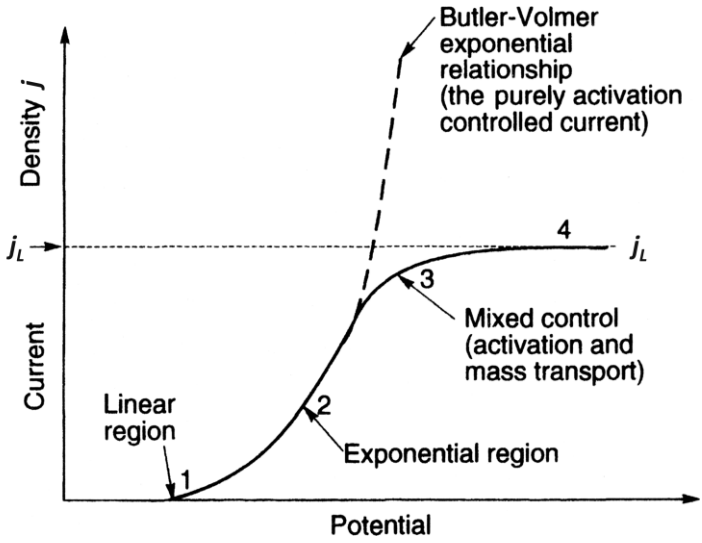

Figure I-8: Typical current density - potential curves for metal electrodeposition showing four regions: (1) linear; (2) exponential; (3) mixed control; and (4) limiting current density region. Reproduction with the permission of John Wiley & Sons, Inc.†[136]

If the charge transfer is the RdS, the current density j flowing in the cell is given by the **Butler-Volmer equation**:

$$j = j_0 \left(e^{\frac{(1-\alpha)nF\eta}{RT}} - e^{\frac{-\alpha nF\eta}{RT}} \right) \qquad (I\text{-}13)$$

with α the charge transfer coefficient and j_0 the exchange current density.

The current density depends linearly on the overpotential at very low voltages (Figure I-8(1)) whereas they are related by an exponential law at higher potentials (2). At very high overpotential (4), the metal-electrolyte interface is ion depleted and each metal ion reaching the electrode is directly reduced. The rate-determining step is then mass transport. The Nernst diffusion-layer model – which

† Reprinted from *Modern Electroplating*, 5th Edition, Schlesinger, Mordechay; Paunovic, Milan, Fundamental considerations, p6, Copyright (2010), with permission from John Wiley & Sons, Inc.

assumes a linear concentration gradient of the electrolyte in the Nernst diffusion layer – thus suggests the existence of a **limiting diffusion** current density j_L that only depends on the electrolyte concentration as shown in equation (I-14):

$$j_L = \frac{nFDC_O^*}{\delta} \qquad (I\text{-}14)$$

where C_O^* is the concentration of the bulk, D the diffusion coefficient of the metal ion, F the Faraday constant, n the number of charges involved in the reduction of the metal ion and δ the thickness of the Nernst diffusion layer. Equation (I-14) suggests that at high enough overpotentials, the electrodeposition current is independent of the applied potential and depends only on the electrolyte concentration.

3.2. Au and Ag electrolytes and current efficiency

For the electrodeposition of Au in the nanochannels of etched ion-track templates, two different electrolytes were used, namely Au(1)-cyanide (AuCN) electrolyte and Au(1)-sulfite (AuSF) electrolyte. In these electrolytes, the Au(1) complexes are $[Au(CN)_2]^-$ and $[Au(SO_3)]^-$ respectively. For the electrodeposition of Ag and AuAg, a cyanide electrolyte was used. The Ag(1) complex is $[Ag(CN)_2]^-$. The properties of these three complexes are summarized in Table I-1. It is noted that the cyanide complex is very stable in aqueous solution whereas the sulfite electrolyte is much less stable and tends to decompose spontaneously at room temperature to form solid Au. To avoid unprompted decay, the sulfite-based gold electrolyte is stored at 4 °C until use. In addition, the commercial electrolyte used (Make-up Gold-SF, 15 g/L, METAKEM GmbH) contains several stabilizing additives. The cyanide electrolytes were prepared at GSI from $KAu(CN)_2$ and $KAg(CN)_2$ powders (Carl Roth). To maintain the pH of the cyanide based electrolytes basic (pH ~ 13), all solutions were prepared with Na_2CO_3 (99.5%, Sigma Aldrich) at a concentration of 0.25 M/L.

Table I-1: Properties of Au(1) and Ag(1) complexes used for electrodeposition of Au and AuAg

Metal complex	**Stability constant** [137,138]	**Half reaction**	E^0 **vs. standard hydrogen reference** [139,140]
$[Au(CN)_2]^-$	10^{39}	$[Au(CN)_2]^- + e^- \rightarrow Au + 2CN^-$	-0.595
$[Ag(CN)_2]^-$	10^{20}	$[Ag(CN)_2]^- + e^- \rightarrow Ag + 2CN^-$	-0.446
$[Au(SO_3)]^-$	10^{10}	$[Au(SO_3)]^- + e^- \rightarrow Au + 2SO_3^-$	0.111

According to the half reaction provided in Table I-1, one single electron (n = 1) is used for the reduction of one atom of Au or Ag. Thus, it is possible to correlate the charge Q used during the potentiostatic electrodeposition of these metals (experimentally obtained by integration of the *I-t* curves):

$$Q = \int I\,dt \qquad \textit{(I-15)}$$

with the mass m_{elect} theoretically deposited defined as

$$m_{elect} = \frac{Q * M}{F * n} = \frac{Q * M}{F} \qquad \textit{(I-16)}$$

Where M is the molar mass and F the Faraday number (96485 C·mol^{-1}).

Thus by comparing the mass computed from the *I-t* curves m_{elect} with the mass effectively electrodeposited and weighted m_{weig}, it is possible to estimate the current efficiency (equation (I-17)) of the electrodeposition process as a function of the utilized conditions.

$$\text{current efficiency} = \frac{m_{weig}}{m_{elect}} \qquad \textit{(I-17)}$$

The **cyanide-based** electrolytes were used for the co-deposition of Au and Ag. The detailed compositions of the various solutions used are detailed in Chapter II. Both metals crystallise in the face-centred cubic (fcc) close-packed structure, with very similar lattice parameters (4.0862 Å for Au and 4.0782 Å for Ag).[141] In addition, their electronegativities (χ(Au) = 1.19 and χ(Ag) = 1.08) are also

comparable.[140] Thus, the **Au-Ag alloy** (AuAg) system is generally considered as a perfect solid solution at any composition as shown in the AuAg phase diagram (Figure I-9).

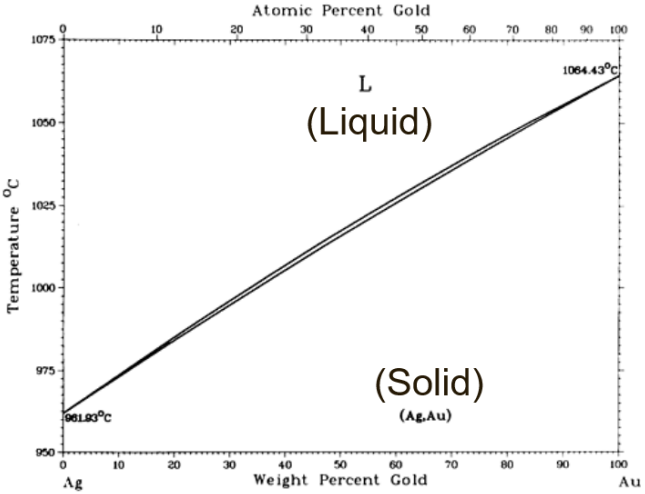

Figure I-9: AuAg phase diagram. Reproduced with permission of ASM International‡[18]

Standard electrodeposition from cyanide electrolytes is performed at 60 °C by applying a negative potential of - 1.1 V vs. Ag/AgCl reference. Here the sputtered Au film on one side of the membrane serves as working electrode and a Pt coil is used as counter electrode. Experimental details for this type of deposition are available in Chapter II.

For the electrodeposition of gold backelectrodes and for the electrodeposition of nanocones, the commercial AuSF electrolyte was employed as received. Standard electrodeposition from AuSF is performed at 60 °C by applying a - 0.375 V potential vs. Ag/AgCl reference between the working electrode (sputtered Au)

‡ Reproduced from *ASM Handbook*, Baker, Hugh, Volume 3: Alloy Phase Diagrams, Copyright (1992), with permission from ASM International.

and the counter electrode (Au coil). More experimental details are available in Chapter IV.

4. Characterization methods

The **crystallographic orientation** of the nanowire arrays embedded in the PC membrane was analyzed by *X-ray diffraction (XRD),* using the Cu K_α radiation of a Seifert X-ray generator and HZG-4 goniometer in Bragg-Brentano geometry. For further characterization of the electrodeposited nanostructure, the PC membrane was dissolved by three consecutive dichloromethane baths. The nanostructures are then either directly studied on their backelectrode after drying or transferred by drop casting onto a substrate of interest.

Scanning electron microscopy (SEM) images were obtained with a field-emission scanning microscope (FESEM) JSM-7401F (JEOL) operated at 10 or 20 kV and a JSM-6510 (JEOL) operated at 27 kV (Bergische Universität Wuppertal). Both secondary electron images (SEI) and lower secondary electron images (LEI) were obtained using the JSM-7401F to combine high spatial resolution and topological information on the studied sample. Scanning transmission electron microscopy (STEM) mode of the JSM-7401F was also used for detailed compositional and **morphological characterization** of nanowires deposited on transmission electron microscope grids.

For *transmission electron microscopy* (TEM) analysis of AuAg nanowires, lacey-carbon/copper grids (CuC) were employed, while silicon nitride (Si_3N_4) TEM membranes (20 nm thickness, Plano GmbH), were used for the fabrication and investigation of porous wires, because they are resistant to nitric acid. **Geometry and crystallinity** of the nanowires were investigated by bright-field (BF), high-angle annular dark-field (HAADF) and high-resolution TEM (HRTEM) imaging in a probe corrected JEOL ARM200F operated at 200 kV at the MPI for Solid State Research of Stuttgart.

The **composition** of the various nanostructures was studied by *energy dispersive X-ray spectroscopy (EDX)*. The average composition of nano-objects was measured in the SEM with the EDX detector of the JSM-7401F (Bruker). Spectra recorded applying an acceleration voltage of 20 kV were analyzed using the Bruker Quantax Software with the M-lines of both Au and Ag. Composition analysis – with a spatial resolution between 0.3 and 3 nm depending on the position and thickness of the given wire – was undertaken by EDX using a JEOL Centurio detector with a solid angle of 0.98 sr in the JEOL ARM200F. For quantification, the standard-less Cliff-Lorimer technique was applied using the Au-M and Ag-L lines in Thermo Scientific NSS software 3.2. Standard HAADF imaging and EDX analysis is performed within a delay of 72 h after dissolution of the polymer template.

The **topography** of large samples was measured by *optical profilometry* with a MicroProf® profilometer (FRT GmbH). The CHR 150 optical sensor illuminates the sample with split white light using passive chromatic aberration optics. Using a miniaturized spectrometer, the sensor detects which wavelength is reflected by the sample and thus determines the height of the sample. Vertical resolution of the spectrometer is about three nm whereas the lateral resolution determined by the optical spot size and the step motors is about 2 µm.

5. Summary

In this first section, we reviewed the basics of the template method used in this work. At first, the swift heavy ion irradiation of PC leads to the formation of ion-tracks. Then, the selective chemical etching of these tracks is applied to obtain nanochannels with tunable geometries. After introducing the bases of electrochemistry, the dealloying process employed to form porous gold from AuAg alloys was presented. Finally, the major analysis methods used to characterize nanostructures, namely XRD, SEM, TEM, EDX and optical profilometry were presented. In the following chapters, the experimental

condition for the fabrication of PAuNWs (Chapter II) and AuNCs (Chapter IV) as well as their characterizations will be detailed.

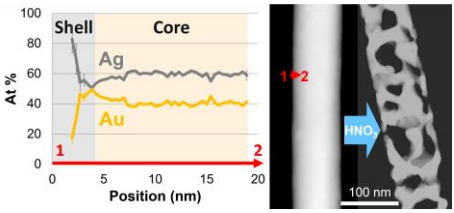

Chapter II

Porous gold nanowires synthesized by dealloying of AuAg alloy nanowires

In the present chapter, the fabrication and characterization of nanowires by electrodeposition of AuAg into the nanochannels of etched ion-track polymer membranes is described. Crystallinity, morphology, and composition of wires with various diameters from 30 to 400 nm are investigated by means of XRD, high-resolution SEM, TEM, STEM, and EDX analysis. EDX analysis with very high spatial resolution (below 1 nm) reveals the presence of surface enrichment. A Ag-rich layer in $Au_{40}Ag_{60}$ wires and a Au-rich layer in $Au_{60}Ag_{40}$ wires with thicknesses between 1 and 4 nm are observed. Furthermore, the dealloying process is investigated on both types of wires. We show that Ag-rich wires become porous whereas Au-rich wires remain solid cylinders. The results clearly indicate that the analyzed AuAg nanowires do not consist of homogeneous solid solution, but surface effects before and during the dealloying play an important role for the final morphology of the wires.

Results exposed in this chapter are partly published in [142,143].

(142) Burr, L.; Schubert, I.; Sigle, W.; Trautmann, C.; Toimil-Molares, M. E. Surface Enrichment in Au–Ag Alloy Nanowires and Investigation of the Dealloying Process. J. Phys. Chem. C 2015, 119 (36), 20949–20956, DOI: 10.1021/acs.jpcc.5b05596.

(143) Schubert, I.; Burr, L.; Trautmann, C.; Toimil-Molares, M. E. Growth and Morphological Analysis of Segmented AuAg Alloy Nanowires Created by Pulsed Electrodeposition in Ion-Track Etched Membranes. Beilstein J. Nanotechnol. 2015, 6, 1272–1280, DOI: 10.3762/bjnano.6.131.

1. Introduction to dealloying of AuAg

Bulk materials and thin films with nanoporosity attract great attention due to their high surface-to-volume ratio. Even though nanoporosity is not a defined standard by the IUPAC – which set the term microporosity for structures with pores with diameter below 2 nm and mesoporosity for pores dimensions ranging between 2 and 50 nm [144] – it is commonly defined as porosity with dimensions between 1 and 100 nm.[145] In this thesis, all the porous structures treated are mesoporous but are described with the generic term nanoporous. Historically, nanoporous Au was the first system to be studied serving as a model system for corrosion.[52] Its relatively easy fabrication by wet chemistry and its attractive physical and chemical properties are most interesting for both fundamental research and applications.[6] Most of the nanoporous structures are obtained by dealloying, which consists in selectively leaching the less noble metal of a given alloy. This rather simple process can be applied to many different alloys and allows good control over the porosity.[146–148]

As above-mentioned, the dealloying corresponds to the selective dissolution of one of the constituent of a solid solution alloy. The more electrochemically active element, often the less noble metal is preferentially leached from the alloy by galvanic corrosion. The **corrosion** process depends strongly on the environmental conditions and can result, under specific circumstances, in the formation of nanoporous material. Already used by pre-Columbian civilizations to purify the surface of gold based artifacts and make them look more attractive, the interest for gold dealloying returned with Forty et al. and their corrosion studies.[6,52,149] Since the 1970s, the AuAg system serves as model for the investigation of dealloying and the fabrication of nanoporous structures. The recent interest in such systems results in a better understanding of the prerequisite for nanoporosity

formation.[6] During the dealloying process, structural, kinetic, and thermodynamic considerations account in the competition between **dissolution** and **diffusion**. One of the first models proposed by Pickering and Wagner included the bulk diffusion of silver to the electrolyte according to a vacancy-mediated process.[150] Because diffusion processes are known to be extremely slow and due to the lack of experimental evidence, Erlebacher and Sieradzki proposed a surface diffusion model.[35,151] It is notorious that surface diffusion is faster than bulk diffusion but the evolution of imaging techniques as well as in situ observations evidence even accelerated surface diffusion in contact with an electrolyte.[152]

In a first model, only the geometric conditions of percolation – i.e. formation of a continuous path – of Ag atoms are considered as a minimum structural requirement. In the case of face centered cubic crystal lattice such as for AuAg, the percolation limit is derived about 20 at.% Ag. At such low Ag concentration, dealloying has never been experimentally observed. As a matter of fact, a monoatomic wide "pore" issued by the dissolution of a 1 atom wide percolation path present several counter arguments for porosity evolution. First, except for the surface Ag atom, all atoms of a monoatomic path below the surface have a high coordination number, which result in the necessity of a prohibitive driving force to allow their dissolution. Second, the diffusion of the electrolyte in such a small "pore" may also be problematic. Finally, the pore can easily be blocked by the diffusion of a Au atom, which would permanently stop the porosity evolution. Thus, the removal of one single Ag surface atom does not provide sufficient access to the deeper layers.

More recent models developed with Kinetic Monte Carlo simulations, assume that the dissolution of Ag atom is favorable only when their coordination number (i.e. the number of direct neighbors, CN) is strictly below 10 and estimate percolation limit of about 55 at.%. This value is close to the parting limit observed experimentally between 55 and 60 at.%.

The geometric considerations presented above are independent on the experimental conditions and thus only correlate the possibility of porosity

evolution in a AuAg system with its composition. A better understanding of the porosity evolution also needs to consider surface diffusion of Au atoms as well as thermodynamic requirements. Corrosion can occur only if the potential difference between the electrolyte and the metal is negative. At low potential, the dissolution of Ag is slow and the Au enrichment of the surface by diffusion leads to passivation. The consequences of Ag atom dissolution driven by the electrolyte-alloy potential difference are the decrease of free energy of the system. This stabilization is due to the loss of highly electrochemically active Ag. On the other hand, the free energy increases due to the creation of new surfaces. Thus, the porosity evolution only occurs above a **critical potential** E_c where the silver dissolution related loss of energy counteracts and overpasses the energy gain due to surface increase. In other words, above E_c the dissolution phenomenon occurs at a rate high enough to compete with the displacement of Au atom. As mentioned above, the porosity evolution is the result of a kinetic competition between the re-arrangement of the Au atoms by surface diffusion and the dissolution of Ag atoms.

Logically and consistently with structural considerations, the higher the coordination number, the stronger the binding to the metal lattice, and the lower the rate of dissolution. For all atoms where dissolution is relevant, the Ag atoms embodied in a flat surface (CN = 9) are more difficult to remove. Thus, the rate-limiting step is the formation of terrace vacancies (for low energy (111)-oriented surface). Dissolution then proceeds layer by layer as shown in Figure II-1. To minimize the surface energy, gold atoms diffuse and form clusters that locally passivate the alloy. The continuation of Ag dissolution results in the formation of mounds (Figure II-1C). Due to Au diffusion to Au rich areas, mound bases that become poor of gold are corroded, resulting in the formation of a ligament as shown in Figure II-1D.

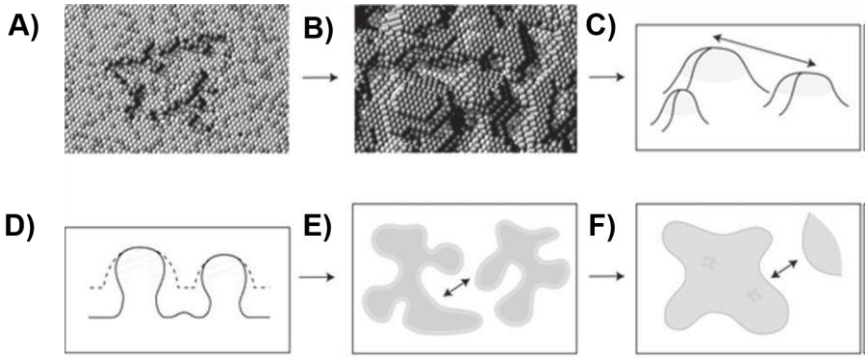

Figure II-1: Scheme of various steps of porosity formation: (A) formation of terrace vacancy by dissolution of Ag (RdS), (B) layer by layer continuation of the dissolution and (C) formation of Au enriched mounds by surface diffusion; (D) ligament formation by Au depletion at the base of the mounds and (E) branching of the ligament to form a porous network; (F) Continuation of the corrosion process leading to coarsening of the ligaments. Reproduced by permission of The Royal Society of Chemistry [§]

When the ligament extend, i.e. when the diffusion path to the Au-rich cluster is too long, Au atoms aggregate and form new clusters leading to the formation of new ligaments. This process finally results in the formation of a 3D nanoporous network of Au rich ligaments. Kinetic Monte Carlo simulations taking into account the structural limitations as well as the kinetics of dissolution and surface diffusion process yield percolation limits of about 60 at.%, very close to the experimental parting limit.[153]

Experimentally, highly oxidative solutions (such as sulfuric or nitric acid) or an externally applied potential between the alloy and a counter electrode in the electrolyte are used to place the system above the critical potential. In the presence of an electrolyte, the *enhanced surface diffusion of Au atoms* results in the continuation of corrosion after initial porosity formation. The size of Au clusters

[§] Reproduced from *Nanoporous Gold : From an Ancient Technology to a High-Tech Material*, Wittstock, Arne; Biener, Jürgen; Bäumer, Marcus; Fundamental Physics and Chemistry of Nanoporosity Evolution During Dealloying, p11-28, Copyright (2012), with permission from The Royal Society of Chemistry; http://dx.doi.org/10.1039/9781849735285-00011 .

and of voids then tends to increase in volume. This results in the coarsening of the porous structures (Figure II-1F). Several strategies have been developed to counteract coarsening with the dealloying applied at low temperature to minimize Au surface diffusion or using Pt atoms that are less labile to reduce Au atom mobility. Porosity thus obtained can reach 2-5 nm whereas typical porosity is about 10 nm.[147,154,155] In this work, dealloying was obtained by free corrosion in concentrated nitric acid without applying any external potential.

To combine the advantages of porous gold and 1D nanostructures we fabricated porous Au nanowires (PAuNWs). The aim was to investigate by high spatial resolution techniques if the percolation model applies to nanowires. The fabrication of PAuNWs by a single-bath electrodeposition of AuAg alloy in templates and subsequent dealloying was first demonstrated by Searson et al.[53–55] Alternative methods such as multistep preparation of segmented wires,[55,56,156] direct electrodeposition, electrochemical fabrication from ionic liquids [157] or galvanic replacement reaction [48,158] were developed to synthesize porous Au nanowires with various shapes and morphologies. The coalescence of colloidal Au or Ag nanoparticles on the functionalized walls of a porous AAO membranes results in the fabrication of porous nanotubes with high surface area.[159,160]

In the past, the influence of the initial AuAg wire composition and the dealloying parameters on the resulting porosity was investigated in most cases for wire diameters larger than 200 nm.[49,53–58] However, many applications require porous Au wires with smaller wire diameters and higher surface-to-volume ratio. Previous studies on porous gold systems were performed by scanning electron microscopy (SEM) or low resolution transmission electron microscopy (TEM) that did not reveal details of the elemental composition.[6,161] Due to recent improvements in scanning transmission electron microscopy (STEM) as well as energy dispersive X-ray (EDX) detectors, new effects such as phase segregation have become observable. Only few works report on the use of these techniques to study AuAg nanoparticles or nanoclusters.[162–164] Phase segregation in particles with characteristic dimensions below 10 nm leads to the formation of Ag or Ag

oxide shells. However, these effects were observed only after galvanic reactions in an electrolyte [162,163] or after extended storage times (e.g. years).[164]

In this work is dealloying was applied to AuAg nanowires. The percolation threshold is mainly given by the 3D geometric atomic configuration.[153,165] We expected that the high surface-to-volume ratio combined with the surface tensions arising from the strong curvature of wires surfaces might modify the diffusion/dissolution properties of the Au and Ag elements. The fabrication of AuAg alloy nanowires by potentiostatic electrodeposition using a single-bath electrolyte was presented in several previous works.[49,51,53–55,143,166–169] Thus Searson and al used various mixture of $KAu(CN)_2$ and $KAg(CN)_2$ with concentration between 10 and 100 mM and pH adjusted to 13 with 0.25 M Na_2CO_3.[49,53–55] They performed CV analysis on flat surface and used AAO membrane as template to electrodeposit NWs with diameter larger than 200 nm at - 1.2 V (vs. Ag/AgCl) at 60 °C. On the other hand, Karim et al. mainly electrodeposited at GSI Au in etched ion-track templates from commercial cyanide bath.[166–168,170] Finally, Schubert et al. used pulse deposition of Au and AuAg to fabricate segmented nanowires.[143,169,171–173] Similar experimental conditions (electrolyte composition, potential, temperature) are used in this work.

This chapter describes the potentiostatic electrodeposition of AuAg nanowires with controlled compositions and with diameters below 400 nm. The wires are deposited in etched ion-track templates using a single bath electrolyte. A detailed compositional and crystallographic analysis of AuAg alloy nanowires before and after silver dissolution in acidic solution is presented. The dealloying process of individual cylindrical wires with various sizes and compositions is characterized by means of TEM for the crystallinity and EDX for the elemental analysis.

2. Experimental

This section presents the experimental details of the various steps necessary to synthesize porous gold nanowires and to be able, in a near future, to measure their electrical and thermal conductivities.

2.1. Fabrication of templates with cylindrical nanochannels

Etched ion-track membranes with parallel oriented nanochannels of different well-defined diameters were fabricated by irradiating 30 μm polycarbonate (PC) foils (Makrofol N, Bayer AG) with 2 GeV Au ions at the UNILAC linear accelerator of GSI Helmholtz Centre for Heavy Ion Research (Darmstadt, Germany). The irradiation was performed in a vacuum under normal beam incidence, applying a fluence of 10^9 ions/cm^2. The ion tracks were selectively dissolved and enlarged into cylindrical channels by chemical etching using an aqueous solution of 2 M NaOH at T = 50 °C. Prior to the etching, the irradiated membranes were exposed to UV light from both sides, each for 1 h. Etching times of 60, 30, 15, 7.5, and 3.25 min were applied to obtain nanochannels with diameter ranging from 380 nm to 35 nm. Before electrodeposition into the nanochannels, a working electrode was prepared by sputtering a thin (~100 nm) Au layer on one side of the membrane using an Edwards Sputter Coater S150B. This thin layer was subsequently reinforced by electrodeposition of a ~ 20 μm thick Cu layer using a copper-sulfate-based electrolyte (238 g/L Cu_2SO_4 and 21 g/L H_2SO_4, 60 °C, 7 min). For this purpose, a Cu rod served as counter electrode in a two-electrode configuration at room temperature.

2.2. Au and AuAg reduction

Table II-1: Applied electrolytes and their respective compositions

Electrolyte name	Acidity neutralizer	Electrolyte composition	Au:Ag ratio
Au50	0.25 M Na_2CO_3	50 mM $KAu(CN)_2$	1:0
Au20	0.25 M Na_2CO_3	20 mM $KAu(CN)_2$	1:0
Ag50	0.25 M Na_2CO_3	50 mM $KAg(CN)_2$	0:1
Ag20D	0.25 M Na_2CO_3	20 mM $KAg(CN)_2$	0:1
Au50Ag50	0.25 M Na_2CO_3	50 mM $KAu(CN)_2$ 50 mM $KAg(CN)_2$	1:1
Au50Ag20	0.25 M Na_2CO_3	50 mM $KAu(CN)_2$ 20 mM $KAg(CN)_2$	5:2
Buffer	0.25 M Na_2CO_3	/	/

For the electrodeposition of Au and AuAg, cyanide electrolytes were used. $KAu(CN)_2$ (Carl Roth) and $KAg(CN)_2$ (Sigma Aldrich) were mixed with various concentration and the pH set basic (pH ≥ 13) with 0.25 M/L Na_2CO_3 (>99.8%, Carl Roth). The various electrolytes considered in this work are listed in Table II-1. A Reference 600 potentiostat from Gamry Instruments, Inc. is used to apply and vary the potential as well as to measure the resulting current. In all cases, the cell and the electrolyte are warmed up for 30 min at 60 °C before operating at the same temperature.

Cyclic voltammograms (CVs) were performed by sweeping the potential between the working electrode and a Ag/AgCl reference electrode. A platinum coil served as counter electrode. The CVs were performed applying scan rates of 100, 20 and 5 mV/s and step size of 5 mV between 0 and - 1.5 V (vs. Ag/AgCl reference). Various types of working electrodes were investigated. Macroscopic disc electrodes consisting of a Au sputter coated polymer foils served as reference surfaces whereas sputtered Au layer at the bottom of the nanochannels was used to investigate the effect of the nanostructuring of the working electrode. This is in fact an array of nanoscopic sized recessed electrodes. Thus, the influence of the membrane was studied by comparing the CVs performed on the following

working electrodes: (1) Au-coated planar surface (A = 0.5 cm^2), Au-coated membrane with (2) cylindrical nanochannels of diameter 400 nm and density of 10^7 cm^{-2} (A = 0.014 cm^2) and, (3) nanochannels of diameter 45 nm and density 10^9 cm^{-2} (A = 0.018 cm^2). The surface of the Pt coil counter electrode was geometrically evaluated to A = 0.9 cm^2.

To estimate the current efficiency of the various electrolytes, potentiostatic electrodeposition at - 1.1 V vs. Ag/AgCl reference was performed on flat surfaces of Au sputter coated on PC films (A = 1.8 cm^2). The mass of the deposit was measured using a Scaltec SBA32 scale and was then compared to the measured electrodeposited charge.

The nanochannels of the Au-coated PC templates were filled by AuAg electrodeposited at 60 °C from aqueous electrolytes containing 0.25 M Na_2CO_3, $KAu(CN)_2$, and $KAg(CN)_2$ in different ratios, namely (1) 50 mM of $KAu(CN)_2$ and 50 mM of $KAg(CN)_2$ (Au:Ag ratio 1:1, solution **Au50Ag50**) and (2) 50 mM of $KAu(CN)_2$ and 20 mM of $KAg(CN)_2$ (Au:Ag ratio 5:2, solution **Au50Ag20**). A constant potential of - 1.1 V vs. Ag/AgCl reference electrode was applied. As reference, pure Au and pure Ag nanowires were grown from 20 mM solutions (**Au20** and **Ag20**) of the corresponding pure element-cyanide electrolytes.

2.3. Nanowire cleaning and transfer

For further investigations, the PC membranes were dissolved in dichloromethane. To remove all organic residues, the nanowires were rinsed in several consecutive **dichloromethane bathes** by centrifugation and dispersion. During the centrifugation, the nanowires agglomerate at the bottom of the centrifugation tube. The supernatant dichloromethane contaminated with polymer was then selectively removed by pipetting. To re-disperse the nanowires, fresh dichloromethane (~ 3 mL; 99.8%, Carl Roth) was used in combination with ultrasonication (5 s). (Tip: ultrasonication can be used for 1 s before the addition of dichloromethane to easily re-disperse the wires in the residual dichloromethane; dilution and dispersion in fresh dichloromethane is then very easy) The concentrated solution was then mechanically stirred using an IKA®

VORTEX GENIUS 3 for at least 1h prior to the next centrifugation step. To avoid irreversible agglomeration during centrifugation, the centrifugation speed and duration were adapted to the wire diameter as shown in Table II-2.

Table II-2: Centrifugation and sedimentation parameters for the cleaning and transfer of nanowires

Nanowire diameter (nm)	**Centrifugation speed (RPM)**	**Centriugation time (min)**	**Sedimentation time**
< 50	4000	60	> 10 h
50 - 100	4000	30	< 1 h
100 - 200	4000	15	< 10 min
> 200	3000	15	< 10 min

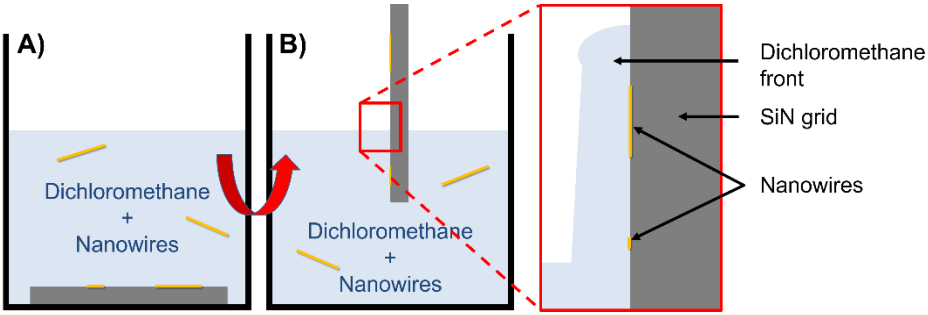

Figure II-2: Schematic of (A) the sedimentation of the nanowires and (B) the extraction of SiN grids covered with nanowires. Attention is given the dichloromethane front that should flow down without breaking (i.e. evaporation of dichloromethane)

For HRTEM and EDX analysis, the wires were directly drop-casted onto the CuC grids. For the dealloying and subsequent analysis, AuAg nanowires were transferred to the SiN grids by sedimentation. For this, the substrate was horizontally immersed in a highly diluted nanowire in dichloromethane solution for a defined time (Figure II-2A). The **sedimentation** time required to obtain sufficient wire density on the substrate strongly depends on both nanowire concentration in the solution and the diameter of the nanowires. In the present case, the deposition of nanowire on TEM grids was controlled by varying the

sedimentation time. A general trend is given in Table II-2. The extraction of the substrate appeared to be of critical importance for both the mechanical sustainability of the SiN membranes and the cleanliness of the nanowires. The substrate was then slowly taken off the nanowire mixture as illustrated in Figure II-2B so that the dichloromethane flows down and does not evaporate. In the case of nanostructured substrates, this step was performed with the structures normal to the moving direction. This technique is also efficient for the deposition of nanowires across tranches. The sedimentation technique has also been proven to work for other materials such as Bi_2Te_3 and Sb nanowires.

2.4. AuAg dealloying

For the dealloying of AuAg nanowires by selective dissolution of Ag, the substrate with randomly distributed nanowires were immersed in 65% nitric acid (HNO_3, LS Labor-Service GmbH) at room temperature for 3 h. The samples were then rinsed with water two times and dried with a nitrogen jet.

3. Results and discussion

This section presents the analysis of the electrodeposition process by monitoring the growth of the nanowires in the nanochannels of PC templates. The dimensions of the wires are discussed in relation with the etching conditions. Finally, the composition, morphology, and crystallography of the nanowires are presented.

3.1. Analysis of AuAg electrodeposition process

3.1.1. Electrodeposition efficiency

In most of the previous works, a current efficiency of 100% is assumed for the interpretation of the cyclic voltammograms and electrodeposition curves. The current efficiency depends on various parameters such as the concentration, the presence of additives, or the potential. Here we study the current efficiency of the employed electrolytes by performing potentiostatic deposition over large flat working electrodes and comparing the measured charge to the deposited charge.

On the one hand, the working electrode was chosen with surface sufficiently large to enable the determination of the deposited Au (or Ag) mass with satisfactory precision. On the other hand, the electrodeposition was performed under identical conditions as the deposition of nanowires. The deposition current was measured whereas a constant potential of - 1.1V (vs. Ag/AgCl) was applied. After 1h of deposition, the mass of the deposit is compared to the electrodeposited charge by analyzing the current-time curves. The experimental *U-t* and *I-t* curves obtained for electrolyte **Au20** and **Ag20** are presented in Figure II-3.

Analysis of the I-t curves

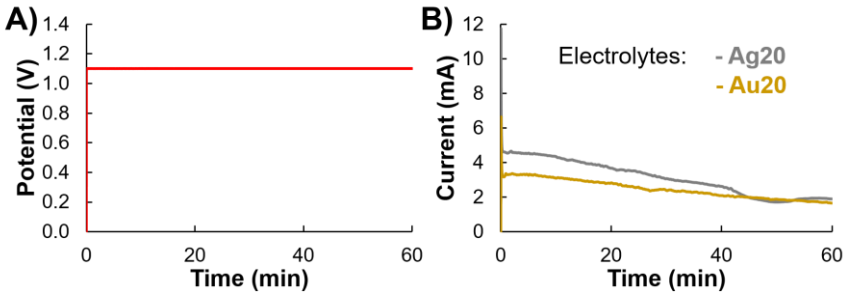

Figure II-3: (A) U-t and (B) I-t curves for potentiostatic electrodeposition of Au and Ag on a flat Au surface

As shown in Figure II-3, independently on the electrolyte, all *I-t* curves exhibit identical trends (also for electrolytes **Au50** and **Ag50** not shown here). In a first time, a current spike is observed within the first seconds of the deposition. Then, the current decreases steadily until the deposition process is stopped. This behavior is typical for electrodeposition in the diffusion-limited regime. When the potential is applied, the ions in solution start to migrate, the analytes close to the surface of the working electrode are reduced, depleting the electrolyte close to the electrode (i.e. the formation of the diffusion layer). These cumulative effects (migration, diffusion, and chemical heterogeneous reaction) lead to high initial cell currents. After complete depletion of the diffusion layer, the current is regulated by the diffusion of electrolyte through the expanding diffusion layer.

Therefore, according to the **Cottrell equation**, the current declines with time:

$$I(t) = \frac{nFAD^{\frac{1}{2}}C_O^*}{\pi^{1/2}t^{1/2}} \qquad (II\text{-}1)$$

with n the number of electron involved in the reaction, F the Faraday constant, A the surface area of the working electrode, D the diffusion coefficient of the metal ion, C_O^* its concentration in the bulk and t the time.

Our experiment, however, show strong deviation from the $t^{-\frac{1}{2}}$ time dependency and can be explained by experimental limitations: (1) our experiments are conducted in a cell with electrolyte volume of about 6 mL where the bulk concentration C_O^* of active species is not constant over time and decreases. As an example, for the 20 mM $KAu(CN)_2$ electrolyte (**Au20**), the Au^+ mass in the 6 mL cell is about 23.6 mg to compare with the 13.9 mg of electrodeposited gold in one hour. Therefore, C_O^* decreases by more than half over the electrodeposition time and reduces the current. (2) At 60 °C, convection in the cell cannot be excluded, which possibly results in higher currents than expected as well as irregular *I-t* curves. Consequently, one has to take into account that the current efficiencies given in Table II-3 are measured with a significant bulk concentration drop that is not encountered for NWs deposition because the working electrode dimension as well as the deposited masses are much smaller.

Current efficiencies

Table II-3: Electrodeposition efficiency for various electrolytes at - 1.1V (vs. Ag/AgCl) and 60 °C

Electrolyte name	Electrolyte	Concentration (mM/L)	Electrodeposition efficiency (at. %)
Au50	$KAu(CN)_2$	20	77± 2
Au20	$KAu(CN)_2$	50	88 ± 1
Ag50	$KAg(CN)_2$	20	85 ± 2
Ag20	$KAg(CN)_2$	50	95 ± 1

Table II-3 displays the current efficiency calculated according to equation (I-17) for the various pure element electrolytes on flat surfaces. The current efficiency are calculated as detailed in section 3.2 from chapter I, with *Q* derived by integration of the experimental curves and m_{weig} being directly weighted with a scale. High current efficiencies (> 75%) are observed for all electrolytes tested. The errors on the current efficiencies provided in Table II-3 originate from the scale inaccuracy. We observe that the electrodeposition is in average more efficient for Ag-cyanide electrolytes than for Au cyanide electrolytes with similar concentration. In addition, a higher efficiency is obtained for higher concentrations. Therefore, 50 mM $KAu(CN)_2$ and 50 mM $KAg(CN)_2$ electrolytes have deposition efficiencies close to 100%. The reduction of current efficiency experienced with a diminution of electrolyte concentration may probably be explained by the stability of the cyanide complexes. Actually, Au and Ag cyanide complexes are very stable, especially in basic media, leading to reduction at very negative potentials. Therefore, the co-reduction of hydrogen ions may be observed, which reduces the Au/Ag reduction current efficiency. Since the diffusion coefficient of $Au(CN)_2^-$ and $Ag(CN)_2^-$ are rather similar (about 1.6×10^{-5} $cm^2 \cdot s^{-1}$),[137,174–176] the difference of efficiency between Au and Ag cannot be explained by the diffusion process. A probable explanation is related to the reduction potentials for Au and Ag as well as the chemical reduction processes. These effects were investigated by cyclic voltammetry (CV) in the next section.

3.1.2. Cyclic voltammetry analysis of Au and AuAg reduction

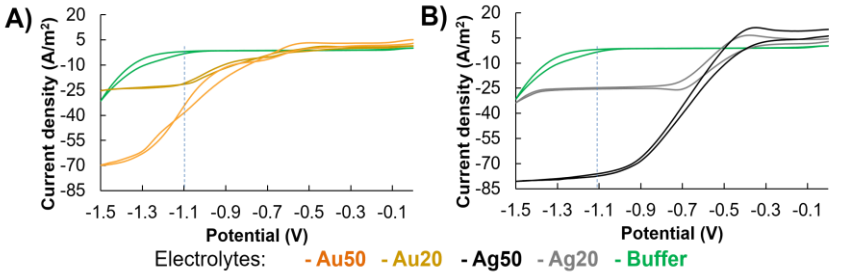

Figure II-4: Cyclic voltammograms performed on Au-sputtered flat surfaces at 5 mV·s^{-1} for (A) Au and (B) Ag electrolytes of different composition

The voltage characteristics of the electrodeposition process were studied by cyclic voltammetry on the two systems described in the previous section: (1) planar electrodes and (2) recessed nanoelectrode arrays. To simplify the reading of the cyclic voltammograms, only the second out of three consecutive cycles are displayed. Cyclic voltammograms were first performed on planar working electrodes. Figure II-4A shows the cyclic voltammograms obtained by slow voltage sweeping (5 mV·s^{-1}) for various electrolytes on flat gold surfaces. The green curve, corresponding to the CV of the 0.25 M Na_2CO_3 buffer solution, exhibits no specific peak between 0 and - 1.1 V. The current increase observed at voltages that are more negative is attributed to H_2 evolution and is observed on every curve. On the other hand, electrolytes **Au50** to **Au50Ag20** have characteristic *j-U* curves.

Study of the reduction processes

Figure II-4 evidences that the onset of $Ag(CN)_2^-$ reduction occurs closer to 0 V (B) than for $Au(CN)_2^-$ ions (A). In fact, whereas the equilibrium potential for Au^+/Au is more positive than for Ag^+/Ag, the equilibrium potential for the $Ag(CN)_2^-/Ag$ couple is more positive than that of the $Au(CN)_2^-/Au$ couple (see Chapter I). Accordingly, the reduction peak (or inflection), indicating diffusion

limited deposition is approached at a more negative potential for gold electrolytes than for silver electrolytes.

Further information is obtained by the shape of the CVs and concerns the reaction scheme. Both gold based electrolytes **Au50** (50 mM $KAu(CN)_2$) and **Au20** (20 mM $KAu(CN)_2$) contain two waves and current-potential plateaus (Figure II-4A). This behavior is attributed to two distinct reduction processes possible for gold cyanide anions. The first plateau observed at less negative voltage is attributed to a **two-step reduction** of $Au(CN)_2^-$, which is assigned to the adsorption of $Au(CN)_{ads}$:[55,137]

$$Au(CN)_2^- \rightleftarrows AuCN_{ads} + CN^- \qquad (II\text{-}2)$$

followed by the reduction of gold by electron exchange which has been determined to be the rate limiting step:[177]

$$AuCN_{ads} + e^- \rightleftarrows Au + CN^- \qquad (II\text{-}3)$$

At more negative potential, gold is stripped from its two cyano ligands in a single reduction step:

$$Au(CN)_2^- + e^- \rightleftarrows Au + 2 * CN^- \qquad (II\text{-}4)$$

Ag electrolytes **Ag50** and **Ag20** exhibit a single wave *I-U* shape with only one plateau (Figure II-4B); this indicates that the reduction of $Ag(CN)_2^-$ proceed directly to the metallic Ag in **one step**:

$$Ag(CN)_2^- + e^- \rightleftarrows Ag + 2 * CN^- \qquad (II\text{-}5)$$

In addition, the potential difference between the oxidation and reduction peak, about 250 mV for **Ag20** and higher than 500 mV for **Ag50** is a clear sign that this reaction is not a reversible reaction. This observation is consistent with previous works where the reduction of $Ag(CN)_2^-$ is considered as **quasi-reversible.** This quasi-reversibility is in between the electrochemical reversibility, where the rate

of electron transfer occurs quickly compared to the rate of diffusion, and irreversibility where the electron transfer is much slower.

Additionally, the absence of stressed reduction peaks and the quasi-sigmoidal shape of the curves show that the slow scan rate operated for the CVs in Figure II-4 approaches the **steady-state conditions**.

Plateaus are observed at highly negative potential for both Au and Ag electrolytes. This constant current indicates a **diffusion-limited regime**. Consequently, the current is independent on the applied potential, and depends only on electrolyte parameters such as the concentration. This statement is in agreement with experimental observations, since the diffusion limited current is directly proportional to the electrolyte concentration, with currents for electrolyte **Ag20** and **Au20** about 2.5 times smaller than for electrolytes with higher concentrations (**Ag50** and **Au50**).

Figure II-4 shows a clear dependence of the reduction peak (or inflection) on the electrolyte concentration. For the gold-based electrolytes, the reduction potentials are shifted to more negative potential with an increase of concentration. Therefore, the two-step reduction plateau is observed around - 0.65 V for electrolyte **Au20** (lower concentration) and about - 0.75 V for electrolyte **Au50** (higher concentration). The difference is more obvious for the direct reduction plateau, about - 1.1 V for **Au20** and < - 1.3 V for **Au50**. A similar shift is observed for Ag-based electrolytes, with a diffusion limited plateau starting at about - 0.7 V for the electrolyte **Ag20** (lower concentration) and < - 1.0 V for **Ag50** (higher concentration).

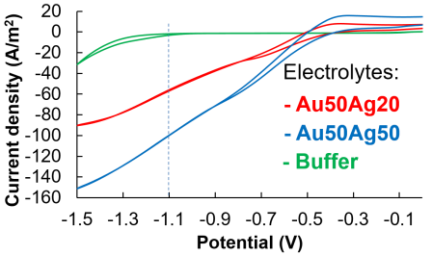

Figure II-5: CVs on flat surfaces performed at 5 mV·s^{-1} for electrolytes containing both Au and Ag cyanide salts with different concentrations

Concerning the *mixed electrolytes* **Au50Ag50** and **Au50Ag20**, the CVs (Figure II-5) contain the characteristic shapes and currents of both individual Au and Ag electrolytes. As a matter of fact, electrolyte **Au50Ag50** with a Au concentration equivalent to electrolyte **Au50** and a Ag concentration identical to solution **Ag50** exhibits a CV quasi equivalent to the *sum of the CVs* from electrolyte **Au50** and **Ag50**. Similar observations can be obtained with solutions **Au50Ag20**, **Au50**, and **Ag20**. Therefore, at potentials above - 0.8 V, the CV shape and current values are dominated by the silver contribution whereas at potentials below - 0.8 V, Au contribution starts to become significant and leads to further increase of the current. It is then expected that the composition of AuAg deposited from a single bath at constant potential can be estimated considering the individual electrolyte contribution in combination with the currents efficiencies. Assuming a current efficiency of 100% for all species, a rough estimation of alloy deposit composition can be obtained by comparing the current densities at - 1.1 V. For **Au50Ag50** electrolyte, the current ratio of **Au50** and **Ag50** yields ≈ 66 Ag at.%. A composition of ≈ 38 Ag at.% is predicted from **Au50** and **Ag20** CVs for deposit from electrolyte **Au50Ag20**.

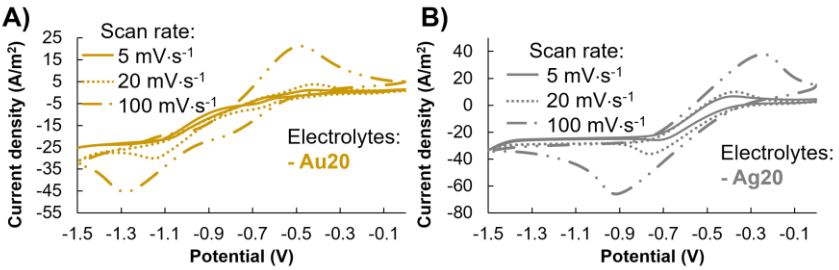

*Figure II-6: CVs of (A) Au electrolyte **Au20** and (B) Ag electrolyte **Ag20** at various scan rates*

Figure II-6 the representative CVs at various scan rates of 5, 20, and 100 $mV \cdot s^{-1}$ respectively. For both Au and Ag cyanide electrolytes (**Au20** and **Ag20**), the shape of the CV evolves from quasi-sigmoidal at low scan rates to peak shaped CVs at high scan rates. This *change of shape* is associated to a change in deposition regime that approaches the steady-state deposition conditions for the lower scan-rates. Another possible contribution originates from the cell geometry itself that may induce a modification of the diffusion layer geometry. Simulations are necessary to consider any deviation from the planar diffusion model. The *difference in peak current* between low and high scan rate can be explained by the proportionality between the peak current and the square root of the scan rate. On the other hand, the *shift in potential* of the reduction peak with the scan rate is more complex. For both gold and silver, the reduction peaks shift to more negative potentials when increasing the scan rate. In addition, it is observed that the electrolyte concentration also influences the reduction potential peak position. As observed above for CVs at 5 $mV \cdot s^{-1}$, the increase of electrolyte concentration results in a shift of the reduction peak to more negative potentials. This is also observed for faster scans (not shown).

Influence of the experimental conditions

In this section, we try to explain the different observations made in Figure II-6 (e.g. shift of the reduction peak). The cyclic voltammograms expressed as the current density vs. applied potential (*j-U* curves) obtained by linear sweeping of

the potential relate the various processes leading to potential dragged heterogeneous chemical reaction. Contributions to the current originate from the combination of mass transfer current, electron transfer current, additional chemical reactions currents, as well as other non-faradaic currents issued from the reaction cell itself. Assuming a perfect reaction cell with no capacitance nor uncompensated resistance, the current is determined by the limiting step: either mass transfer or electron exchange reaction. In the case of gold, the preceding chemical reaction, i.e. the adsorption of gold, may also influence the current at low voltages, but will be considered negligible in a first time. Therefore, the rates of both processes, respectively characterized by the **mass transfer coefficient** m_T and the **electrochemical rate constant** k_0 are of critical importance. It is noted that, in opposition to k_0, m_T is not an intrinsic property of the reaction cell but depend on the scan rate υ. The mass transfer coefficient is a function of the square root of the electrolyte diffusivity but also inversely proportional to the square root of the scan rate υ (thus dependent on probing conditions).

Matsuda and Ayabe introduced in 1955 the dimensionless parameter Λ defined by:

$$\Lambda = \frac{k_0}{\left(\frac{nF}{RT} D_O^{\alpha} D_R^{1-\alpha} \upsilon\right)^{\frac{1}{2}}} \qquad \textit{(II-6)}$$

to enable the distinction between the different types of heterogeneous reaction: reversible, quasi-reversible and irreversible.[178] They also give a general expression for the current density in potential sweeping conditions:

$$j = nFAC_O^* D_O^{\frac{1}{2}} \left(\frac{nF}{RT} \nu\right)^{\frac{1}{2}} \psi(E, \Lambda) \qquad \textit{(II-7)}$$

$\psi(E, \Lambda)$ is a peak shaped function that is numerically evaluated by Nicholson for various electrodeposition conditions.[179] Experimentally, $\psi(E, \Lambda)$ reflects the contribution of **kinetic** and **mass transfer** on the current during the voltage sweep. For high values of Λ, i.e. the reaction is reversible; the function ψ is then

independent on Λ. On the other hand, Matsuda and Ayabe show that for quasi-reversible and irreversible reactions, Λ influences the position of the maximum of $\psi(E,\Lambda)$ such as an increase of Λ lead to a shift of the oxidation and reduction peak so that the distance between them decreases. From the definition of Λ, it is then easy to see that higher scan rate lead to a wider splitting between oxidation and reduction peaks. In agreement with the shift of the reduction peak observed in Figure II-6, this confirms the quasi-reversibility of the gold reduction reaction. On the other hand, the contribution from the concentration is less direct and may influence Λ by modifying the diffusion coefficient of the analytes since the diffusion coefficient D depends on the media.

Additional contributions from non-faradaic currents such as capacitive effect or the presence of uncompensated resistance cannot be fully excluded. **Capacitance effect** can originate from the double layer. The current from a capacitor being linearly proportional to the voltage scan rate, capacitance current resulting from linear potential sweeps is then constant. Thus capacitive effect may affect the current flowing through the cell but has limited influence on the peak potential. Differently, the presence of **uncompensated resistance**, due to the resistance of the electrolyte separating the reference electrode and the working electrode, may influence the peak potential. Ohm's law allows to estimate the potential shift as $E_{R_u} = I * R_u$. Hence, reduction peaks are shifted to more negative potentials and oxidation peaks to more positive potentials.

Recessed nanoelectrode arrays: influence of the nanochannels

After the study of electrolyte properties by CV on flat surface, the effect of the nanostructuring of the working electrode was investigated. During electrodeposition, the metal ions have to flow through the long and narrow nanochannels of the etched ion-track PC template before being reduced at the Au coated bottom of the nanochannels acting as working electrode. Individual channels can be considered as *recessed micro/nano electrodes* and the complete working electrode as an array of randomly distributed recessed microelectrodes.

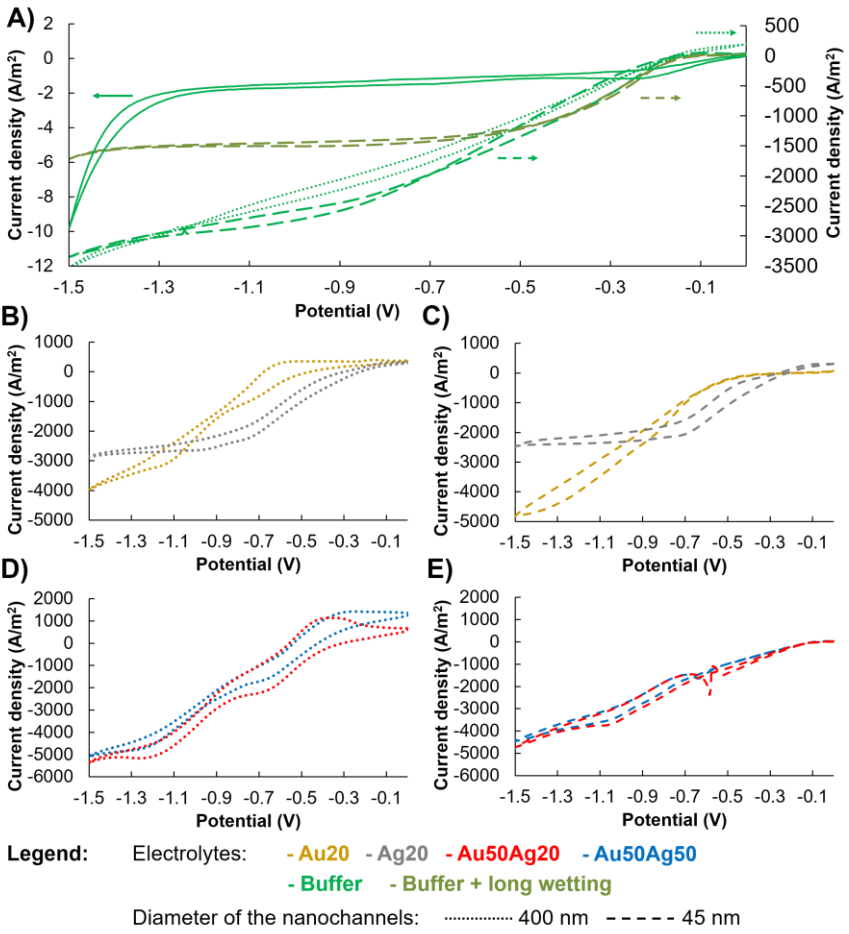

Figure II-7: Cyclic voltammograms of cyanide based electrolytes performed in the nanochannels of etched ion-track PC membranes with two different diameters (400 and 45 nm) at a scan rate of 20 mV·s⁻¹. (A) CV of buffer solution in nanochannels compared with similar CV on flat surface (solid line). (B and D) CVs of Au, Ag, and mixture electrolytes in 400 nm channels. (C and E) CVs of Au, Ag, and mixture electrolytes in 45 nm channels

Figure II-7 shows several CV performed in nanochannels with two different diameters of channels: 400 and 45 nm. The respective densities of channels are of 10^7 and 10^9 channels·cm^{-2}. The total surface area of the working electrode are similar for cells of 1.2 cm of diameter (1.4×10^{-2} and 1.8×10^{-2} cm^2) but the area is

more than 10 times smaller than the surface of the flat working electrode treated above. For better comparison, the CVs are thus expressed in term of current densities. Due to the limited volume of the nanochannels, low scan rates of 5 $mV \cdot s^{-1}$ could not be used because the deposition proceeds through the complete pore faster than the duration of a complete voltage cycle. At a scan rate of 20 $mV \cdot s^{-1}$ as presented in the CV of Figure II-7 three consecutive cycles are possible without outgrowing the membrane.

Figure II-7A compares the CVs of the buffer in the nanopores (dashed lines) and on a flat surface (solid line) obtained at the same scanning rate. On flat Au surfaces, no peaks are observed in the CVs of the buffer. The current increase at highly negative potential is associated to hydrogen evolution. However, the shape of the voltammograms using nanochannels differs from the ones obtained on flat surfaces, exhibiting a delayed current drop and longer decrease of the current while sweeping the voltage towards more negative values. On top of this, the current densities measured in nanopores are about 1000 time higher than for flat surfaces. These effects are very surprising since no reaction is expected for potentials above - 1.0 V for the 0.25 M Na_2CO_3 aqueous solution. It is probably related with non-faradaic effects. Considered independently, each nanochannel is a recessed disk electrode with its individual uncompensated resistance and capacitance. The nanochannel array is then a parallel array of these resistances and capacitances. As a result, the resistance of the array does not differ significantly from the resistance of an individual resistance since $1/R_T = \sum 1/R_{\parallel}$. On the other, the **capacitance increases** of the array is considerably higher with $C_T = \sum C_{\parallel}$. In addition, both resistance and capacitance may be enhanced by the high aspect ratio of the nanochannels.

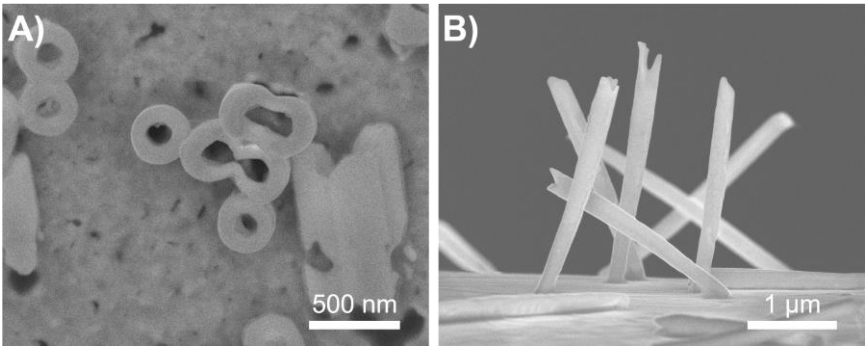

Figure II-8: SEM images of (A) sputtered gold in ~ 400 nm large nanochannels after template removal exhibiting ring-like shapes instead of nanodisc electrode and (B) free standing nanowires with various tip shapes

The shape of the sputtered gold that serves as working electrode at the bottom of the pore may also influence the current. Because the current is proportional to the electrode area, any deviation from the flat disk will lead to a surface area increase. Figure II-8A illustrates this deviation from recessed disk electrode. When sputter-coating Au on one side of the track-etched membrane, gold is obviously also deposited on the wall of the pore opening. In particular, for larger channel diameters, the pore is not closed and the sputtered gold has a **ring-like shape.** Deviation from nanodisc electrode may also initiate during CV measurement and/or deposition of material. Nanowires do not have flat top surfaces as shown in Figure II-8B, especially under fluctuating growth conditions as during voltage sweeps. Tokuda et al.[180] observed the influence of the shape of recessed microelectrode made of carbon fibers and suggested that the real surface area of the electrode may influence the peak and the limiting current. However, he also noticed that the propagation of the diffusion layer through the pore might screen this effect. Another contribution to the high current observed for nanostructured working electrodes may be an oxidation reaction at the counter electrode. In fact, gas evolution has been detected in this work at highly negative potentials on the platinum counter electrode indicating the possible formation of O_2.

Takashi Ito et al.[181] observed a strong influence of the quality of the contact between the sputtered gold and the template. According to their study, the solution creeps in between the membrane and the gold electrode and increases the capacitive currents.

The green khaki dashed curve in Figure II-7A shows the effect of additional wetting time in the membrane with 45 nm channels prior voltage sweeping. After extended wetting time of the membrane (~ 2h instead of 30 min), CVs show similar behaviors at low voltages but deviates at more negative voltages. The constant current observed at potential below - 0.5 V is consistent with a capacitive current, which is by definition proportional to the scan rate. The effect of partial wetting, with the presence of air bubbles blocking nanochannels of an array, has been investigated by CV in [181]. As expected, the measurements tend to show lower current when not all nanochannels are conducting. However, this is in opposition to the experimental observations of Figure II-7A. Another possibility relates with the interaction between buffer and polycarbonate surface. At pH 13, the buffer solution is basic and contains hydroxide molecules that *further etch* the PC. Thus, the diameter of the pores may increase during the wetting time. Finally, because of their fabrication process, the pores of the membranes used for CVs may not be completely closed. A *leakage* of the solution on the backside of the working electrode would undoubtedly influence the total cell current. Therefore, because we are not sure if some pores are blocked, if further etching occurs, or if leakages play a role, our CV study only provides **qualitative** information.

Reduction of Au and Ag in nanochannels

Figure II-7B and D show CVs of single metal electrolyte (**Au20** and **Ag20**, in B) and mixtures (**Au50Ag50** and **Au50Ag20**, in D) performed in arrays of nanochannels of 400 nm. Though the "peak" shape of the CVs is less pronounced than on flat surfaces at the same scan rate, they present **similar behaviors**. The "peak" positions are similar for both, single metal electrolytes and mixtures. Likewise, CVs at higher scan rates (not shown) display more pronounced peak-shaped curves and alike shifts of the peak potential. The evolution to sigmoidal

curves even at higher scan rate has already been investigated by several groups and is attributed to the change of diffusion regime depending on the scan rate.[180–182] At high scan rates, the diffusion layer is trapped in the nanochannel and the *diffusion is then linear*, hence the **peak shaped** CVs. At lower scan rate, the diffusion layer exits the nanochannels and the *diffusion becomes radial*, resulting in **sigmoidal curves**.

Figure II-7C and E show CVs of electrolyte **Au20** and **Ag20** (C) and **Au50Ag50** and **Au50Ag20** (E) performed in arrays of 45 nm wide nanochannels. All CVs in these small channels have a sigmoidal shape. Only the CVs issued from the mixtures exhibit a pseudo peak at - 1.1 V. It should be noted that the sharp peak observed at about - 0.6 V in the CVs of electrolyte **Au50Ag20** are attributed to organic impurities. This strong shift toward the **radial diffusion** mode for nanochannels with small diameters is consistent with the conclusions from Lavacchi et al. who simulated CVs in inlaid microelectrode with various aspect ratio.[183] Nevertheless, the absence of oxidation currents for gold and mixed electrolytes as well as the absence of two steps for gold reduction is striking. On the one hand, regarding the high current measured in the absence of electrolyte (Figure II-7A), it is probable that the faradaic current might be masked by non-faradaic currents. On the other hand, such CVs may also result from a strong shift of the oxidation and reduction peaks in opposite directions. However, this second option is less probable since peak-shaped CVs obtained at faster scan rates (100 $mV \cdot s^{-1}$, not shown) for **Au50Ag50** and **Au50Ag20** that exhibit oxidation peaks.

To summarize on CV results, the measurements:

- Confirm for flat surfaces the reduction mechanisms for both gold- and silver-cyanide electrolytes.
- Evidence the strong influence of the electrolyte (concentration) on the deposition rate.
- Show that voltammograms of mixed electrolytes can be deduced from the CVs of individual metal electrolytes. Hence, the composition of the deposit can be forecasted from CVs.

- Exhibit higher current densities in arrays of nanochannels. These currents are mostly attributed to non-faradaic currents originating from the cell configuration.
- Attest that the chemical reduction reaction process is similar in nanochannels and on flat surfaces. Small potential shifts are attributed to non-faradaic contributions.
- Prove that in all cases, the reduction of Au and Ag cyanide electrolyte is performed in diffusion-controlled regime (or close to).

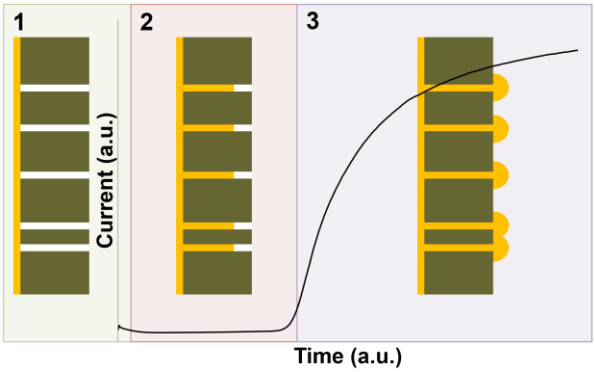

Figure II-9: Scheme and current-vs.-time curve monitored during the electrodeposition of gold into the nanochannels of a template separated in three major steps. (1) Initiation of deposition (green), (2) growth of wires at constant current (red), and (3) growth of caps (violet)

3.2. Nanowire electrodeposition

The observations and interpretations made in this section are in agreement with previous works from our groups with other materials[91,184–186] and other types of membranes.[187] The current-vs.-time (*I-t)* electrodeposition curves exhibit similar characteristics for all samples. Figure II-9 shows a representative *I-t* curve for the potentiostatic reduction of gold in nanochannels. The potentiostatic deposition of gold at 60 °C and -1.1 V vs. Ag/AgCl can be separated into three major steps. In a short initial time (few seconds), a peak current is measured current (Figure II-9, green). This step is attributed to the initial reduction of the ions at the working

electrode and the formation of a diffusion layer. An additional decrease of the surface may also occur at the beginning of the deposition when the deposition initiate on tube like structure (as shown in Figure II-8A) and convert to solid cylindrical wires. During this transition time, the depletion of the diffusion layer spreads until a steady-state regime in diffusion-limited conditions is reached. Afterwards, since the nanochannels are cylindrical, the surface area of the working electrode is constant. As a consequence of the **constant surface area** and of the **diffusion limited regime**, the current is constant during the growth of the wires (Figure II-9, red). Once the nanochannels are completely filled, gold outgrows the membrane. Outside the nanochannels, the electrodeposition process is not constricted by the channels and growth continues in all directions. This results in the formation of so-called caps on the other side of the membrane. The surface area of these caps thus enlarges with time, resulting in a fast increase of the current (Figure II-9, violet).

By following the current evolution during the potentiostatic electrodeposition of Au and AuAg, it is thus possible to *control the length* of the wires. The maximum length of the wire is the foil thickness when the electrodeposition is usually stopped just before the formation of caps starts.

3.3. Morphology and composition of nanowires before and after dealloying

This section presents the results obtained on the characterization of AuAg NWs before and after dealloying by XRD, TEM, and EDX. Special focus is given to the local composition of the nanowires. The consequences of the observed surface enrichment are discussed.

3.3.1. Geometry of as-deposited wires

The geometry of the as-deposited nanowires was examined by SEM directly after the dissolution of the membrane.

Diameter of the nanowires

Figure II-10 exhibit SEM images of NWs with various diameters obtained by electrodeposition in templates etched for (A) 15 min, (B) 7.5 min, and (C) 3.25 min. After the dissolution of the membrane, the diameter of at least 80 nanowires is measured on a central position on nanowires lying on the back electrode (as in Figure II-10) or on wires transferred on a CuC TEM grid (as shown later in Figure II-13 and Figure II-14).

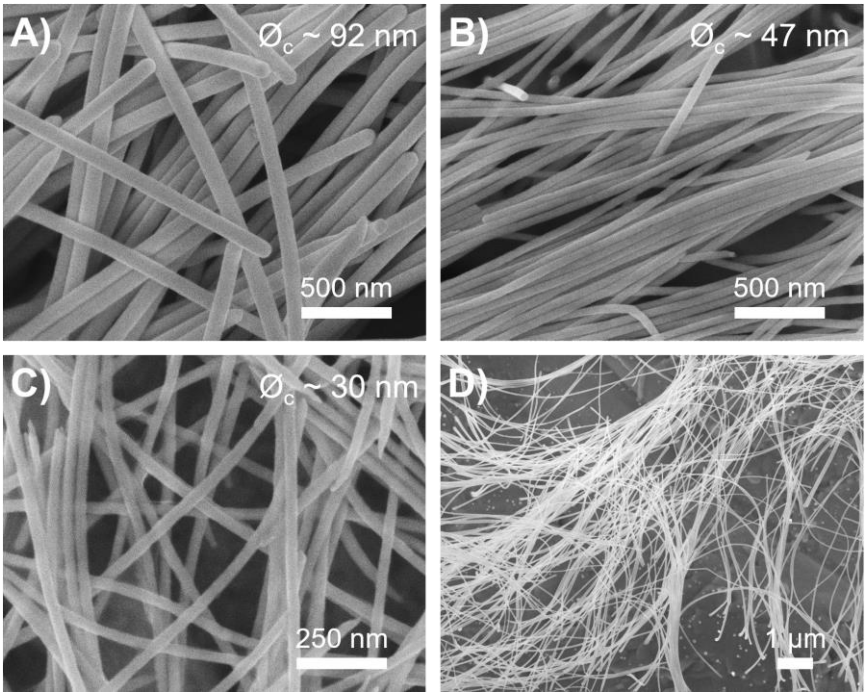

Figure II-10: SEM images of nanowires with diameter of (A) ~ 92 nm, (B) ~ 47 nm and (C) ~ 30 nm, lying on the backelectrode after the dissolution of the membrane. (D) Low magnification SEM image of ~ 92 nm wires behaving like spaghettis

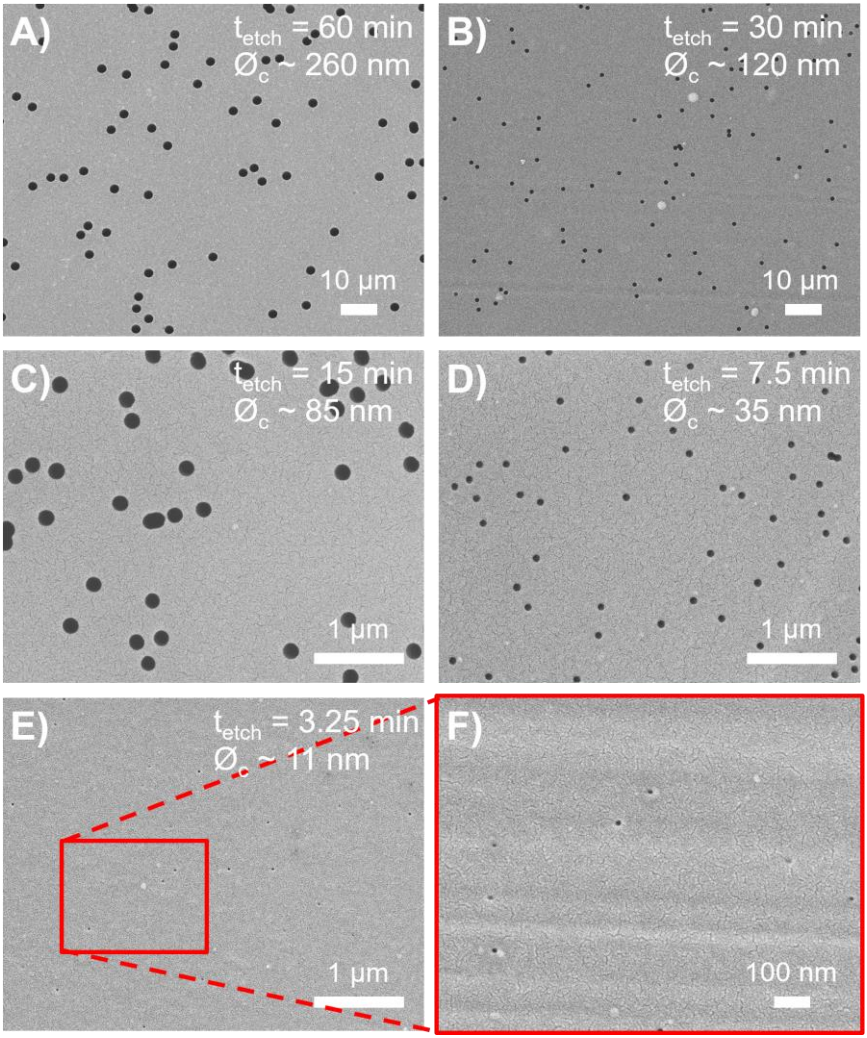

Figure II-11: SEM images of the top surface of PC templates etched for (A) 60, (B) 30, (C) 15, (D) 7.5 and (E and F) 3.25 min. The diameter of the nanochannels (black disks) directly depends on the etching time

For comparison, we also determined the mean diameter of many nanochannels on the template surface by means of SEM (after sputtering of Pt). The nanochannels are visible as black disks in Figure II-11 and we measured their diameter ($Ø_c$).

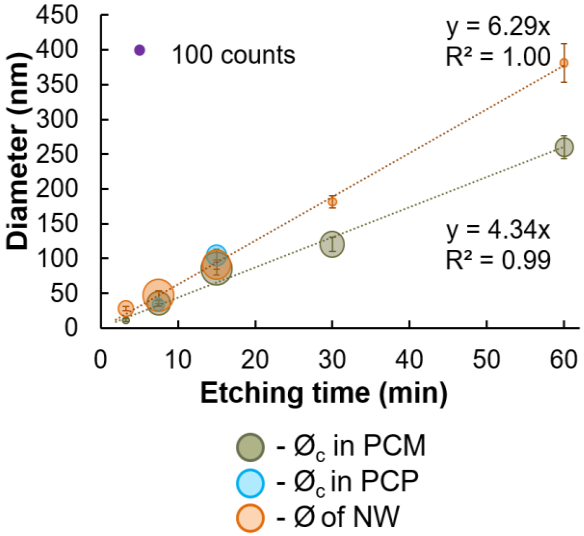

Figure II-12: Diameter of nanochannels in PC (Makrofol (PCM) and Pokalon (PCP)) and of nanowires electrodeposited in PCM membranes as a function of the etching time. The size of the disc symbols represents the number of analyzed channels or wires (violet circle = 100 counts). The lines are linear fits to the data

Figure II-12 displays the average diameters of the nanowires as a function of the etching time applied for the fabrication of the templates (orange). The surface diameter of the nanochannels is displayed for Makrofol PC (PCM) membranes in dark green. To illustrate the statistical significance, the sizes of the data symbol are scaled to the number of analyzed objects. The error bars correspond to the 1 sigma width of the diameter dispersion.

For wire diameter below 100 nm, the distribution is only of a few nanometers, whereas it enlarges up to about 60 nm for the 380 nm large wires. Thin nanowires with diameter below 100 nm are fairly cylindrical (Figure II-10). In opposition, thick wires with larger diameter can slightly deviate from the **cylindrical shape** as illustrated in Figure II-13.

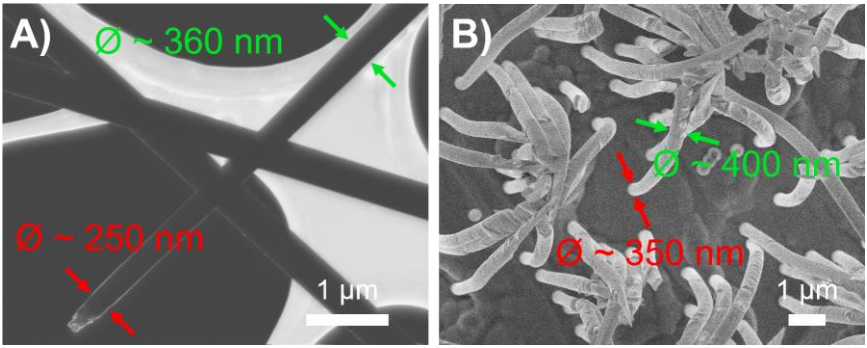

Figure II-13: SEM images of ~ 380 nm wide nanowires with bullet like tip on (A) CuC TEM grid and (B) backelectrode. The diameter of the nanowire end (red) is smaller than the middle of the nanowire (green)

Wires with 180 (not shown) and 380 nm (Figure II-13) diameters have **bullet like** ends in opposition to the thinner wires. Therefore, the evaluation of the diameter may differ as a function of the position of the measurement, hence a large size distribution. In addition, wires with large diameters are synthesized in membrane with lower densities (10^8 nanochannels·cm^{-2} for wire diameter of 180 nm and 10^7 nanochannels·cm^{-2} for wire diameter of 380 nm) which also decrease the number of measurements and thus the precision of the error.

Figure II-12 evidences that the **radial etching rate** in PC is approximately **constant** for etching times equal or higher to 3 min and 15 s. The radial etching rate of PCM is 4.34 nm/min for isotropic etching at 60 °C with 2 M NaOH. The etching rate deduced from systematic wire diameter measurements is 6.29 nm·min^{-1}. This difference of ~ 2 nm·min^{-1} may be explained by two additive effects. The first is that the wires are deposited from a basic aqueous solution at high temperature. As mentioned before, the pores may be *etched further* by the electrolyte during the membrane wetting and electrodeposition steps. The second effect is that the wire diameter is measured in the middle of the wire, i.e. where the diameter is the larger, whereas the nanochannel diameter is measured at the surface of the membrane. Thus the deviation from the cylindrical shape at the pore opening (wire tip) has to be considered. In addition, the measurement of the

nanochannel diameter is also influenced by the necessity of sputtering a thin layer of platinum for SEM study.

The production of PCM membranes being stopped by its producer, replacement polymers have to be considered for future works. Preliminary etching test were performed on another type of PC membranes: Pokalon PC (PCP). For comparison, PCP membranes were etched for 7.5 and 15 min (blue in Figure II-12). For short etching time of 7.5 min, the nanochannel diameter is approximately equivalent to that of PCM membrane. For a longer etching time of 15 min, a deviation of 20 nm is observed. These results are consistent with previous work where a linear dependence of weight loss as been established for PCM etching whereas PCP radial etching rate increases with time.[133]

Length of the nanowires

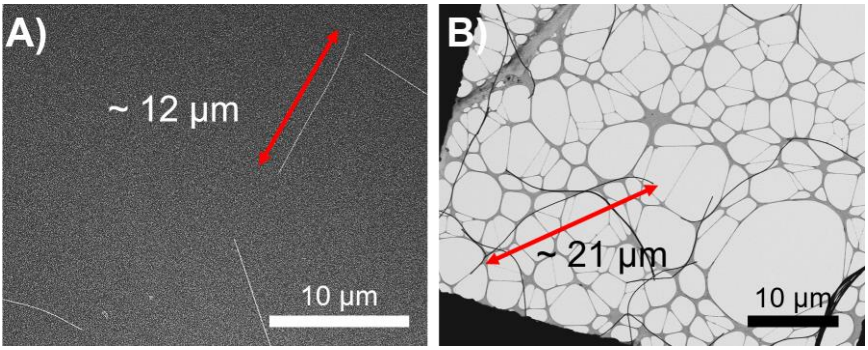

Figure II-14: SEM images of (A) ~ 47 nm nanowires on a silicon substrate and (B) ~ 92 nm nanowires on a CuC TEM grid. The length of the nanowires fluctuates between 10 and 30 µm

Figure II-14 exhibits SEM images of nanowires with two different diameters of 47 and 92 nm after their transfer on a substrate. The wires tend to be shorter after membrane dissolution and multiple cleaning steps. For wire synthesis, a 30 µm thick template was completely filled until caps growth. The expected wire length should thus be 28-30 µm. However, as seen in Figure II-14, the length of the nanowires fluctuates between 10 and 30 µm. The length of the wires transferred to a substrate is observed to depend on their diameter. Thin wires (< 50 nm) are

in general shorter with lengths between 5 and 15 µm. Wires with Ø ≈ 92 nm have a typical length of 15-20 µm. Larger wires (not shown here), obviously mechanically more stable, often have a length close to the theoretical length of 28-30 µm. Various effects may explain the shortness of the nanowires. (1) Nanowires are fragile and the **ultrasonication** treatments performed during the wire cleaning may lead to wire breaking. (2) The **limited wetting** of the small nanochannels may result in large wire growth-rate discrepancy, hence various wire lengths. These two effects are consistent with longer wires when their diameter is larger. However, the wire robustness also changes with the **composition**. Ag wires are in general shorter than gold equivalent ones.

3.3.2. Nanowire composition before and after dealloying

The diameter values presented above are averaged over several wire/membrane batches whereas the following compositional and morphological analyses are based on a small number of wires. Cylindrical AuAg nanowires with three different diameters, namely 85, 45, and 30 nm, and lengths between 10 and 20 µm were analyzed with respect to their composition and morphology before and after dealloying.

Table II-4: Averaged Ag content (at.%) in the nanowires measured by EDX spectroscopy before and after dealloying as a function of the initial diameter. Due to their fragility, dealloying of 30 nm thick wires was not performed

	Before dealloying Atomic % of Ag			**After dealloying Atomic % of Ag**	
Initial diameter (nm) / **Electrolyte**	85	45	30	85	45
50 mM $KAu(CN)_2$ 50 mM $KAg(CN)_2$	62 ± 4	60 ± 4	63 ± 3	8 ± 6	5 ± 6
50 mM $KAu(CN)_2$ 20 mM $KAg(CN)_2$	41 ± 4	38 ± 4	39 ± 3	39 ± 5	36 ± 3

The **average compositions**, measured by EDX-TEM for AuAg nanowires deposited using different electrolytes, before and after dealloying, are reported in Table II-4. Before dealloying, nanowires electrodeposited at - 1.1 V vs. Ag/AgCl

from electrolyte with $KAu(CN)_2$:$KAg(CN)_2$ ratio of 1:1 (Ag50Au50) and 5:2 (Au50Ag20) exhibit an average Ag concentration of about 60 at.% and 40 at.% respectively. For the chosen potential applied during electrodeposition, the wire composition is independent from the wire diameter. In addition, EDX measurements at various positions of a given wire reveal a rather **constant composition** along the nanowire. In few cases, fluctuations by a maximum of 10% along the about 20 µm wire length was observed. This is a strong indication that the electrodeposition occurs close to the diffusion-limited regime where mass transport is the rate-limiting step. This result is consistent with a previous investigation using cyclic voltammetry.

Regarding the wire composition after the dealloying process, the nanostructures obtained by dealloying of Ag-rich wires ($Au_{40}Ag_{60}$) contain very **little remaining Ag** (< 10 at.%, Table II-4). On the contrary, the dealloyed $Au_{60}Ag_{40}$ nanowires do not exhibit significant composition changes.

Pure Au and pure Ag wires electrodeposited under the same conditions as the alloy nanowires were checked by EDX in SEM. In both cases, the wires exhibit elemental purity without indication of contamination with other materials.

3.3.3. Formation of porous Au wires by dealloying

To observe the morphology evolution of AuAg nanowires dealloyed in nitric acid, nanowires before and after dealloying were analyzed by SEM and STEM. Panels A and B of Figure II-15 show HAADF images of nanowires synthesized using the Au50Ag50 electrolyte with diameters of 85 and 45 nm, respectively. The left images are representative for the as deposited wire, and the right images show typical wires after dealloying.

After the dissolution of the membrane and before dealloying, alloy (left images in Figure II-15) metal nanowires are **cylindrical** and exhibit very **smooth** surfaces for all compositions and diameters. After dealloying (right images), wires with very different morphologies are obtained. The dealloying in HNO_3 of $Au_{40}Ag_{60}$ wires results in **highly porous** nanostructures. In the case of large nanowires (Ø = 85 nm), dealloying leads to continuous random porosity (Figure II-15A), with

ligament sizes between 5 and 30 nm. In addition, the average size of the ligaments and pores does not seem to depend significantly on the wire diameter. Consequently, the small wires (initial diameter 45 nm) consist of partly discontinuous sections exhibiting rather irregular contour (Figure II-15B, Figure II-16C).

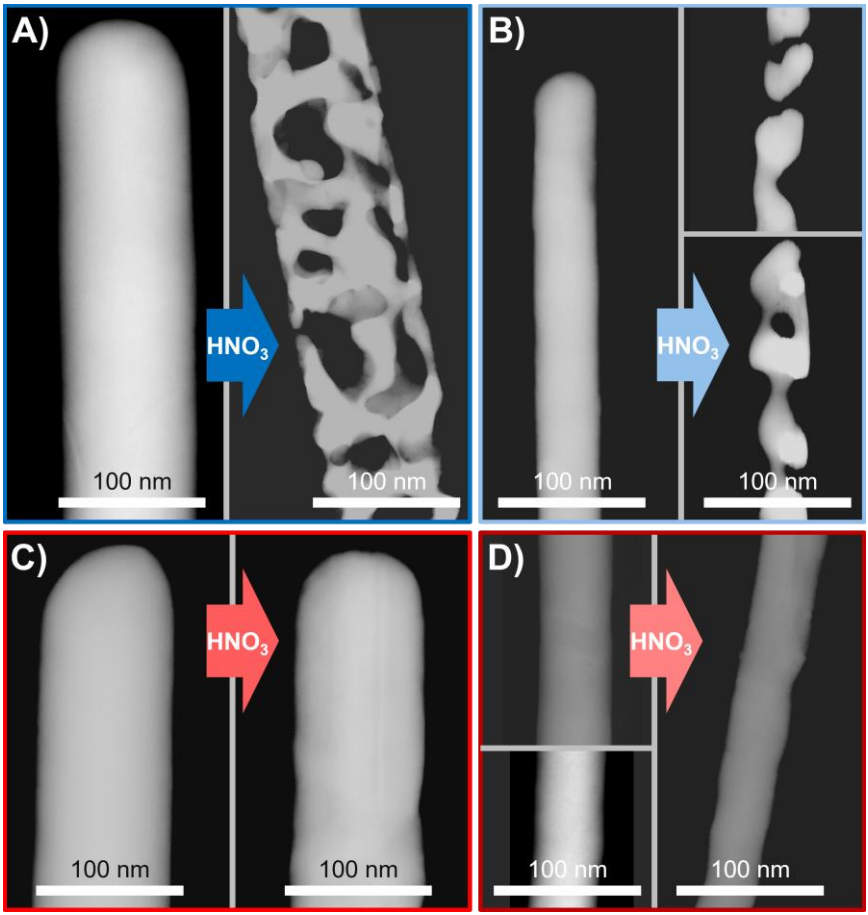

Figure II-15: Dark-field TEM images of AuAg nanowires before (left) and after (right) dealloying in HNO_3: (A) $Au_{40}Ag_{60}$ nanowire, initial diameter 85 nm; (B) $Au_{40}Ag_{60}$ nanowire, initial diameter 45 nm; (C) $Au_{60}Ag_{40}$ nanowire, initial diameter 85 nm; (D) $Au_{60}Ag_{40}$ nanowire, initial diameter 45 nm

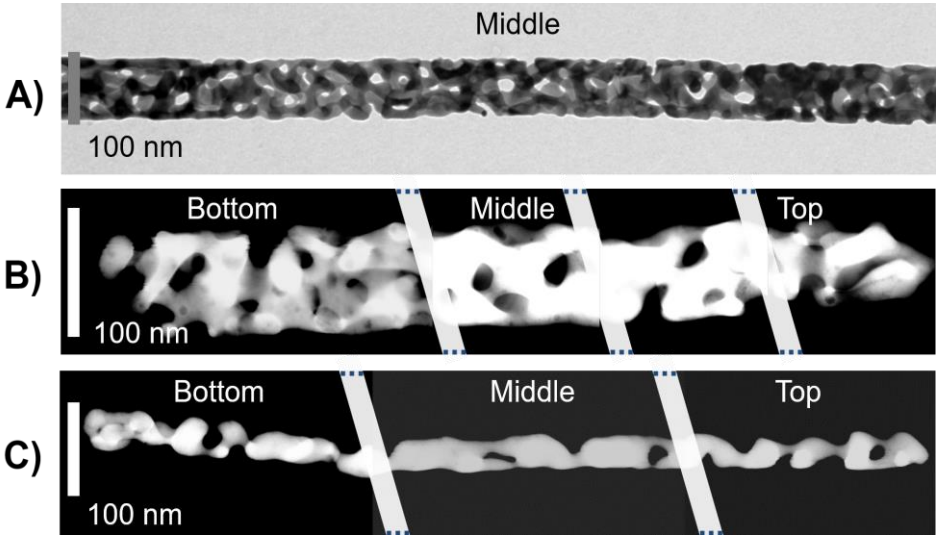

Figure II-16: (A) TEM and (B and C) HAADF images of several sections of one single (A and B) 85 nm and (C) 45 nm dealloyed $Au_{40}Ag_{60}$ nanowire. Bottom, middle, and top determine the position of the section of the wire imaged in the TEM

Figure II-16 shows images of different sections of an 85 nm porous gold nanowires (PAuNWs; A and B) and of a 45 nm PAuNW (C). Figure II-16 thus demonstrate that the porosity of the nanowires obtained by the dealloying of $Au_{40}Ag_{60}$ nanowire is homogeneous along their complete length.

In contrast, nanowires synthesized from an electrolyte with a significantly lower Ag concentration ($KAu(CN)_2$:$KAg(CN)_2$ ratio of 5:2; Figure II-15 C, D) do not exhibit any porosity after dealloying. Only the **surface roughness** slightly increases.

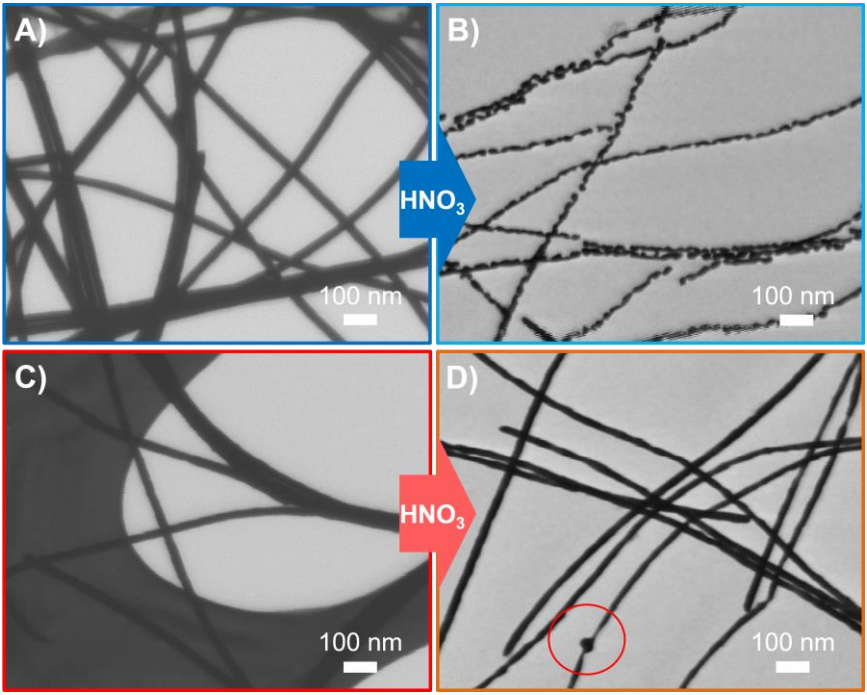

Figure II-17: STEM images of 30 nm AuAg nanowires before (left) and after (right) dealloying. (A and B) $Au_{40}Ag_{60}$ nanowires, nanowires after dealloying are not continuous (B); (C and D) $Au_{60}Ag_{40}$ nanowires, nanowires after dealloying exhibit strong diameter fluctuations (D)

In agreement with HAADF observations (Figure II-15), the STEM study of the dealloying of thin wires (Ø = 35 nm reveals that the $Au_{40}Ag_{60}$ wires are **no longer continuous** anymore. As shown in Figure II-17B, the dealloyed wires consist in a series of droplets either connected by several nanometers large interconnects or separated by few nanometers. On the other hand, the $Au_{60}Ag_{40}$ nanowires are continuous but exhibit **diameter fluctuations** as evidenced by the red circle in Figure II-17D. It is highly probable that similar roughness is present on larger wires of similar composition after dealloying but is hardly observed due to the lower curvature of the wires. SEM study of dealloyed $Au_{40}Ag_{60}$ nanowires with larger diameters (180 and 380 nm, presented in the next chapter in Figure III-7,

page 101) and similar compositions exhibit cognate porosities which are consistent with previous works from Searson et al.[49,53,54,188]

3.3.4. Wires crystallinity

To gain further insight into the dealloying process, the crystalline structure and local composition distribution of the nanowires both before and after dealloying were analyzed. Prior to dealloying, we measured the crystallographic orientation of the nanowire arrays still embedded in the membranes using XRD.

Figure II-18A shows XRD patterns of four different nanowire arrays with 85 nm diameter (from top to bottom: **Au**, $Au_{60}Ag_{40}$, $Au_{40}Ag_{60}$, and Ag), deposited at the same potential and temperature. The corresponding alloy concentrations are tabulated in Table II-4. The XRD patterns of both alloy nanowire arrays, $Au_{60}Ag_{40}$ and $Au_{40}Ag_{60}$ display all reflection peaks, namely (111), (200), (220), (311) and (222), indicating that **various orientations** of the crystals with respect to the wire axis are present in each sample. The analysis of the peak intensities indicates a small preferred (111) texture. The corresponding reflections are found at the same positions for both samples as expected because Au and Ag possess almost identical lattice parameters (4.0862 Å for Au and 4.0782 Å for Ag).[141] Interestingly, XRD patterns of pure Au (top, orange) and Ag (bottom, grey) nanowires exhibit less reflection peaks and reveal a **preferred crystallographic orientation** along the (200) and (220) direction, respectively. Since all other syntheses and geometrical parameters were the same, these results reveal a strong influence of the electrolyte composition and concentration on the crystallographic orientation of the arrays.

Figure II-18B shows the XRD patterns of three arrays of $Au_{40}Ag_{60}$ nanowires with wire diameters of 85, 45 and 30 nm. The number of reflections and their relative intensities are the same indicating that under these deposition conditions, the wire *diameter has no significant influence* on the crystallographic orientation.

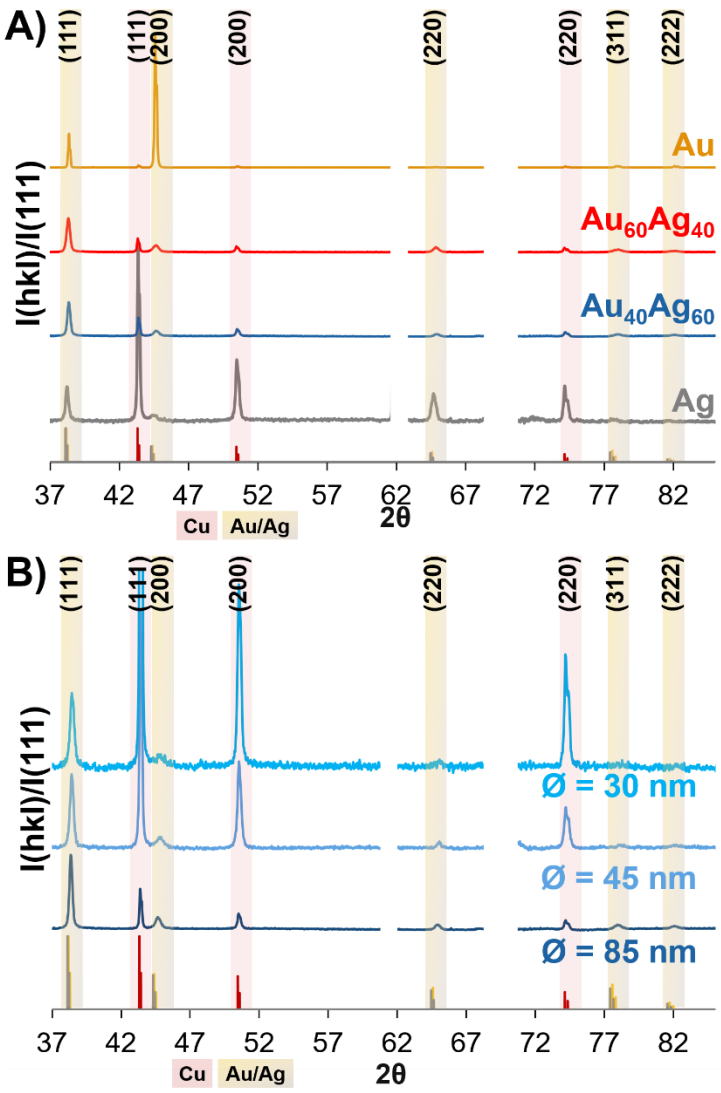

Figure II-18: XRD patterns of (A) arrays of nanowires with diameter 85 nm and various compositions and (B) arrays of $Au_{40}Ag_{60}$ nanowires with diameters 85, 45, and 30 nm. The vertical lines at the bottom indicate the intensities of the corresponding polycrystalline powder reference samples. All diffractograms as well as the reference values are normalized to the (111) orientation of gold

The crystallinity of single nanowires before and after dealloying in HNO_3 was studied by using TEM dark-field and bright-field imaging. In Figure II-19, representative images of sections of $Au_{40}Ag_{60}$ (Ø = 85 nm, Figure II-19A, B, and C) and $Au_{60}Ag_{40}$ (Ø = 45 nm, Figure II-19D, E and F) nanowires before dealloying are depicted at different magnification.

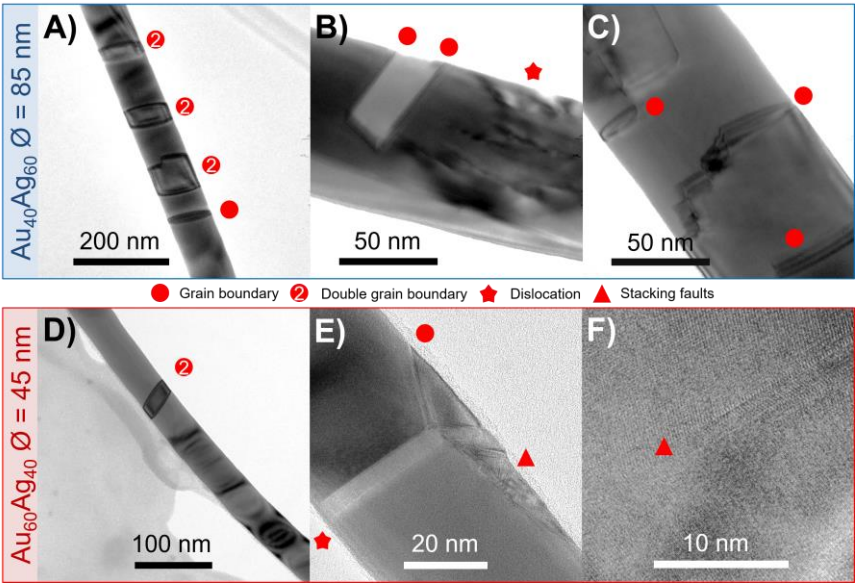

*Figure II-19: Bright-field TEM images of nanowires **before** dealloying: (A, B and C) $Au_{40}Ag_{60}$ nanowires (initial diameter 85 nm) and (D, E and F) $Au_{60}Ag_{40}$ nanowire (initial diameter 45 nm); Red dots mark single and double grain boundaries; red stars indicate dislocations, and red triangles point stacking faults*

Before dealloying, the nanowires consist of micrometer long grains with few crystalline defects and separated by single or multiple **grain boundaries**. Figure II-19A, B and C depict typical grain boundaries, dislocations, and double grain boundaries in $Au_{40}Ag_{60}$ nanowires (Ø = 85 nm). Figure II-19D and E show bright-field images of $Au_{60}Ag_{40}$ nanowires with diameter 45 nm with similar double grain boundary and other defects. Panel F shows HRTEM image of a stacking fault.

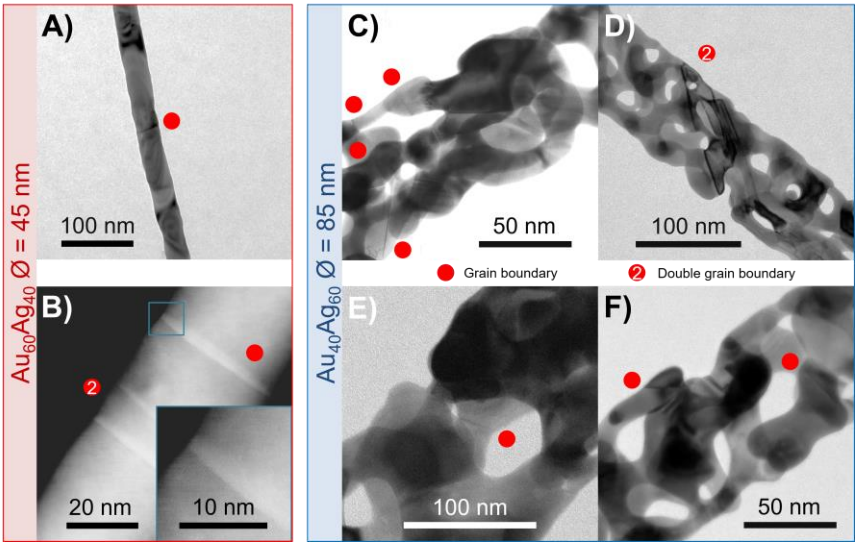

*Figure II-20: (A, C, D, E and F) Bright-field TEM and (B) HAADF images of nanowires **after** dealloying: (A and B) $Au_{60}Ag_{40}$ nanowire (initial diameter 45 nm) and (C, D, E and F) $Au_{40}Ag_{60}$ nanowires (initial diameter 85 nm); Red dots mark single and double grain boundaries*

Figure II-20 shows TEM images of sections of the initially equivalent wires **after dealloying**. Independently of their morphologies, the nanowires remain crystalline after dealloying with micrometer long grains. Figure II-20A and B show representative $Au_{60}Ag_{40}$ nanowire (initial diameter 45 nm) after dealloying in HNO_3 with grain boundaries as well as a double grain boundary. Figure II-20C, D, E, and F show $Au_{40}Ag_{60}$ sections of nanowires with diameter 85 nm after dealloying with various grain boundaries (C, E, and F) and a double grain boundary (D). Our results suggest that the nitric acid treatment does not alter the crystalline defects and the morphology of the wire close to the grain boundaries is similar to that in the middle of the grain. Moreover, the crystalline defects do not seem to influence the dealloying process as observed in Figure II-20D, where the double grain boundary crosses over voids formed by the dealloying process. These results are consistent with previous observations and established notions

that the crystallography of the AuAg is retained during dealloying of bulk samples and thin films.[189–191]

3.3.5. Analysis of the local composition with high spatial resolution energy dispersive X-ray spectroscopy

The crystallographic analysis was complemented by EDX in the scanning TEM mode. Although the size of the probing electron beam at the applied high-current settings was between 0.1 and 0.15 nm, the spatial resolution of the EDX analysis is limited by elastic electron scattering and thus influenced by the sample thickness. The use of a high-resolution TEM such as the JEOL ARM200F with probe correction provides a resolution ranging between 0.3 nm at the wire edge and 3 nm at the wire core.

Surface enrichment of alloy nanowires

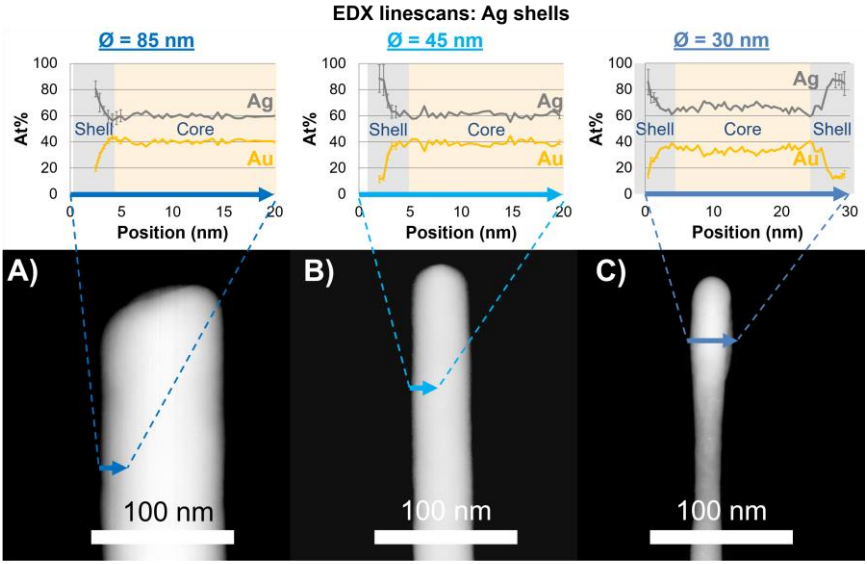

Figure II-21: HAADF images and the corresponding EDX linescans measured before dealloying at the edge of representative $Au_{40}Ag_{60}$ nanowires with diameters (A) 85, (B) 45, and (C) 30 nm. Lengths and positions of the linescans with respect to the nanowires are represented by arrows

We first analyzed the local composition of the $Au_{40}Ag_{60}$ and $Au_{60}Ag_{40}$ nanowires in the TEM before dealloying. Figure II-21 shows HAADF images of representative $Au_{40}Ag_{60}$ nanowires with diameters of (A) 85, (B) 45, and (C) 30 nm together with the corresponding EDX linescan across the nanowire surfaces. Interestingly, for all nanowire diameters, the measured Ag concentration is higher at the surface (written as shell in EDX linescans) than in the inner core of the wires. The Ag content in the nanowire bulk is constant whereas the concentration rises significantly towards the surface of the wire. The high resolution of the measurements allows us to determine a **surface layer** thickness between 1 and 4 nm with a composition of up to 90% of **Ag**. The constant concentration in the inner part of the nanowire observed by EDX together with our TEM investigations of the crystals clearly demonstrates that the body of the nanowire consists of a homogeneous AuAg solid solution. Note that the Ag concentration measured in the core of the wires is slightly higher for the 30 nm diameter wires (Figure II-21C) which is attributed to a higher relative contribution of the surface layer to the total EDX signal due to the higher shell-to-wire volume ratio.

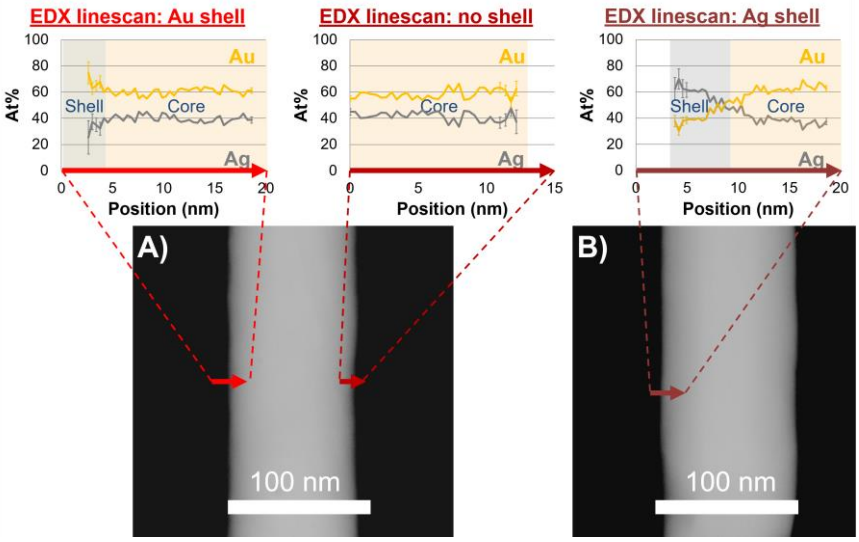

Figure II-22: HAADF images and corresponding EDX linescans measured on different $Au_{60}Ag_{40}$ nanowires (diameter 85 nm) before dealloying. Lengths and positions of the linescans with respect to the nanowires are represented by the arrows

Figure II-22 shows HAADF pictures of two $Au_{60}Ag_{40}$ nanowires with 85 nm diameter before dealloying and three EDX linescans measured across the surface of nanowires. For all of the analyzed $Au_{60}Ag_{40}$ nanowires, most positions along the surface show a **Au-rich shell** as displayed in the left EDX linescan in Figure II-22A. At the surface, the fraction of Ag decreases in average from 40% down to about 10% (25% in Figure II-22A) within few nm thickness. EDX analysis also reveals regions without a Au-rich surface layer (see middle linescan in Figure II-22). A small number of wire regions even exhibit the presence of few nanometer thick Ag enrichment as shown in Figure II-22B. In overall, the analysis indicates a less homogeneous Au surface layer along the wire length compared to the Ag layer discussed above for $Au_{40}Ag_{60}$ wires.

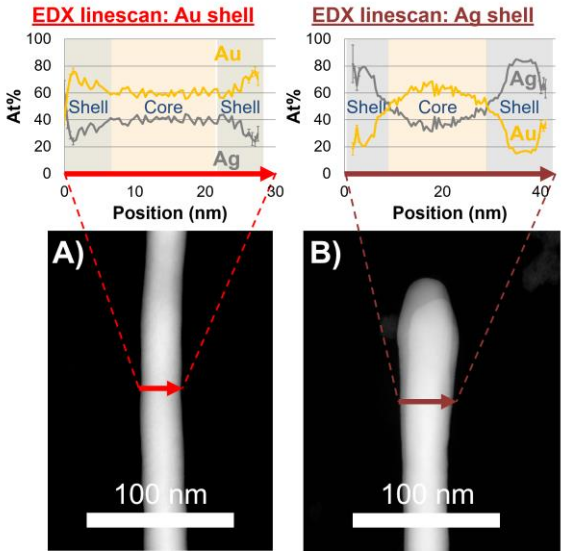

Figure II-23: HAADF images and corresponding EDX linescans measured on $Au_{60}Ag_{40}$ nanowires (diameter 30 nm) before dealloying. Lengths and positions of the linescans with respect to the nanowires are represented by the arrows

Similar results were obtained for the thinner wires as shown in Figure II-23, where HAADF images and the corresponding EDX linescans measured on $Au_{60}Ag_{40}$ nanowires with diameter of 30 nm are depicted. The Au-rich shell is still dominant (Figure II-23A) in most of the analyzed regions of the various wires while few areas indicated the presence of a Ag-rich shell (Figure II-23B).

Our results on $Au_{40}Ag_{60}$ and $Au_{60}Ag_{40}$ nanowires provide evidence of Ag and Au **surface segregation**, respectively, independent of the diameter of the analyzed nanowires. The existence of enriched surfaces or core-shell structure for the initial electrodeposited AuAg nanowires has not been previously reported and is, however, very important for the understanding and interpretation of the subsequent dealloying process. The surface enrichment could possibly originate from an inhomogeneous electrochemical deposition process in the nanochannels of the polymer template due to the presence of negative surface charges on the wall of the channels.[192] An alternative explanation is related to the observation that Ag-rich surfaces appear preferentially – but not exclusively – at the end of the nanowires. Rounding and diameter increase are more obvious in the case of 30 nm diameter nanowires as seen in Figure II-23B. This is a strong indication that the surface enrichment occurs during or after the dissolution of the polymer membrane and originates from segregation and/or surface diffusion, as evidenced in previous works.[164,193] It is noted that our nanowires were not stored in a vacuum but in most cases in dichloromethane and/or in air on a substrate for 2 - 3 days prior to TEM analysis. However, Ag is known to have a lower surface energy,[194,195] which is inconsistent with the existence of the Au-rich surface layer observed on $Au_{60}Ag_{40}$ wires. Further investigations are required to understand how the surface enrichment processes are influenced by the different sample preparation steps, namely, the pore etching process, the electrodeposition, and the polymer dissolution. The enrichment of the surface of the alloy nanowires can have a direct impact on the dealloying process and on the resulting morphology of the dealloyed nanowires.

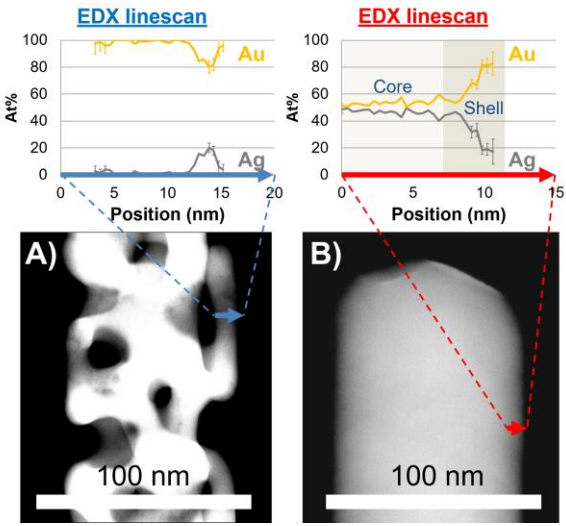

Figure II-24: HAADF images and corresponding EDX linescans measured on (A) a $Au_{40}Ag_{60}$ nanowire and (B) a $Au_{60}Ag_{40}$ nanowire (initial diameters 85 nm) after dealloying in HNO_3. Lengths and positions of the linescans with respect to the nanowires are represented by the arrows

Local composition of dealloyed nanowires

Local high-resolution EDX analysis of the AuAg nanowires after dealloying is presented in Figure II-24. The HAADF images show the structures obtained after dealloying of 85 nm diameter of $Au_{40}Ag_{60}$ (Figure II-24A) and $Au_{60}Ag_{40}$ (Figure II-24B) nanowires. The formation of porosity in $Au_{40}Ag_{60}$ is in agreement with percolation simulations for face centered cubic lattice where the parting limit is estimated to be about 58.4 Ag at.%.[153] In Figure II-24A, the EDX linescan shows the composition of a ligament and evidences its almost pure Au composition across the ligament except for a small region (2-3 nm) with 20 at.% of remaining Ag content. **Domains** with Ag concentration up to 30-40 at.% are randomly distributed in the ligaments and are not centered in the middle of the ligament as the dealloying theory suggests.[35]

After dealloying, the $Au_{60}Ag_{40}$ nanowires exhibit a diameter and composition similar to that of the initial nanowires (Figure II-24B). They also have a relatively

homogeneous Au-rich shell. This finding is consistent with percolation theory calculations and experimental observations where the limit for porosity evolution is obtained for bulk and thin films between 55 and 60 Ag at.%.[6,153] After dealloying, the surface of the $Au_{60}Ag_{40}$ wires is slightly rougher than the initial surface. It is probably due to corrosion occurring at the surface regions where the Au surface layer is discontinuous, as discussed in Figure II-22.

3.3.6. Comments on the stability of the alloy nanowires

In addition to the formation of surfaces layers with composition differing from the bulk, the presence of particles at the surface of old wires was observed in the TEM on some alloy nanowires.

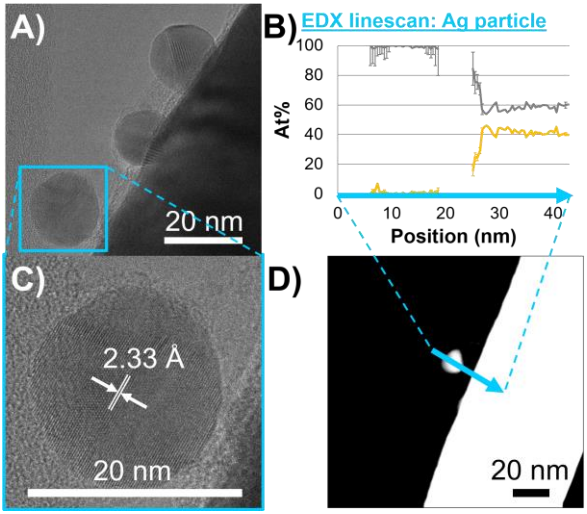

Figure II-25: HRTEM (A and C) and HAADF (D) images and a corresponding EDX linescan (B) measured on $Au_{40}Ag_{60}$ nanowires (diameter 85 nm) with surface nanoparticles before dealloying. Length and position of the linescan with respect to the nanowire is represented by the arrows

Some wires were studied in the TEM several months after transfer on the substrate in contrast to the previous results where TEM and EDX studies were performed 3 days after membrane dissolution. Figure II-25 shows HRTEM and HAADF images of such $Au_{40}Ag_{60}$ nanowires with diameter 85 nm exhibiting the presence

of **nanoparticles at their surface** and a corresponding EDX linescan. The nanoparticles are at the surface of the nanowires but do not look tightly bound to the wire. HRTEM imaging (Figure II-25C) shows that the nanoparticles are crystalline and the lattice parameter of the particles coincide with that of gold or silver. EDX analysis of one particle (Figure II-25B) reveals that the particle is about 100% composed of Ag. The EDX linescan also evidences the net separation between the **Ag particle** and the wire (about 5 nm).

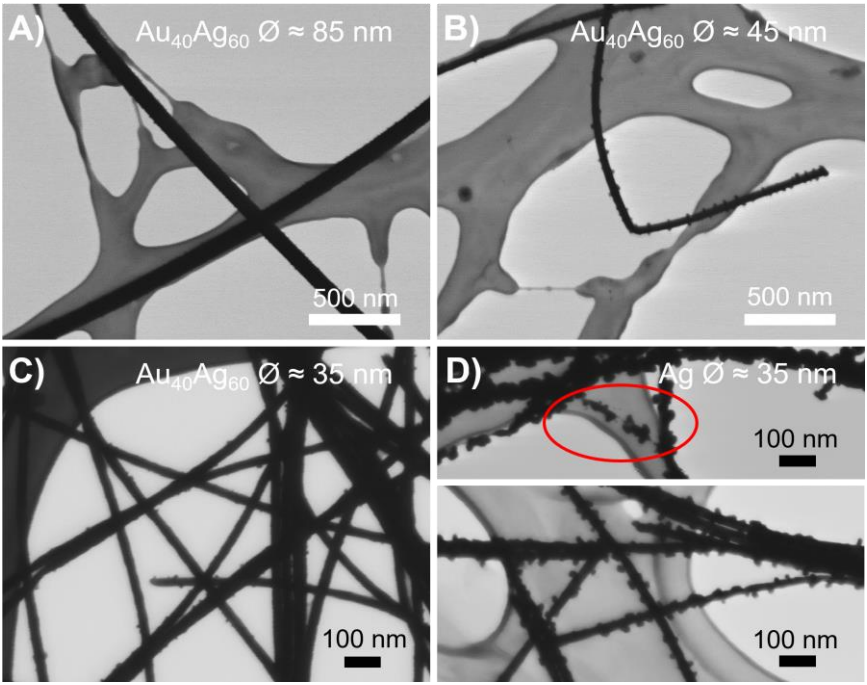

Figure II-26: STEM images of nanowires with different compositions and diameters presenting surface nanoparticles after several weeks in air. (A, B, and C) $Au_{40}Ag_{60}$ nanowires with respective diameter of 85, 45, and 35 nm after several weeks in air. (D) 35 nm large Ag nanowires with pronounced coverage with particles

Consistently with the results introduced previously, a silver shell is also present on the $Au_{40}Ag_{60}$ nanowire, even after several months of storage in air. The Ag nature of the nanoparticles, confirmed by EDX as well as HRTEM, contrast with

other studies where the formation of nanoparticles at the surface of pure Ag nanowires was attributed to the formation of Ag_2S.[196–198]

The presence of particles is also demonstrated by STEM investigations on NWs stored on the wafer in air for several weeks as shown in Figure II-26. The investigation reveals that nanoparticles form on all wires that contain Ag, independently on their diameter. Figure II-26A, B, and C show $Au_{40}Ag_{60}$ nanowires of diameter 85, 45 and 35 nm respectively. Numerous particles appear on small nanowires whereas almost no particles are observed on 85 nm wires at this magnification. The connection between the particles and the wires is not steady, thus quantification of the particle density is not reasonable. Nevertheless, SEM observations show the tendency of an increasing particle number with increasing Ag content in the wires. In the case of pure Ag nanowires with diameter of 35 nm, the particles have dimensions comparable to the wire diameter, which leads to discontinuous wires as shown circled in red in Figure II-26D. This behavior is clearly *different from Rayleigh instability*, which forms regularly spaced spherical droplets with diameter larger than the wire diameter. It has to be emphasized that, no particles could be found on nanowires directly after membrane dissolution and transfer to the substrate.

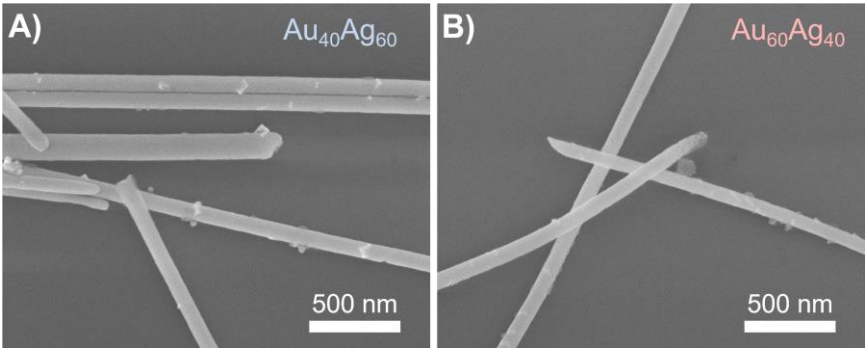

Figure II-27: SEM images of (A) $Au_{40}Ag_{60}$ and (B) $Au_{60}Ag_{40}$ nanowires with 85 nm diameter stored on a silicon substrate at 60 °C in air for 72h

The influence of different **storage conditions** has also been considered. Nanowires stored as dichloromethane suspended solution for long periods (before

transfer) do not exhibit nanoparticles directly after the transfer (not shown). Similarly, nanowires kept on the substrate in dichloromethane are not covered by particles. However, it cannot be excluded that the nanoparticles are washed away when taking the sample out of the organic solvent. Nanowires stored at higher temperature (60 °C) in air feature very fast the presence of particles as shown in Figure II-27D and E. Thus, the formation of particles directly depends on the surrounding media and is enhanced by **temperature**. These considerations are consistent with the surface diffusion and segregation already mentioned. Surprisingly, particles can also be observed on $Au_{60}Ag_{40}$ nanowires Figure II-27E that exhibit Au surface enrichment (see section 3.3.5). However, such wires also exhibit inhomogeneity of the gold layer that may explain the particle evolution.

Our observations raise the question of the stability of the nanowires containing Ag. Further systematic investigations are necessary to better understand the influence of the temperature and other external parameters on the diffusion of Au and Ag as well as to comprehend the surface segregation occurring on the alloy nanowires.

4. Summary

The synthesis as well as the characterization of porous gold nanowires has been presented in this chapter. First, the analysis of the electrodeposition process evidences that cyanide based electrolytes enable high current efficiencies and depend on the metal ion type and concentration. Cyclic voltammetry confirms that the reduction of Au salt can follow a 2-step path at intermediate voltage or, like Ag, a one-step reduction at very negative voltage. In addition, Au and Ag can be co-deposited from a single bath electrolyte. Operating in a recessed geometry (i.e. in nanochannels) exhibits similar reduction processes and the strong current density increase is mainly attributed to non-faradaic currents such as capacitance and uncompensated resistance of the electrolyte in the nanochannels. Because the potentiostatic reduction of Au and Ag at - 1.1 V occurs close to diffusion-limited regime, the growth of the nanowires can be precisely controlled, with the

differentiation of the various deposition steps: initiation, wire growth, and cap growth. Moreover, the composition is expected to be homogeneous along the wire deposition and can be tailored by monitoring the constitution of the electrolyte. The wires fabricated are cylindrical, independently on their composition and for all diameters equal or below 100 nm, whereas larger wires have bullet like endings. XRD and TEM demonstrate that all nanowires studied are polycrystalline, independently on the diameter and composition. The grains are several micron long and often separated by double grain boundaries consisting in two grain boundaries spaced by only few tenth of nanometers. Compositional analysis by EDX in the TEM shows surface segregation in alloy nanowires. Ag surface enrichment of 1 to 4 nm is observed on all measured $Au_{40}Ag_{60}$ nanowires whereas a discontinuous Au layer is detected on $Au_{60}Ag_{40}$ nanowires. Additionally, the formation of Ag nanoparticles has been observed on Ag containing nanowires with various compositions and seems to be enhanced by temperature. The dealloying of nanowires with composition of $Au_{40}Ag_{60}$ gives rise to porous nanowires with ligaments between 5 and 30 nm. Consequently, thin nanowires with diameter below 50 nm before dealloying are not always continuous after HNO_3 treatment. TEM analysis confirms that the crystalline defects seem neither to be affected by dealloying nor to influence the process. After dealloying, the residual Ag is of only few percent and is mainly situated in small Ag rich domains. Surface roughness is obtained by dealloying of $Au_{60}Ag_{40}$ nanowires and no change in composition is observed.

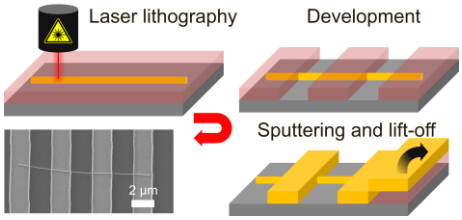

Chapter III

Contacting individual nanowires for transport measurements

The recent interest in gold nanostructures, especially for sensing and transparent conductive films purposes is triggering many investigations of the transport properties of gold and silver nanowires.[12,49,199–205] The electrical conductivity of gold wires with various diameters and crystallinities has been studied. It was shown that for diameters below 100 nm, the surface scattering of the electrons adds to their scattering at the grain boundaries, thus modifying the conductivity.[206] Lilley et al. measured nonlinear resistance as a function of the current for Au nanowires that was induced by surface contamination.[39] Porous nanowires provide even higher surface-to-volume ratio compared to solid cylindrical wires, being thus particularly interesting for sensing. Due to their interesting surface chemistry, gold nanowires functionalized with enzymes have been used for biosensing and electrochemical sensing. A. Roy et al. demonstrated by simulation that bare ultrathin Au nanowires may also sense chemical molecules such as carbon monoxide or CH_3S.[207] Nevertheless, only very few studies focused on the electrical properties of porous gold nanowires and their applicability for sensing.[49,50,208] Furthermore, no study shows the effect of residual silver (more

sensitive to oxidation and chemical reactions) on the wire conductivity and on the performance of the sensor.

This chapter presents the development of a set of methods developed at the GSI Helmholtz Center and at the Hochschule RheinMain that will allow in a near future to measure, in our laboratories, the transport properties of such wires. In the first part of this chapter, the optical lithography is introduced followed by a detailed description of the process developed to deposit four-point contacts on nanowires. Special observations when using measurement chips, including trenches, are discussed together with the challenges for electrical and thermal characterization of porous nanowires.

1. Introduction to optical lithography

From the Greek – lithos: „stone“ and grapho: „to write“ – the optical lithography is a process used to selectively pattern a surface. One of the major applications of this technique, since its beginning, is the fabrication of integrated circuits.[9] Lithographic techniques are also commonly used in research to build up new micro or nano structures, to selectively modify them or to electrically connect structures of very small dimensions. Two different approaches for lithography coexist. Based on the same principle, they can be distinguished by the role of the shaped resist layer. Figure III-1 depicts the two processes. In both cases, the initial step consists of the homogeneous coating of a substrate (often a silicon wafer) with resist. Typically applied from a solution by spin coating, resists are organic polymers with high sensitivity to a specific wavelength. This resist **coating** step (A) includes the promotion of adhesion by surface treatment of the substrate, the spreading of the solvated resist on the substrate and soft baking to evaporate solvent leftovers. The second major step is the selective **exposure** of the resist (B). Traditionally, resists are exposed to UV through a mask. Thus, the alignment of the mask is critically important. Depending on the resist, a post-exposure baking may be required. Depending on the type of resist, the **development** of the resist consists in the selective removal of irradiated (positive resist) or non-

irradiated (negative resist) domains. Positive resists are more sensitive to chemical dissolution after exposure, thus the exposed resist is dissolved by the developer (C). On the contrary, negative resist harden with light exposure. Consequently, the developed design will be the negative of the exposure pattern. The developed resist then serves as **template** for further operations. On the one hand, optical lithography may be adopted to modify the structure of a preexisting homogeneous surface as shown in D1 and E1. An example can be the selective etching of a silicon wafer according to the resist template using fluorhydric acid solution. Plasma etching can also be used. Alternatively, optical lithography is used to deposit a new patterned surface layer as displayed in D2 and E2. Material is then deposited in the open areas of the resist that serves as template. Sputtering or evaporation is commonly used to deposit thin coatings but electrodeposition or electroless deposition may also be used to form the lithographically patterned structures. After the patterning step (D), the resist is removed in a step called **lift-off** (E). During lift-off, all layers on top of the resist are also evacuated.

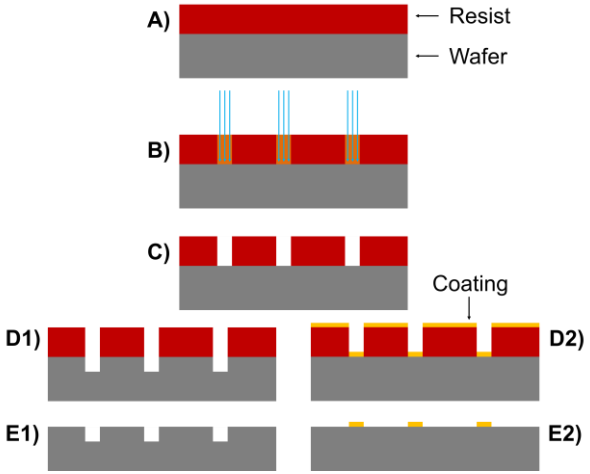

Figure III-1: Simplified scheme of the major steps of lithography: (A) coating of substrate/wafer with resist, (B) selective illumination of resist, (C) development by selective dissolution of irradiated resist, (D1) texturing of the substrate through the resist mask, (D2) selective coating of the wafer through the resist template, (E1 and E2) lift-off: removal of resist from wafer including all layers on top of the resist

The selective exposition of the photoresist is mostly achieved by using masks. However, while the use of irradiation masks is most appropriated for large-scale production on large wafers, laser lithography presents the advantage to be more flexible. Laser lithography applies the focused beam of a laser to irradiate predetermined positions of a sample. Usually coupled with an optical microscope, it allows to precisely select the area to expose and to easily modify the irradiation pattern. Thus, laser lithography is particularly appropriated to design patterns on top of randomly distributed nanostructures such as our nanowires. In this thesis, this method was applied to electrically contact solid and porous gold nanowires. In addition, special chips were developed for future standard processing by multiple step optical mask lithography. The fabrication of these so-called z-chips by multiple step optical mask lithography is performed at the Hochschule RheinMain by Prof. Dr. F. Völklein and is described in the following publications.[209,210]

2. Experimental

2.1. Preparation of nanowires

Nanowires were prepared in two manners, illustrated in Figure III-2. One consisted in the fabrication of electrical connections by laser lithography on top of the nanowires lying on a flat silicon wafer (Figure III-2A). In the second one, the nanowires were drop-casted on prefabricated substrates with cantilevers arrays or trenches arrays (Figure III-2B).

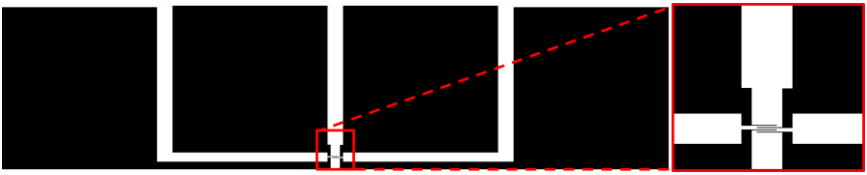

Figure III-2: Scheme of (A) a nanowire with top contacts prepared by lithography and (B) a suspended nanowire on top of contact lines

Samples for optical lithography

For laser lithography, the nanowires were *transferred* on flat silicon wafers (Figure III-2A) with ~ 100 nm thermal oxide SiO_2 (Si-Mat, P/Boron <100>, 256-306 µm; wafer diameter up to 2 inches) according the method introduced in Chapter II.2.3. Such Si substrates were chosen because of the insulating properties of the silicon oxide necessary to allow electrical measurement of the metallic nanowires. After the transfer of the wires, the wafers were *cleaned* of all impurities by ultrasonication in acetone bathes (2×30 s), flushing with acetone and subsequently with isopropanol. Finally, the substrate is dried using a nitrogen jet. The presence of the nanowires after this cleaning process proves their strong adhesion to the substrate.

Substrates with trenches

In preparation for future measurements of transport or mechanical properties, nanowires disconnected from the substrate were also considered. For example, the measurement of the thermal properties of porous gold nanowires requires having suspended wires to minimize the heat loss in the wafer. Hence, nanowires were spread across trenches and arrays of cantilevers (Figure III-2B). On the one hand, silicon wafers with 2 and 10 µm wide trenches were provided by Dr. Laurent Belliard (Acoustique pour les nanosciences group of the Institut des Nanoscience, Paris, France). On the other hand, Z-chips, consisting of an array of metallized silicon cantilevers were provided by Prof. Dr. Friedemann Völklein (Institute for Microtechnologies of the Hochschule RheinMain, Rüsselsheim, Germany). The cantilevers were fabricated with width of 4 and 8 µm and spaced by 4 µm. To spread the nanowires across the trenches, the nanowires were dispersed randomly on the chips according to the method introduced in Chapter II.2.3.

2.2. Laser lithography on wafers with nanowires

The wafers with randomly distributed nanowires were coated with resist by spin coating. For wires with diameter below 100 nm, the resist AZ1505 was used whereas the resist AZ1518 was employed to coat thicker wires. For both resists, the spin coating procedure consists in first spreading the resist at 500 RPM for 5 s and then flatten the resist at 4000 RPM for 40 s. Theoretical coating thicknesses according to the manufacturer MicroChemicals are respectively about 0.5 and about 2 µm. After spin coating, the resist was soft backed at 100 °C for 60 s and subsequently cooled down to room temperature prior illumination.

Laser lithography was then performed at GSI using a Heidelberg Instrument µPG 101 equipped with diode laser with a wavelength of 405 nm. Using the optical microscope integrated in the lithography setup, the exposure pattern is centered on the nanowires of interest. The illumination is performed with the laser diode at a power of 10 mW in the case of the thin resist and 11 mW for the thickest resist and, using filters, the light intensity is set to 70% of the diode power.

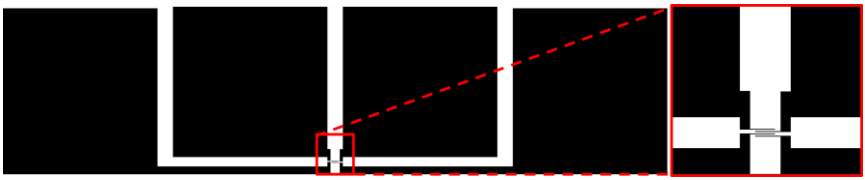

Figure III-3: Schematic of the illumination pattern used for laser lithography. The inset magnifies on the 1.5 µm large contacts that are spaced by 2.5 µm. Each microscopic contact is associated with a patch of 400×400 to 500×500 µm²

Figure III-3 display a typical design used for the illumination. For 4 contacts, it consists of a row of 4 macroscopic patches (400×400 to 500×500 µm²) connected to 4 microscopic contacts of 1.5 µm width and spaced by 2.5 µm (inset). After illumination, the patterns are developed using dilution of the developer AZ351B (MicroChemicals) with water (1:4). Development process is done at room temperature for 45 and 50 s under constant manual agitation (for resists AZ1505 and AZ1518, respectively). The sample is then transferred to a first water flow

bath for 1 min and is immersed in a second water bath for several minutes. After complete drying of the sample, it is sputtered with a ~ 5 nm thick Cr adhesion layer and a thicker gold layer. The Au sputtered layer was coated thick enough to completely embed the nanowire. The lift-off was performed in two consecutive steps. First, the sample was inserted diagonally in an acetone bath (sample inclined by 45° with the sputtered side oriented downward). After a maximum of 12 hours of immersion, the lift-off was finalized using acetone flow.

2.3. Dealloying of AuAg nanowires

To perform measurements on porous nanowires, the contacted alloy wires were dealloyed on their substrate by immersion in HNO_3 (67%) for 3h. In the case of nanowires spread over trenches, the same methodology was applied.

3. Observation of connected nanowires

3.1. Lithographic contacts on top of individual nanowires on Si wafers

Figure III-4 shows representative examples of individual nanowires under four contacts fabricated by laser lithography. The contacts thus fabricated have in average a width of ~ 2 µm and are spaced by ~ 2 µm. Therefore, the minimum length of nanowires to be measured by 4-point contacts is ~ 14 µm. Figure III-4A shows an 85 nm nanowire connected with 4 contacts and Figure III-4B displays a shorter nanowire with diameter of 45 nm. The nanowire is consequently only connected with two contacts. In addition to the length of thin nanowires due to their fragile structure (see Chapter II.3.3.1), their small diameter make the observation and selection of nanowires by optical microscopy challenging.

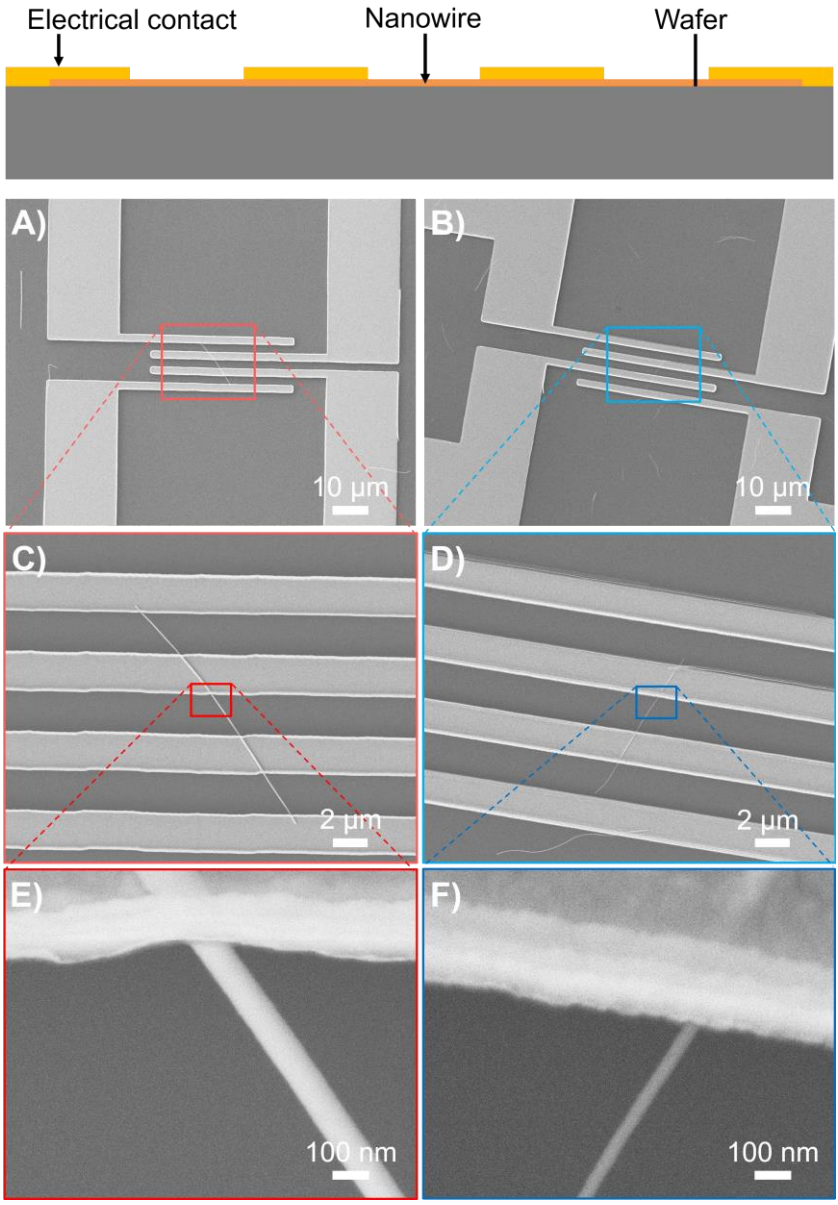

Figure III-4: Scheme and SEM images of 4-point contacts on an individual nanowire with diameter of 85 nm (A, C, and E) and 40 nm (B, D, and F)

It is also noted that the contact pattern exhibited in Figure III-4B coincide with the lithographic mask proposed in Figure III-3. The Heidelberg Instrument µPG 101 lithography utilized to illuminate the resist allows to rotate the designs so that every nanowires can be addressed. However, inherently to the laser displacement process, the illumination of a rotated design is more time consuming than the illumination of "inline" designs such as the one presented in Figure III-3. Therefore, designs with various contact orientations were employed. Thus, the contacts illustrated in Figure III-4A originate from the illumination of another pattern.

Figure III-4E and F show that the edges of the contact consist in thin walls (lighter area of the contact). These unwanted features should not affect electrical measurements. They probably originate from the use of positive resists and the presence of tilted resist walls after development. In order to avoid the presence of these features, it is necessary to fabricate a resist design with undercuts. Impossible to obtain with positive resist, they are achievable using negative resist. However, negative resists implies to expose the complete sample but the pattern, which is complicated and time consuming for laser lithography. Nielsch et al.[211] proposed to use multilayers of positive resists to obtain such undercuts and avoid the presence of these walls.

3.2. Nanowires on pre-fabricated substrates

Besides of lithographic contacting, we alternatively tried to deposit nanowires across trenches and cantilevers of pre-structured wafers.

3.2.1. Suspended cylindrical nanowires

Figure III-5 schematically represents nanowires lying over tranches and Figure III-5A and B shows corresponding SEM images of suspended nanowires with 85 nm diameter. The inter-trench spacing in Figure III-5A and B are 10 and 2 µm, respectively. Figure III-5A shows that the randomly distributed nanowires are not robust enough to lie across 10 µm wide trenches but instead bend and adopt the shape of the trench. For smaller gaps between the trenches, stable wire deposition

is possible as illustrated in Figure III-5B, showing a nanowire across several 2 µm wide trenches.

Similar results were obtained for the deposition of nanowires on cantilevers arrays. Figure III-6 shows a scheme of a nanowire on top of cantilevers metallized with a thin gold layer as well as SEM images of such nanowires with various diameter. Figure III-6A and B show 26 to 30 µm long nanowires with diameter 380 nm crossing several cantilevers without deformation. Figure III-6C and D display randomly distributed 85 nm nanowires (similar to the ones in Figure III-5) on top of a metallized cantilever array illustrating that they can hang across gaps of at least 5 µm. Finally, Figure III-6E and F exhibit SEM images of thin nanowires (40 nm) lying over two cantilevers separated by ~ 5 µm. Such thin nanowires slightly bend but do not break as observed in Figure III-6E. Thus, all types of as-deposited nanowires presented in this work may be spread over trenches or cantilevers arrays if the distance between them is not too large. This is critically important in order to be able to measure mechanical and transport properties of these nanowires without influence of the substrate before and after dealloying.

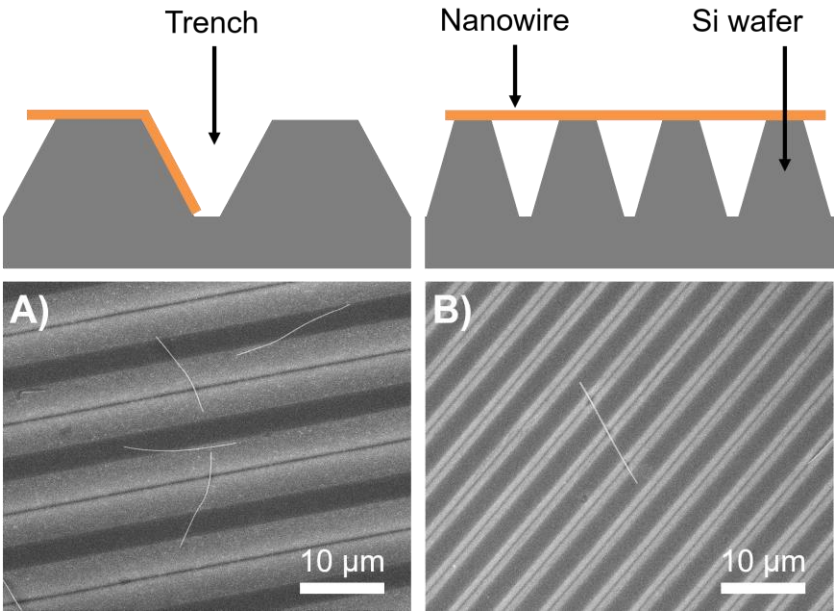

Figure III-5: Scheme in cross-sectional view of a nanowire standing across trenches and plan-view SEM images of 85 nm nanowires over (A) 10 µm and (B) 2 µm wide trenches

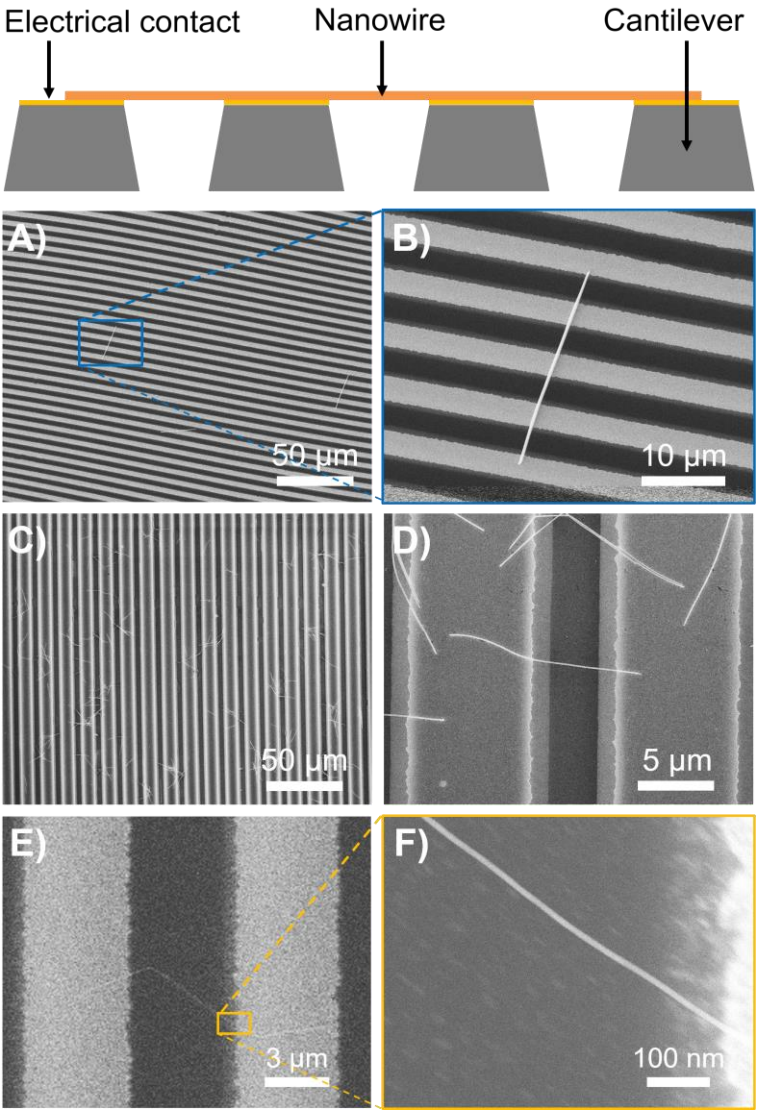

Figure III-6: Schematic representation of a nanowires lying on the metallized cantilevers of a z-chip and SEM images of such nanowires with diameter of (A,B) 380 nm, (C,D) 85 nm and (E,F) 40 nm. The metallized surfaces of the cantilevers appear in the SEM images in light grey

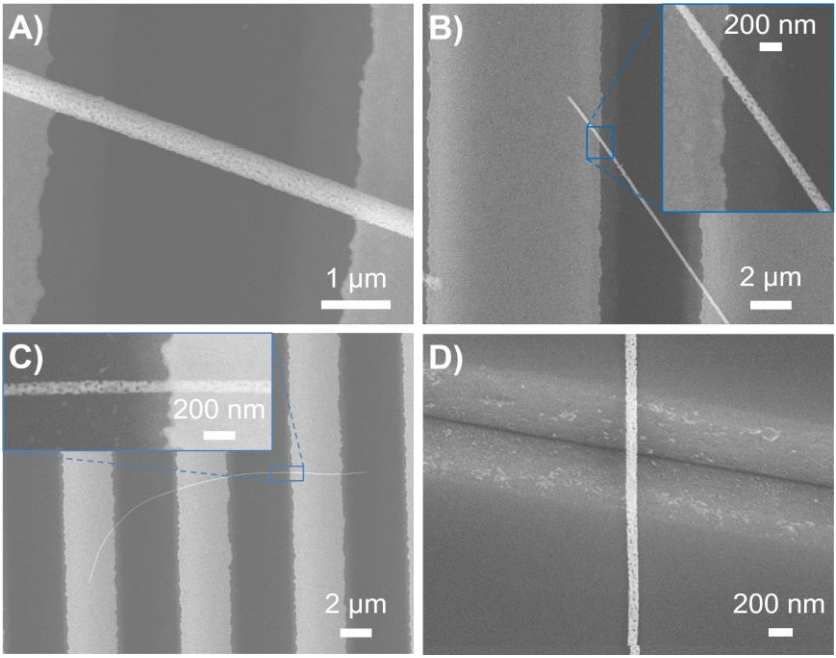

Figure III-7: SEM images of nanowires with various diameters over (A, B and C) cantilevers separated by 3-5 µm and (D) 2 µm trenches. PAuNWs of initial diameter (A) ~ 380 nm, (B) ~ 180 nm, and (C and D) ~ 85 nm

3.2.2. Dealloying of suspended nanowires

Dealloying was performed on $Au_{40}Ag_{60}$ nanowires suspended across cantilever arrays and trenches. Figure III-7A, B and C exhibit nanowires with initial diameters of 380, 180, and 85 nm after their dealloying on cantilevers arrays. All dealloyed nanowires exhibit high porosity and remain continuous. In addition, no evident sign of bending induced by the dissolution of the Ag could be evidenced. Similar observations are made for nanowires above trenches as shown in Figure III-7D. These results indicate that pre-mounted AuAg nanowires can be dealloyed by nitric acid. This is very promising for the future measurement of multiple parameters on one single chip with suspended nanowires.

3.3. Challenges of electrical characterization of Au nanowires

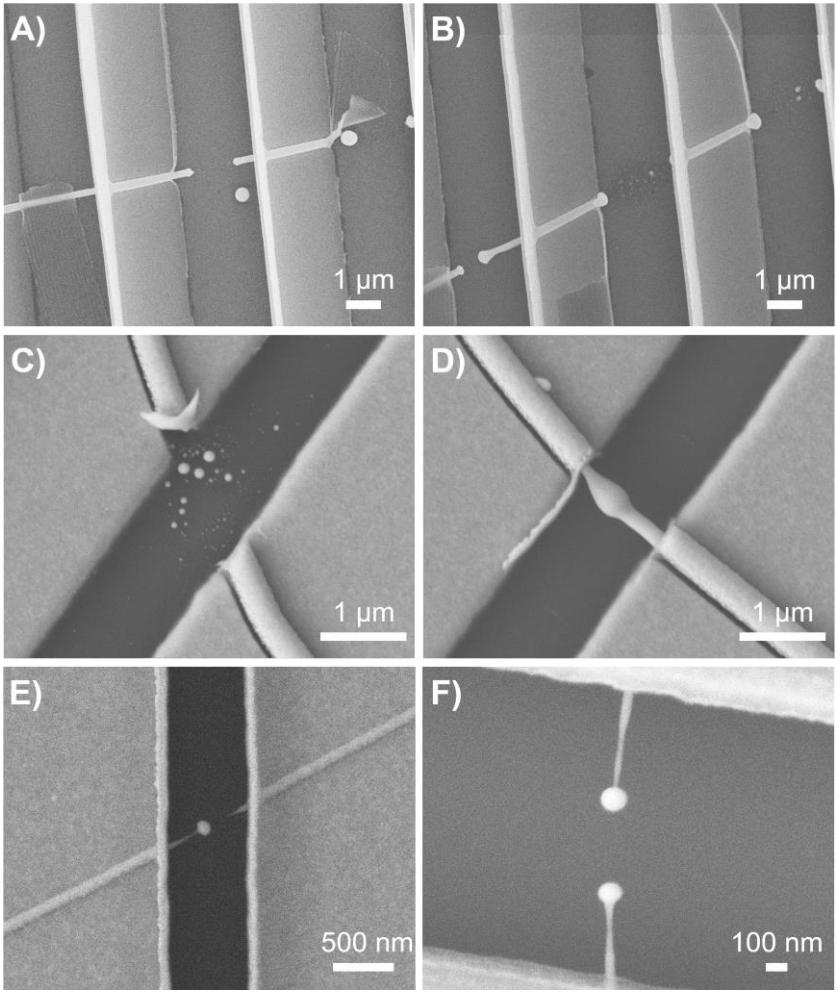

Figure III-8: SEM images of damaged nanowires contacted with 4-point contact. (A, B, C, and D) Ø ≈ 185 nm and (E and F) Ø ≈ 45 nm. (A and B) melting of the nanowires after current sweep between -10 and 10 µA using a Keithley 2600A; (C and D) burning of the nanowire due to strong transient current applied by an ohmmeter; (E and F) failure of nanowires after manipulation

Electrical transport measurements of Au based nanowires are very challenging. Due to the very small dimensions, and because gold is an excellent conductor, the measurement of the electrical transport in nanowires is delicate.

The measurement of the electrical properties of our nanowires are planned but could not be done due to time constrains in this thesis. What is important for these measurements is (1) to assemble a setup able to apply very low current and to measure correspondingly small voltages, (2) manipulate nanowires always shortcut and grounded to avoid premature failure of the nanowires, and (3) ensure the good quality of the contacts. Exemplary failure resulting from non-respect of theses experimental conditions are presented in Figure III-8.

In Figure III-8C, the nanowire failure was observed after an uncontrolled voltage was applied with an ohmmeter with low internal resistance. This figure suggests that the wire is partly or completely evaporated subsequently to the electrical discharge. The gold then condensate on the wafer and forms an array of randomly distributed gold nanoparticles over several μm^2. Consistently with the hypothesis of a sudden temperature rise, signs of heat induced instabilities are observed on the wire on the other side of the contact and which was not electrically connected (Figure III-8D).

Nanowires with ~ 200 nm were connected for 4-point contact measurements with a source-meter device (Keithley 2600A) in order to attempt preliminary conductivity measurements by applying currents between 1 and 10 µA. This current is much smaller than mA currents applied in previous studies from our group.[206,212] The absence of meaningful conductivity measurement is explained by the failure of the nanowires as illustrated in Figure III-8A and B. Two possible explanation coexist for the wire breakdown. On the one hand, wire manipulation, grounding, and shortcut issues may justify the breakdown. On the other hand, in opposition to previous studies, the nanowires tested here are not measured in the membrane. Hence, the nanowire do not benefit from the stabilization by the membrane. Moreover, the resistance is measured on a much shorter wire section: 2 µm instead of 30 µm. Thus, the measured resistance is expected significantly

smaller in our case. I suggest to use a **nanovoltmeter** able to measure the voltage drop between the inner contacts whereas applying a current as low as few 100 of nA.

In Figure III-8E and F, the two thin nanowires were not measured nor connected to any measurement device. The failure observed is the consequence of careless manipulation and touching contact with gloves. Nanowire failure was already studied by D. Aherne and can be initiated by both **electromigration** and **joule heating** at small dimensions.[213] It is also observed that this second effect occurs at the center of the wires that is to say at equal distance from each contacts whereas the first happen closer to the electrical contact. This supports failures through joule heating; the nanowire parts near the contact evacuate the heat more efficiently through the contact than the center of the wires that is only in connected to thermal insulators: air and silicon oxide. However, careful and repeatable measuring of transport properties as well as breakdown current is necessary to attest this hypothesis.

In the future measurements, several effects will be investigated: the influence of the wire (1) diameter, (2) composition, (3) porosity, and the influence of (4) the substrate on the electrical and thermal conductivity of the nanowires as well as on their failure.

4. Summary

In this chapter, the optimized conditions to connect individual AuAg nanowires by laser lithography have been determined. This method allows applying 4-point electrical contacts on top of nanowires with diameter as small as 45 nm and minimum length of 14 µm. AuAg nanowires with diameters down to 40 nm can also be efficiently transferred on trenches and cantilever substrates of various geometries. The successful dealloying of such suspended AuAg nanowires is also demonstrated. This will enable to study thermal and electrical properties of nanowires as function of the diameter, composition, and shape in the near future.

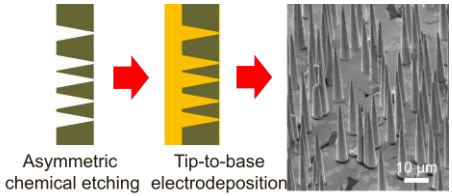

Chapter IV

Freestanding vertically aligned Au nanocones

The fabrication of Au nanocones (AuNCs) as well as arrays of vertically aligned freestanding gold nanocones with µm-size bases and nm-size tips is discussed. Compared to cylindrical nanowires, the conical geometry provides excellent contact to the solid substrate, thus improving the electrical and thermal conductivity of the system and rendering excellent mechanical stability. First, the fabrication of conical nanochannels in polycarbonate will be introduced and studied by SEM. The tip-to-base electrodeposition of AuNCs arrays and single AuNCs will then be presented as well as the optimization of the potentiostatic electrochemical deposition from a gold sulfite electrolyte.

Part of the results presented in this chapter originate from the following publications [214,215].

(213) Pérez-Mitta, G.; Burr, L.; Tuninetti, J. S.; Trautmann, C.; Toimil-Molares, M. E.; Azzaroni, O. Noncovalent Functionalization of Solid-State Nanopores via Self-Assembly of Amphipols. *Nanoscale* **2016**, *8* (3), 1470–1478, DOI: 10.1039/C5NR08190D.

(214) Burr, L.; Serbun, P.; Reimuth, C.; Heider, B.; Krieg, J.; Spende, A.; Movsesyan, L.; Schubert, I.; Trautmann, C.; Toimil-Molares, M. E. Vertically Aligned Freestanding Gold Nanocone Arrays. In preparation. 2016.

1. Introduction to conical nanostructures

Most applications of nanowires require their assembly into 3D structures. However, nanowires have too low mechanical stability to allow the fabrication of self-sustaining structures from individual nanowire with high aspect ratio. One solution relies on the fabrication of a network of interconnected nanowires. Another proficient alternative are the nanocones, consisting of a large µm-size base and a sharp nm-size tip. When the nanocone is fixed to a support, the large base provides **enhanced mechanical stability**, whereas the small tip confers a high aspect ratio and attractive "nano" properties to the structure. Moreover, electrical and thermal contact to the support is improved in comparison to equivalent nanowire structures. Therefore, such cones are very attractive for a wide range of applications.

One of the most active research fields concerns the use of nanocones to mimic the surface of lotus leaves and to fabricate highly hydrophobic self-cleaning surfaces.[94,216,217] Similar surfaces covered with nanocone arrays are also used as antireflective coatings,[94] solar cells,[218] or sensing surfaces.[219,220] In particular, metallic nanocones are investigated to act as antenna, taking advantages of the **localization of the electromagnetic field** at the nano-tip.[40,63,100,221] Near field enhancement in the gap of a dimer antennas has been proven to be highly efficient [40,172,173,222] and even higher enhancement are expected for biconical dimer structures.[223] Taking profit of the optical properties of gold nanoparticles, gold nanocones may also serve as optical antennas or bases for SERS sensors.[61–63] Mounted on a cantilever, single gold nanocones may be used as scanning probe tip for atomic force microscopy. The optical properties of such a tip allows near-field enhanced scanning optical microscopy probes to resolve ultra-fine topographical details.[63] Gold nanocones, as Au nanowires, can also be used as nanoelectrode to probe chemical electrolyte [59,60] or to apply a potential directly to a living cell. Last but not least, arrays of nanocones can serve as cold cathodes for various vacuum electronics applications as already mentioned in the introduction of the thesis. In all the applications mentioned above, the device properties will

strongly depend on shape, aspect ratio, density, periodicity, and morphology of the nanostructures.

Metal cathodes with conical geometry have been fabricated using various techniques, including nanotransfer printing,[98] ultrasound assisted interfacial synthesis,[100] lithography and related techniques.[37,40,63,94,221,224] However, for most methods the aspect ratio of the cones is below 10. By ion track technology and electrodeposition, nanocones with high aspect ratio can easily be synthesized.[91,225] When using the template method, the nanocones were electrodeposited from the large base to the nano tip directly on a conductive substrate. Due to inhomogeneous growth, this process results in the fabrication of nanocones with various lengths and tip diameter. In addition, gold nanocones electrodeposited from base to tip have ring-like hollow bases which reduce significantly their mechanical stability.[225]

The fabrication of the template is of critical importance for the synthesis of nanocones. However, in addition to their use as template, such structures also have wide range of potential applications including molecular sieves, nanofluidics, energy conversion and biosensors.[226–230] For the latest, the synthetic nanochannels aim to mimic the biological pores of lipidic membranes. The current rectification properties of these bio-inspired membranes have been proven highly dependent on the geometry of the nanopores and the surface properties of the channel walls. The manipulation of both the geometry and the surface charge of nanochannels is reported in several studies [106,127,135,231,232] and conical nanochannels are excellent candidates. Until recently, covalent chemistry has been used almost exclusively to functionalize the channels of polymeric membranes. G. Perez-Mitta et al. demonstrated that single conical channels in PC fabricated according to the method presented above can rapidly and efficiently be modified by amphiphilic self-assembly to tune their ionic transport properties.[214]

Therefore, due to their strategic interest for various applications, several studies report on the fabrication of conical nanochannels. The ion-track technology is one of the most active research field and different polymers were already investigated

such as polyimide, polyethylene terephthalate or polycarbonate.[128,231–235] The etching of the conical nanochannels is mostly obtained using NaOH:MeOH aqueous mixtures in asymmetric conditions.[236] The influence of the etchant composition on the nanochannels has also been investigated in several works. A general trend: the cone angle broadens with an increase of the organic solvent content. For most studies, the geometry of the nanochannels is investigated by SEM measurement of the *large opening* side of the channels as shown later in Figure IV-3A and C. Due to the very low channel density, the *small opening* of the channel – on purpose extremely small (typically below 10-20 nm) – is almost impossible to detect and measure. The small opening is derived from the analysis of ionic transport measurements inside the channel.[127,237] A second method for the investigation of the channel morphology/geometry is the *replica method* where the channels are used as template. This second method is employed in this work with the fabrication of gold nanocones. A third method to observe the nanochannels consists in the study by SEM of cross-sections of membranes.

In this work, the fabrication of randomly distributed vertically aligned gold nanocones (AuNC) by electrodeposition in etched ion-track polymer membranes with conical channels is presented. Other than in [238], a thin metal working electrode was sputtered on the membrane side with small channel diameters, so that the electrodeposition of gold starts at the small **tip** and continues towards the large **base** opening. Outgrowing the membrane, the process was continued to form caps and then a macroscopic layer that provides stability and support to the system. The density of cones is varied between 10^4 and 10^7 cm^{-2}, while their dimensions are controlled by modifying the etching process and/or the template thickness. With this method, nanocones exhibiting lengths between 10 and 100 µm, base diameter ($Ø_{base}$) in the micrometer range and tip diameter ($Ø_{tip}$) down to 50 nm were fabricated.

2. Experimental

Figure IV-1 summarizes the various steps already introduced in chapter I applied to the fabrication of gold nanocones.

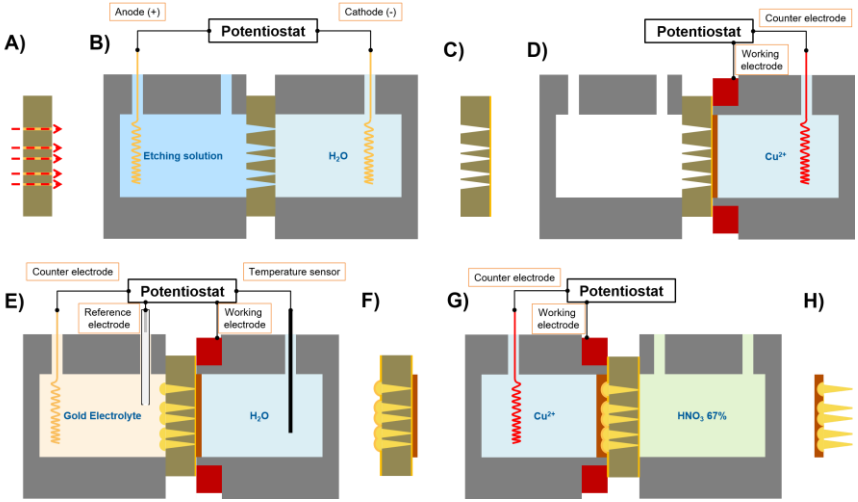

Figure IV-1: Schematic representation of the major steps involved in the fabrication of freestanding AuNC arrays: (A) irradiation of PC foils with swift heavy ions, (B) asymmetric etching of conical channels, (C) sputtering of conductive Au thin film on small opening of channels, (D) electrodeposition of a Cu sacrificial backelectrode, (E) electrodeposition of Au in conical channels, (F) sputtering of a Au layer on caps after complete filling of the channels, (G) dissolution of the Cu sacrificial backelectrode and electrodeposition of the Cu interconnecting substrate, (H) dissolution of PC membrane to obtain free standing vertically aligned Au nanocones

2.1. Fabrication of templates with conical nanochannels

In a first step, polycarbonate (PC) foils (30, 60 and 100 µm thick Makrofol N, Bayer AG; 20 and 30 µm thick Pokalon; LOFO) were irradiated at GSI (Figure IV-1A). We applied three different configurations during the irradiations. (1) PC foils were irradiated at fluences between 10^4 and 10^7 tracks·cm^{-2}. (2) PC foils were irradiated placing a metallic shadow mask (thickness 200 µm) with a regular distribution of round holes (diameter ~ 150 µm, pitch size ~ 320 µm) in front of

the membrane. The metallic mask stops the ions and thus patterns the irradiated areas. (3) PC foils were irradiated with a single ion. Therefore, a strongly defocused beam was applied in combination with a metallic shadow mask with a single hole (diameter ~ 200 µm). A silicon surface barrier detector placed behind the sample was used to detect the passage of the single ion and the beam is subsequently deflected.

The ion tracks were sensitized by UV irradiation (30 W, T-30M, Vilber Lourmat) on both sides for 1 h. Ion tracks were then selectively dissolved and enlarged into conical channels by **asymmetric chemical etching** in a two-compartment cell.[233,239] We used an aqueous **9M NaOH:MeOH** (typically 40:60) **etching solution** in one compartment and a water stopping bath in the second one (Figure IV-1B). Performed at 30 °C, various etching times were investigated, depending on the membrane thickness. To improve the homogeneity of the nanochannels formation, the etching solution was rapidly injected in the cell using a syringe. Au coil electrodes were then manually inserted in the cell few seconds (typically 30 s for reproducibility) after the beginning of the etching and a potential of 1 V was applied to monitor the channel breakthrough (Figure IV-1B). In addition, the voltage was applied so that the etching of the small pore opening is minimized. The potential was set negative in the water stopping solution to repel the etching OH^- ions from the tip.

The channel diameter was measured at the surface of the PC membrane by scanning electron microscope (SEM). The geometry of the channels is studied by cross sectional SEM imaging. Therefore, two techniques to **brittle fracture** PC membranes were developed. In the first *multistep technique*, the etched ion-track membranes were irradiated with swift heavy ions (5×10^{10} ions·cm^{-2}) followed by UV treatment for 24 h on each side. High ion fluence was necessary since the pristine PC is almost transparent to UV and only the damaged tracks absorb.[125] The membrane was then broken in liquid nitrogen by slight bending of the foil with tweezers to obtain sharp cross-sections for imaging. An alternative *single*

chemical step technique consisted in immersing the PC membrane in Aqua Regia solution for extensive time periods (≥ 2 months) to render them brittle.

For SEM study, a thin Pt layer (< 5 nm) was sputtered on top of the sample with a Cressington Sputter Coater 108auto/SE (20 s, 0.01 mBar, 30 mA).

Prior to electrodeposition, a **sacrificial** thin Au **backelectrode** (~ 100 nm) was sputtered on the polymer foil side with the small channel openings to block the channels and served as working electrode (Figure IV-1C). Subsequently, a thicker Cu layer is electrodeposited from a copper sulfate based electrolyte ($CuSO_4$ 238 g/L + H_2SO_4 21 g/L) by applying - 0.6 V between the gold sputtered layer and a copper wire acting as counter electrode for 5 min at 60 °C (Figure IV-1D).

2.2. Nanocone electrodeposition

Prior to any electrochemical process, both electrolyte and cells were warmed up to 60 °C for 30 min. The electrodeposition and cyclic voltammetry analysis of the electrolyte was carried out in a **three electrode configuration**, using a Ag/AgCl reference electrode and a gold coil as a counter electrode. A *commercial gold sulfite electrolyte* (Gold-SF, METAKEM, 15g/L) was employed for the growth of most of the nanocones. The cyanide based electrolyte introduced in the previous section was also used (**Au20**, 0.25 M Na_2CO_3 + 20 mM $KAu(CN)_2$) for comparison. For this electrolyte, a Pt coil was used as counter electrode.

The current efficiency of the sulfite electrolyte was estimated by potentiostatic electrodeposition at - 0.375 V vs. Ag/AgCl reference on a flat surface of sputtered gold (A = 1.8 cm^2). Deposited charge and deposited mass were then compared.

To grow the cones, gold was potentiostatically deposited in the conical channels from **tip-to-base** at 60 °C. The deposition process was carried out until the channels were completely filled and the gold subsequently deposit hemi-spherically (so-called caps) on the channel large opening side (Figure IV-1E). Potentials ranging from - 0.3 to - 0.8 V were tested to determine an optimal voltage of - 0.375 V vs. Ag/AgCl for the electrodeposition of Au from the AuSF electrolyte. Electrodeposition from this commercial electrolyte in conical

nanochannels was also explored in a two-electrode configuration for comparison with previous works. In this case, constant voltages between - 1.0 and - 0.5 V were applied between the sputtered working electrode and a gold coil that served as counter electrode.

2.3. Preparation of freestanding nanocone arrays

To obtain freestanding nanocones on a **solid substrate**, several steps were required. First, a thin layer of gold was sputtered on top of the caps to electrically connect them (Figure IV-1F). The sacrificial Cu backelectrode on the tip side was then dissolved with concentrated HNO_3 (Figure IV-1G). Third, the nanocones were mechanically bound on the base side by subsequent electrodeposition of a **copper interconnecting layer** (- 0.6 V, $CuSO_4$ 238 g/L + H_2SO_4 21 g/L, 60 °C, 7 min ~ 10-20 µm). Finally, the PC template and the Au remaining from the sacrificial backelectrode were dissolved and washed away by successive dichloromethane baths (Figure IV-1H). This resulted in vertically aligned freestanding gold nanocone arrays on Cu substrate. This process allows other materials to be deposited as interconnecting substrate (e.g. Au). For further studies, the gold nanocone arrays were fixed on flat aluminum holders using silver glue.

3. Results and discussion

3.1. Templates with conical nanochannels

In order to understand the formation of conical nanochannels, the current flowing during etching through the membrane is analyzed. The etching behavior of single nanochannel is also linked with the etching of arrays. Then the morphology of the channels is investigated by cross-section imaging of our membranes and related with the shape of the nanocones electrodeposited in them.

3.1.1. Analysis of asymmetric etching

By applying a potential difference of 1 V between two Au electrode immersed respectively in the etching bath and the stopping solution (Figure IV-1B), the ionic current flowing during the etching through the membrane can be monitored. Figure IV-2 shows representative etching curves for 30 µm thick PC foils irradiated with 10^6 ions·cm^{-2} (A) and one single ion (B).

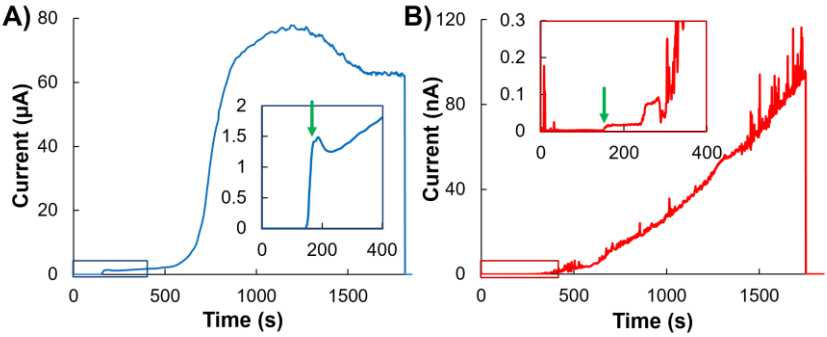

Figure IV-2: Representative I-t curves recorded during etching of conical nanochannels in PC irradiated with (A) 10^6 ions·cm^{-2} and (B) a single track. Etching is initiated 20 s before the measurement start. The green arrows point channel breakthrough times, i.e. when the channels open

In both cases, only noise is recorded during the three first minutes of etching when the pore is not yet open. The moment at which the first channel opens is called the breakthrough and once open, ions can flow through the membrane and current can be recorded. Strong deviations of the **breakthrough** time (up to 30 s) are observed, especially for single pores. These probably originate from two separate factors. On the one hand, the membranes are known to have high *surface roughness* on one side (up to few µm). Thus, depending on the position of the track, the effective track length will be longer or shorter than the nominal 30 µm thickness of the PC foil, hence resulting in longer or shorter etching times. This effect is more significant for single ion-track membranes because higher track densities lead to an averaging of the breakthrough time of all individual channels. On the other hand, the etching *temperature* may fluctuate. This is an inherent

problem of the heater used to stabilize temperature of the cells at 30 °C. Few degrees difference can then lead to strong etching rate variations. However, this effect can be minimized by preheating the etching cells and solutions, and by using etching durations longer than the heating-cooling period of the heater. In addition, errors of few seconds inherent to the manipulation of the setup for insertion/removal of the etching solution and the two Au electrode cannot be discarded.

After the breakthrough, ions can flow through the membrane and a net current is recorded. In the case of a single channel (Figure IV-1B), the current is very small after the breakthrough (few tens of pA) and almost constant for few hundreds of seconds. After 300 to 500 s, the current starts to rise regularly. The increase of the current is attributed to the **enlargement of the nanochannel** with increasing etching time. A second effect relates to the *contamination of the stopping bath* induced by the ion transfer through the pore. Consequently, the conductivity of the deionized water increases and allows higher currents to be recorded between the two electrodes. Current fluctuations are also observed after the channel breakthrough. Partially originating from the ambient noise, another source of current variations can be the presence of *dangling bonds* as reported by Siwy et al.[232,233] Partly attached to the membrane, dangling bonds may vacillate in the small aperture of the conical channels resulting in an oscillation of the effective channel diameter and thus influencing the ionic flow through it. The etching results presented in this work are consistent with previous works on the etching of single conical nanochannels. Thus, various additional effects such as the influence of the UV sensitization [239] or the influence of the etching residues [122] on the etching rate may also be relevant to explain the etching behavior.

In the case of parallel nanochannel arrays (Figure IV-1A), the concomitant breakthrough of several pores results in higher currents (from several hundredth of nA to few µA). The current jump last about 10 s and is attributed to the discrepancy of the channel breakthrough time. After a small current spike, the current slowly increases. Between 500 and 800 s, a stronger current increase is

measured before stabilizing until the end of the 30 min etching. On the one hand, this *I-t* curve for etching of **multiple channels** is consistent with the currents recorded for single channels. The current through the membrane initiates with the breakthrough of the first pore and is very fast limited when almost all the channels are open. The slow increase of the current after channel breakthrough may coincide with the opening of few additional channels and to the slow enlarging of all of them. In addition, ionic contamination of the stopping bath reduces the resistance of the cell. On the other hand, the current is not perfectly proportional to the number of nanochannels (compared to the single channel). The breakthrough current recorded for the channel array is only about 10000 time higher than the single channel breakthrough current (instead of 10^6). The second *current rise* 500 to 800 s after the beginning of the etching does not coincide with the addition of etching curves from several single channels. The difference is even more obvious when comparing the current after 30 min of etching; of ~ 0.1 µA for the single nanochannel (Figure IV-1B) it is only ~ 1000 time higher for the channel array (~ 60-80 µA in Figure IV-1A). Part of the current recorded for multichannel is related to the regular current increase observed for single channels. However, its evolution cannot be justified only by this contribution. One possible explanation relates with the enlarging of the channels and electrical stopping. Though the **electrical stopping** should be more or less equivalent for single and multi-channel etching (parallel array of channels is in a rough approximation equivalent to a parallel array of equal resistances), the **chemical stopping** on the other hand may be significantly different. Actually, identical etching cells are used. Thus, the volume of stopping solution is similar for single and multi-channel etching. The stopping solution is much faster contaminated in multi-channel membranes and may not slow down the tip etching as efficiently as in single pores. Therefore, larger tip openings are expected for arrays and the current increase observed during etching is expected to be linked to an enlarging of the channels.

For the PC membranes (Makrofol) used in this work, it is possible to estimate the track etching rate according to equation (I-4) from Chapter I (p21) adapted to asymmetric etching. Thus according to Figure IV-2,

$$v_t = \frac{l_T(t=0)}{t_b} \approx \frac{30\ \mu m}{200\ s} \approx 0.15\ \mu m/s \approx 9\ \mu m/min \qquad (IV\text{-}1)$$

for etching at 30 °C with 9M aqueous NaOH:MeOH solution with ratio 40:60. Comment: the breakthrough times pointed by the green arrows in Figure IV-1 indicate ~ 170 s, but the t_b used in the equation takes into account the 30 s necessary to insert the electrode in the etching cells. The results are summarized in Table IV-1 for Makrofol PC irradiated with a fluence of 10^6 ions·cm^{-2} or below. It is noted that the breakthrough times provided in the table are average times from the etching of several membranes. As mentioned above, strong deviations (up to 60 s for thicker membranes) can be observed. Despite the **low reproducibility**, unfortunately very common for conical etching, general etching trends are observed. Surprisingly, the etching of 100 µm thick PCM membranes requires more than 30% extra time than expected for channel breakthrough. A possible explanation is the deepness of the pore that increases the *diffusion* path for etching agent as well as for the extraction of etching residues. Another possibility relates with the *UV penetration* in the membrane; due to the thickness of the polymer, UV may not irradiate the polymer track uniformly and reduce the etching rate. This explanation seems less probable regarding the transparency of PC to UV and the large angular distribution of UV incident light. The last possibility relates with the influence of the *track density* on the etching rate.

Table IV-1: Average breakthrough time of conical nanochannels for different polycarbonate foils and different density of irradiation. Etching solution: 9M aqueous NaOH:MeOH with ratio 40:60

Membrane type and thickness (µm)	**PCM 20**	**PCM 30**	**PCM 60**	**PCM 100**	**PCP 20**	**PCP 30**
Irradiation fluence (ions·cm^{-2})	10^6	10^6	10^5	10^4	10^6	10^6
Breakthrough time (s)	130	200	360	900	60	120

Table IV-2 exhibits the average breakthrough times for the etching of conical pores in 30 µm thick PCM membranes irradiated with various fluences. The etching was performed in every cases using the standard etching solution at 30 °C. The track density has a very low impact on the etching rate for fluences below 10^6 ions·cm^{-2}. For a fluence of 10^7 ions·cm^{-2}, the track etching rate almost doubles. No consistent explanation was found up to now to clarify this effect because the ions used for the irradiations are identical (Z, energy) and effect of the fluence have been observed on the radial etching rate only for higher fluences (10^9 ions·cm^{-2}).[133] Though the etching solution was fresh for each sample, the effect of *etching residues* may differ with the channel density. This should be investigated for example by using an etching solution saturated with etchant residues.[122,131]

Table IV-2: Average breakthrough time of conical nanochannels as function of the irradiation fluence. Etching solution: 9M aqueous NaOH:MeOH with ratio 40:60, membrane: 30 µm thick PCM

Irradiation fluence (ions·cm^{-2})	**10^4**	**10^5**	**10^6**	**10^7**
Opening time (s)	210 s	200 s	200 s	110 s

3.1.2. Channel morphology

To fully describe the morphology of the nanochannels, the membranes were studied by SEM. Figure IV-3 exhibits SEM images of conical nanochannels observed under two different orientations. The left images (A and C) are obtained by placing a membrane perpendicularly to the electron beam with the large

channel opening facing the beam. Except for the thin *conductive Pt layer* sputtered onto the membrane, no specific treatment was necessary to measure the diameter of the large opening of the channels. Right images (B and D) are **cross-section** images of the membrane. To obtain Figure IV-3B and D, **brittle fracturing** of the membrane was executed by a combination of *swift heavy ion* and *UV irradiation embrittlement* as well as *low temperature fracturing* as presented in section IV.2.1. Under these conditions, the foils easily break yielding cross-section of the nanochannels without plastic deformation of the polycarbonate.

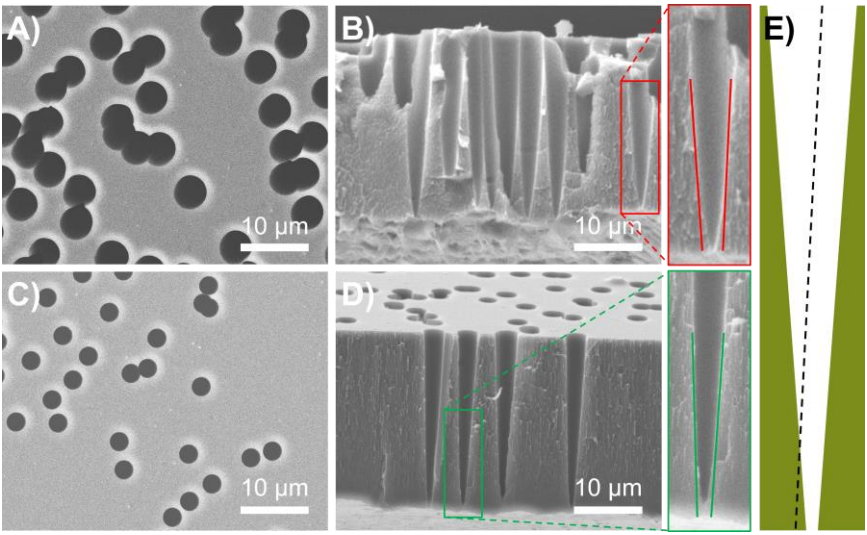

Figure IV-3: SEM images of nanochannels obtained with various etching times. (A and B) are etched for 30 min whereas (C and D) are etched for 15 min in 9M aqueous NaOH:MeOH (40:60). (A and C) are top views of the nanochannel large opening. (B and D) are the respective cross section images. (E) Scheme of a channel and a fracture plan (dashed line) that is not perpendicular to the membrane

All channels displayed in Figure IV-3 originate from the etching of polymer membranes having track densities of 10^6 tracks·cm^{-2} with the standard etching solution at 30 °C (c.f. section IV.2.1). Figure IV-3A and B depict the channels etched for 30 min whereas Figure IV-3C and D show channels after 15 min

etching. The nanochannels resulting from this asymmetric etching are in both cases **conical**. The base diameters of the channels are about 2.5 µm and 4.0 µm for 15 and 30 min etching respectively. The tip diameter of the channels was too small to be analyzed in our SEM. The non-linear dependence of the large opening diameter with etching time (the diameter does not double) is consistent with the non-linearity of the radial etching rate as a function of the pore diameter (Chapter I). The dilution of the etching solution with the stopping solution after the breakthrough may also contribute to the decreasing of the radial etching rate with time. The base diameters obtained for both cross-section and top-view images of the same sample are similar. Thus, treatment performed to brittle fracture the membrane (Figure IV-3B and D) has only low impact on the membrane. The membrane thickness after fracturing, between 27 and 30 µm, is also in agreement with the PC foil manufacturer data and the etching step performed. The channels walls do not form perfect cones but the tips have *bullet-like shape*, especially for longer etching times. The insets of Figure IV-3 evidence the non-linearity of the channel edge observed in cross-section. This bullet-like shaped channels were first observed by P. Apel et al.[131] when surfactant was used during the etching. It is believed that the bullet-like shape observed in Figure IV-3 originates from the brittle breaking of the membrane. Performed manually, the *fracture plan* can deviate from the desired 90° angle to the membrane plane as represented schematically in Figure IV-3E. The fracture plan is also often passing next to the exact tip position, thus appearing as channels with no small opening as the channel presented in the inset of Figure IV-3D.

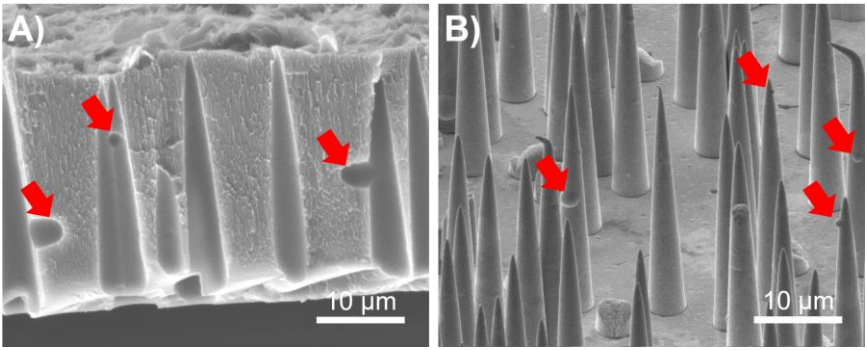

Figure IV-4: SEM images of (A) membrane cross-section and (B) corresponding nanocones

Figure IV-4 exhibits SEM images of conical channels (30 min etching under standard conditions) and of nanocones electrodeposited in an equivalent template (electrodeposition will be discussed in the following section). As expected, the nanocones are **perfect replica of the nanochannels**. Similar base diameters are observed for both channels and cones. The presence of *cavities* in the PC templates (due to material inhomogeneity; red arrows, Figure IV-4A) explain the *bulb-like* defects on the cone surfaces (red arrows, Figure IV-4B). Compared to fractured cross-sections, the replica technique provides the advantage that the polymer matrix does not need to be modified. However, the influence of the electrolyte on the electrodeposition as well as the effects of membrane dissolution in dichloromethane needs to be accounted.

The embrittlement of the PC to obtain cross-section suitable for the analysis of the channel shape is difficult. Taken independently, extensive irradiation with swift heavy ions or UV exposure does not enable brittle fracturing of the PC membrane, even at temperatures as low as - °C. (1) The *extensive ion irradiation* was observed to irremediably modify the PC template with black coloring and bending of the foils, which remain pliable. (2) E*xtensive UV exposure* (~ 30 days) leads to a decrease of foil thickness from 30 µm down to about 20-23 µm as shown in Figure IV-5. In addition, *the shape of the channels is modified.* The conical shape is almost not visible for membranes etched for 30 min and the diameter of

the channel is about 1 µm larger than in Figure IV-3. Similarly, membranes etched for 15 min (Figure IV-5B) exhibit increased base diameter but also display biconical shape, with at the tip, diameter increasing up to the µm range as circled in red. Thus, even though the irradiation fluence as well as the UV exposure are minimized (as presented above), their effects cannot be fully neglected. They are especially relevant for the study of nanoscopic features such as the channel small openings, where small effects are more relevant. Therefore, cross section analysis can only be used for **qualitative analysis of the channel morphology** and illustration.

A third technique for sharp fracturing of PC templates* based on ice-embedded membrane breaking proved its inefficiency. Finally, the embrittlement method based on the **immersion in Aqua Regia** (section 2.1) is also performant. This technique presents the major advantage that it does not require heavy ion accelerators.

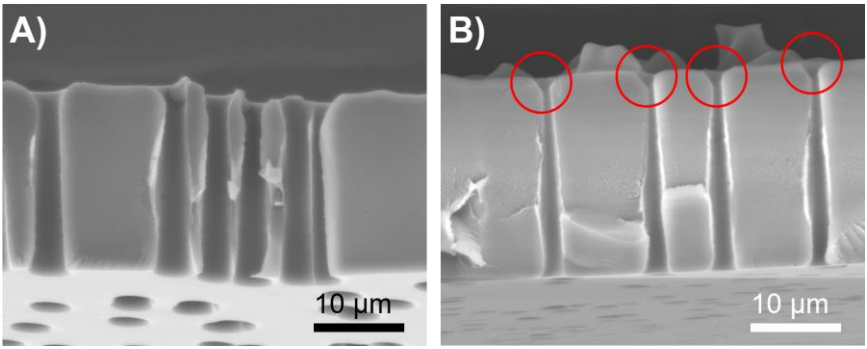

Figure IV-5: Cross-section images of conical nanochannels after more than 30 days of UV irradiation. Nanochannels etched for 30 min (A) and 15 min (B) under standard conditions. Red circles point biconical shape of the tips

Figure IV-6A and B exhibit cross-sections images obtained from the same sample resulting from multiple irradiation and cold fracturing in Figure IV-6A whereas

* Method: Membrane frozen in deionized water at -18 °C for 24h. The breaking of the ice pellet is then performed manually on a straight edge.

Figure IV-6B is obtained after Aqua Regia hardening. These images prove that the two techniques presented are **equivalent** and enable brittle fracture of PC samples.

In addition, these techniques can be used for imaging other track geometries as shown in Figure IV-6. The embrittlement works well for PC membranes with thickness up to 60 µm (Figure IV-6E and F) and is expected to operate also for thicker membranes. In collaboration with L. Movsesyan, various *nanochannels geometries* have been investigated. Figure IV-6C displays a cross-section of an array of **cylindrical nanochannels** with channel diameter as small as 100 nm and density of 10^9 cm^{-2}. **3D networks of nanochannels** could also be imaged, more details on their fabrication are available in [121,240]. In the inset of Figure IV-6B, channels oriented along three irradiation orientations are distinguishable. The fourth orientation being almost parallel to the direction of observation cannot be identified. Channels parallel to the x- and y-axis are in the fracture plane whereas channels parallel to the z-axis are penetrating the membrane. Geometries that are more complex have been achieved by multiple heavy ion irradiation – etching sequences. Thus, low density of conical channels (Figure IV-6D) or large vertical cylindrical channels (F) can be overlapped to 3D networks of thin nanochannels. These complex membranes are of particular interest for template use as explained by L. Movsesyan in her thesis.[240]

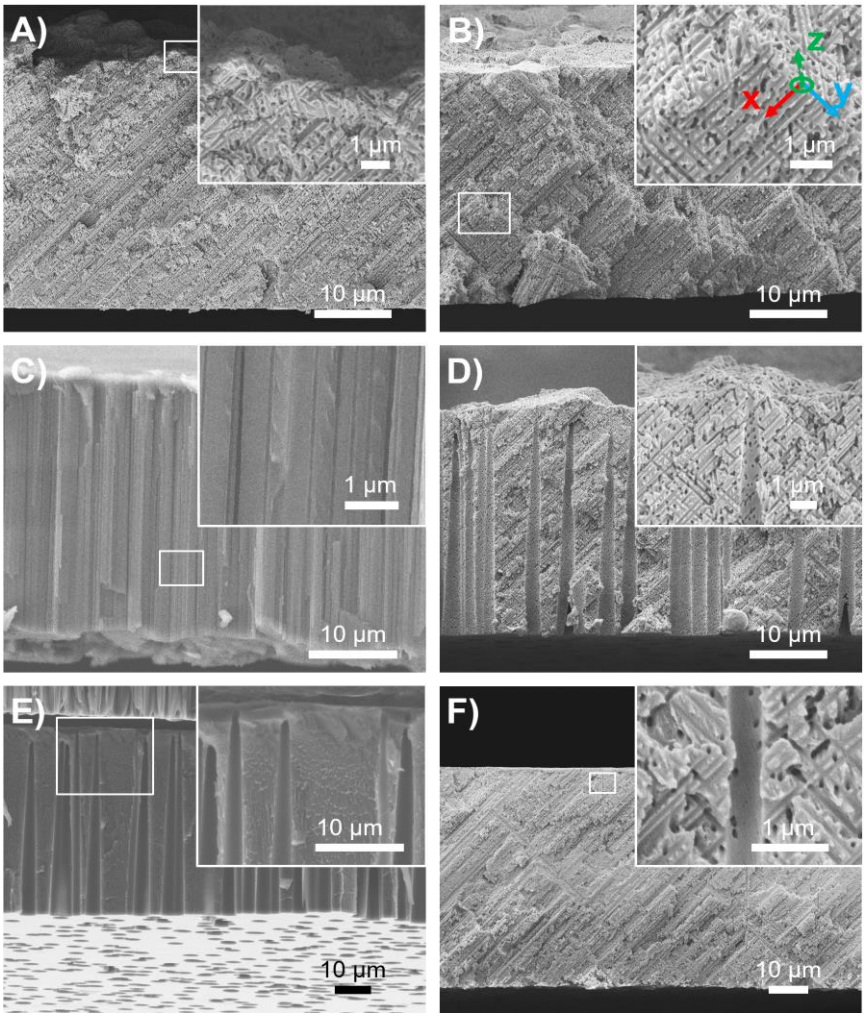

Figure IV-6: SEM cross-section images of nanochannel networks (A and B), parallel array of nanochannels (C), conical nanochannels (E), overlapping of 3D network and conical channels (D), or cylindrical channels (F). Initial membrane thickness of 30 µm (A, B, C, and D) and 60 µm (E and F)

The interaction between Aqua Regia and the polymer is attributed to the *nitrogen dioxide and chlorine gases* resulting from the decomposition of the mixture. It has also been observed that PET and Teflon bottles become brittle after long

contact with the yellow gas mixture. Therefore, it seems probable that the Aqua Regia embrittlement can be **adapted** to other templates such as PET or even PI membranes.

To summarize the fabrication of nanochannels presented above:

- Conical channels are obtained in PC membrane by asymmetric etching
- Track etching rate and breakthrough time can be determined by conductommetric study of the etching
- Two methods to image the conical shape of the channels, fracture cross-section and replica by electrodeposition were successfully developed
- Replicas and cross-section imaging provide consistent information on the shape of the nanochannels.

3.2. Electrodeposition

To fabricate gold nanocone arrays, the electrodeposition of the gold in templates with conical nanochannels was investigated. In opposition to previous works, the present nanocones are grown from the tip to the base by means of a sacrificial working electrode. Based on previous works of the group,[166,225] electrodeposition in two-electrode configuration was first considered. To improve the deposition, potentiostatic chemical reduction of Au in a three-electrode configuration was then explored. Finally, the fabrication of single nanocones will be discussed.

3.2.1. Two electrode potentiostatic deposition

The electrodeposition of gold from a commercial sulfite-based electrolyte has been extensively reported.[166,168,170,206,212,225] The results of these investigations suggest optimal electrodeposition of gold at 50 °C by the application of a constant voltage of - 0.6 V between the cathode (the Au sputtered layer on the membrane) and an anode consisting in a gold coil immersed in the electrolyte. Nanowires electrodeposited under these conditions were proved polycrystalline by means of XRD and TEM. J. Krieg reported the use of these experimental conditions for the electrodeposition of AuNCs in PC templates.[225] The cones obtained by potentiostatic deposition of gold from the **base to the tip** resulted in hollow gold

cones with very *low mechanical stability*. In addition, the inhomogeneous growth of the gold nanocones induced *large distribution of cone lengths* as well as a *large effective cone tip diameters* in the case of shorter cones.

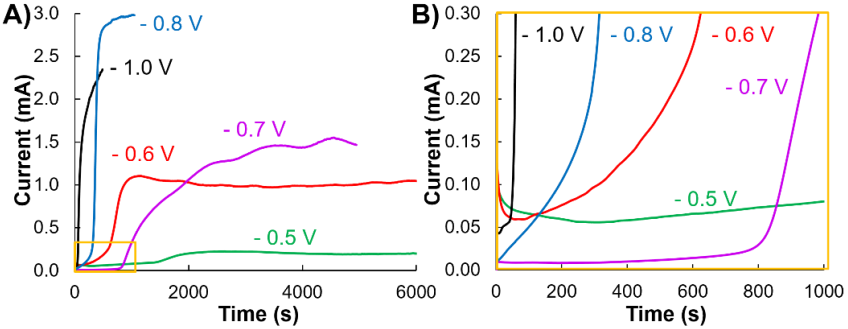

Figure IV-7: I-t curves for the potentiostatic electrodeposition of Au from commercial electrolyte (Metakem, AuSF) at various potentials in templates with 10^6 conical channels·cm^{-2}. (B) Initial phase of I-t curves

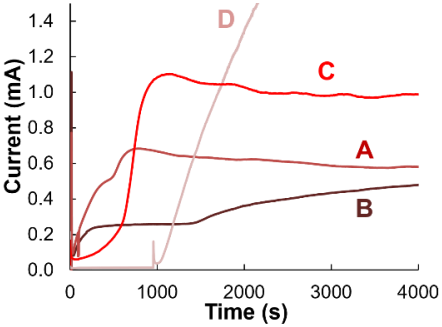

Figure IV-8: I-t curves of different potentiostatic electrodepositions of Au from commercial electrolyte (Metakem, AuSF) at - 0.6 V in identical membranes

In order to improve the electrodeposition of gold, the filling of the conical channels is performed from the **tip to the base**. Hence, diffusion of the gold ions proceeds through the large pore opening and allows *solid growth* of the gold. We etched series of membranes under the same conditions and used them to grow Au applying voltages between - 0.5 V and - 1.0 V. The *I-t* curves are shown in Figure IV-7. At voltages more negative than - 0.8 V, the gold cones have a *rough*

surfaces and the filling percentage of the conical channels is very low. At potential of - 0.5 V, the electrodeposition is extensively slow without achieving high filling of the channels. Cones with *smooth surfaces and sharp tips* are obtained for both - 0.6 V and - 0.7 V. Surprisingly, the current recorded for deposition at - 0.7 V is significantly lower than for the lower voltage and the current increase is observed after longer deposition times. The consequence of the lower current and small deposited charge for depositions at - 0.7 V is a lower filling percentage of the channels than for higher voltages. At - 0.6 V, optimal filling up to 66% of the channels is achieved. The electrodeposition in the 2-electrode configuration has a **very low reproducibility** as shown in Figure IV-8. The *I-t* electrodeposition curves resulting from the same electrodeposition conditions have *various shapes*: two plateau steps (**A** and **B**) vs. continuous current increase (**C** and **D**). The *filling* percentages resulting from these depositions also differ. Due to the *absence of reference* electrode, the constancy of the potential cannot be verified and thus does not allow detailed understanding of the electrodeposition process in a 2-electrode configuration. In addition, because of the incomplete filling of the channels of the templates, parasitic structures are observed as presented in Figure IV-9.

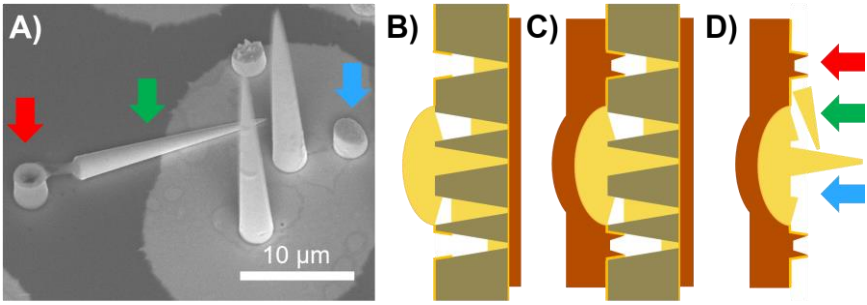

Figure IV-9: (A) SEM image displaying parasitic structures on a AuNC array. Schematic representation of the formation of parasitic structures: (B) cap growth in empty pores leading to cone bases (blue arrows), (C) electrodeposition of the interconnecting substrate in the empty pores leading to tubes (red arrows), (D) dissolution of the template releasing incompletely grown wires (green arrows)

Figure IV-9A shows an SEM image on which the three different **parasitic structures** observed on our arrays: **cone bases** (blue arrow), **tubes** (red arrow), and **tumbled cones** (green arrow). The formation of these parasitic structures during the fabrication process is schematically depicted in Figure IV-9B, C and D. Thus, **cone bases** (blue arrows) are formed by *cap overgrowing* into neighboring empty or partially filled channels. The surface of the cone bases is inclined because its growth starts from the center of the cap and stops once the adjacent empty channel is fully covered. **Tubes** (red arrows) are formed in empty or partially filled channels that are not covered by caps during the sputtering of the *interconnecting Au top-layer* after cap growth (Figure IV-9C) which leads to tubular growth of copper inside the channels. Finally, the dissolution of the polymer membrane leads to the tumbling of NCs that had not reached the top of their channel and were not connected to the conductive top layer (Figure IV-9D). This explanation is in complete agreement with our observation that homogeneous growth clearly decreases the amount of parasitic structures on the sample.

3.2.2. Three electrode potentiostatic deposition

To improve the electrodeposition process and reproducibly product nanocones arrays, potentiostatic electrodeposition of gold from the same commercial electrolyte (AuSF, Metakem) was investigated in a **three-electrode configuration**. As *reference*, a *Ag/AgCl electrode* was used. Following the manufacturer suggestions, the electrodeposition temperature was set to 60 °C.

Electrolyte properties

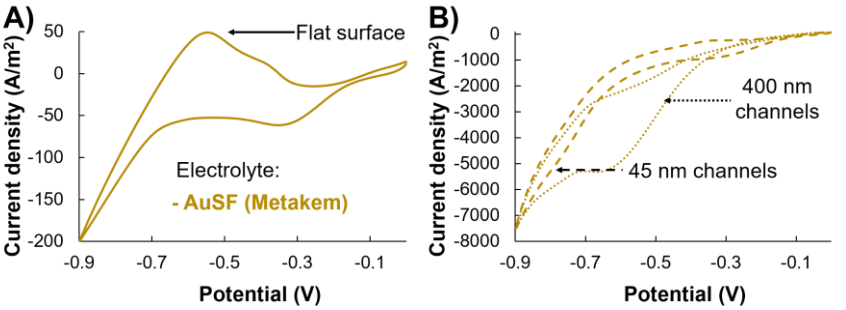

Figure IV-10: Cyclic voltammograms of commercial AuSF electrolyte (Metakem) on (A) flat working electrode and on (B) working electrode in cylindrical nanochannels of 45 and 400 nm diameter. Scan rate: 100 mV·s^{-1}

The reduction of gold from commercial AuSF electrolyte was investigated by means of cyclic voltammetry. The second cycle of each CV performed at scan rate of 100 mV·s^{-1} is displayed in Figure IV-10. CVs of AuSF are performed between 0 and - 0.9 V vs. Ag/AgCl reference. On a flat Au surface (Figure IV-10A), the CV exhibits one **single reduction peak** between - 0.3 and - 0.4 V. The current plateau observed at more negative voltages demonstrates that the reduction occurs in **diffusion-limited regime** at such voltages. A strong current increase is observed for highly negative voltages. This current rise, as well as the oxidation peak observed at about - 0.6 V is attributed to the reduction/oxidation of *additives* in the electrolyte. Hydrogen evolution is not expected at such "low" voltages and the brownish color of gold deposited at these potentials confirms the poor quality of the deposit. Adsorption of sulfur probably passivates the surface leading to the formation of cavities. The color change of gold deposited at high overpotentials from AuSF may result from the embodiment of organic molecules as well as solvent.

To study the effect of the *nanostructuring of the working electrode*, similar voltammograms were recorded inside **cylindrical nanochannels** of PC membranes (Figure IV-10B). We used cylindrical nanochannels instead of

conical ones to keep the area of the working electrode constant during the various voltage cycles. As for cyanide-based electrolytes, the current densities measured for the CVs of AuSF inside nanochannels are much higher than on flat surfaces. A strong *shift* of the diffusion limited reduction peak is observed in large nanochannels of 400 nm with a peak between - 0.6 and - 0.7 V vs. Ag/AgCl. On the other hand, the reduction in 45 nm nanochannels is similar to flat surfaces and only exhibit a slight shift toward sigmoidal behavior. In both cases, the absence of the oxidation peak is surprising but could not be explained.

For all three cases, the presence of a **single reduction peak** is in agreement with the **one step reduction process** given in the literature.[139]

Optimization of the electrodeposition process

To determine the optimal voltage for the fabrication of AuNCs, gold was potentiostatically electrodeposited in similar membranes with conical nanochannels at various potentials and the resulting structures were studied by SEM. Figure IV-11A presents current vs. time (*I-t*) curves recorded during the electrodeposition of gold within the conical channels of several PC membranes etched under the same conditions. The applied potential was varied between - 0.325 and - 0.800 V vs. Ag/AgCl. In all cases, the channel density was ~ 5×10^5 cm^{-2}, the channel lengths of ~ 28 µm, the base diameters $Ø_{base}$ of ~ 3 µm and the tip diameters $Ø_{tip}$ smaller than 100 nm as measured by SEM. Most of the *I-t* curves exhibit similar behavior: while gold is electrodeposited in the conical nanochannels from the small tip to the large base (**tip-to-base**), the *current increases continuously* with time (see for example the deposition curve at - 0.375 V). Then, a *faster increase of the current* is observed (blue arrow) when gold grows outside the channels and forms **caps with hemispherical shapes**. Finally, the current starts to *decrease* slowly (red arrow). This is attributed to the formation of a continuous gold layer by **overlapping of the caps** and/or to a decrease of the Au concentration in the electrolyte.

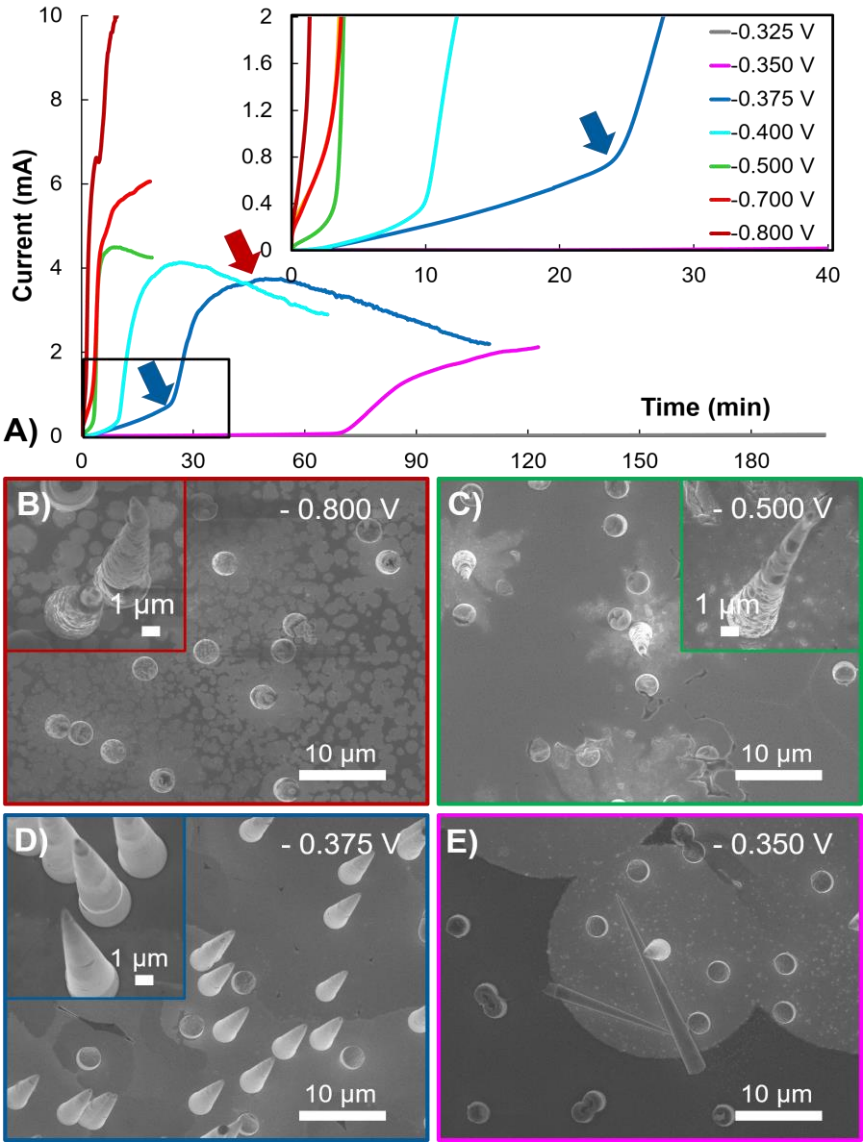

Figure IV-11: (A) Current-time curves recorded during the electrodeposition of gold in conical channels (tip-to-base) at various potentials and corresponding SEM images of nanocones arrays deposited at (B) - 0.800 V, (C) - 0.500 V, (D) - 0.375 V and (E) - 0.350 V

Figure IV-11B to E show representative SEM images of nanocone arrays deposited at (A) - 0.800, (B) - 0.500, (C) - 0 .375 and (D) - 0.350 V. At large negative applied voltages (U < - 0.400 V), the deposition is very fast (< 10 min). The resulting cones are **inhomogeneous** and have **rough surfaces** (Figure IV-11B, C). At less negative voltages (U > - 0.350 V) the electrodeposition reaction does not occur or is very slow resulting in a **very low density** of cones (Figure IV-11E). We found that ***U* = - 0.375 V** vs. Ag/AgCl yields the most homogeneous growth, with more than 50% of the channels completely filled and with NCs exhibiting smooth surfaces (Figure IV-11D). In addition, the conformal filling of the nanochannels as observed in Figure IV-4 *validates the use of this potential for replica purposes*.

The *current efficiency* measured for potentiostatic electrodeposition at - 0.375 V vs. Ag/AgCl for 1 h is 99 ± 2%. Thus, the analysis of the charge electrodeposited at this voltage during the cone growth (first period of the deposition with a small current increase) enables an easy estimation of channel filling.

Vertically aligned freestanding nanocones arrays

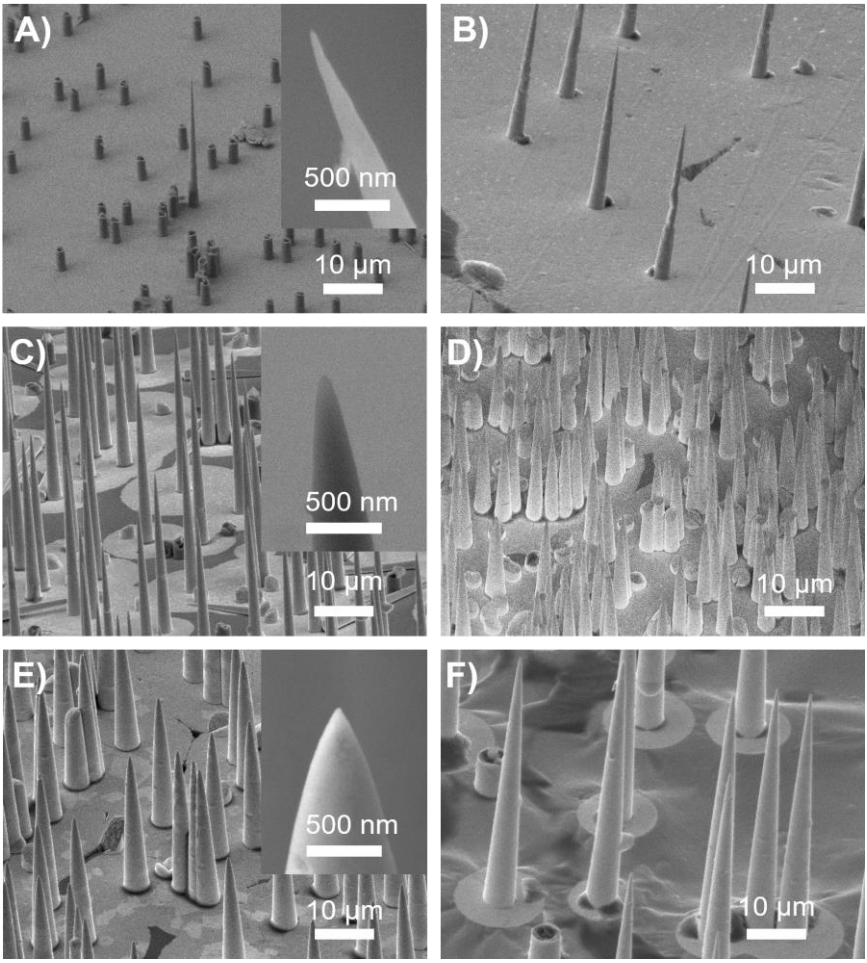

Figure IV-12: SEM images of vertically aligned freestanding Au nanocones deposited at -0.375 V vs. Ag/AgCl imaged under 45°. Arrays of 27 µm long nanocones with density ~ 10^6 cone·cm^{-2} and $Ø_{base}$ = (A) 2, (C) 2.5 and (E) 4 µm and $Ø_{tip}$ < 100 nm (insets). Arrays of nanocones with $Ø_{base}$ = 2.5 µm and density (B) ~ 10^5 cone·cm^{-2}, and (D) ~ 10^7 cones·cm^{-2}; (F) array of 56 µm long nanocones

The optimized electrodeposition conditions presented above were applied to synthesize arrays of nanocones with various **geometries** and **densities**. Figure

IV-12 shows SEM images of nanocones electrodeposited in three 30 µm thick PC templates asymmetrically etched for (A, C) 15 min and (E) 30 min corresponding to a base diameters of (A) 2 µm, (C) 2.5 µm and (E) 4 µm, respectively. The cone base diameter in (A) is slightly smaller because the etching was performed with a 9M aqueous NaOH:MeOH mixture with 60:40 ratio instead of 40:60 for the others. In all three cases, the nanocone **tips are sharp with sizes below 100 nm** (see insets) but for larger cones, the tips tend to have a bullet-like shape (inset in Figure IV-12E). This *bullet like shape* was already observed earlier (see section IV.3.1.2). The experimental filling of the channels observed for nanocones appears to be dependent on the cone dimensions. For large cone diameters, very high channel filling is achieved and very few parasitic structures are present. On the contrary, for cones with thin bases (Figure IV-12A) only few nanocones grow fully and remain attached to the membrane. The absence of broken cones and the low density of incompletely grown cones would suggest that only few cones grew due to moderate wetting of the channels. Trials to improve the wetting by means of multiple wetting steps with both ethanol and electrolyte did not improved the cone density. Another explanation relies on the **obstruction** or **closing** of the nanochannels at their tips. The second point will be discussed in more details in a following section presenting the fabrication of single nanocones.

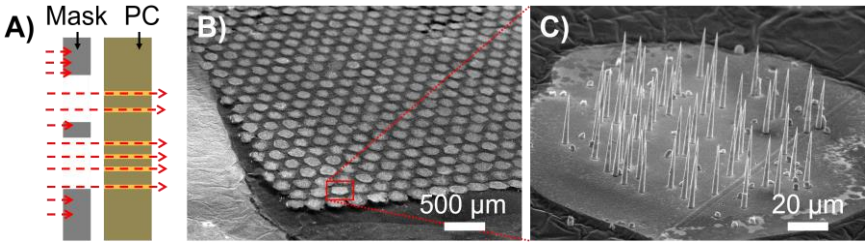

Figure IV-13: (A) Schematic representation of swift heavy ion irradiation with mask. SEM image of (B) a patterned nanocone array and (C) high magnification on a single AuNC patch

The average *distance between cones* has been varied by using templates exposed to different ion fluences. Figure IV-12B and D show exemplary arrays with

expected cone densities of 10^5 cones·cm^{-2} and 10^7 cones·cm^{-2}, respectively. 56 µm long AuNCs were obtained by electrodeposition in 60 µm thick membranes (Figure IV-12F). In this case, etching time of 30 minutes resulted in cones with $Ø_{base}$ = 5 µm and $Ø_{tip}$ < 100 nm. The difference between the initial membrane thickness and the final cone length is due to etching of the bulk polymer.[127]

Patches of AuNCs regularly distributed on the cathode area were fabricated for field emission measurements. The cone formation was confined to limited domains using a *metallic shadow mask* during the irradiation as schematically represented in Figure IV-13A. Figure IV-13B shows an overview SEM image of a pre-structured sample. Figure IV-13C displays a single patch of nanocones (density = 3×10^5 cones·cm^{-2}, cone length 27 µm, $Ø_{base}$ = 2.5 µm, $Ø_{tip}$ < 100 nm). The regular distribution of patches is of particular interest for field emission (FE) applications because it enables to increase the distance between the nanocones and to form patterned arrays of emitters. Another advantage of the patch structure is the possible *identification and labeling* of individual AuNCs in each patch and their subsequent analysis by SEM of the nanocones before and after the FE measurements.

As illustrated by the SEM images, the vertically aligned and freestanding nanocones are **mechanically stable**. Figure IV-14A displays SEM images of tilted cones synthetized by electrodeposition in *inclined nanochannels*. Such channels are obtained by irradiating the PC under a predefined angle. Figure IV-14A shows nanowires tilted by 40° from the surface normal. **Tilted cones** are also mechanically stable and do not bend under their own weight. Note: arrays of tilted cones mimic at the skin of seals (used as ski climbing skins since long times) and are thus attractive for possi application where *unidirectional sliding* is required at the microscopic scale.

Figure IV-14C and D display SEM images of cones after applying strong mechanical forces during handling with tweezers (Figure IV-14C), and after intense agitation during the membrane dissolution process (Figure IV-14D). These images prove the strong mechanical stability and the *soft behavior* of the

cones where the cone bases remain attached to the interconnecting substrate and the **cones bend** instead of breaking. This effect can be of particular interest for applications where the *contamination* with nanoparticles should be avoided such as interaction with biologic samples. These results demonstrate that the electrochemical growth from tip-to-base yields *homogeneous filling along their length* and thus a *large contact* to the supporting conductive layer.

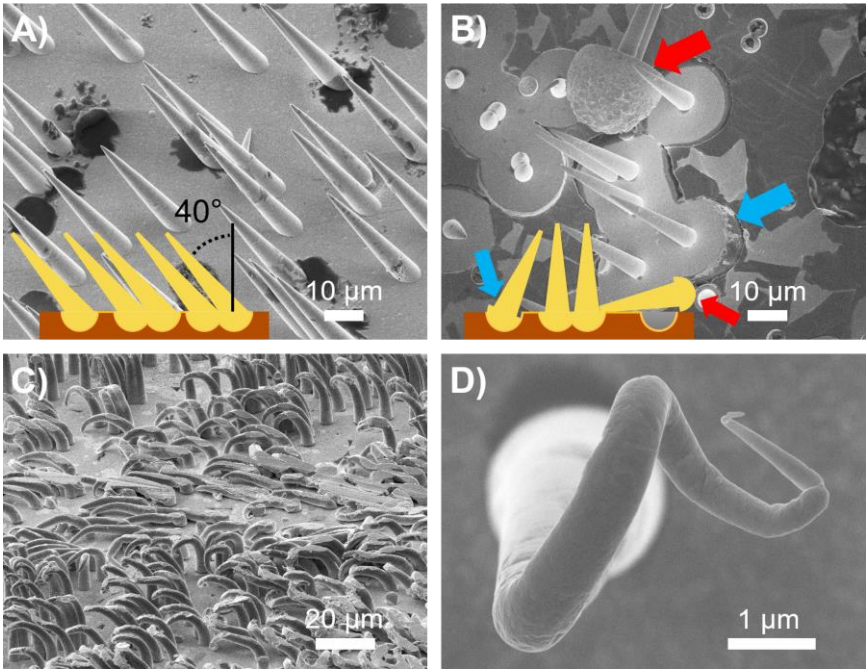

Figure IV-14: SEM images and schematic of (A) tilted cones (40° with respect to substrate normal) observed from above, (B) nanocones detached from the interconnecting substrate layer. The blue arrows points a group of caps detaching from the interconnecting substrate layer, the red arrows indicate a fully decoupled hemispherical cap overlaying the interconnecting substrate layer. SEM images of bended nanocones, (C) after applying pressure with tweezers, and (D) after intense dichloromethane flushing

We have seen that nanocones are very stable and that they bend but do not break due to their strong binding to their large caps. However, the major weakness of the nanocone arrays relies on the attachment of the cone to the conductive support layer. As observed in Figure IV-14B, instead of breaking at the base, the

nanocones may decouple from their support together with their caps (blue arrows) or even completely **detach from their substrate** (red arrows). Figure IV-14B highlights the importance of the conductive support layer and the quality of its deposition. This problem can be minimized by growing caps so that they overlap and form a *solid and continuous layer*. Alternatively, the contact between supporting layer and caps can be optimized by using the same material as for the cones (i.e. gold instead of copper). Figure IV-14B also confirms the *hemispherical shape of the caps*.

3.2.3. Nanocones deposited from other electrolytes

To further improve the filling of conical channels, test electrodepositions were performed from **cyanide based gold electrolyte** under various conditions. Preliminary results are presented here and may provide an interesting alternative for cone fabrication.

Figure IV-15 shows selected SEM images of Au cones synthesized with a cyanide-based electrolyte containing 20 mM $KAu(CN)_2$ and 0.25 M Na_2CO_3 at 60 °C. A platinum coil acted as counter electrode and a Ag/AgCl electrode served as reference. Potentiostatic electrodeposition of Au at - 1.1 V vs. Ag/AgCl resulted in the fabrication of cones with relatively *smooth surfaces* as shown in Figure IV-15B. The cone density obtained at this potential is very low as presented in Figure IV-15A. On the contrary, for potentiostatic electrodeposition performed at - 0.9 V vs. Ag/AgCl, almost all conical nanochannels are filled and *high cone density* is achieved (Figure IV-15C). However, these cones have rough surfaces as revealed in Figure IV-15D and flakes decorate their surface. Surprisingly, the cones exhibit signs of **faceting**, which is even more obvious when the nanocones are electrodeposited at constant current. Figure IV-15F exposes a **faceted cap** (left side) as well as faceting of the cone itself (right side). This is a clear sign that the electrodeposition of gold from cyanide-based electrolyte under such conditions influences the texture and crystallinity of Au nanocones. Surprisingly, the channel filling rate was relatively high in comparison with the inhomogeneous caps size distribution (Figure IV-15E).

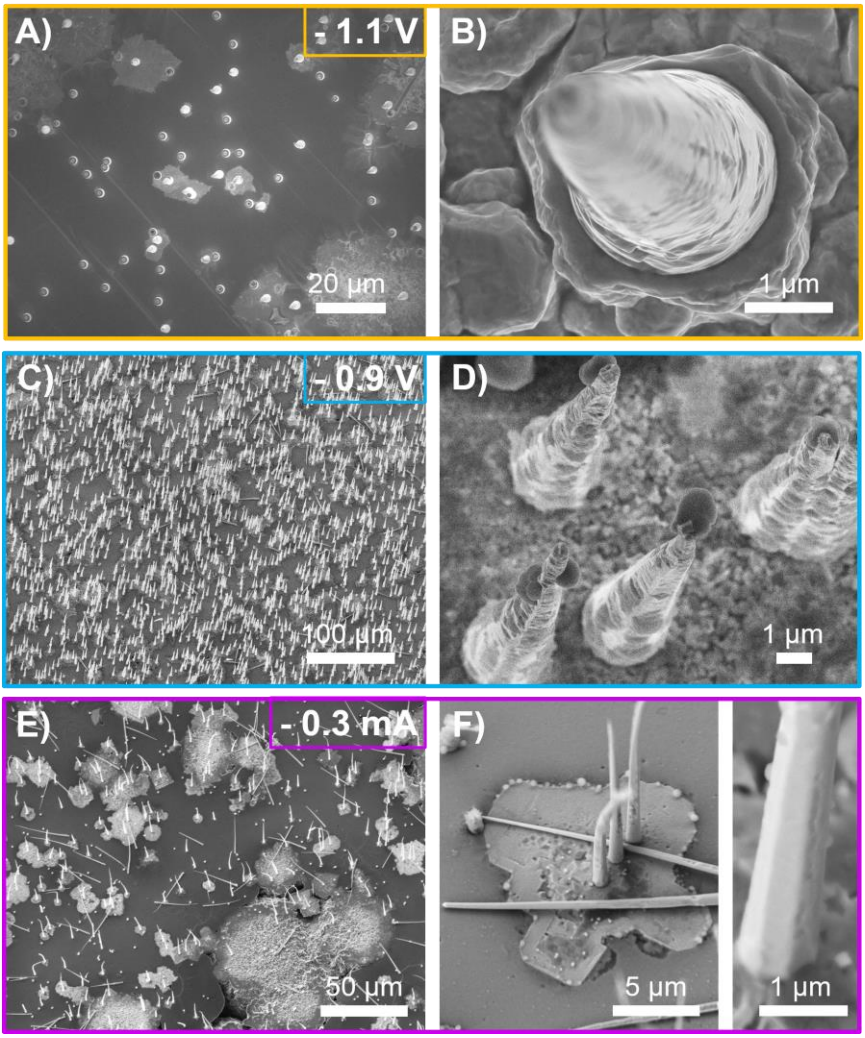

Figure IV-15: SEM images of Au nanocones electrodeposited from a $KAu(CN)_2$ solution. Potentiostatic electrodeposition of Au at (A and B) - 1.1 V and (C and D) - 0.9 V vs. Ag/AgCl. (E and F) Galvanostatic deposition of Au at - 0.3 mA

The fabrication of AuNCs from cyanide-based electrolyte is promising; especially for tailoring the crystalline properties of the cones, but further investigations are

required for the fabrication of cones with controlled dimensions for future applications.

3.3. Single nanocones

The fabrication of single nanocones is interesting for various applications (e.g. AFM tips on cantilever) but is also particularly important to understand the synthesis process as well as the properties of individual nanocones. The fabrication of single nanocones is performed under the same conditions and according to the same parameters as for nanocone arrays presented above.

3.3.1. Single conical nanochannels

The etching of single conical channels is performed according to the procedure presented above (section 3.1.1). The etching of a single conical nanochannel with a sharp tip is problematic because (1) the breakthrough time has a reproducibility deviating up to 50% and (2) the pore does not always remain open after etching. To test the effects of membrane *drying* (mandatory for sputtering the sacrificial backelectrode), the open or close status of the pore is tested by conductommetry in a 1 M KCl aqueous solution. The current flow through the channel is recorded by sweeping the potential between the two gold electrode immersed on each compartment of the electrochemical cell (Figure IV-16A). Figure IV-16B shows representative *I-U* curves. *Open pores* let the current flow through them and a current of few nA is recorded. In some cases, *I-U* curves have *rectifying behavior*, i.e the ions flow preferentially in one direction. Such rectifying behavior is known to depend on the surface functionalization of the polymer as well as on the pH of the solution, but was not analyzed in this study. Here, the presence of a current was only used to identify the open or close status of the pores. For half of the pores etched according to the standard process, no current was recorded, meaning that the **half of the channels is closed after drying**. The channels may be *blocked* by dirt or any impurities. Capillary forces generated during the membrane drying may also induce a *collapse* of the channel tip. In some rare cases, the channel opens during the voltage cycling as shown by the blue curves in Figure IV-16B.

This channel opening can be induced by the *wetting* of the membrane during the measurement but also by the *unblocking* of the channel tip due to the potential induced movement of the ions.

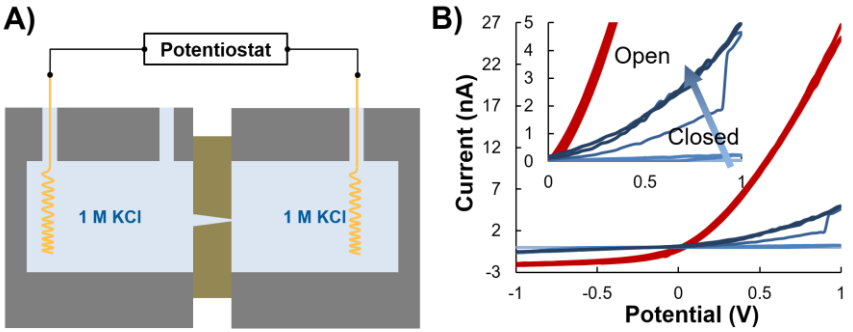

Figure IV-16: (A) Scheme of the setup used for measuring the opening of single nanopores by conductommetry and (B) typical conductommetric measurements of two different single conical nanochannels: red curves = channel already open in a 30 µm thick membrane, blue curves = channel re-opening after second I-U cycle in a 20 µm thick membrane leading to an increase of current flowing through the pore (blue arrow)

The frequent pore collapse obtained for etching under standard conditions (9M aqueous NaOH:MeOH 40:60 during 15 min at 30 °C) is also valid for arrays. It is thus not surprising that the percentage of *channel filling* is rarely higher than 60-70%. Hence, channel closing during the cones fabrication process may partly explain the presence of *parasitic structures* shown in Figure IV-9.

3.3.2. Potentiostatic electrodeposition of single gold nanocones

The electrodeposition of gold in single conical nanochannels is also very challenging. Figure IV-17 shows representative *I-t* curves for the electrodeposition of five equivalent single cones. All the curves presented in Figure IV-17 correspond to the electrodeposition of gold in single conical nanochannels etched in 30 µm thick PC membrane under standard conditions. The electrodepositions are identically performed at - 0.375 V vs. Ag/AgCl. We see that each *I-t* curves is different with *very small reduction currents.* This is due

to the dimension of the working electrode, ranging from few nm^2 at the beginning of the deposition up to few μm^2 after complete filling of the channel. Thus, various effect such as *vibrations* and other *noises* affect the quality of the recorded current.

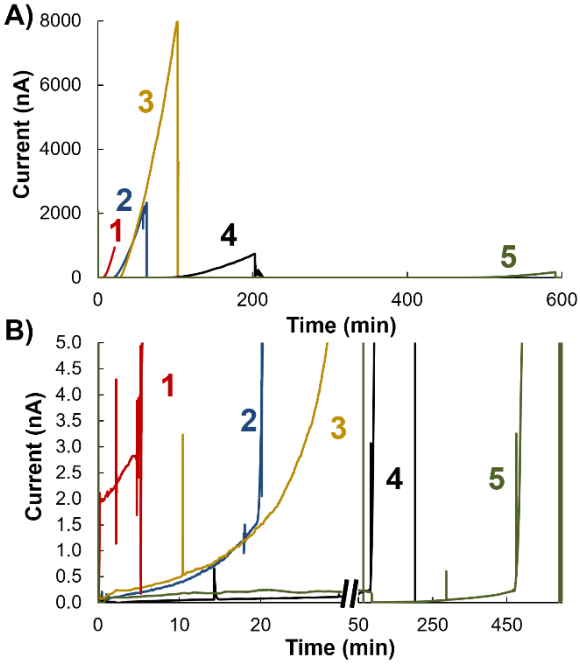

Figure IV-17: (A) I-t curves recorded for the potentiostatic deposition of gold at - 0.375 V vs. Ag/AgCl in five similar membranes with a single conical nanochannel. (B) Focus on the initial stage of the electrodeposition at low currents

Figure IV-18 focuses on the *I-t* curve **4** from Figure IV-17 to understand in detail the electrodeposition of the single cones. The process can be separated in **three steps**. The first step is attributed to the **deposition of gold** in the single conical nanochannel (green background). Within the first 50 min, the current – of few tenth of pA – increases slowly with time (Figure IV-18B). Assuming electrodeposition occurring in *diffusion limited conditions* and *linear diffusion* in the nanochannel, the current should be proportional to the surface area of the

working electrode. Thus, the current should be proportional to the square of the diameter of the nanochannel at any time. However, the current, in the present example increases only from ~ 20 pA up to ~ 230 pA, that is to say by a factor 10 instead of the expected factor of ~ 1000 considering that the nanocone has a sharp tip ($Ø_{tip}$ ~ 50 nm) and large base ($Ø_{base}$ ~ 3 µm). Obviously, this simple consideration is not realistic.

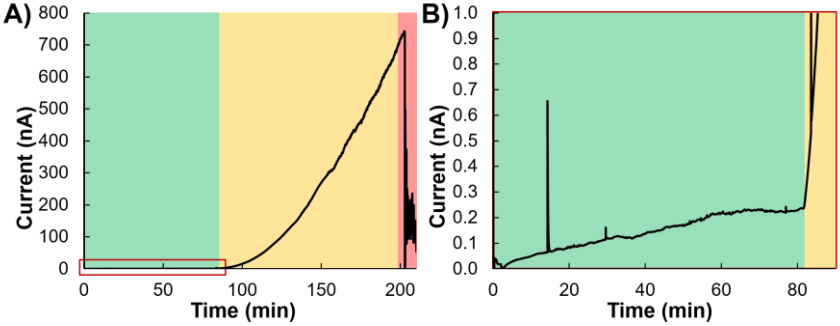

*Figure IV-18: Representative I-t curves for the electrodeposition of Au from AuSF electrolyte in the single conical channel **4**. Green area: cone growth in the channel, Yellow area: cap growth outside the channel, Red area: current breakdown*

The second step of the electrodeposition (yellow background in Figure IV-18) corresponds to the fast increase of the current from the pA-nA to µA regime. It is attributed to the growth of the **hemispherical cap** at the base of the cone. Similar behavior is observed for all electrodepositions as shown in Figure IV-17. Figure IV-17B also evidences that the *time necessary to fill the nanochannel and initiate the growth of the caps fluctuate from one deposition to another*. Cone deposition as fast as 6 minutes can be observed (**1**), but full growth of single cones can last up to 8 h (**5**). For most of the depositions, the transition from cone growth to cap evolution can clearly be identified: **1** ~ 5 min, **2** ~ 20 min, **4** ~ 1 h 20 min and **5** ~ 8 h. Smooth transitions are also observed as for curve **3** at ~ 25 min. It is noted that the fast increase of the current attributed to the cap growth is consistent with an unrestricted surface area expansion of the working electrode in the form of hemisphere.

The last step of the electrodeposition process, labelled with a red background in Figure IV-18A, corresponds to an **electrical breakdown**. Thus, for curve **4**, at t ~ 3 h 30 min, the current suddenly drops from ~ 0.7 µA down to 0. This is attributed to the partial *melting* of the cone tip due to the very high current density flowing through it. We note that if the cone tip is of expected diameter ~ 50 nm, the resulting current density before breakdown is estimated to about 3.5×10^5 A/cm^2. This result is significantly lower that breakdown current measurements performed by Enculescu et al. on Cu nanocones and Karim et al. on Au nanowires embedded in a polymer membrane that sustain current densities up to 10^8 A/cm^2.[206,241] However, Figure IV-17A clearly evidences that not only the deposition but also the breakdown currents differ from one sample to another with failure occurring at a current as low as 200 nA (curve **5**) or as high as 8 µA (curve **3**). The analysis of the cone dimension is necessary to understand these large differences.

3.3.3. SEM analysis of single nanocones

To analyze single nanocones in the SEM, the growth of a conductive interconnecting support layer and removal of the membrane (described in chapter 2.3) is mandatory.

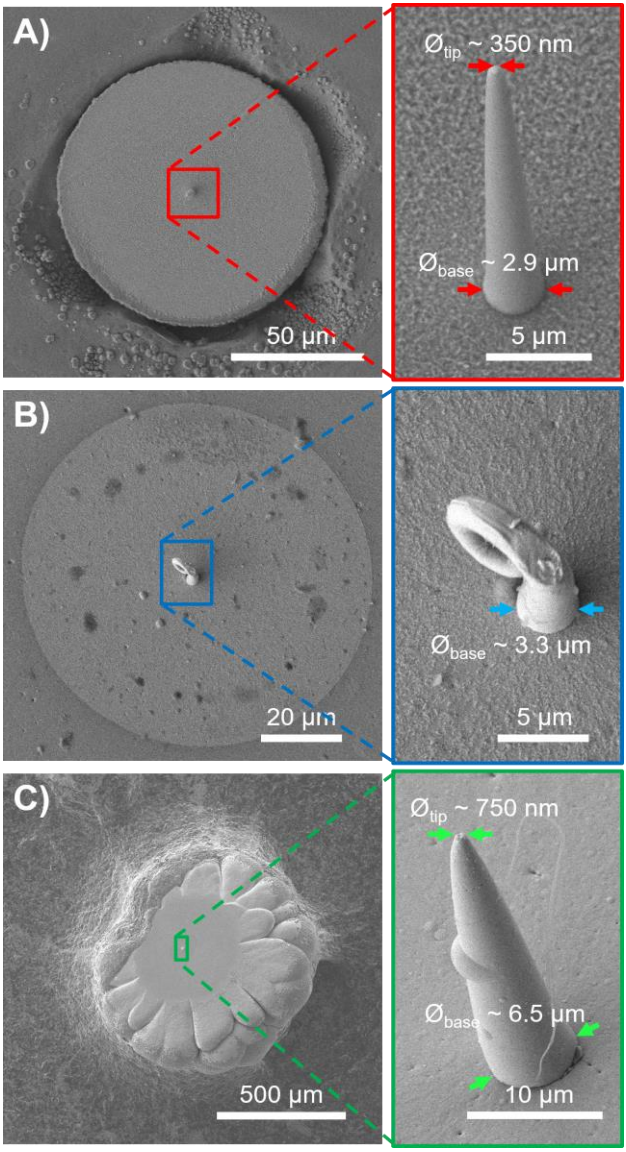

Figure IV-19: SEM images of single nanocones electrodeposited in single nanochannels etched under standard conditions for (A, B) 15 min and (C) 30 min. (A) Freestanding cone and (B) cone damaged after complete synthesis process and dissolution of the membrane. (C) Freestanding cone attached to the cap, which mechanically detached from the membrane after electrodeposition

Figure IV-19 exhibits SEM images of three different single nanocones electrodeposited in single nanochannels asymmetrically etched for 15 min (A and B) and 30 min (C). The dimensions of the single cones are significantly different from cones originating from arrays fabricated with identical conditions. As shown previously in Figure IV-12, the average base diameter for cones from arrays is 2.5 and 4 µm for templates respectively etched for 15 and 30 min. The tip diameter in both cases is in average below 100 nm. The **base diameters** of the single nanocones measured in Figure IV-19A and B are ~ 2.9 and ~ 3.3 µm, respectively, i.e. **larger** than expected value of ~ 2.5 µm. The **large tip** of about 350 nm in diameter (Figure IV-19A) is also larger than in the case of arrays. An even larger deviation is observed for single cones deposited in a single nanochannel etched asymmetrically for 30 min as presented in Figure IV-19C. The base diameter is more than 50% larger than equivalent cones from arrays and the tip of about 750 nm is much larger than expected. Due to the fragile nanosize, it cannot be excluded that the uppermost tip of the nanocone broke off, especially for the cone presented in Figure IV-19C where the template was not chemically dissolved. In that case, the giant cap (almost 1 mm diameter) induced the fall of the cone from the membrane. The fact that the cone remained attached to the cap is an additional proof of the *strong connection between cones and caps*. All single cones measured up to now were observed with **larger bases (and tips)** than the ones obtained in arrays. This is a clear sign that there exist a difference between the etching of a single ion-track and an array of ion-tracks. These observations are corroborated by studies from A. Spende et al.[242] who also measured geometry fluctuations in single conical nanochannels and the resulting nanotubes.

The cone corresponding to electrodeposition *I-t* curve **4** from Figure IV-17 and analyzed in Figure IV-18 is depicted in Figure IV-19A. The charge electrodeposited during the period attributed to the cone electrodeposition is Q_{cone} ~ 7.3×10^{-7} C.

Considering the density of gold d and the molar mass M, the corresponding volume $V_{cone}(Elec)$ of electrodeposited gold can be calculated:

$$V_{cone}(Elec) = \frac{Q_{cone} * M}{n * F * d} \approx 7.7 * 10^{-17}\ m^3 \qquad (IV\text{-}2)$$

This volume is in good agreement with the cone volume $V_{cone}(SEM)$ calculated from the dimensions of the cone measured by SEM:

$$V_{cone}(SEM) = \frac{\pi}{3} * \left(\left(\frac{\emptyset_{tip}}{2}\right)^2 + \frac{\emptyset_{tip}}{2} * \frac{\emptyset_{base}}{2} + \left(\frac{\emptyset_{base}}{2}\right)^2\right) \approx 7.0 * 10^{-17}\ m^3 \qquad (IV\text{-}3)$$

Similarly, the volume of the cap (assuming a perfect half-sphere with diameter 98 µm) is in perfect agreement with the volume determined from the electrodeposition *I-t* curves.

This result validates the interpretation of the electrodeposition curves presented above as well as the interpretation of the electrodeposition process for AuNC arrays. Thus, the slow current increase observed for arrays of nanocones is attributed to the growth of the cones (involving the increase of the surface of the working electrode; Figure IV-11). On the other hand, the presence of parasitic structures is related to the blocking of part of the nanochannels as well as the discrepancy in cone growth rate (as observed for single nanocones).

3.3.4. Nanocone growth model

The last open question in the gold nanocone fabrication is the electrodeposition process itself. Enculescu et al. reported that the planar diffusion model applies for Cu electrodeposition from tip-to-base.[241] Here we analyze the electrodeposition of Au in single conical nanochannels, which is not proven to follow the same process. The different electrodeposition curves suggest deviations from one to the other deposition. To illustrate the complexity of the electrodeposition process in conical nanochannels, two experimental *I-t* electrodeposition curves are confronted with *simulated curves*.

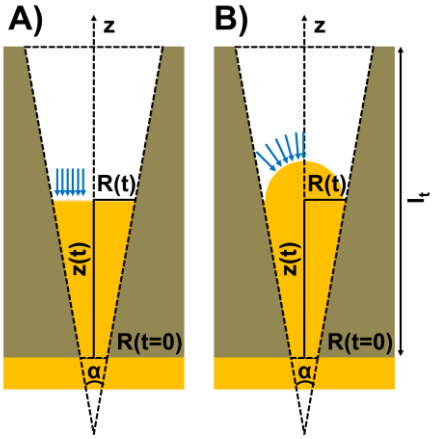

Figure IV-20: Schematic representation of the nanochannel geometry and of the various diffusion geometries: (A) planar diffusion and (B) hemispherical diffusion

In our model, we consider two major *assumptions*:

- The rate determining step is the mass transport.
- The nanocone growth is linear in the nanochannel.

The first one is related with *cyclic voltammograms* presented above. They suggest that electrodeposition of Au occurs in **diffusion limited regime** at potentials < -0.3 V vs. Ag/AgCl. The second, also observed for electrodeposition in cylindrical nanochannels, is **arbitrarily imposed constant** for growth in conical nanochannels and induces:

$$z(t) = GR * t \quad with \quad GR = \frac{dz}{dt} = const \qquad (IV\text{-}4)$$

with $z(t)$ being the length of the growing cone, GR the growth rate and t the time. For better correlation, GR is experimentally determined for each example as the time needed for the whole cone deposition divided by the cone length. Table IV-3 tabulates the various GR for the electrodeposition of single nanocones presented in Figure IV-17.

Table IV-3: Growth rates and deposition times for the electrodeposition of various single nanocones produced under identical experimental conditions (presented in Figure IV-17)

Electrodeposition N° from Figure IV-17	**1**	**2**	**3**	**4**	**5**
Growth rate in nm·s^{-1}	94	24	19	5	1
Deposition time (min)	5	20	25	80	480

Two diffusion geometries are considered, namely **planar** and **hemispherical** diffusion, as shown in Figure IV-20 that schematically represents the conical nanochannel and its various geometrical parameters. The radius of the cone at any time $R(t)$ is geometrically defined as a function of the cone length $z(t)$ and the cone angle (α) by the relation:

$$R(t) = \tan\left(\frac{\alpha}{2}\right) * z(t) \qquad (IV\text{-}5)$$

Consequently, depending on the diffusion geometry considered, the disc surface area A_{disc} and the hemisphere surface area A_{hemi} of the cone-electrolyte interface are determined for any time t as:

$$A_{disc} = \pi * R(t)^2 = \pi * (\tan\left(\frac{\alpha}{2}\right) * GR * t)^2 \qquad (IV\text{-}6)$$

and:

$$A_{hemi} = 2 * \pi * R(t)^2 = 2 * \pi * (\tan\left(\frac{\alpha}{2}\right) * GR * t)^2 = 2 * A_{disc} \qquad (IV\text{-}7)$$

Using the first assumption above mentioned it is possible to estimate the cathodic current by solving *Fick's first* (**steady-state**) or *second law* (**time-dependent**) of diffusion in correlation with the electrochemical reaction arising at the cathode. In the first case, the deposition is assumed to be instantaneously in dynamic equilibrium. In the second case, the deposition evolves with time to reach the dynamic equilibrium. Table IV-4 provides the equation of the current as a

function of time for **potential leap** experiments for diffusion limited electrodeposition under different conditions.[243]

Table IV-4: Mass-transport limiting current as a function of time for various diffusion models and regimes. $A = A_{disc}$ in planar and inlaid disk models and $A = A_{hemi}$ in the hemi-spherical model

Diffusion geometry	**Planar**		**Inlaid Disk**	**Hemi-spherical**	
Diffusion regime	Steady-state	Time-dependent	Steady-state	Steady-state	Time-dependent
Current	$\frac{nFADC_0^*}{\delta}$	$\frac{nFA\sqrt{D}C_0^*}{\sqrt{\pi t}}$	$\frac{4nFADC_0^*}{4(l_t - z(t)) + \pi R}$	$\frac{nFADC_0^*}{R}$	$\frac{nFAC_0^*}{} * \left(\frac{D}{R} + \frac{\sqrt{D}}{\sqrt{\pi t}}\right)$

n is the number of electron involved in the electrochemical reaction, F the Faraday number, D the diffusion coefficient of the ion of interest and C_0^* the bulk electrolyte concentration. It is noted that the time dependent equation of the current for planar diffusion correspond the *Cottrell* equation (II-1) introduced in Chapter II.

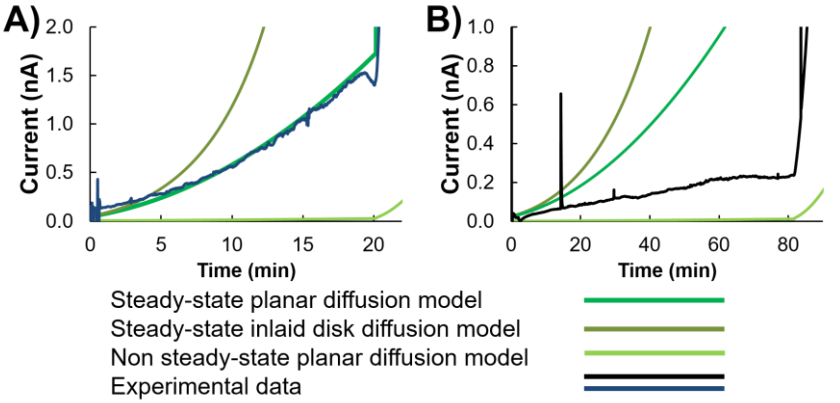

*Figure IV-21: I-t electrodeposition curves of single nanocones (A) **2** and (B) **4** overlapped with theoretical I-t curves assuming diffusion limited reaction under different conditions*

In Figure IV-21, the green and the dark green curves are the currents expected in *steady-state* conditions whereas the light green curve corresponds to the *time-*

dependent growth of the diffusion layer. On the other hand, the green and light green curves assume planar diffusion in the single conical channels without additional consideration whereas the **inlaid disk diffusion** (dark green) model supposes that the *diffusion layer is restricted to the inside of the nanochannel*.

Figure IV-21A shows the experimental *I-t* curves **2** (from Figure IV-17) and compares it with the three different models involving **linear diffusion** above mentioned. For these models, a GR of 24 nm·s^{-1} as well as deposition time of 20 min (Table IV-3) was used to fit the calculated current with the experimental curve. Figure IV-21A suggests that the **planar diffusion model in steady-state conditions** fits the best the experimental current with $n = 1$, $C_0^* = 15\ \mathrm{g/L}$, $D = 1 * 10^{-5}\ \mathrm{cm^{-2} \cdot s^{-1}}$ and δ arbitrarily fixed to the initial nanochannel length 30 µm. The channel dimensions estimated from SEM observations (Figure IV-19B) yield a base diameter of 3.3 µm and a tip diameter of ~ 500 nm. The *diffusion coefficient* of gold sulfite is not provided by the manufacturer and strongly depends on the electrolyte composition. Therefore, a standard diffusion coefficient for aqueous electrolytes (D ~ 1×10^{-5} cm^2·s^{-1}), was chosen for our simulations. Figure IV-21A also evidences that the inlaid disk model quickly overestimates the current whereas the non steady-state model underestimates the current. Even though the planar diffusion model seems to coincide the best, it is important to remember that we arbitrarily selected a constant thickness for the diffusion layer (30 µm). In addition, as noticed in the previous section, this model does not fully explain the **initial current**, whose experimental value is systematically higher than for calculated *I-t* curves, even when considering very large tip diameters.

Figure IV-21B compares the experimental *I-t* curves **4** (from Figure IV-17) with the same 3 models, assuming a GR of 5 nm·s^{-1} and a deposition time of 80 min (Table IV-3). Figure IV-21B evidences that none of these models are able to simulate the current expected for this cone with dimension $Ø_{tip}$ = 350 nm and $Ø_{base}$ = 2.9 µm (Figure IV-19A). As for the inlaid disk model (where the current increases due to the reduction of the diffusion layer thickness), the planar

diffusion model very fast overestimates the current under steady-state assumption. In addition, the **quasi-linearity** of the experimental *I-t* curve contrasts the $t^{3/2}$ time dependency of the planar diffusion model. We consider in the following curves a more complex diffusion geometry including a hemispherical gold-electrolyte interface.

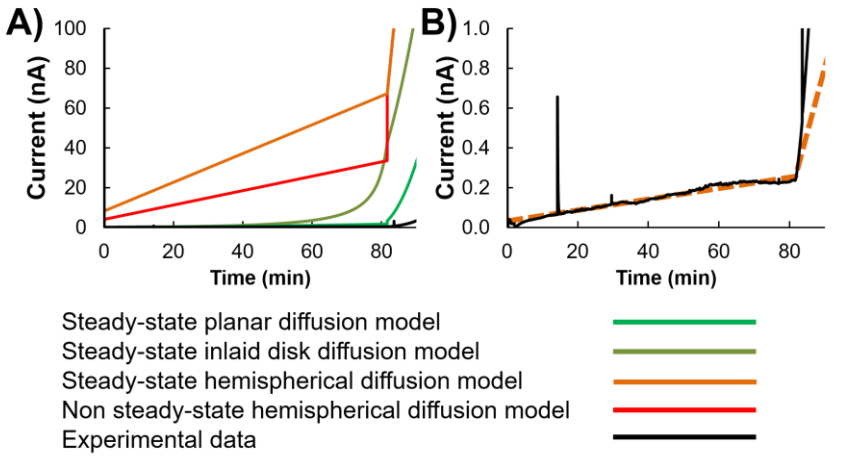

*Figure IV-22: Experimental and simulated I-t electrodeposition curves of sample **4** with different diffusion coefficients (A) D = 1×10^{-5} cm^2·s^{-1} and (B) D = 3.8×10^{-8} cm^2·s^{-1}*

Figure IV-22 presents simulated and experimental electrodeposition curves for the single cone **4** from above. For the simulated curves in Figure IV-22A, all non-geometrical parameters are identical to the one used in the simulations of Figure IV-21. It thus shows that *higher electrodeposition currents* are expected in the case of **hemispherical diffusion** than for planar diffusion. This result is in agreement with the diffusion-limited process where the electrodeposition rate is expected to be proportional to the working electrode surface area. With no surprise, the simulated current with the diffusion coefficient of $D = 1 \times 10^{-5}$ cm^2·s^{-1} is much higher than the experimental current (solid black line at the very bottom of Figure IV-22B). In Figure IV-22B, a much smaller diffusion coefficient $D = 3.8 \times 10^{-8}$ cm^2·s^{-1} was considered for gold sulfite ions. The rate-limiting step of diffusion in hemispherical geometry under steady-state

conditions exhibits a **linear time dependency** and thus fits well the experimental current-time values.

Looking at the two cases, sample **2** and **4**, it seems that different diffusion models fit the experimental data. This does not make really sense and no conclusion is possible because the diffusion coefficient D is unknown for the present electrolyte and both models are too simple. However, the **steady-state regime** assumption seems to be correct for two electrodepositions studied since the initial transient current lasts less than 20 s. This observation is in agreement with *microelectrode* models.

In conclusion, the manipulation of the single nanocone, even embedded in the template, is very challenging. Because of the small contact area established by the single cone with the membrane, grown Au nanocones are sensitive to vibrations and to manipulation as well as rather fragile, particularly when removing the template. We estimated that only one third of the single nanocones survive the entire fabrication procedure, i.e. only ~ 10% of the etched membranes result in the successful fabrication of single nanocones. This very **low yield** combined with the **low reproducibility** is not very promising for mass production of single nanocones.

4. Summary

A new process for the fabrication of Au nanocones was developed by inverting the cone growth, from base-to-tip to tip-to-base. At first, the production of templates with conical nanochannels was presented and evidenced the etching dependence on the polymer type and on the ion-track density. Arrays of nanochannels could be reproduced, whereas the production of single nanochannels was very unequal. The analysis of the electrochemical reduction of Au from AuSF commercial bath by CV indicated the direct reduction of gold. As for cyanide-based electrolytes, the strong current increase in recessed geometry of the working electrode was mainly attributed to non-faradaic currents. A direct

dependence between the electrodeposition potential and the nanocone morphology was shown with strong surface roughness at very negative voltages. The electrodeposition of Au in a two-electrode configuration was abandoned for the potentiostatic growth at - 0.375 V vs. Ag/AgCl in a three-electrode arrangement. In this way, in combination with the tip-to-base growth, higher reproducibility in terms of filling percentages and filling rates was achieved thus minimizing the apparition of parasitic structures. The synthesis of single AuNCs had a low efficiency as well as a little reproducibility. Nevertheless, the successful electrodeposition of single AuNCs confirms the interpretation of the electrodeposition curves with identifiable steps: growth initiation, cone growth, and cap growth. Modeling of the *I-t* curves supports two possible diffusion limited models for the cone growth: inlaid disk and hemispherical diffusions. The potentiostatic electrodeposition of gold in conical channels of a template from tip-to-base was demonstrated to be efficient for the fabrication of freestanding nanocones with various base diameters, lengths, and tip diameters below 100 nm. The brittle fracture developed in this chapter confirms that the nanocones are perfect replicas of the channel. Arrays of vertically aligned nanocones can thus be patterned and the nanocones evidence high mechanical stability as well as good contact to the substrate.

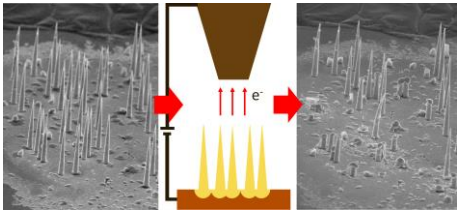

Chapter V

Field emission of patterned arrays of nanocones

In this chapter, the field emission from selected domains of nanocones is tested. First, the patterned arrays were characterized by means of SEM, optical profilometry and voltage scans. Next, voltage sweeps were performed on specified emitters and exhibit enhancement factors between 200 and 1000 as well as maximum current ranging from ~ 1 to 100 µA for cone arrays patterned in patches. The consequences of the measurements such as the melting of the nanocones are then described. Finally, the proof of concept for the fabrication of Spindt-type emitters based on AuNCs is demonstrated.

Part of the results presented in this chapter will be published in [215].

(214) Burr, L.; Serbun, P.; Reimuth, C.; Heider, B.; Krieg, J.; Spende, A.; Movsesyan, L.; Schubert, I.; Trautmann, C.; Toimil-Molares, M. E. Vertically Aligned Freestanding Gold Nanocone Arrays. In preparation. 2016.

1. Introduction to field emission

The electron source is the most important component of vacuum devices, since it determines their suitability, stability, and efficiency. Currently, the most advanced type of electron source is based on electron field emission more commonly named field emission (FE). The emission process is based on **tunneling** of electrons through the narrowed potential barrier into vacuum under the application of an electric field.[244] This quantum-mechanical effect occurs in high electric fields and in opposition to other techniques does not require high temperature or light, justifying the "cold cathode" denomination of such emitters. FE emitters offer several additional advantages, such as fast response time, confined electron energy spread (below 1 eV), low power consumption, and high efficiency as compared to thermionic or photo-induced electron emission.[245]

Field emission was first observed by R.W. Wood at the end of the 19th century. R.H. Fowler and L.W. Nordheim developed the theory of FE based on the quantum-mechanical tunneling of electrons through the surface potential barrier.[245] The **Fowler-Nordheim (FN) theory** relates the emitted current density to the local electrical field and the material work function. The FN theory considers the emission from a flat metal surface that follows the Sommerfeld free-electron model. The external potential barrier is assumed to be fully induced by electrostatic forces. Even though the FN theory is largely simplifying the system, it has been evidenced to describe most systems with good accuracy. The FN expression of the current density j is given by:

$$j = \frac{A\beta^2 E^2}{\varphi} \times \exp\left(-\frac{B\varphi^{\frac{3}{2}}}{\beta E}\right) \qquad (V\text{-}1)$$

with A = 1.54×10^{-6} A·eV·V^{-2} and B = 6.83×10^{9} eV$^{-3/2}$·V·m^{-1}, φ is the work function and E is the applied electric field. The enhancement factor β is a correction factor related to the geometry of the emitter and the induced modification of the geometry of the electrical field. Based on equation (V-1), the emission can be tuned by increasing the electrical field, decreasing the work

function of the emitter, or improving the enhancement factor. Thus, to improve the electrical efficiency of a cold cathode, the choices of the material and of its shape are of critical importance.

According to the field emission theory,[72,73,245] **quasi-one dimensional nanostructures** with high aspect ratio such as nanotubes, nanowires (NWs) or nanocones (NCs) are expected to yield high field enhancements, which strongly depend on the number density of nanostructures and their morphology. Since the 1970's and the development of the first Spindt-type molybdenum field emitter arrays,[246] several types of materials have been considered for the fabrication of high current and/or highly effective field emission cathodes.[247] Carbon-based field emitters, fabricated by chemical vapor deposition, have attracted extensive attention in the last decades due to their naturally high aspect ratio as well as remarkable physical and chemical properties.[248] However, applications of carbon-nanotube field emitters are still limited because their non-uniform and fast growth as well as mutual shielding and heating effects lead to inhomogeneous FE properties.[249–251] In contrast, silicon tips with controlled geometries and orientations can be fabricated directly on a substrate, yielding rather uniform and almost stable emission. Nonetheless, the emission current values of silicon tips are at nA-level per tip, hundred times smaller than the current value from a single carbon nanotube.[252,253] In addition, the low conductivity of semi-conducting materials hinders the emission performances of high aspect ratio structures.[254] In this respect, noble metal NWs are considered as very promising field emitters, combining both high conductivity and high aspect ratio. Encouraging FE results were already reported on cobalt,[255] copper,[256] silver,[257] bare and gold-coated nickel,[258,259] and gold NWs.[260,261] A serious drawback of these cylindrical nanostructures is their low mechanical stability. High-aspect ratio wires with thin diameters easily bend leading to wire clustering instead of individual freestanding emitters. Also the thermal stability has been shown to be problematic due to limited ring-like contact with the substrate.[262] Conical nanostructures exhibiting µm-sized base contact and nm-sized tips are promising to overcome these

problems and were developed by electrodeposition in asymmetric etched ion-track membranes to overcome the limitations of the NWs arrays.[263]

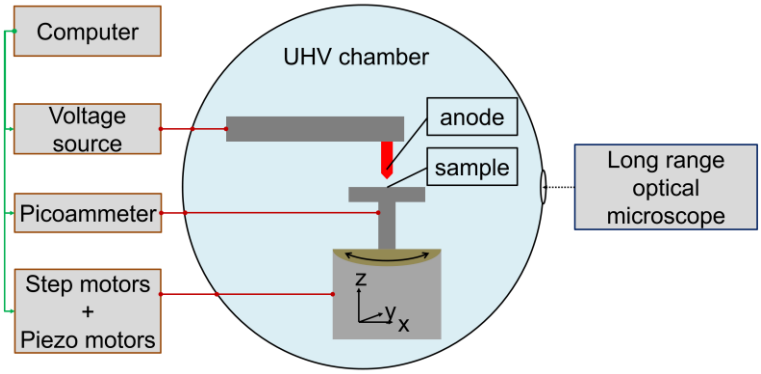

Figure V-1: Schematic of field emission measurement setup

2. Experimental

The FE properties of structured AuNC array cathodes with high (3×10^5 cm^{-2}) and low (1.5×10^4 cm^{-2}) effective number density of emitters were investigated at the Bergische Universität Wuppertal with a field emission scanning microscope (FESM) in an *ultra-high vacuum* chamber at a base pressure of 10^{-9} mbar.[264] Figure V-1 shows a schematic of the experimental setup. The FESM comprises a *fixed micro-tip*, which serves as anode, and a motorized stage controlled with step- and piezo-motors, which also allows manual tilting for alignment. The anode is made of tungsten in a shape of truncated cone of diameter $Ø_a$ = 152 µm to measure the FE from entire AuNC patches, whereas a tip-like anode of $Ø_a$ = 6 µm is used to measure the emission current of individual or few nanocones. The high voltage feedthrough for the anode is connected to a high voltage power supply (FuG, HCN 100M-10000), capable of biasing up to 10 kV and delivering up to 10 mA, while the cathode is connected to a picoammeter (Keithley 6485 or Keithley 610C). The anode-cathode distance (Δz) is controlled with a *long-distance microscope* (Questar QM100), and the actual electric field E is

determined as ratio of the applied voltage U and Δz. However, during the local measurements, the real distance and, hence, macroscopic electric field is calibrated for each patch/emitter by the linear extrapolation of the PID-regulated $U(z)$ dependence (for a fixed current of 1nA) to zero voltage.[265] All measurements are controlled via computer using a specially designed LabVIEW program. Local FE measurements were performed on various emitters to determine their onset field E_{on} (for 1 nA), their field enhancement factor β, and their maximum I_{max} before breakdown.

3. Results and discussion

The field emission characteristics of patch-structured AuNC cathodes with different number densities in the patches of 4.2 (± 1.5)×10^4 NC/cm^2 (low density) and 3.0 (± 0.8) ×10^5 NC/cm^2 (high density) have been measured. The studied nanocones were chosen with a length of ~ 30 µm, base diameter of ~ 2.5 µm and tip diameter typically below 100 nm. The high-density sample was employed to probe the field emission characteristics of entire cone patches as emitters. For this, a truncated tungsten cone with a diameter of 152 µm served as anode. In contrast, a small tip-like tungsten anode of 6 µm in diameter was used to probe the low density array, to distinguish the few emitters present in each patch and to estimate the influence of mutual shielding.

3.1. Field emission mapping by voltage scans

The morphology of the samples fixed on the FE sample holder was first analyzed by optical profilometry. For both samples, the patches and individual emitters were located by performing a voltage scan at constant current of 1 nA prior further FE measurements.

Figure V-2 presents the surface morphology of the two samples glued on their FE holder obtained by *optical profilometry*. It is thus clearly evidenced that the samples are not perfectly flat and reveal **surface roughness**. To perform voltage

scans over defined areas, the sample was inclined manually until it was perpendicular to the tungsten anode.

Figure V-3 exhibits two **voltage scans** performed on the samples by applying a *fixed current* (1 nA) between the sample and the anode at constant distance. The presence of an *emitter* results in a **voltage drop** whereas a high voltage is required to tunnel electrons from flat areas. The SEM images of the corresponding areas are superimposed to the voltage scans (Figure V-3) and expose the direct relation between cones and emission. The inset SEM images evidence the different cone density of the two samples (Figure V-3). For the *high cone density* sample (Figure V-3A) scanned with a large anode ($Ø_a$ = 152 µm), the *cone patches* correspond to the *areas emitting* at low voltage. In the case of *low cone density* (Figure V-3B), *emission from individual cones* is resolved using a 6 µm anode. The red arrows show the presence of a cone (white dot surrounded by a light disk corresponding to the cap), which also fit to the measurement of a voltage drop. The same cone is also marked in the SEM image (inset).

The SEM inset image of Figure V-3A also shows that the continuation of the electrodeposition with high cone density results in caps overlapping and forming a large single cap per patch. Due to their thickness, the large caps are heavy and have high mechanical stability compared to the thin interconnecting substrate layer. Hence, the *surface roughness* of the high-density sample observed in Figure V-2A is attributed to the bending of the interconnecting substrate layer and the *independent orienting of each patch* during fixation on the FE holder.

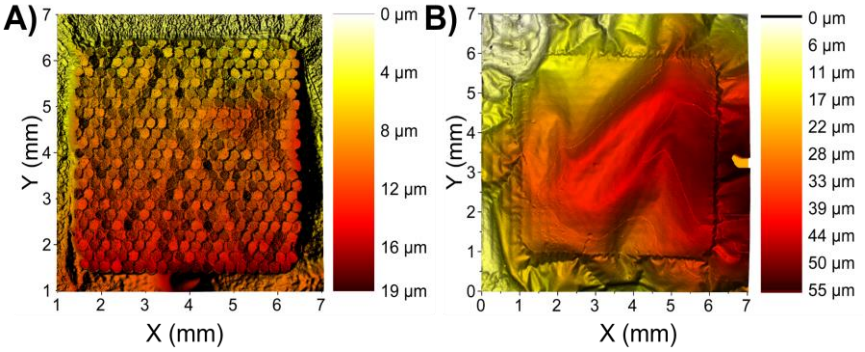

Figure V-2: Surface morphology measured by optical profilometry of (A) high effective cone density sample and (B) low effective cone density sample

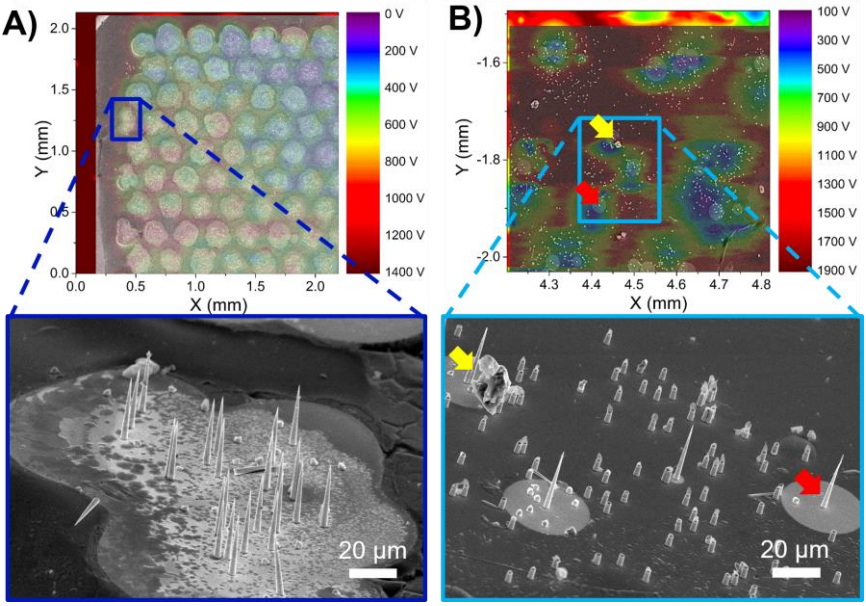

Figure V-3: Voltage scans superimposed with corresponding SEM image of (A) high effective cone density array and (B) low effective cone density array. Insets show a higher magnification of one patch of cones and evidence the cone density difference, inset in (B) is rotated, the red and yellow arrow mark respectively the same cone and dirt in the voltage-scan and in the SEM image

If less cones grow, caps are too far apart to overlap (Figure V-3B). Thus, the caps follow the orientation directed by the bending of the interconnecting layer. Therefore, Figure V-2B exhibits low surface roughness and the surface morphology of the sample is dominated by the *waviness of the interconnecting layer*.

3.2. Field enhancement factor and maximum emission current

To characterize the FE of nanocones, *I-E* curves were recorded by sweeping the electrical field between the AuNCs and the tungsten anode. For each emitter, the local electrical field *E* was calibrated by means of *U(z)* plots.[263,265]

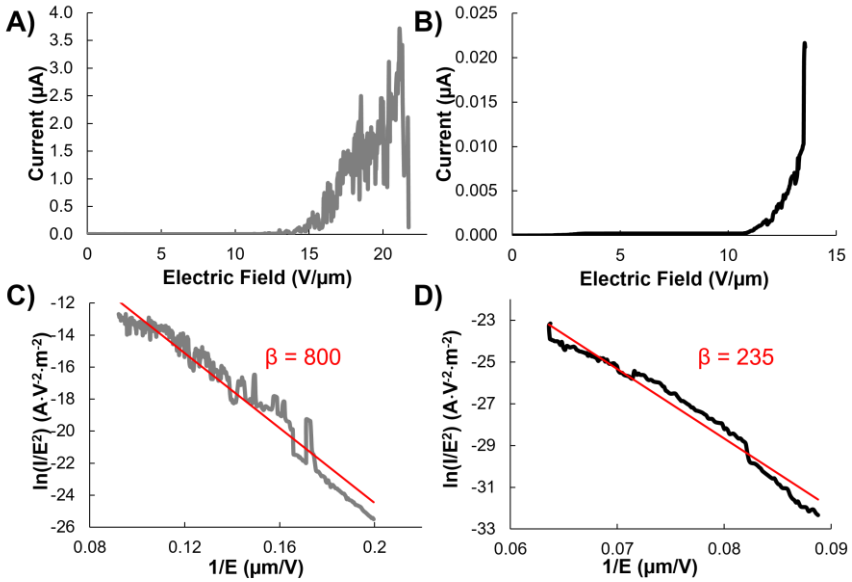

Figure V-4: Representative I-E plots (A and B) and corresponding FN plots (C and D) for the patch samples with (A and C) nominal cone density of 3×10^5 cm^{-2} measured with a large tungsten anode ($Ø_a$ = 152 μm) and (B and D) for an individual AuNC of a patch with a cone density of 4×10^4 cm^{-2} measured with a tip-like anode ($Ø_a$ = 6 μm)

Figure V-4 displays representative *I-E* curves as well as the corresponding Fowler-Nordheim (FN) plots for the two types of samples. The onset field E_{on} (1

nA) was found to be between 5 and 11 V/µm for patch emitters (11 V/µm in Figure V-4A) measured with the truncated tungsten cone. On the other hand, values between 10 and 35 V/µm for individual cones emitters (11 V/µm in Figure V-4B) measured with the small tungsten tip anode.

The *FN plot* is commonly used to analyze and understand the field emission behavior.[244] Using the FN expression of the current density j given in equation (V-1) and applying the definition of the current density: $j = I/S$, with S being the emitting surface, as well as switching to FN coordinate, we obtain:

$$\ln\left(\frac{I}{E^2}\right) = -\frac{B\varphi^{\frac{3}{2}}}{\beta E} + \ln\left(\frac{AS\beta^2}{\varphi}\right) \qquad (V\text{-}2)$$

where A = 1.54×10^{-6} A·eV·V^{-2} and B = 6.83×10^{9} eV$^{-3/2}$·V·m^{-1}, φ is the work function and E is the applied electric field. Straight lines are expected in FN coordinates for electron emission following the *quantum mechanical tunneling* laws. The FN plots insets in Figure V-4 derived from corresponding *I-E* curves thus confirm the tunneling behavior of the NC emitters. The effective field enhancement factor β of the emitters is extracted from the slope of the straight line. Assuming the work function of AuNCs to be φ = 5.1 eV (for Au),[266] the β of the AuNC patch (Figure V-4C) and of the single AuNC (Figure V-4D) amount 800 and 235, respectively.

The enhancement factors β calculated from the FN plots and breakdown current (I_{max}) were measured for several patches of both samples. We found that for both samples, β and I_{max} highly fluctuate among emitters, with β varying between 200 and 1000 and I_{max} between 0.7 and 106 µA (~ 3.5 µA at 21 V/µm in Figure V-4A). No direct relation between the number of emitters and the onset field or the maximum current could be evidenced.

3.3. Effect of field emission on nanocones

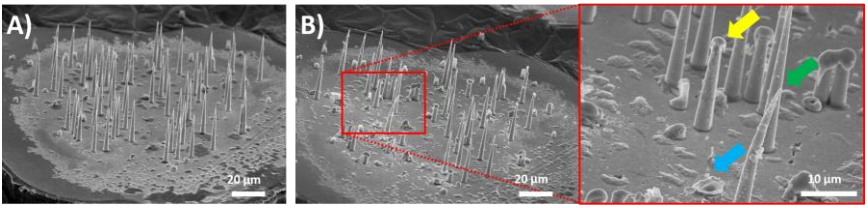

Figure V-5: SEM images of a high effective nanocone density patch emitter before (A) and after (B) field emission measurements

To evaluate the stability of the nanocones, and to analyze the factors that cause failure of the emitters at high currents, all patches were investigated by SEM before and after FE measurements. Figure V-5 displays an example of a nanocone patch imaged under 60° (cone density: 3×10^5 cm^{-2}, anode $Ø_a$ = 152 µm). Before the measurements (Figure V-5A), all the freestanding nanocones exhibit **sharp tips**. Figure V-5B shows the same array after field emission measurements. After the FE measurements, part of the nanocones remain freestanding and maintain their original morphology, whereas the rest appear damaged. The aspect of the cones within the given area differs significantly. Some NCs are completely *melted* or *evaporated* (blue arrow). For some cones, bending is observed (green arrow). For others the sharp tip is only *partly melted* and transformed into a "mushroom like" cap (yellow arrow). These observations strongly indicate that **not every cone contribute** in the same manner to the field emission of the patch, probably due to screening effects and disparities in tip sizes.

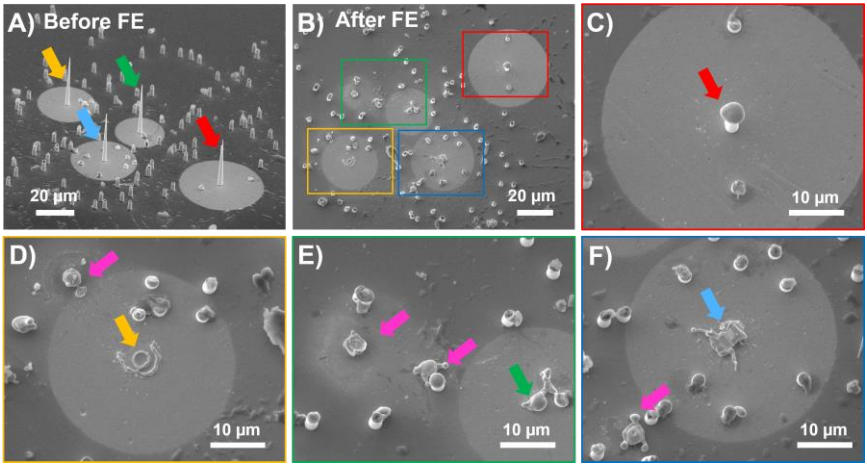

Figure V-6: SEM images of a low effective cone density patch before (A) and after field emission measurements (B-F). Emitters before and after emission are indicated by (C) red, (D) yellow, (E) green, and (F) blue arrows. Pink arrows point parasitic structures damaged after field emission measurements

Similar results are observed for the cathode with lower cone densities. Figure V-6 shows SEM images of nanocones (A) before (tilt = 60°) and (B) after field emission measurements (tilt = 20°). The four cones are damaged by the high current densities flowing during the field emission measurements. Figure V-6C shows a half-molten cone with a mushroom shape (red arrow). Figure V-6D exhibits an evaporated cone(yellow arrow). Figure V-6E and F show cones molten down to their base (blue and green arrows). In addition to the damaged cones, damaged tubes are also observed (pink arrows).

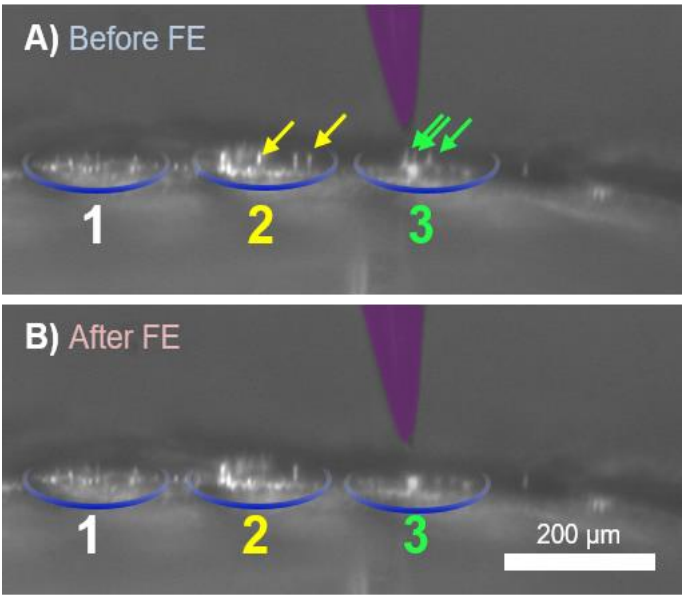

Figure V-7: Optical microscopy images of emitters before (A) and after (B) voltage sweeping up to the breakdown current. The arrows mark the cones disappearing during the measurement. The tungsten anode is colorized in purple

Figure V-7 depicts *optical microscopy* images of nanocone emitters from the low-density sample before (A) and after (B) local FE measurements. The various patches in the optical focus are underlined in blue whereas the anode is colored in purple. The 6 µm anode is placed over a patch with 3 individual cones (green arrows). By careful comparison, we observe that after the FE breakdown, the three cones are melted as shown in Figure V-6B. It also worth mentioning that two cones from a neighbor patch in the optical focus range (yellow arrows) disappear after FE breakdown, indicating melting or evaporation. In the case of the low effective cone density samples, the field emission of 5 patches were measured. For most of the measurements, partial or complete **melting of several cones in the neighbor patches**, up to a distance of ~ 500 µm from the measured patch, is observed by optical microscopy and confirmed by SEM.

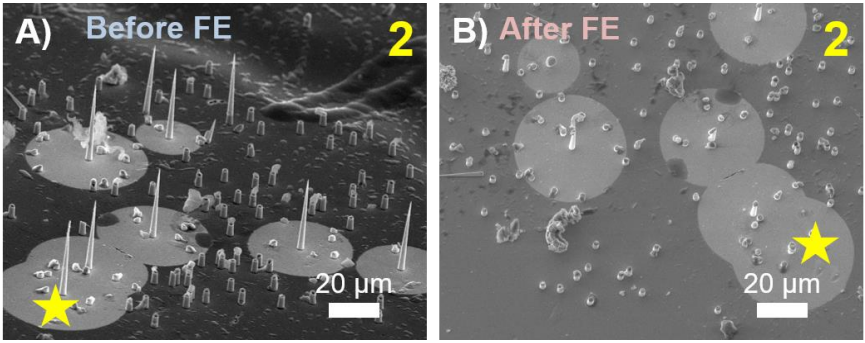

Figure V-8: SEM images of patch 2 from Figure V-7 that was not tested for FE (A) before and (B) after the field emission measurements of neighbor patches. The yellow star marks the same cone on both images

Figure V-8 shows SEM images of the cone patch 2, neighbor of the patch 3 measured for field emission and exposed in Figure V-6. SEM images before (A) and after (B) field emission evidence the melting of the nanocone from this **neighbor patch** that was *never measured directly*. Since patch 3 was the first measured and several other patches around patch 2 where measured afterwards, the cones visible in patch 2 after the FE measurements in Figure V-7 were probably damaged during the measurement of another patch.

Optical study of the electrical breakdown evidences the disappearance of nanocones that is attributed to their melting or evaporation. The optical images taken after the voltage scan but before the local FE measurement (Figure V-7A) prove that cones still exist after the voltage scan. However, **early partial melting** of the emitters due to *transient currents* during the **voltage scans** cannot be discarded. In addition, the contribution of nanocones over **long distance** effect should be investigated in more details because it may induce higher current values and overestimation of the anode-cathode distance using the *U(z)* plots. These long distance effects can be avoided by measuring the FE characteristics of single nanocones.

3.4. Spindt-type field emitters fabrication: proof of concept

The tip-to-base electrodeposition of Au in conical nanochannels of etched ion-track templates is very efficient for the fabrication of freestanding nanocone arrays with cones of identical dimensions. A similar method proposed by Duan et al. also showed that the tip-to-base process is adequate for Cu.[267] In near future, the **tip-to-base** method might be used for the electrodeposition of nanocones of *other metals*, *metal oxides*, or *conductive polymer* of interest depending on the application. The fabrication of hydrophobic *polymer* nanocones according to the presented process can be an elegant alternative for the fabrication of super-hydrophobic coatings. Concerning the field emission applications, another emitter geometry might be considered. Independently on the material, another challenge for field emission applications of nanocones is their **integration** into **operational systems**. The major disadvantage of the tip-to-base deposition is the weak wire-substrate stability and the resulting lack of planarity that is preventing homogeneous emission. However, the tip-to-base growth of nanocones is perfectly appropriated and very promising for the fabrication of **Spindt-type field emitters**.

Figure V-9 schematically represents the major steps required. The initial step consists of the fabrication of AuNCs in a PC template (Figure V-9A). To fabricate the FE counter electrode (also called gate), consisting in a conducting layer with separate apertures for each conical emitter, we propose to electrodeposit a sacrificial Cu half-sphere on top of each cone that will serve as sputtering masks (Figure V-9B). After the deposition of the FE counter electrode (e.g. by sputtering), the dissolution of the Cu half-sphere lead to circular apertures in the electrode layer centered on the cone tip as represented in Figure V-9C. Finally, the selective etching of the unprotected polymer around the cones should provide interesting nano-Spindt arrays (Figure V-9D).

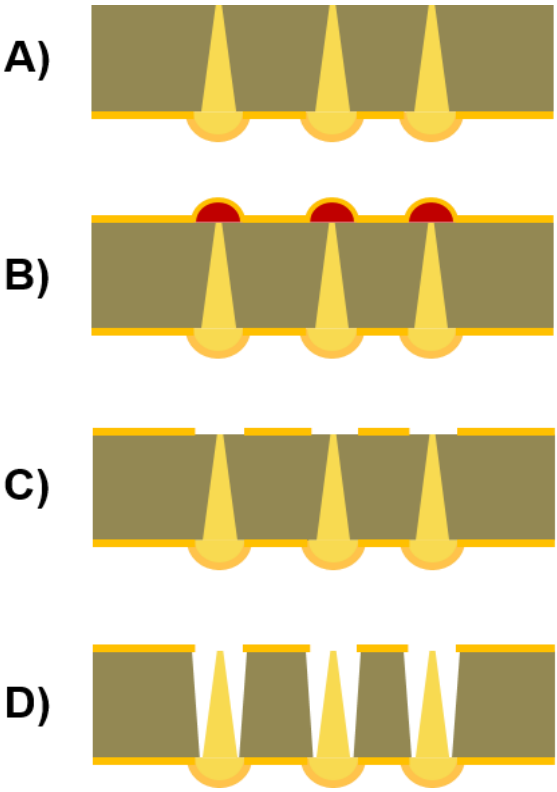

Figure V-9: Scheme of the four major steps proposed to fabricate nanocones in a Spindt-type emitter configuration. (A) Fabrication of nanocones, (B) electrodeposition of sacrificial Cu mask on the top of each cone tip and sputtering conductive Au anode on top, (C) removal of the Cu mask and (D) etching of polymer around the cone

Such Spindt-type arrays have several advantages: (1) the distance between cathode and anode is maintained constant by the polymer film. (2) The **planarity** of the sample is expected to be less critical for such emitters, and (3) the **mechanical stability** is provided by the membrane itself. In principle, *flexible emitters* can be obtained. Moreover, the fabrication process presented above is highly **tunable**: the composition and dimensions of the cones as well as other properties of arrays can easily be modified as seen in section IV.3. In addition,

the dimension of the apertures in the FE counter electrode can also be controlled by tailoring the electrodeposition of the sacrificial copper half-sphere.

Preliminary tests were performed on *nanowire arrays* and are presented in Figure V-10. For this test, Au nanowires were grown in cylindrical nanochannels. The electrodeposition was stopped after the increase in deposition current indicating the complete filling of the channels. In the next step, **Cu caps** were then **potentiostatically electrodeposited** at - 0.08 V on top of the wire ends, i.e. on the other side of the template. The Cu deposition was performed in a $CuSO_4$ (238 g/L) + H_2SO_4 (21 g/L) mixture at room temperature and a Cu wire immersed in the electrolyte served as anode. In a third step, a thin Au layer is sputtered on top of the polymer membrane and of the Cu half-spheres. The Cu half-spheres covered by Au were observed by SEM (Figure V-10A). The sacrificial Cu half-spheres were then dissolved in concentrated nitric acid. Figure V-10B displays the **ring-like apertures** resulting from the dissolution of the copper. The remaining half-spheres observed at the center of each aperture correspond to the *gold caps* originating from the nanowire growth. Such issue is not expected for Cu deposition at the tips of nanocones grown from the tip to the base. It is noted that nanowires were used for this preliminary tests instead of nanocone arrays, because they are deposited from tip-to-base using a gold layer connecting all the tips (sacrificial backelectrode, see Chapter IV.2.2) that is removed only when the membrane is dissolved. A requirement for the successful fabrication of Cu half-spheres is the use of an entirely soluble **sacrificial backelectrode** for the cone electrodeposition. Cr thin film is a potential candidate.

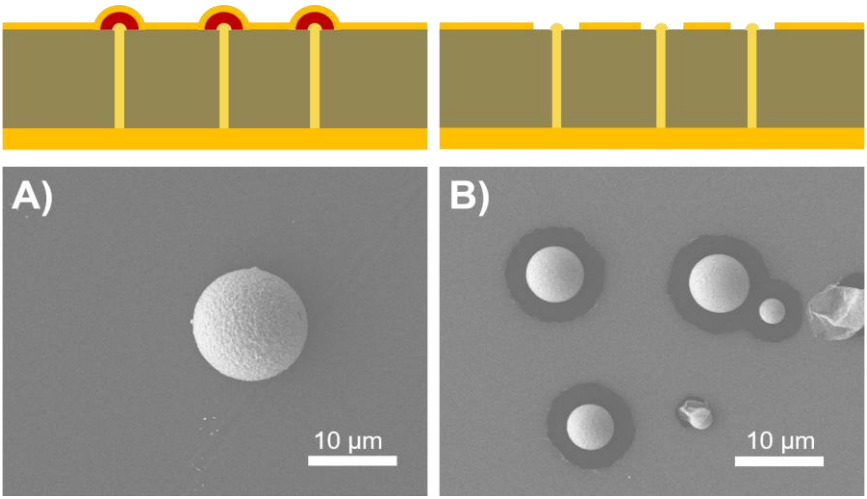

Figure V-10: SEM images and schematic representation of (A) a Cu half-sphere deposited on the top end of a nanowire and (B) ring-like apertures in the sputtered Au layer after the dissolution of the Cu half-spheres revealing gold caps in their center

One of the biggest challenges of this process will probably be the homogeneous growth of Cu half-spheres on top of all nanocones. If a nanocone does not have sacrificial Cu on its tip, it will remain connected to the FE counter electrode and will act as a shortcut. In addition, if the half-spheres do not have identical diameters, the emission of the array will not be homogeneous.

4. Summary

Field emission measurements on vertically aligned freestanding AuNC patterned arrays fabricated by electrodeposition in etched ion-track templates from tip-to-base are presented. Voltage scans enabled to locate the emitters and to identify them in correlation with SEM observations. For high cone densities, cone patches could be distinguished whereas individual cones could be isolated on the emission map of the sample with low effective cone density. The study of the emission by voltage sweeps indicated that all emitters follow the Fowler-Nordheim emission theory but no correlation between the number of cones and the emission was

revealed. The high aspect ratio of the structures and the sharp tips with diameters below 100 nm lead to low onset fields (down to 5 V/µm) and high maximum emission currents (up to 10-100 µA) for structured AuNC arrays. After voltage scans and/or voltage sweeps, several AuNCs emitters were molten or evaporated but not all cones are affected. SEM studies of the samples after FE measurements also suggested that parasitic structures with low aspect ratio as well as cones very far from the point of measurement (≥ 10 times the cone length) might also contribute to the emission current. Further studies should focus on measuring the field emission of individual cones. This will allow studying the influence of the material, the geometry, the tip diameter, and of the morphology independently and in detail. Finally, the procedure to fabricate Spindt-type field emitters based on the template growth of cones and electrodeposition of sacrificial copper mask on each cone tip was introduced, and the proof of concept experimentally demonstrated.

Conclusion and Outlook

This thesis presents the synthesis and characterization of three different types of gold-based nanostructures, namely solid AuAg alloy nanowires, nanoporous gold nanowires, and gold nanocones. The synthesis of these structures is based on ion-track technology and electrodeposition methods that were investigated and optimized.

The synthesis of AuAg nanowires with tailored composition and diameter was achieved by electrodeposition of AuAg alloy in cylindrical nanochannels of etched ion-track templates. The analysis of the electrochemical reduction of Au and Ag yields high current efficiencies. The potentiostatic electrodeposition at -1.1 V vs. Ag/AgCl occurs close to the diffusion-limited regime. The composition of AuAg nanowires is thus only determined by the electrolyte composition. The deposition was shown to be independent of the channel size. All nanowires fabricated at such a potential consist of long single-crystalline sections. $Au_{40}Ag_{60}$ and $Au_{60}Ag_{40}$ nanowires were synthesized and subsequently analyzed by means of high-resolution transmission electron microscopy coupled with energy dispersive X-ray spectroscopy with high spatial resolution showed clear evidence of surface segregation. $Au_{60}Ag_{40}$ nanowires were found to have a Au-rich surface layer whereas $Au_{40}Ag_{60}$ nanowires rather form a Ag-rich surface layer. This explains why Au-rich nanowires cannot be dealloyed and thus remain solid. Contrarily, dealloying of Ag-rich wires yields highly porous nanostructures made of a network of interconnected ligaments with small domains of residual silver. Crystalline defects seem neither to influence nor to be affected by dealloying. Our approach allows the fabrication of continuous porous gold nanowires with diameters as small as 85 nm. This size limit appears because nanowires with smaller initial diameter dealloy into single ligaments and tend to fragment.

The fabrication of sensors based on the synthesis of such porous gold nanowires requires electric contacts and device integration. As a first step towards contacting

template-released nanowires with diameters as small as 45 nm, laser lithography based contacts were developed. In parallel, nanowires were placed on pre-fabricated chips and trenches. Successful dealloying was demonstrated for as-contacted nanowires. Preliminary characterization of electrical and thermal transport properties of solid and porous cylindrical nanowires are currently under test at the Hochschule RheinMain.

The synthesis of gold nanocones was achieved by electrodeposition from tip-to-base in conical-shaped nanochannels of etched ion-track membranes. Asymmetrical etching of ion tracks yields nanochannels with slightly tunable cone angles. The electrodeposition processes using a commercial Au electrolyte is shown to occur close to the diffusion limit. The reduction process of Au inside single conical nanochannels from the tip to the base provides clear identification of the three main electrodeposition steps: initiation, cone growth, and cap formation. This information permits controlled deposition of the cones and enables high efficiency of the electrodeposition as well as minimization of parasitic structures such as tubes or incomplete cone bases. By growing the cones from tip to base, high reproducibility of the synthesis process is achieved. Vertically aligned freestanding gold nanocones of homogeneous lengths and with sharp tips as small as 50 nm are successfully produced. Their mechanical stability is excellent, the risk of breaking cones is low, and the contact to the substrate is outstanding. Compared to nanocone arrays, the fabrication of a single nanocone is more challenging due to rather large scattering of the breakthrough time when etching membranes with an individual ion track. In addition, the unpredictable closing of single channels with very small opening is problematic. After the dissolution of the membrane, single nanocones are also more vulnerable to external harm and thus often suffer from bending of distortion.

The field emission properties of our nanocone arrays are promising. Voltage scans allow mapping of patterned nanocones arrays. For low cone densities, even single nanocone emitters could be identified. Field emission measurements from nanocone arrays follow the Fowler-Nordheim model, but large discrepancies of

enhancement factors and breakdown currents are observed. Optical and scanning electron micrographs reveal inhomogeneous contributions of the cones to the emission current as well as contributions of nanocones positioned far away (distances higher than 10 times the cone length). This effect is partly attributed to the non-planarity of the samples. Although the new growth technique developed here provides highly improved substrate contact, some of the nanocones are molten or even completely evaporated after field emission. For better integration in operating systems, the synthesis of arrays of Spindt-type cold emitter based on the electrodeposition of gold nanocones is proposed. Preliminary tests demonstrate proof of concept.

The application of solid and porous nanowires as well as nanocones requires a detailed physical and chemical characterization in particular, their electrical transport properties. The results achieved in this thesis will serve as a starting base for further studies.

The synthesis conditions developed in this work can be adapted to the fabrication of porous gold nanowire networks. It has already been demonstrated that interconnected nanowires provide sufficient mechanical stability to manipulate the 3D systems.[78,79,240,242] Adding nanoporosity to such 3D-networks would enable the fabrication of highly porous systems with bimodal porosity. Such structures are of interest for catalysis where the macroscopic porosity (tuned by the spacing of the nanowires) yields efficient fluidic flow through the device whereas the nanoporosity (obtained by dealloying) catalyzes chemical reactions. The influence of surface segregation of AuAg nanowires evidenced in this work can be further explored regarding mechanical properties and chemical activity of porous nanostructures. Deeper insight is necessary to better understand environmental factors on surface segregation and how the surface layer affects chemical, optical, or mechanical properties of nanowires. Also the time dependence of the segregation process is of great interest concerning the applicability of ultrathin nanowires in devices. Surface segregation of AuAg

nanowires also creates new opportunities. Considering the possibility of complete segregation of alloy nanowires by aging might enable the production of core-shell nanowires. Likewise, ultrathin nanowires or nanotubes could be produced by selective removal of one of the components of core-shell nanowires.

Our field emission studies of nanocone arrays shows that fundamental understanding of the process can only be achieved by analyzing the emission of single nanocones. The fabrication of single nanocones is challenging and needs to be optimized, in particular, regarding the etching process of single ion tracks and the manipulation of single nanochannels and nanocones samples.

The tip-to-base cone synthesis process demonstrated in this work with gold may also be applied to a large variety of materials like metals, semiconductors, and conductive polymers. Thus, arrays of vertically aligned freestanding nanocones with tunable geometry and densities open interesting new perspectives for many other applications.

Symbols

AuCN	Au(1)-cyanide electrolyte
AuNC	Gold nanocone
AuSF	Au(1)-sulfite electrolyte
BF	Bright field
C_O^*	Electrolyte bulk concentration
CuC	Lacey-carbon/copper TEM grids
CV	Cyclic voltammogram/voltammetry
EDX	Energy dispersive X-ray
E_{on}	Onset field
FE	Field emission
FN	Fowler-Nordheim
HAADF	High-angle annular dark-field
I_{max}	Breakdown current
j, j_0, j_L	Current density, exchange current density, limiting current density
M	Atomic mass / molar mass
MeOH	Methanol
n	Number of charge of the ion/number of electron involved in a chemical reaction
NaOH	Sodium hydroxide
NC	Nanocone
NW	Nanowire
Ø, $Ø_a$, $Ø_c$, $Ø_{tip}$, $Ø_{base}$	Diameter, Tip diameter of the field emission anode, Nanochannel diameter, Cone tip diameter, Cone base diameter
PAuNW	Porous gold nanowire
PC, PCM, PCP	Polycarbonate, Makrofol PC, Pokalon PC
SEM	Scanning electron microscopy
SiN	Silicon nitride TEM grids
STEM	Scanning transmission electron microscopy
TEM	Transmission electron microscope
UV	Ultra-violet
v_b	Bulk etching rate

v_r	Radial etching rate
v_t	Track etching rate
XRD	X-Ray diffraction
Z	Atomic number
β	Field enhancement factor

About the Author

EDUCATION

2012 – 2016 **PhD student** in the Materials Science Department, *Technische Universität Darmstadt, Darmstadt, Germany*

Topic: Ion-track technology based synthesis and characterization of gold and gold alloys nanowires and nanocones

2009 – 2012 **Engineering diploma** of the ECPM, *ECPM (The European Engineering school of Chemistry, Polymers and Materials Science), Strasbourg, France*

Specialization: Materials Sciences

2009 – 2012 **Master of Science** diploma with high honors, *Université de Strasbourg, Strasbourg, France*

Specialization: Materials Sciences

Topic: "Photonic crystals from silica and iron oxide nanoparticles"

AWARDS

Oct. 2015 **Giersch-Excellence-Grant**, *Stiftung Giersch and the Helmholtz Graduate School for Hadron and Ion Research for FAIR*

Sept. 2014 **Best student presentation**, *in symposium B: Organized nanostructures and nano-objects: fabrication, characterization and applications, E-MRS Fall 2014, European Material Research Society Fall Meeting and Exhibit 2014*

PUBLICATIONS

2016 Pérez-Mitta, G.; Burr, L.; Tuninetti, J. S.; Trautmann, C.; Toimil-Molares, M. E.; Azzaroni, O. Noncovalent Functionalization of Solid-State Nanopores via Self-Assembly of Amphipols. *Nanoscale* **2016**, *8* (3), 1470–1478, DOI: 10.1039/C5NR08190D.

2015 Burr, L.; Schubert, I.; Sigle, W.; Trautmann, C.; Toimil-Molares, M. E. Surface Enrichment in Au–Ag Alloy Nanowires and Investigation of the Dealloying Process. *J. Phys. Chem. C* **2015**, *119* (36), 20949–20956, DOI: 10.1021/acs.jpcc.5b05596.

Schubert, I.; Burr, L.; Trautmann, C.; Toimil-Molares, M. E. Growth and Morphological Analysis of Segmented AuAg Alloy Nanowires Created by Pulsed Electrodeposition in Ion-Track Etched Membranes. *Beilstein J. Nanotechnol.* **2015**, *6*, 1272–1280, DOI: 10.3762/bjnano.6.131.

Schubert, I.; Sigle, W.; Burr, L.; Aken, P. A. Van; Trautmann, C.; Toimil-molares, E. Fabrication and Plasmonic Characterization of Au Nanowires with Controlled Surface Morphology. *Adv. Mater. Lett.* **2015**, *6* (5), 377–385, DOI: 10.5185/amlett.2015.5721.

2014 Dyzynski, M.; Burr, L.; Trautmann, C.; Schubert, I. Synthesis of AuxAg1−x Nanowire-Networks with Controlled Composition and Defined Wire Diameter. *GSI Sci. Rep.* **2014**.

2012 Burr, L.; Alber, I.; Trautmann, C. Thermal Instability of Porous Gold Nanowires. *GSI Sci. Rep*. **2012**, 417.

2011 Oertel, A. M.; Ritleng, V.; Burr, L.; Chetcuti, M. J. Synthesis and Structural Characterization of Half-Sandwich Nickel Complexes Bearing Two Different N-Heterocyclic Carbene Ligands. *Organometallics* **2011**, 30 (24), 6685–6691, DOI: 10.1021/om200864z.

CONTRIBUTIONS TO CONFERENCES

2015 ***Oral presentation***: Burr, L.; Serbun P.; Reimuth C.; Heider, B.; Schubert, I.; Muller, G.; Trautmann, C.; Toimil-Molares M.E. Electrodeposition of single gold nanocones and multi-cone arrays for field emission. *EDNANO 11, 11th International Workshop on Electrodeposited Nanostructures*, Balatonfüred, Hungary

Oral presentation: Burr, L.; Alber, I.; Sigle, W.; Trautmann, C.; **Toimil-Molares M.E.** Dealloying of electrochemically grown Au-Ag nanowires. *E-MRS Spring 2015, European Material Research Society Spring Meeting and Exhibit 2015*, Lille, France

Oral presentation: Burr, L.; Alber, I.; Sigle, W.; Trautmann, C.; Toimil-Molares M.E. Dealloying of electrochemically grown Au-Ag nanowires. *MRS Spring 2015, Material Research Society Spring Meeting and Exhibit 2015*, San Fransisco, USA

2014 ***Poster***: Burr, L.; Alber, I.; Sigle, W.; Trautmann, C.; Toimil-Molares M.E. Dealloying of electrochemically grown Au-Ag nanowires. *First International Symposium on Nanoporous Materials by Alloy Corrosion*, Lake Bostal, Germany

Poster: Burr, L.; Alber, I.; Heider, B.; Reimuth, C.; Dyzynski, M.; Sigle, W.; Trautmann, C.; Toimil-Molares M.E. Dealloying of gold-based nanostructures. *SNI 2014, German Conference for Research with Synchrotron Radiation, Neutrons and Ion Beams at Large Facilities 2014*, Bonn, Germany

Poster: Burr, L.; Alber, I.; Sigle, W.; Trautmann, C.; Toimil-Molares M.E. Dealloying of electrochemically grown Au-Ag nanowires. *E-MRS Fall 2014, European Material Research Society Fall Meeting and Exhibit 2014*, Warsaw, Poland

Poster: Burr, L.; Alber, I.; Sigle, W.; Trautmann, C.; Toimil-Molares M.E. Dealloying of electrochemically grown Au-Ag nanowires. *Gordon Research Conference on Electrodeposition*, University of New England, Biddeford, USA

Poster: Burr, L.; Alber, I.; Sigle, W.; Trautmann, C.; Toimil-Molares M.E. Investigation of the dealloying of electrochemically grown AuAg nanowires. *EDNANO10, 10th International Workshop on Electrodeposited Nanostructures*, Oberwesel, Germany

Poster: Burr, L.; Reimuth, C.; Alber, I.; Trautmann, C.; Toimil-Molares M.E. Conical gold nanowires fabricated by electrodeposition. *EDNANO10, 10th International Workshop on Electrodeposited Nanostructures*, Oberwesel, Germany

2013 ***Oral presentation***: Burr, L.; Nanostructures prepared by ion-track technology, *HGS-HIRe Graduate days*, Worms, Germany

SUPERVISION OF BACHELORS AND INTERNS

2015	Xavier Hartmann; Ecole supérieure de biotechnologie de Strasbourg
	Internship: Synthesis of single and arrays of gold nanocones
2014	Anton Langhans; Hochschule RheinMain;
	Internship: Elektrochemische Abscheidung von konischen Goldnanodrähten und deren Variation
	Ben Heider; Technische Universität Darmstadt;
	Internship: Electro-chemical deposition of conical gold nanowires in a three-electrode setup
	Bachelor thesis: Fabrication of gold nanocones for field emission measurements in a triode configuration
	Christoph Reimuth; Technische Universität Darmstadt;
	Internship: Electrochemical deposition of conical gold nanowires
	Bachelor thesis: Fabrication and characterization of conical gold nanowires

Acknowledgements

Last but not least, I would like to use this opportunity to express my deep and sincere gratitude to all people that supported me during the three last years.

My first acknowledgement is dedicated to my supervisor, Prof. Dr. Christina Trautmann for giving me the possibility to work in the Materials Research Department of GSI and to teach me how to become a researcher. I am also very grateful to Dr. Maria Eugenia Toimil-Molares for introducing me to nanotechnologies, guiding my research, as well as for her insightful comments and her continuous support. Thank you for the proofreading of my thesis and helping me clarifying my mind when I was confused. Your care and goodwill was very much appreciated. Furthermore, I would like to thank my bosses ☺ for trusting in my work and encouraging me all along the 3 years of my PhD. I really appreciated their availability to answer my numerous questions. I am also very grateful for the opportunity I had to participate to several national and international conferences.

Beside my supervisors, I would like to thank Prof. Dr. Ralph Krupke, Prof. Dr. Robert Stark and Prof. Dr. Friedemann Völklein (Hochschule RheinMain) for being members of my thesis committee. Special thanks to Prof. Dr. Friedemann Völklein for the continuous follow-up on my work as member of my HGS-Hire graduate school committee as well as for his suggestions and help for the preparation of nanostructures for future measurement of the transport properties.

My sincere acknowledgments also go to Dr. Wilfried Sigle from the MPI for Solid State Research of Stuttgart who granted me access to the high resolution TEM and made all the studious TEM measurements presented in this work. Many thanks for introducing me to this interesting instrumentation and for helping me understand the results obtained. I also want to thank Dr. Pavel Serbun from the Bergische Universität Wuppertal for performing with assisting me during all the field emission measurements and helping me analyse the data.

Dr. Ina Schubert möchte ich für die Ratschläge und hilfreichen Diskussionen bezüglich der Gold Nanostrukturen herzlich danken.

Je souhaiterais aussi exprimer mes sincères remerciements à Prof. Dr. Gérard Hopfgartner pour la relecture attentive de mon manuscrit et pour son aide précieuse tout au long de ma thèse.

Mein besonderer Dank gilt auch Christoph Reimuth, Ben Heider, Anton Langan und Xavier Hartmann. Ihre Arbeit an den konischen Nanodrähte half mir sehr und bei ihrer Einarbeitung verbesserte ich meine Wissenvermittlung sehr.

Vielen Dank an Janina Krieg und Anne Spende, meine privaten Deutschlehrerinnen die mein Deutsch sehr verbesserten und von denen ich über vielfälligste Thema, wie Forschung und Wissenschaft oder Deutschland, viel gelernt habe.

Many thanks to Liana Movsesyan and Gonzalo Pérez-Mitta with whom I performed several joint experiments and with whom I had very fruitful discussions.

I am also very grateful to Dr. Wouter Maijenburg, Marco Cassineli, Michael Wagner, Dimitri Khaghani, Peter Katrík, and the MF group for the great working atmosphere. I will always remember the numerous stimulating scientific and non-scientific discussions, the sleepless nights of beam-time and all the fun we had in the last 3 years.

Merci à tonton GG et à ma marraine de m'avoir motivé à faire une thèse et d'avoir inspiré ma vocation scientifique.

Je souhaiterais remercier toute ma famille, en particulier mes parents et ma petite sœur pour leur soutien indéfectible, et ce depuis toujours. Sans eux, je ne serais pas celui que je suis. Maintenant je peux enfin répondre à la question presque pas redondante de maman : "As-tu déjà commencé l'introduction ?".

Enfin, je voudrais remercier de tout mon cœur Marie qui m'accompagne depuis presque 10 ans et a supporté ma thèse ainsi que tout ce que cela implique. Merci pour ton Courage et ton Amour!

The financial support from DFG and HGS-Hire was very much appreciated.

References

(1) Moore, G. Cramming More Components Onto Integrated Circuits, Electronics,(38) 8. **1965**, *38* (8).

(2) Rao, C., Müller, A., C. K. *The Chemistry of Nanomaterials*; Wiley-VCH Verlag GmbH & Co. KGaA: Weinheim, FRG, **2004**.

(3) Bhushan, B. *Encyclopedia of Nanotechnology*; Springer Netherlands: Dordrecht, **2012**; Vol. 53.

(4) Wautelet, M. *Nanotechnologies*, Second Edi.; The Institution of Engineering and Technology, London, United Kingdom, **2006**.

(5) Bond, G. C.; Louis, C.; Thompson, D. T. *Catalysis by Gold*; Catalytic Science Series; Imperial College Press, **2006**; Vol. 6.

(6) Wittstock, A.; Biener, J.; Bäumer, M. *Nanoporous Gold : From an Ancient Technology to a High-Tech Material*; RSC Nanoscience & Nanotechnology; Royal Society of Chemistry: Cambridge, **2012**.

(7) Daniel, M. C.; Astruc, D. Gold Nanoparticles: Assembly, Supramolecular Chemistry, Quantum-Size-Related Properties, and Applications Toward Biology, Catalysis, and Nanotechnology. *Chem. Rev.* **2004**, *104* (1), 293–346, DOI: 10.1021/cr030698+.

(8) Sigma-Aldrich. Gold Nanoparticles: Properties and Applications http://www.sigmaaldrich.com/materials-science/nanomaterials/gold-nanoparticles.html (accessed Jan 11, 2016).

(9) Levinson, H. J. *Principles of Lithography*, 3rd ed.; SPIE Press: Bellingham, Washington USA, **2005**.

(10) Pazos-Pérez, N.; Baranov, D.; Irsen, S.; Hilgendorff, M.; Liz-Marzán, L. M.; Giersig, M. Synthesis of Flexible, Ultrathin Gold Nanowires in Organic Media. *Langmuir* **2008**, *24* (17), 9855–9860, DOI: 10.1021/la801675d.

(11) Hong, X.; Wang, D.; Yu, R.; Yan, H.; Sun, Y.; He, L.; Niu, Z.; Peng, Q.; Li, Y. Ultrathin Au-Ag Bimetallic Nanowires with Coulomb Blockade Effects. *Chem. Commun. (Camb).* **2011**, *47* (18), 5160–5162, DOI: 10.1039/c1cc10903k.

(12) Honeychurch, K. C.; Boujtita, M.; Davis, F.; Higson, S. P. J.; Metters, J. P.; Banks, C. E.; Rawson, F. J.; Francioso, L.; Yarman, A.; Turner, A. P. F.; et al. *Nanosensors for Chemical and Biological Applications*; Elsevier, **2014**.

(13) Wang, J. Biomolecule-Functionalized Nanowires: From Nanosensors to Nanocarriers. *ChemPhysChem* **2009**, *10* (11), 1748–1755, DOI: 10.1002/cphc.200900377.

(14) Wang, J. Nanomaterial-Based Electrochemical Biosensors. *Analyst* **2005**, *130*, 421–426, DOI: 10.1039/b414248a.

(15) Rolison, D. R. Catalytic Nanoarchitectures--the Importance of Nothing and the Unimportance of Periodicity. *Science* **2003**, *299* (5613), 1698–1701, DOI: 10.1126/science.1082332.

(16) Intel. Intel 14 nm technology

http://www.intel.com/content/www/us/en/silicon-innovations/intel-14nm-technology.html (accessed Dec 12, 2015).

(17) Lide, D. R.; Baysinger, G. CRC Handbook of Chemistry and Physics. **2004**.

(18) Baker, H. ASM Handbook, Vol. 3: Alloy Phase Diagrams. In *ASM Handbook*; Baker, H., Ed.; **1991**.

(19) Ullmann, F.; Bohnet, M. *Ullmann's Encyclopedia of Industrial Chemistry*; Wiley-VCH Verlag GmbH & Co. KGaA: Weinheim, Germany, **2000**; Vol. 35.

(20) Chopra, K. L.; Bobb, L. C.; Francombe, M. H. Electrical Resistivity of Thin Single-Crystal Gold Films. *J. Appl. Phys.* **1963**, *34* (6), 1699, DOI: 10.1063/1.1702662.

(21) Sondheimer, E. H. The Mean Free Path of Electrons in Metals. *Adv. Phys.* **1952**, *1* (1), 1–42, DOI: 10.1080/00018735200101151.

(22) Museum, B. Lycurgus cup

http://www.britishmuseum.org/research/collection_online/collection_object_details.aspx?objectId=61219&partId=1&searchText=Lycurgus Cup (accessed Dec 22, 2015).

(23) Eustis, S.; el-Sayed, M. a. Why Gold Nanoparticles Are More Precious than Pretty Gold: Noble Metal Surface Plasmon Resonance and Its Enhancement of the Radiative and Nonradiative Properties of Nanocrystals of Different Shapes. *Chem. Soc. Rev.* **2006**, *35* (3), 209–217, DOI: 10.1039/b514191e.

(24) Haruta, M.; Kobayashi, T.; Sano, H.; Yamada, N. Novel Gold Catalysts for the Oxidation of Carbon Monoxide at a Temperature Far below 0.DEG.C. *Chem. Lett.* **1987**, No. 2, 405–408, DOI: 10.1246/cl.1987.405.

(25) Haruta, M. Chance and Necessity: My Encounter with Gold Catalysts. *Angew. Chem. Int. Ed. Engl.* **2013**, 2–7, DOI: 10.1002/anie.201305987.

(26) Edwards, P. P.; Johnson, S. R.; Jones, M. O.; Porch, A.; Johnston, R. L. *The Size – Induced Metal – Insulator Transition in Colloidal Gold*; Elsevier Masson SAS, **2001**; Vol. 132.

(27) Sun, Y.; Ye, J.; Shan, Z.; Minor, A. M.; Balk, T. J. The Mechanical Behavior of Nanoporous Gold Thin Films. *JOM* **2007**, *59* (September), 54–58, DOI: 10.1007/s11837-007-0118-0.

(28) Hakamada, M.; Mabuchi, M. Mechanical Strength of Nanoporous Gold Fabricated by Dealloying. *Scr. Mater.* **2007**, *56* (11), 1003–1006, DOI: 10.1016/j.scriptamat.2007.01.046.

(29) Biener, J.; Hodge, A. M.; Hayes, J. R.; Volkert, C. a; Zepeda-Ruiz, L. a; Hamza, A. V; Abraham, F. F. Size Effects on the Mechanical Behavior of Nanoporous Au. *Nano Lett.* **2006**, *6* (10), 2379–2382, DOI: 10.1021/nl061978i.

(30) Mameka, N.; Wang, K.; Markmann, J.; Lilleodden, E. T.; Weissmüller, J. Nanoporous Gold—Testing Macro-Scale Samples to Probe Small-Scale Mechanical Behavior. *Mater. Res. Lett.* **2015**, *3831* (October), 1–10, DOI: 10.1080/21663831.2015.1094679.

(31) Chen, J.; Saeki, F.; Wiley, B. J.; Cang, H.; Cobb, M. J.; Li, Z.-Y.; Au, L.; Zhang, H.; Kimmey, M. B.; Li, X.; et al. Gold Nanocages: Bioconjugation and Their Potential Use as Optical Imaging Contrast Agents. *Nano Lett.* **2005**, *5* (3), 473–477, DOI: 10.1021/nl047950t.

(32) Cherevko, S.; Chung, C. H. Gold Nanowire Array Electrode for Non-Enzymatic Voltammetric and Amperometric Glucose Detection. *Sensors Actuators, B Chem.* **2009**, *142* (1), 216–223, DOI: 10.1016/j.snb.2009.07.023.

(33) Kisner, A. Ultrathin Gold Nanowires – Chemistry, Electrical Characterization and Application to Sense Cellular Biology, RWTH Aachen University, **2012**.

(34) Xia, X.; Wang, Y.; Ruditskiy, A.; Xia, Y. 25th Anniversary Article: Galvanic Replacement: A Simple and Versatile Route to Hollow Nanostructures with Tunable and Well-Controlled Properties. *Adv. Mater.* **2013**, *25* (44), 6313–6333, DOI: 10.1002/adma.201302820.

(35) Erlebacher, J.; Aziz, M. J.; Karma, A.; Dimitrov, N.; Sieradzki, K. Evolution of Nanoporosity in Dealloying. *Nature* **2001**, *410* (6827), 450–453, DOI: 10.1038/35068529.

(36) Wirtz, M.; Martin, C. R. Template-Fabricated Gold Nanowires and Nanotubes. *Adv. Mater.* **2003**, *15* (5), 455–458, DOI: 10.1002/adma.200390106.

(37) Kontio, J. M.; Simonen, J.; Tommila, J.; Pessa, M. Arrays of Metallic Nanocones Fabricated by UV-Nanoimprint Lithography. *Microelectron. Eng.* **2010**, *87* (9), 1711–1715, DOI: 10.1016/j.mee.2009.08.015.

(38) Kontio, J. M.; Husu, H.; Simonen, J.; Huttunen, M. J.; Tommila, J.; Pessa, M.; Kauranen, M. Nanoimprint Fabrication of Gold Nanocones with ~10 Nm Tips for Enhanced Optical Interactions. *Opt. Lett.* **2009**, *34* (13), 1979, DOI: 10.1364/OL.34.001979.

(39) Lilley, C. M.; Huang, Q. Surface Contamination Effects on Resistance of Gold Nanowires. *Appl. Phys. Lett.* **2006**, *89* (20), 203114, DOI: 10.1063/1.2388133.

(40) Stade, F.; Heeren, A.; Fleischer, M.; Kern, D. P. Fabrication of Metallic Nanostructures for Investigating Plasmon-Induced Field Enhancement. *Microelectron. Eng.* **2007**, *84* (5-8), 1589–1592, DOI: 10.1016/j.mee.2007.01.256.

(41) Skrabalak, S.; Chen, J.; Sun, Y.; Lu, X. Gold Nanocages: Synthesis, Properties, and Applications. *Acc. Chem. Res.* **2008**, *41* (12), 1587–1595.

(42) Hirsch, L. R.; Stafford, R. J.; Bankson, J. a; Sershen, S. R.; Rivera, B.; Price, R. E.; Hazle, J. D.; Halas, N. J.; West, J. L. Nanoshell-Mediated near-Infrared Thermal Therapy of Tumors under Magnetic Resonance Guidance. *Proc. Natl. Acad. Sci.* **2003**, *100* (23), 13549–13554, DOI: 10.1073/pnas.2232479100.

(43) Shi, P.; Zhang, J.; Lin, H.-Y.; Bohn, P. W. Effect of Molecular Adsorption on the Electrical Conductance of Single Au Nanowires Fabricated by Electron-Beam Lithography and Focused Ion Beam Etching. *Small* **2010**, *6* (22), 2598–2603, DOI: 10.1002/smll.201001295.

(44) Zeis, R.; Mathur, A.; Fritz, G.; Lee, J.; Erlebacher, J. Platinum-Plated Nanoporous Gold: An Efficient, Low Pt Loading Electrocatalyst for PEM Fuel Cells. *J. Power Sources* **2007**, *165* (1), 65–72, DOI: 10.1016/j.jpowsour.2006.12.007.

(45) Yang, D.; Fonseca, L. F. Wet-Chemical Approaches to Porous Nanowires with Linear, Spiral, and Meshy Topologies. *Nano Lett.* **2013**, *13* (11), 5642–5646, DOI: 10.1021/nl403314m.

(46) Wang, J.; Gao, H.; Sun, F.; Xu, C. Nanoporous PtAu Alloy as an Electrochemical Sensor for Glucose and Hydrogen Peroxide. *Sensors Actuators, B Chem.* **2014**, *191*, 612–618, DOI: 10.1016/j.snb.2013.10.034.

(47) Costa, J. C. S.; Corio, P.; Camargo, P. H. C. Silver–gold Nanotubes Containing Hot Spots on Their Surface: Facile Synthesis and Surface-Enhanced Raman Scattering Investigations. *RSC Adv.* **2012**, *2* (26), 9801, DOI: 10.1039/c2ra21562d.

(48) Mohl, M.; Kumar, A.; Mohana Reddy, A. L.; Kukovecz, A.; Konya, Z.; Kiricsi, I.; Vajtai, R.; Ajayan, P. M. Synthesis of Catalytic Porous Metallic Nanorods by Galvanic Exchange Reaction. *J. Phys. Chem. C* **2010**, *114* (1), 389–393, DOI: 10.1021/jp9083508.

(49) Liu, Z.; Searson, P. C. Single Nanoporous Gold Nanowire Sensors. *J. Phys. Chem. B* **2006**, *110* (9), 4318–4322, DOI: 10.1021/jp056940t.

(50) Zhang, X.; Li, D.; Bourgeois, L.; Wang, H.; Webley, P. A. Direct Electrodeposition of Porous Gold Nanowire Arrays for Biosensing Applications. *ChemPhysChem* **2009**, *10* (2), 436–441, DOI: 10.1002/cphc.200800538.

(51) Schubert, I.; Sigle, W.; Burr, L.; Aken, P. A. Van; Trautmann, C.; Toimil-molares, E. Fabrication and Plasmonic Characterization of Au Nanowires with Controlled Surface Morphology. *Adv. Mater. Lett.* **2015**, *6* (5), 377–385, DOI: 10.5185/amlett.2015.5721.

(52) Forty, A. Corrosion Micromorphology of Noble Metal Alloys and Depletion Gilding. *Nature* **1979**, *282*, 597–598.

(53) Ji, C.; Searson, P. C. Fabrication of Nanoporous Gold Nanowires. *Appl. Phys. Lett.* **2002**, *81* (23), 4437–4439, DOI: 10.1063/1.1526920.

(54) Ji, C.; Searson, P. C. Synthesis and Characterization of Nanoporous Gold Nanowires. *J. Phys. Chem. B* **2003**, *107* (19), 4494–4499, DOI: 10.1021/jp0222200.

(55) Ji, C.; Oskam, G.; Ding, Y.; Erlebacher, J. D.; Wagner, A. J.; Searson, P. C. Deposition of Au[sub x]Ag[sub 1−x]/Au[sub y]Ag[sub 1−y] Multilayers and Multisegment Nanowires. *J. Electrochem. Soc.* **2003**, *150* (8), C523, DOI: 10.1149/1.1585053.

(56) Johnson, L. P.; Matisons, J. G. Synthesis of High Aspect-Ratio Gold Nanowires with Highly Porous Morphology. *ISRN Nanomater.* **2012**, *2012*, 1–9, DOI: 10.5402/2012/502960.

(57) Burdick, J.; Alonas, E.; Huang, H.-C.; Rege, K.; Wang, J. High-Throughput Templated Multisegment Synthesis of Gold Nanowires and Nanorods. *Nanotechnology* **2009**, *20* (6), 065306, DOI: 10.1088/0957-4484/20/6/065306.

(58) Yoo, S.-H.; Park, S. Platinum-Coated, Nanoporous Gold Nanorod Arrays: Synthesis and Characterization. *Adv. Mater.* **2007**, *19* (12), 1612–1615, DOI: 10.1002/adma.200602551.

(59) Arrigan, D. W. M. Nanoelectrodes, Nanoelectrode Arrays and Their Applications. *Analyst* **2004**, *129* (12), 1157–1165, DOI: 10.1039/b415395m.

(60) Murray, R. W. Nanoelectrochemistry: Metal Nanoparticles, Nanoelectrodes, and Nanopores. *Chem. Rev.* **2008**, *108* (7), 2688–2720, DOI: 10.1021/cr068077e.

(61) Fleischer, M.; Stade, F.; Heeren, A.; Häffner, M.; Braun, K.; Stanciu, C.; Ehlich, R.; Hörber, J. K. H.; Meixner, A. J.; Kern, D. P. Nanocones on Transparent Substrates for Investigations in Scanning Probe Microscopes. *Microelectron. Eng.* **2009**, *86* (4-6), 1219–1221, DOI: 10.1016/j.mee.2008.11.091.

(62) Huttunen, M. J.; Mäkitalo, J.; Kauranen, M. Polarization-Controllable Winged Nanocone Tip Antenna. *J. Nonlinear Opt. Phys. Mater.* **2011**, *20* (04), 415–425, DOI: 10.1142/S0218863511006212.

(63) Fleischer, M.; Weber-Bargioni, A.; Altoe, M. V. P.; Schwartzberg, A. M.; Schuck, P. J.; Cabrini, S.; Kern, D. P. Gold Nanocone Near-Field Scanning Optical Microscopy Probes. *ACS Nano* **2011**, *5* (4), 2570–2579, DOI: 10.1021/nn102199u.

(64) Filip, V.; Filip, L. D.; Okuyama, F. Miniature X-Ray Tubes: Current State and Future Prospects. *J. Instrum.* **2013**, *8* (03), T03005–T03005, DOI: 10.1088/1748-0221/8/03/T03005.

(65) Sugie, H.; Tanemura, M.; Filip, V.; Iwata, K.; Takahashi, K.; Okuyama, F. Carbon Nanotubes as Electron Source in an X-Ray Tube. *Appl. Phys. Lett.* **2001**, *78* (17), 2578–2580, DOI: 10.1063/1.1367278.

(66) Basu, A.; Swanwick, M. E.; Fomani, A. a; Velásquez-García, L. F. A Portable X-Ray Source with a Nanostructured Pt-Coated Silicon Field Emission Cathode for Absorption Imaging of Low-Z Materials. *J. Phys. D. Appl. Phys.* **2015**, *48* (22), 225501, DOI: 10.1088/0022-3727/48/22/225501.

(67) Cheng, S.; Hill, F. A.; Heubel, E. V.; Velasquez-Garcia, L. F. Low-Bremsstrahlung X-Ray Source Using a Low-Voltage High-Current-Density Nanostructured Field Emission Cathode and a Transmission Anode for Markerless Soft Tissue Imaging. *J. Microelectromechanical Syst.* **2014**, *24* (2), 373–382, DOI: 10.1109/JMEMS.2014.2332176.

(68) Booske, J. H. Plasma Physics and Related Challenges of Millimeter-Wave-to-Terahertz and High Power Microwave Generation. *Phys. Plasmas* **2008**, *15* (5), 055502, DOI: 10.1063/1.2838240.

(69) Booske, J. H.; Dobbs, R. J.; Joye, C. D.; Kory, C. L.; Neil, G. R.; Park, G.-S.; Park, J.; Temkin, R. J. Vacuum Electronic High Power Terahertz Sources. *IEEE Trans. Terahertz Sci. Technol.* **2011**, *1* (1), 54–75, DOI: 10.1109/TTHZ.2011.2151610.

(70) Busta, H. H.; Pogemiller, J. E.; Zimmerman, B. J. The Field Emitter Triode as a Displacement/pressure Sensor. *J. Micromechanics Microengineering* **1993**, *3* (2), 49–56, DOI: 10.1088/0960-1317/3/2/003.

(71) Murakami, H.; Hirakawa, M.; Tanaka, C.; Yamakawa, H. Field Emission from Well-Aligned, Patterned, Carbon Nanotube Emitters. *Appl. Phys. Lett.* **2000**, *76* (13), 1776, DOI: 10.1063/1.126164.

(72) Saito, Y. *Carbon Nanotube and Related Field Emitters*; Wiley-VCH Verlag GmbH & Co. KGaA: Weinheim, Germany, **2010**.

(73) Seidel, M.; Zapfe, K. *Vacuum Electronics*; Springer Berlin Heidelberg: Berlin, Heidelberg, **2008**.

(74) Possin, G. E. A Method for Forming Very Small Diameter Wires. *Rev. Sci. Instrum.* **1970**, *41* (5), 772, DOI: 10.1063/1.1684640.

(75) Trautmann, C.; Brüchle, W.; Spohr, R.; Vetter, J.; Angert, N. Pore Geometry of Etched Ion Tracks in Polyimide. *Nucl. Instruments Methods Phys. Res. Sect. B Beam Interact. with Mater. Atoms* **1996**, *111* (1-2), 70–74, DOI: 10.1016/0168-583X(95)01264-8.

(76) Vetter, J.; Spohr, R. Application of Ion Track Membranes for Preparation of Metallic Microstructures. *Nucl. Instruments Methods Phys. Res. Sect. B Beam Interact. with Mater. Atoms* **1993**, *79* (1-4), 691–694, DOI: 10.1016/0168-583X(93)95444-A.

(77) Vetter, J. SEM Investigations of Etched Heavy Ion Tracks. *Scanning* **2008**, *16* (2), 118–122, DOI: 10.1002/sca.4950160209.

(78) Wagner, M. F. P.; Völklein, F.; Reith, H.; Trautmann, C.; Toimil-Molares, M. E. Fabrication and Thermoelectrical Characterization of Three-Dimensional Nanowire Networks. *Phys. status solidi* **2016**, *10*, n/a – n/a, DOI: 10.1002/pssa.201532616.

(79) Movsesyan, L.; Schubert, I.; Yeranyan, L.; Trautmann, C.; Eugenia Toimil-Molares, M. Influence of Electrodeposition Parameters on the Structure and Morphology of ZnO Nanowire Arrays and Networks Synthesized in Etched Ion-Track Membranes. *Semicond. Sci. Technol.* **2016**, *31* (1), 014006, DOI: 10.1088/0268-1242/31/1/014006.

(80) Martin, C. R. Nanomaterials: A Membrane-Based Synthetic Approach. *Science* **1994**, *266* (5193), 1961–1966, DOI: 10.1126/science.266.5193.1961.

(81) Martin, C. R. Membrane-Based Synthesis of Nanomaterials. *Chem. Mater.* **1996**, *8* (8), 1739–1746, DOI: 10.1021/cm960166s.

(82) Hulteen, J. C.; Martin, C. R. A General Template-Based Method for the Preparation of Nanomaterials. *J. Mater. Chem.* **1997**, *7* (7), 1075–1087, DOI: 10.1039/a700027h.

(83) Martin, C. R. Template Synthesis of Electronically Conductive Polymer Nanostructures. *Acc. Chem. Res.* **1995**, *28* (2), 61–68, DOI: 10.1021/ar00050a002.

(84) Furneaux, R. C.; Rigby, W. R.; Davidson, A. P. The Formation of Controlled-Porosity Membranes from Anodically Oxidized Aluminium. *Nature* **1989**, *337* (6203), 147–149, DOI: 10.1038/337147a0.

(85) Masuda, H.; Fukuda, K. Ordered Metal Nanohole Arrays Made by a Two-Step Replication of Honeycomb Structures of Anodic Alumina. *Science (80-.).* **1995**, *268* (June), 1466–1468, DOI: 10.1126/science.268.5216.1466.

(86) Nielsch, K.; Choi, J.; Schwirn, K.; Wehrspohn, R. B.; Gösele, U. Self-Ordering Regimes of Porous Alumina: The 10% Porosity Rule. *Nano Lett.* **2002**, *2* (7), 677–680, DOI: 10.1021/nl025537k.

(87) Poinern, G. E. J.; Ali, N.; Fawcett, D. *Progress in Nano-Engineered Anodic Aluminum Oxide Membrane Development*; **2010**; Vol. 4.

(88) Chakarvarti, S. K.; Vetter, J. Template Synthesis—a Membrane Based Technology for Generation of Nano-/micro Materials: A Review. *Radiat. Meas.* **1998**, *29* (2), 149–159, DOI: 10.1016/S1350-4487(98)00009-2.

(89) Fischer, B. E.; Heiß, M.; Cholewa, M. About the Art to Shoot with Single Ions. *Nucl. Instruments Methods Phys. Res. Sect. B Beam Interact. with Mater. Atoms* **2003**, *210*, 285–291, DOI: 10.1016/S0168-583X(03)01038-3.

(90) Spohr, R.; Zet, C.; Eberhard Fischer, B.; Kiesewetter, H.; Apel, P.; Gunko, I.; Ohgai, T.; Westerberg, L. Controlled Fabrication of Ion Track Nanowires and Channels. *Nucl. Instruments Methods Phys. Res. Sect. B Beam Interact. with Mater. Atoms* **2010**, *268* (6), 676–686, DOI: 10.1016/j.nimb.2009.12.017.

(91) Toimil-Molares, M. E. Characterization and Properties of Micro- and Nanowires of Controlled Size, Composition, and Geometry Fabricated by Electrodeposition and Ion-Track Technology. *Beilstein J. Nanotechnol.* **2012**, *3* (1), 860–883, DOI: 10.3762/bjnano.3.97.

(92) Thurn-Albrecht, T.; Schotter, J.; Kastle, G. A.; Emley, N.; Shibauchi, T.; Krusin-Elbaum, L.; Guarini, K.; Black, C. T.; Tuominen, M. T.; Russell, T. P. Ultrahigh-Density Nanowire Arrays Grown in Self-Assembled Diblock Copolymer Templates. *Science (80-.).* **2000**, *290* (5499), 2126–2129, DOI: 10.1126/science.290.5499.2126.

(93) Siegel, J.; Heitz, J.; Řezníčková, A.; Švorčík, V. Preparation and Characterization of Fully Separated Gold Nanowire Arrays. *Appl. Surf. Sci.* **2013**, *264*, 443–447, DOI: 10.1016/j.apsusc.2012.10.041.

(94) Toma, M.; Loget, G.; Corn, R. M. Fabrication of Broadband Antireflective Plasmonic Gold Nanocone Arrays on Flexible Polymer Films. *Nano Lett.* **2013**, *13* (12), 6164–6169, DOI: 10.1021/nl403496a.

(95) Sergelius, P.; Moreno, J. M. M.; Rahimi, W.; Waleczek, M.; Zierold, R.; Görlitz, D.; Nielsch, K. Electrochemical Synthesis of Highly Ordered Nanowires with a Rectangular Cross Section Using an in-Plane Nanochannel Array. *Nanotechnology* **2014**, *25* (50), 504002, DOI: 10.1088/0957-4484/25/50/504002.

(96) Dawson, K.; Wahl, A.; Murphy, R.; O'Riordan, A. Electroanalysis at Single Gold Nanowire Electrodes. *J. Phys. Chem. C* **2012**, *116*, 14665–14673.

(97) Huczko, A. Template-Based Synthesis of Nanomaterials. *Appl. Phys. A Mater. Sci. Process.* **2000**, *70* (4), 365–376, DOI: 10.1007/s003390051050.

(98) Kim, T.; Kim, J.-H.; Son, S. J.; Seo, S.-M. Gold Nanocones Fabricated by Nanotransfer Printing and Their Application for Field Emission. *Nanotechnology* **2008**, *19* (29), 295302, DOI: 10.1088/0957-4484/19/29/295302.

(99) Vazquez-Mena, O.; Villanueva, G.; Savu, V.; Sidler, K.; van den Boogaart, M. A. F.; Brugger, J. Metallic Nanowires by Full Wafer Stencil Lithography. *Nano Lett.* **2008**, *8* (11), 3675–3682, DOI: 10.1021/nl801778t.

(100) Zhang, P.; He, J.; Ma, X.; Gong, J.; Nie, Z. Ultrasound Assisted Interfacial Synthesis of Gold Nanocones. *Chem. Commun.* **2013**, *49* (10), 987–989, DOI: 10.1039/C2CC37713F.

(101) Fleischer, M.; Weber-Bargioni, A.; Cabrini, S.; Kern, D. P. Fabrication of Metallic Nanocones by Induced Deposition of Etch Masks and Ion Milling. *Microelectron. Eng.* **2011**, *88* (8), 2247–2250, DOI: 10.1016/j.mee.2011.02.090.

(102) Zheng, R. K.; Chan, H. L. W.; Choy, C. L. A Simple Template-Based Hot-Press Method for the Fabrication of Metal and Polymer Nanowires and Nanotubes. *Nanotechnology* **2005**, *16* (9), 1928–1934, DOI: 10.1088/0957-4484/16/9/085.

(103) Spende, A.; Sobel, N.; Lukas, M.; Zierold, R.; Riedl, J. C.; Gura, L.; Schubert, I.; Moreno, J. M. M.; Nielsch, K.; Stühn, B.; et al. TiO 2 , SiO 2 , and Al 2 O 3 Coated Nanopores and Nanotubes Produced by ALD in Etched Ion-Track Membranes for Transport Measurements. *Nanotechnology* **2015**, *26* (33), 335301, DOI: 10.1088/0957-4484/26/33/335301.

(104) Sobel, N.; Hess, C.; Lukas, M.; Spende, A.; Stühn, B.; Toimil-Molares, M. E.; Trautmann, C. Conformal SiO 2 Coating of Sub-100 Nm Diameter Channels of Polycarbonate Etched Ion-Track Channels by Atomic Layer Deposition. *Beilstein J. Nanotechnol.* **2015**, *6* (1), 472–479, DOI: 10.3762/bjnano.6.48.

(105) Yu, S.; Li, N.; Wharton, J.; Martin, C. R. Nano Wheat Fields Prepared by Plasma-Etching Gold Nanowire-Containing Membranes. *Nano Lett.* **2003**, *3* (6), 815–818, DOI: 10.1021/nl0340576.

(106) Chad Harrell, C.; Siwy, Z. S.; Martin, C. R. Conical Nanopore Membranes: Controlling the Nanopore Shape. *Small* **2006**, *2* (2), 194–198, DOI: 10.1002/smll.200500196.

(107) Quednau, S. Galvanisch Erzeugte Mikro- Und Nanodrähte Für Die Gasflusssensorik, Technische Universität Darmstadt, **2015**.

(108) Hottes, M.; Dassinger, F.; Muench, F.; Rauber, M.; Stegmann, C.; Schlaak, H. F.; Ensinger, W. Patterned Arrays of Capped Platinum Nanowires with Quasi-Elastic Mechanical Response to Lateral Force. *Appl. Phys. Lett.* **2015**, *106*, 053109, DOI: 10.1063/1.4907550.

(109) GSI Helmholtzzentrum für Schwerionenforschung GmbH. Universal Linear Accelerator of GSI https://www.gsi.de/en/research/accelerator_facility/linear_accelerator.htm (accessed Sep 14, 2015).

(110) Hellborg, R.; Whitlow, H. J.; Zhang, Y. *Ion Beams in Nanoscience and Technology*; Particle Acceleration and Detection; Springer Berlin Heidelberg: Berlin, Heidelberg, **2010**.

(111) Spohr, R. *Ion Tracks and Microtechnology*; Friedr. Vieweg & Sohn Verlagsgesellschaft mbH: Wiesbaden, **1990**.

(112) Fleischer, R. L.; Price, P. B.; Walker, R. M. *Nuclear Tracks in Solids*; University of California Press, **1975**.

(113) Trautmann, C. Observation and Chemical Treatment of Heavy-Ion Tracks in Polymer. *Nucl. Instruments Methods Phys. Res. B* **1995**, *105*, 81–85.

(114) Dehaye, F.; Balanzat, E.; Ferain, E.; Legras, R. Chemical Modifications Induced in Bisphenol A Polycarbonate by Swift Heavy Ions. *Nucl. Instruments Methods Phys. Res. Sect. B Beam Interact. with Mater. Atoms* **2003**, *209* (September 2015), 103–112, DOI: 10.1016/S0168-583X(02)02048-7.

(115) Zhu, Z.; Jin, Y.; Liu, C.; Sun, Y.; Hou, M.; Zhang, C.; Wang, Z.; Liu, J.; Chen, X.; Li, B.; et al. Chemical Modifications of Polystyrene under Swift Ar Ion Irradiation: A Study of the Energy Loss Effects. *Nucl. Instruments Methods Phys. Res. Sect. B Beam Interact. with Mater. Atoms* **2000**, *169* (1-4), 83–88, DOI: 10.1016/S0168-583X(00)00021-5.

(116) Fink, D. *Fundamental of Ion-Irradiated Polymers*; Springer Berlin Heidelberg, **2004**.

(117) Virk, H. S.; Kaur, S. A.; Randhawa, G. S. Effects on Insulators of Swift-Heavy-Ion Irradiation: Ion-Track Technology. *J. Phys. D. Appl. Phys.* **1998**, *31* (21), 3139–3145, DOI: 10.1088/0022-3727/31/21/020.

(118) Steckenreiter, T.; Balanzat, E.; Fuess, H.; Trautmann, C. Pyrolytic Effects Induced by Energetic Ions in Polymers. *Nucl. Instruments Methods Phys. Res. Sect. B Beam Interact. with Mater. Atoms* **1999**, *151* (1-4), 161–168, DOI: 10.1016/S0168-583X(99)00093-2.

(119) Sun, Y.; Zhu, Z.; Wang, Z.; Jin, Y.; Liu, J.; Hou, M.; Zhang, Q. Swift Heavy Ion Induced Amorphisation and Chemical Modification in Polycarbonate. *Nucl. Instruments Methods Phys. Res. Sect. B Beam Interact. with Mater. Atoms* **2003**, *209* (September 2015), 188–193, DOI: 10.1016/S0168-583X(02)02027-X.

(120) Ziegler, J. F. SRIM http://www.srim.org/ (accessed Feb 16, 2015).

(121) Rauber, M.; Alber, I.; Müller, S.; Neumann, R.; Picht, O.; Roth, C.; Schökel, A.; Toimil-Molares, M. E.; Ensinger, W. Highly-Ordered Supportless Three-Dimensional Nanowire Networks with Tunable Complexity and Interwire Connectivity for Device Integration. *Nano Lett.* **2011**, *11* (6), 2304–2310, DOI: 10.1021/nl2005516.

(122) Cornelius, T. W.; Apel, P. Y.; Schiedt, B.; Trautmann, C.; Toimil-Molares, M. E. M. E.; Karim, S.; Neumann, R. Investigation of Nanopore Evolution in Ion Track-Etched Polycarbonate Membranes. *Nucl. Instruments Methods Phys. Res. B* **2007**, *265* (2), 553–557, DOI: 10.1016/j.nimb.2007.10.004.

(123) Zhu, Z.; Kelley, M. J. IR Spectroscopic Investigation of the Effect of Deep UV Irradiation on PET Films. *Polymer (Guildf).* **2005**, *46* (20), 8883–8891, DOI: 10.1016/j.polymer.2005.05.135.

(124) Ferain, E.; Legras, R. Track-Etch Templates Designed for Micro- and Nanofabrication. *Nucl. Instruments Methods Phys. Res. Sect. B Beam Interact. with Mater. Atoms* **2003**, *208*, 115–122, DOI: 10.1016/S0168-583X(03)00637-2.

(125) Ferain, E.; Legras, R. Heavy Ion Tracks in Polycarbonate. Comparison with a Heavy Ion Irradiated Model Compound (Diphenyl Carbonate). *Nucl. Instruments Methods Phys. Res. Sect. B Beam Interact. with Mater. Atoms* **1993**, *82* (4), 539–548.

(126) Apel, P.; Schulz, A.; Spohr, R.; Trautmann, C.; Vutsadakis, V. Track Size and Track Structure in Polymer Irradiated by Heavy Ions. *Nucl. Instruments Methods Phys. Res. Sect. B Beam Interact. with Mater. Atoms* **1998**, *146* (1-4), 468–474, DOI: 10.1016/S0168-583X(98)00445-5.

(127) Apel, P. Y.; Blonskaya, I. V; Orelovitch, O. L.; Sartowska, B. a; Spohr, R. Asymmetric Ion Track Nanopores for Sensor Technology. Reconstruction of Pore Profile from Conductometric Measurements. *Nanotechnology* **2012**, *23* (22), 225503, DOI: 10.1088/0957-4484/23/22/225503.

(128) Apel, P. Y.; Akimenko, A. P.; Blonskaya, I. V.; Cornelius, T.; Neumann, R.; Schwartz, K.; Spohr, R.; Trautmann, C. Etching of Nanopores in Polycarbonate Irradiated with Swift Heavy Ions at 15K. *Nucl. Instruments Methods Phys. Res. Sect. B Beam Interact. with Mater. Atoms* **2006**, *245* (1), 284–287, DOI: 10.1016/j.nimb.2005.11.164.

(129) Peng, L.; Apel, P. Y.; Maekawa, Y.; Yoshida, M. Conductometric Study of the Radial Track Etch Rate: Free Shape Analysis. *Nucl. Instruments Methods Phys. Res. Sect. B Beam Interact. with Mater. Atoms* **2000**, *168* (4), 527–532, DOI: 10.1016/S0168-583X(00)00052-5.

(130) Apel, P. Y.; Blonskaya, I. .; Oganessian, V. .; Orelovitch, O. .; Trautmann, C. Morphology of Latent and Etched Heavy Ion Tracks in Radiation Resistant Polymers Polyimide and Poly(ethylene Naphthalate). *Nucl. Instruments Methods Phys. Res. Sect. B Beam Interact. with Mater. Atoms* **2001**, *185* (1-4), 216–221, DOI: 10.1016/S0168-583X(01)00967-3.

(131) Apel, P. Y.; Blonskaya, I. V; Dmitriev, S. N.; Orelovitch, O. L.; Sartowska, B. a. Structure of Polycarbonate Track-Etch Membranes: Origin of the "paradoxical" Pore Shape. *J. Memb. Sci.* **2006**, *282* (1-2), 393–400, DOI: 10.1016/j.memsci.2006.05.045.

(132) Zhu, Z.; Maekawa, Y.; Liu, Q.; Yoshida, M. Influence of UV Light Illumination on Latent Track Structure in PET. *Nucl. Instruments Methods Phys. Res. Sect. B Beam Interact. with Mater. Atoms* **2005**, *236* (1-4), 61–67, DOI: 10.1016/j.nimb.2005.03.251.

(133) Sertova, N.; Balanzat, E.; Toulemonde, M.; Trautmann, C. Investigation of Initial Stage of Chemical Etching of Ion Tracks in Polycarbonate. *Nucl. Instruments Methods Phys. Res. Sect. B Beam Interact. with Mater. Atoms* **2009**, *267* (6), 1039–1044, DOI: 10.1016/j.nimb.2009.02.045.

(134) Picht, O.; Müller, S.; Alber, I.; Rauber, M.; Lensch-Falk, J.; Medlin, D. L.; Neumann, R.; Toimil-Molares, M. E. Tuning the Geometrical and Crystallographic Characteristics of Bi 2 Te 3 Nanowires by Electrodeposition in Ion-Track Membranes. *J. Phys. Chem. C* **2012**, *116* (9), 5367–5375, DOI: 10.1021/jp210491g.

(135) Siwy, Z.; Gu, Y.; Spohr, H. A.; Baur, D.; Wolf-Reber, A.; Spohr, R.; Apel, P.; Korchev, Y. E. Rectification and Voltage Gating of Ion Currents in a Nanofabricated Pore. *Europhys. Lett.* **2002**, *60* (3), 349–355, DOI: 10.1209/epl/i2002-00271-3.

(136) Schlesinger, M.; Paunovic, M. *Modern Electroplating*; John Wiley & Sons, Inc., **2010**.

(137) Kohl, P. a. Electrodeposition of Gold. In *Modern Electroplating*; John Wiley & Sons, Inc.: Hoboken, NJ, USA, **2011**; pp 115–130.

(138) Nollet, L. M. L.; De Gelder, L. S. P. *Handbook of Water Analysis*, Third Edit.; CRC. Press, **2014**.

(139) Dimitrijević, S.; Rajčić-Vujasinović, M.; Trujić, V. Non-Cyanide Electrolytes for Gold Plating - a Review. *Int. J. Electrochem. Sci.* **2013**, *8* (5), 6620–6646.

(140) Plieth, W. *Electrochemistry for Materials Science*, First Edit.; Elsevier, **2008**.

(141) Institute of Experimental Mineralogy; Russian Academy of Sciences. WWW-MINCRYST http://database.iem.ac.ru/mincryst/ (accessed Apr 1, 2015).

(142) Burr, L.; Schubert, I.; Sigle, W.; Trautmann, C.; Toimil-Molares, M. E. Surface Enrichment in Au–Ag Alloy Nanowires and Investigation of the Dealloying Process. *J. Phys. Chem. C* **2015**, *119* (36), 20949–20956, DOI: 10.1021/acs.jpcc.5b05596.

(143) Schubert, I.; Burr, L.; Trautmann, C.; Toimil-Molares, M. E. Growth and Morphological Analysis of Segmented AuAg Alloy Nanowires Created by Pulsed Electrodeposition in Ion-Track Etched Membranes. *Beilstein J. Nanotechnol.* **2015**, *6*, 1272–1280, DOI: 10.3762/bjnano.6.131.

(144) Rouquerol, J.; Avnir, D.; Fairbridge, C. W.; Everett, D. H.; Haynes, J. M.; Pernicone, N.; Ramsay, J. D. F.; Sing, K. S. W.; Unger, K. K. Recommendations for the Characterization of Porous Solids. *Pure Appl. Chem.* **1994**, *66* (8), 1739–1758, DOI: 10.1351/pac199466081739.

(145) Lu, G. Q.; Zhao, X. S.; Wei, T. K. *Nanoporous Materials: Science and Engineering*; **2004**; Vol. 4.

(146) Ding, Y.; Erlebacher, J. Nanoporous Metals with Controlled Multimodal Pore Size Distribution. *J. Am. Chem. Soc.* **2003**, *125* (26), 7772–7773, DOI: 10.1021/ja035318g.

(147) Zhang, Z.; Zhang, C.; Gao, Y.; Frenzel, J.; Sun, J.; Eggeler, G. Dealloying Strategy to Fabricate Ultrafine Nanoporous Gold-Based Alloys with High Structural Stability and Tunable Magnetic Properties. *CrystEngComm* **2012**, *14* (23), 8292, DOI: 10.1039/c2ce26187a.

(148) Sun, L.; Chien, C. L.; Searson, P. C. Fabrication of Nanoporous Nickel by Electrochemical Dealloying. *Chem. Mater.* **2004**, *16* (16), 3125–3129, DOI: 10.1021/cm0497881.

(149) Forty, a. J.; Durkin, P. A Micromorphological Study of the Dissolution of Silver-Gold Alloys in Nitric Acid. *Philos. Mag. A* **1980**, *42* (3), 295–318, DOI: 10.1080/01418618008239360.

(150) Pickering, H. W.; Wagner, C. Electrolytic Dissolution of Binary Alloys Containing a Noble Metal. *J. Electrochem. Soc.* **1967**, *114* (7), 698, DOI: 10.1149/1.2426709.

(151) Erlebacher, J. An Atomistic Description of Dealloying. *J. Electrochem. Soc.* **2004**, *151* (10), C614, DOI: 10.1149/1.1784820.

(152) Alonso, C.; Salvarezza, R. C.; Vara, J. M.; Arvia, A. J. The Surface Diffusion of Gold Atoms on Gold Electrodes in Acid Solution and Its Dependence on the Presence of Foreign Adsorbates. *Electrochimica Acta*, **1990**, *35*, 1331–1336.

(153) Artymowicz, D. M.; Erlebacher, J.; Newman, R. C. Relationship between the Parting Limit for de-Alloying and a Particular Geometric High-Density Site Percolation Threshold. *Philos. Mag.* **2009**, *89* (21), 1663–1693, DOI: 10.1080/14786430903025708.

(154) Zhang, Z.; Wang, Y.; Wang, Y.; Wang, X.; Qi, Z.; Ji, H.; Zhao, C. Formation of Ultrafine Nanoporous Gold Related to Surface Diffusion of Gold Adatoms during Dealloying of Al2Au in an Alkaline Solution. *Scr. Mater.* **2010**, *62* (3), 137–140, DOI: 10.1016/j.scriptamat.2009.10.018.

(155) Qian, L. H.; Chen, M. W. Ultrafine Nanoporous Gold by Low-Temperature Dealloying and Kinetics of Nanopore Formation. *Appl. Phys. Lett.* **2007**, *91* (2007), 89–92, DOI: 10.1063/1.2773757.

(156) Laocharoensuk, R.; Sattayasamitsathit, S.; Burdick, J.; Kanatharana, P.; Thavarungkul, P.; Wang, J. Shape-Tailored Porous Gold Nanowires: From Nano Barbells to Nano Step- Cones. *ACS Nano* **2007**, *1* (5), 403–408, DOI: 10.1021/nn700255x.

(157) Hsieh, Y.-T.; Sun, I.-W. One-Step Electrochemical Fabrication of Nanoporous Gold Wire Arrays from Ionic Liquid. *Chem. Commun. (Camb).* **2014**, *50* (2), 246–248, DOI: 10.1039/c3cc46061d.

(158) Gu, X.; Xu, L.; Tian, F.; Ding, Y. Au-Ag Alloy Nanoporous Nanotubes. *Nano Res.* **2010**, *2* (5), 386–393, DOI: 10.1007/s12274-009-9038-3.

(159) Sehayek, T.; Lahav, M.; Popovitz-Biro, R.; Vaskevich, A.; Rubinstein, I. Template Synthesis of Nanotubes by Room-Temperature Coalescence of Metal Nanoparticles. *Chem. Mater.* **2005**, *17* (14), 3743–3748, DOI: 10.1021/cm0501057.

(160) Lahav, M.; Sehayek, T.; Vaskevich, A.; Rubinstein, I. Nanoparticle Nanotubes. *Angew. Chem. Int. Ed. Engl.* **2003**, *42* (45), 5575–5579, DOI: 10.1002/anie.200352216.

(161) Seker, E.; Reed, M. L.; Begley, M. R. Nanoporous Gold: Fabrication, Characterization, and Applications. *Materials (Basel).* **2009**, *2* (4), 2188–2215, DOI: 10.3390/ma2042188.

(162) Slater, T. J. a; Macedo, A.; Schroeder, S. L. M.; Burke, M. G.; O'Brien, P.; Camargo, P. H. C.; Haigh, S. J. Correlating Catalytic Activity of Ag-Au Nanoparticles with 3D Compositional Variations. *Nano Lett.* **2014**, *14* (4), 1921–1926, DOI: 10.1021/nl4047448.

(163) Li, X.; Chen, Q.; McCue, I.; Snyder, J.; Crozier, P.; Erlebacher, J.; Sieradzki, K. Dealloying of Noble-Metal Alloy Nanoparticles. *Nano Lett.* **2014**, *14* (5), 2569–2577, DOI: 10.1021/nl500377g.

(164) Belić, D.; Chantry, R. L.; Li, Z. Y.; Brown, S. a. Ag-Au Nanoclusters: Structure and Phase Segregation. *Appl. Phys. Lett.* **2011**, *99* (17), 171914, DOI: 10.1063/1.3656244.

(165) Sieradzki, K.; Corderman, R. R.; Shukla, K.; Newman, R. C. Computer Simulations of Corrosion: Selective Dissolution of Binary Alloys. *Philos. Mag. A* **1989**, *59* (4), 713–746, DOI: 10.1080/01418618908209817.

(166) Karim, S. Fabrication and Characterization of Gold Nanowires, Philipps-Universität Marburg, **2007**.

(167) Karim, S.; Toimil-Molares, M. E.; Ensinger, W.; Balogh, a G.; Cornelius, T. W.; Khan, E. U.; Neumann, R. Influence of Crystallinity on the Rayleigh Instability of Gold Nanowires. *J. Phys. D. Appl. Phys.* **2007**, *40* (12), 3767–3770, DOI: 10.1088/0022-3727/40/12/031.

(168) Karim, S.; Toimil-Molares, M. E.; Maurer, F.; Miehe, G.; Ensinger, W.; Liu, J.; Cornelius, T. W.; Neumann, R. Synthesis of Gold Nanowires with Controlled Crystallographic Characteristics. *Appl. Phys. A Mater. Sci. Process.* **2006**, *84* (4), 403–407, DOI: 10.1007/s00339-006-3645-6.

(169) Dyzynski, M.; Burr, L.; Trautmann, C.; Schubert, I. Synthesis of AuxAg1−x Nanowire-Networks with Controlled Composition and Defined Wire Diameter. *GSI Sci. Rep.* **2014**.

(170) Liu, J.; Duan, J. L.; Toimil-Molares, E.; Karim, S.; Cornelius, T. W.; Dobrev, D.; Yao, H. J.; Sun, Y. M.; Hou, M. D.; Mo, D.; et al. Electrochemical Fabrication of Single-Crystalline and Polycrystalline Au Nanowires: The Influence of Deposition Parameters. *Nanotechnology* **2006**, *1922* (8), 1922–1926, DOI: 10.1088/0957-4484/17/8/020.

(171) Burr, L.; Alber, I.; Trautmann, C. Thermal Instability of Porous Gold Nanowires. *GSI Sci. Rep.* **2012**, 417.

(172) Alber, I.; Sigle, W.; Demming-Janssen, F.; Neumann, R.; Trautmann, C.; van Aken, P. A.; Toimil-Molares, M. E. Multipole Surface Plasmon Resonances in Conductively Coupled Metal Nanowire Dimers. *ACS Nano* **2012**, *6* (11), 9711–9717, DOI: 10.1021/nn303149p.

(173) Alber, I.; Sigle, W.; Müller, S.; Neumann, R.; Picht, O.; Rauber, M.; van Aken, P. a; Toimil-Molares, M. E. Visualization of Multipolar Longitudinal and Transversal Surface Plasmon Modes in Nanowire Dimers. *ACS Nano* **2011**, *5* (12), 9845–9853, DOI: 10.1021/nn2035044.

(174) Schlesinger, M. Electroless and Electrodeposition of Silver. *Mod. Electroplat. Fifth Ed.* **2011**, 131–138, DOI: 10.1002/9780470602638.ch5.

(175) Arthur, D. Mac. A Study of Gold Reduction and Oxidation in Aqueous Solutions. *J. Electrochem. Soc.* **1972**, No. 100 ml, 672–677.

(176) Cheh, H. Y. Electrodeposition of Gold by Pulsed Current. *J. Electrochem. Soc.* **1971**, *118* (4), 551, DOI: 10.1149/1.2408110.

(177) Sawaguchi, T.; Yamada, T.; Okinaka, Y.; Itaya, K. Electrochemical Scanning Tunneling Microscopy and Ultrahigh-Vacuum Investigation of Gold Cyanide Adlayers on Au(111) Formed in Aqueous Solution. *J. Phys. Chem.* **1995**, *99*, 14149–14155, DOI: 10.1021/j100038a056.

(178) Matsuda, H.; Ayabe, Y. Zur Theorie Der Randles-Sevcikschen Kathodenstrahl-Polarographie. *Zeitschrift für Elektrochemie* **1955**, *59* (6), 494–503.

(179) Nicholson, R. S. Theory and Application of Cyclic Voltammetry for Measurement of Electrode Reaction Kinetics. *Anal. Chem.* **1965**, *37* (11), 1351–1355, DOI: 10.1021/ac60230a016.

(180) Tokuda, K.; Morita, K.; Shimizu, Y. Cyclic Voltammetry at Microhole. **1989**, No. 4, 1763–1768.

(181) Ito, T.; Audi, A. a; Dible, G. P. Electrochemical Characterization of Recessed Nanodisk-Array Electrodes Prepared from Track-Etched Membranes. *Anal. Chem.* **2006**, *78* (19), 7048–7053, DOI: 10.1021/ac061043m.

(182) Dumitrescu, I.; Unwin, P. R.; Wilson, N. R.; Macpherson, J. V. Single-Walled Carbon Nanotube Network Ultramicroelectrodes. *Anal. Chem.* **2008**, *80* (10), 3598–3605, DOI: 10.1021/ac702518g.

(183) Lavacchi, A.; Bardi, U.; Borri, C.; Caporali, S.; Fossati, A.; Perissi, I. Cyclic Voltammetry Simulation at Microelectrode Arrays with COMSOL Multiphysics. *J. Appl. Electrochem.* **2009**, *39* (11), 2159–2163, DOI: 10.1007/s10800-009-9797-2.

(184) Toimil-Molares, M. E.; Chtanko, N.; Cornelius, T. W.; Dobrev, D.; Enculescu, I.; Blick, R. H.; Neumann, R. Fabrication and Contacting of Single Bi Nanowires. *Nanotechnology* **2004**, *15* (4), S201–S207, DOI: 10.1088/0957-4484/15/4/015.

(185) Müller, S.; Schötz, C.; Picht, O. Electrochemical Synthesis of Bi1–x Sb X Nanowires with Simultaneous Control on Size, Composition, and Surface Roughness. *Cryst. Growth Des.* **2012**, *12*, 615–621.

(186) Picht, O. Growth and Characterization of Bismuth Telluride Nanowires, Ruperto-Carola University Heidelberg, **2010**.

(187) Lupu, N. *Electrodeposited Nanowires and Their Applications*; InTech, **2010**.

(188) Liu, Z. Magnetic Nanotubes and Nanoporous Gold Nanowire Sensors, The Johns Hopkins University, Baltimore, Maryland, **2008**.

(189) Parida, S.; Kramer, D.; Volkert, C. A.; Rösner, H.; Erlebacher, J.; Weissmüller, J. Volume Change during the Formation of Nanoporous Gold by Dealloying. *Phys. Rev. Lett.* **2006**, *97* (3), 035504, DOI: 10.1103/PhysRevLett.97.035504.

(190) Ding, Y.; Kim, Y.-J.; Erlebacher, J. Nanoporous Gold Leaf: "Ancient Technology"/Advanced Material. *Adv. Mater.* **2004**, *16* (21), 1897–1900, DOI: 10.1002/adma.200400792.

(191) Zhang, Z.; Wang, Y.; Qi, Z.; Lin, J.; Bian, X. Nanoporous Gold Ribbons with Bimodal Channel Size Distributions by Chemical Dealloying of Al−Au Alloys. *J. Phys. Chem. C* **2009**, *113* (4), 1308–1314, DOI: 10.1021/jp808569g.

(192) Siwy, Z. S. Ion-Current Rectification in Nanopores and Nanotubes with Broken Symmetry. *Adv. Funct. Mater.* **2006**, *16* (6), 735–746, DOI: 10.1002/adfm.200500471.

(193) Wei, L.; Qi, W.; Huang, B.; Wang, M. Surface Segregation of Au–Ag Bimetallic Nanowires. *Comput. Mater. Sci.* **2013**, *69*, 374–380, DOI: 10.1016/j.commatsci.2012.11.038.

(194) Tyson, W. R.; Miller, W. A. Surface Free Energies of Solid Metals: Estimation from Liquid Surface Tension Measurements. *Surf. Sci.* **1977**, *62* (1), 267–276, DOI: 10.1016/0039-6028(77)90442-3.

(195) Bozzolo, G.; Garcés, J. E.; Derry, G. N. Atomistic Modeling of Segregation and Bulk Ordering in Ag-Au Alloys. *Surf. Sci.* **2007**, *601* (9), 2038–2046, DOI: 10.1016/j.susc.2007.02.035.

(196) Kojda, D.; Mitdank, R.; Handwerg, M.; Mogilatenko, A.; Albrecht, M.; Wang, Z.; Ruhhammer, J.; Kroener, M.; Woias, P.; Fischer, S. F. Temperature-Dependent Thermoelectric Properties of Individual Silver Nanowires. *Phys. Rev. B* **2015**, *91* (2), 024302, DOI: 10.1103/PhysRevB.91.024302.

(197) Song, T.-B.; Rim, Y. S.; Liu, F.; Bob, B.; Ye, S.; Hsieh, Y.-T.; Yang, Y. Highly Robust Silver Nanowire Network for Transparent Electrode. *ACS Appl. Mater. Interfaces* **2015**, *7* (44), 24601–24607, DOI: 10.1021/acsami.5b06540.

(198) Elechiguerra, J. L.; Larios-Lopez, L.; Liu, C.; Garcia-Gutierrez, D.; Camacho-Bragado, A.; Yacaman, M. J. Corrosion at the Nanoscale: The Case of Silver Nanowires and Nanoparticles. *Chem. Mater.* **2005**, *17* (24), 6042–6052, DOI: 10.1021/cm051532n.

(199) Hosseinzadeh Khaligh, H.; Liew, K.; Han, Y.; Abukhdeir, N. M.; Goldthorpe, I. a. Silver Nanowire Transparent Electrodes for Liquid Crystal-Based Smart Windows. *Sol. Energy Mater. Sol. Cells* **2015**, *132*, 337–341, DOI: 10.1016/j.solmat.2014.09.006.

(200) Ye, S.; Rathmell, A. R.; Chen, Z.; Stewart, I. E.; Wiley, B. J. Metal Nanowire Networks: The Next Generation of Transparent Conductors. *Adv. Mater.* **2014**, n/a – n/a, DOI: 10.1002/adma.201402710.

(201) Virkar, A.; Li, Y.; Lemieux, M. Metal Nanowire Networks and Transparent Conductive Material, 2012.

(202) Garnett, E. C.; Cai, W.; Cha, J. J.; Mahmood, F.; Connor, S. T.; Greyson Christoforo, M.; Cui, Y.; McGehee, M. D.; Brongersma, M. L. Self-Limited Plasmonic Welding of Silver Nanowire Junctions. *Nat. Mater.* **2012**, *11* (3), 241–249, DOI: 10.1038/nmat3238.

(203) Cui, Y.; Wei, Q.; Park, H.; Lieber, C. M. Nanowire Nanosensors for Highly Sensitive and Selective Detection of Biological and Chemical Species. *Science* **2001**, *293* (5533), 1289–1292, DOI: 10.1126/science.1062711.

(204) Dawson, K.; O'Riordan, a. Towards Nanowire (Bio) Sensors. *J. Phys. Conf. Ser.* **2011**, *307*, 012004, DOI: 10.1088/1742-6596/307/1/012004.

(205) Xing, W.; Hu, J.; Kung, S.; Donavan, K. C.; Yan, W.; Wu, R.; Penner, R. M. A Chemically-Responsive Nanojunction within a Silver Nanowire. *Nano Lett.* **2012**, *12* (3), 1729–1735, DOI: 10.1021/nl300427w.

(206) Karim, S.; Maaz, K.; Ali, G.; Ensinger, W. Diameter Dependent Failure Current Density of Gold Nanowires. *J. Phys. D. Appl. Phys.* **2009**, *42* (18), 185403, DOI: 10.1088/0022-3727/42/18/185403.

(207) Roy, A.; Pandey, T.; Ravishankar, N.; Singh, A. K. Semiconductor-like Sensitivity in Metallic Ultrathin Gold Nanowire- Based Sensors. *J. Phys. Chem. C* **2014**, 18676–18682, DOI: 10.1021/jp5042052.

(208) Minh Vuong, N.; Kim, D.; Kim, H. Porous Au-Embedded WO3 Nanowire Structure for Efficient Detection of CH4 and H2S. *Sci. Rep.* **2015**, *5* (April), 11040, DOI: 10.1038/srep11040.

(209) Eibl, O.; Nielsch, K.; Peranio, N.; Völklein, F. *Thermoelectric Bi2Te3 Nanomaterials*; Wiley-VCH Verlag GmbH & Co. KGaA, **2015**.

(210) Voelklein, F.; C, M.; Reith, H.; Huzel, D. Characterization and Application of Thermoelectric Nanowires. In *Nanowires - Implementations and Applications*; InTech, **2011**.

(211) Bäßler, S. SPP 1386 Doktorandenworkshop, **2013**.

(212) Karim, S.; Ensinger, W.; Cornelius, T. W.; Neumann, R. Investigation of Size Effects in the Electrical Resistivity of Single Electrochemically Fabricated Gold Nanowires. *Phys. E Low-dimensional Syst. Nanostructures* **2008**, *40* (10), 3173–3178, DOI: 10.1016/j.physe.2008.05.011.

(213) Aherne, D.; Satti, A.; Fitzmaurice, D. Diameter-Dependent Evolution of Failure Current Density of Highly Conducting DNA-Templated Gold Nanowires. *Nanotechnology* **2007**, *18* (12), 125205, DOI: 10.1088/0957-4484/18/12/125205.

(214) Pérez-Mitta, G.; Burr, L.; Tuninetti, J. S.; Trautmann, C.; Toimil-Molares, M. E.; Azzaroni, O. Noncovalent Functionalization of Solid-State Nanopores via Self-Assembly of Amphipols. *Nanoscale* **2016**, *8* (3), 1470–1478, DOI: 10.1039/C5NR08190D.

(215) Burr, L.; Serbun, P.; Reimuth, C.; Heider, B.; Krieg, J.; Spende, A.; Movsesyan, L.; Schubert, I.; Trautmann, C.; Toimil-Molares, M. E. Vertically Aligned Freestanding Gold Nanocone Arrays. *Prep.* **2016**.

(216) Liu, K.; Jiang, L. Bio-Inspired Self-Cleaning Surfaces. *Annu. Rev. Mater. Res.* **2012**, *42* (1), 231–263, DOI: 10.1146/annurev-matsci-070511-155046.

(217) Law, J. B. K.; Ng, A. M. H.; He, A. Y.; Low, H. Y. Bioinspired Ultrahigh Water Pinning Nanostructures. *Langmuir* **2014**, *30* (1), 325–331, DOI: 10.1021/la4034996.

(218) Jeong, S.; Garnett, E. C.; Wang, S.; Yu, Z.; Fan, S.; Brongersma, M. L.; McGehee, M. D.; Cui, Y. Hybrid Silicon Nanocone-Polymer Solar Cells. *Nano Lett.* **2012**, DOI: 10.1021/nl300713x.

(219) De Angelis, F.; Gentile, F.; Mecarini, F.; Das, G.; Moretti, M.; Candeloro, P.; Coluccio, M. L.; Cojoc, G.; Accardo, a.; Liberale, C.; et al. Breaking the Diffusion Limit with Super-Hydrophobic Delivery of Molecules to Plasmonic Nanofocusing SERS Structures. *Nat. Photonics* **2011**, *5* (11), 682–687, DOI: 10.1038/nphoton.2011.222.

(220) Chang, W.-Y.; Lin, K.-H.; Wu, J.-T.; Yang, S.-Y.; Lee, K.-L.; Wei, P.-K. Novel Fabrication of an Au Nanocone Array on Polycarbonate for High Performance Surface-Enhanced Raman Scattering. *J. Micromechanics Microengineering* **2011**, *21* (3), 035023, DOI: 10.1088/0960-1317/21/3/035023.

(221) Fleischer, M.; Stanciu, C.; Stade, F.; Stadler, J.; Braun, K.; Heeren, A.; Häffner, M.; Kern, D. P.; Meixner, a. J. Three-Dimensional Optical Antennas: Nanocones in an Apertureless Scanning near-Field Microscope. *Appl. Phys. Lett.* **2008**, *93* (11), 111114, DOI: 10.1063/1.2987485.

(222) Shen, X.-P.; Liu, H.-J.; Fan, X.; Jiang, Y.; Hong, J.-M.; Xu, Z. Construction and Photoluminescence of In2O3 Nanotube Array by CVD-Template Method. *J. Cryst. Growth* **2005**, *276* (3-4), 471–477, DOI: 10.1016/j.jcrysgro.2004.11.394.

(223) Mohammadi, A.; Kaminski, F.; Sandoghdar, V.; Agio, M. Fluorescence Enhancement with the Optical (Bi-) Conical Antenna. *J. Phys. Chem. C* **2010**, *114* (16), 7372–7377, DOI: 10.1021/jp9094084.

(224) Zeeb, B.; Jäger, S.; Schäfer, C.; Nill, P.; Meixner, a. J.; Kern, D. P.; Fleischer, M. Self-Aligned Gold Nanocone Probe Tips. *J. Vac. Sci. Technol. B Microelectron. Nanom. Struct.* **2010**, *28* (6), C6O34, DOI: 10.1116/1.3518461.

(225) Krieg, J. *Fabrication and Characterization of Arrays of Conical Metal Nanowires*; **2010**.

(226) Martin, C. R.; Nishizawa, M.; Jirage, K.; Kang, M.; Lee, S. B. Controlling Ion-Transport Selectivity in Gold Nanotubule Membranes. *Adv. Mater.* **2001**, *13* (18), 1351–1362, DOI: 10.1002/1521-4095(200109)13:18<1351::AID-ADMA1351>3.0.CO;2-W.

(227) Eijkel, J. C. T.; Berg, A. van den. Nanofluidics: What Is It and What Can We Expect from It? *Microfluid. Nanofluidics* **2005**, *1* (3), 249–267, DOI: 10.1007/s10404-004-0012-9.

(228) Wen, L.; Hou, X.; Tian, Y.; Nie, F.-Q.; Song, Y.; Zhai, J.; Jiang, L. Bioinspired Smart Gating of Nanochannels Toward Photoelectric-Conversion Systems. *Adv. Mater.* **2010**, *22* (9), 1021–1024, DOI: 10.1002/adma.200903161.

(229) Guo, W.; Tian, Y.; Jiang, L. Asymmetric Ion Transport through Ion-Channel-Mimetic Solid-State Nanopores. *Acc. Chem. Res.* **2013**, *46* (12), 2834–2846, DOI: 10.1021/ar400024p.

(230) Siwy, Z.; Trofin, L.; Kohli, P.; Baker, L. A.; Trautmann, C.; Martin, C. R. Protein Biosensors Based on Biofunctionalized Conical Gold Nanotubes. *J. Am. Chem. Soc.* **2005**, *127* (14), 5000–5001, DOI: 10.1021/ja043910f.

(231) Vlassiouk, I.; Kozel, T. R.; Siwy, Z. S. Biosensing with Nanofluidic Diodes. *J. Am. Chem. Soc.* **2009**, *131* (23), 8211–8220, DOI: 10.1021/ja901120f.

(232) Siwy, Z.; Apel, P.; Dobrev, D.; Neumann, R.; Spohr, R.; Trautmann, C.; Voss, K. Ion Transport through Asymmetric Nanopores Prepared by Ion Track Etching. *Nucl. Instruments Methods Phys. Res. Sect. B Beam Interact. with Mater. Atoms* **2003**, *208* (1-4), 143–148, DOI: 10.1016/S0168-583X(03)00884-X.

(233) Siwy, Z.; Apel, P.; Baur, D.; Dobrev, D. D.; Korchev, Y. E.; Neumann, R.; Spohr, R.; Trautmann, C.; Voss, K.-O. Preparation of Synthetic Nanopores with Transport Properties Analogous to Biological Channels. *Surf. Sci.* **2003**, *532-535*, 1061–1066, DOI: 10.1016/S0039-6028(03)00448-5.

(234) Ali, M. Functionalization and Application of Ion Track-Etched Nanochannels in Polymer Membranes, Technischen Universität Darmstadt, **2009**.

(235) Apel, P. Swift Ion Effects in Polymers: Industrial Applications. *Nucl. Instruments Methods Phys. Res. Sect. B Beam Interact. with Mater. Atoms* **2003**, *208* (1-4), 11–20, DOI: 10.1016/S0168-583X(03)00634-7.

(236) Schiedt, B. Characterization and Application of Ion Track-Etched Nanopores, University of Heidelberg, **2007**.

(237) Apel, P. Y.; Ramirez, P.; Blonskaya, I. V; Orelovitch, O. L.; Sartowska, B. a. Accurate Characterization of Single Track-Etched, Conical Nanopores. *Phys. Chem. Chem. Phys.* **2014**, *16* (29), 15214, DOI: 10.1039/c4cp01686f.

(238) Alber, I.; Krieg, J.; Müller, C.; Toimil-Molares, M.; Trautmann, C.; Serbun, P.; Jordan, F.; Navitski, A.; Muller, G. Freestanding Copper Nanocones for Field Emission by Ion-Track Technology and Electrodeposition. *Vac. Nanoelectron. Conf.* **2011**, 75–76.

(239) Apel, P. Y.; Blonskaya, I. V.; Dmitriev, S. N.; Orelovich, O. L.; Sartowska, B. a. Ion Track Symmetric and Asymmetric Nanopores in Polyethylene Terephthalate Foils for Versatile Applications. *Nucl. Instruments Methods Phys. Res. Sect. B Beam Interact. with Mater. Atoms* **2015**, 6–10, DOI: 10.1016/j.nimb.2015.07.016.

(240) Movsesyan, L. Synthesis and Characterization of ZnO Nanowires and 3D Nanowire Networks, Technische Universität Darmstadt, **2016**.

(241) Enculescu, I.; Siwy, Z.; Dobrev, D.; Trautmann, C.; Toimil Molares, M. E.; Neumann, R.; Hjort, K.; Westerberg, L.; Spohr, R. Copper Nanowires Electrodeposited in Etched Single-Ion Track Templates. *Appl. Phys. A Mater. Sci. Process.* **2003**, *77* (6), 751–755, DOI: 10.1007/s00339-003-2216-3.

(242) Spende, A. Surface Modification of Etched Ion-Track Polymer Membranes by Atomic Layer Deposition, Technische Universität Darmstadt, **2016**.

(243) Keith B.Oldham, Jan C.Myland, A. M. B. *Electrochemical Science and Technology Fundamentals and Applications*; **2012**.

(244) Fowler, R. H.; Nordheim, L. Electron Emission in Intense Electric Fields. *Proc. R. Soc. A Math. Phys. Eng. Sci.* **1928**, *119* (781), 173–181, DOI: 10.1098/rspa.1928.0091.

(245) Forsey, G. *Field Emission in Vacuum Microelectronics*; Microdevices; Springer US: Boston, MA, **2005**.

(246) Spindt, C. A.; Brodie, I.; Humphrey, L.; Westerberg, E. R. Physical Properties of Thin-film Field Emission Cathodes with Molybdenum Cones. *J. Appl. Phys.* **1976**, *47* (12), 5248–5263, DOI: 10.1063/1.322600.

(247) Fang, X.; Bando, Y.; Gautam, U. K.; Ye, C.; Golberg, D. Inorganic Semiconductor Nanostructures and Their Field-Emission Applications. *J. Mater. Chem.* **2008**, *18* (5), 509–522, DOI: 10.1039/B712874F.

(248) Iijima, S. Helical Microtubules of Graphitic Carbon. *Nature* **1991**, *354* (6348), 56–58, DOI: 10.1038/354056a0.

(249) Nilsson, L.; Groening, O.; Emmenegger, C.; Kuettel, O.; Schaller, E.; Schlapbach, L.; Kind, H.; Bonard, J.-M.; Kern, K. Scanning Field Emission from Patterned Carbon Nanotube Films. *Appl. Phys. Lett.* **2000**, *76* (15), 2071, DOI: 10.1063/1.126258.

(250) Bonard, J.-M.; Weiss, N.; Kind, H.; Stöckli, T.; Forró, L.; Kern, K.; Châtelain, A. Tuning the Field Emission Properties of Patterned Carbon Nanotube Films. *Adv. Mater.* **2001**, *13* (3), 184–188, DOI: 10.1002/1521-4095(200102)13:3<184::AID-ADMA184>3.0.CO;2-I.

(251) Bonard, J.-M.; Klinke, C.; Dean, K. a.; Coll, B. F. Degradation and Failure of Carbon Nanotube Field Emitters. *Phys. Rev. B* **2003**, *67* (11), 115406, DOI: 10.1103/PhysRevB.67.115406.

(252) Dams, F.; Navitski, A.; Prommesberger, C.; Serbun, P.; Langer, C.; Muller, G.; Schreiner, R. Homogeneous Field Emission Cathodes With Precisely Adjustable Geometry Fabricated by Silicon Technology. *IEEE Trans. Electron Devices* **2012**, *59* (10), 2832–2837, DOI: 10.1109/TED.2012.2206598.

(253) Serbun, P.; Bornmann, B.; Navitski, A.; Müller, G.; Prommesberger, C.; Langer, C.; Dams, F.; Schreiner, R. Stable Field Emission of Single B-Doped Si Tips and Linear Current Scaling of Uniform Tip Arrays for Integrated Vacuum Microelectronic Devices. *J. Vac. Sci. Technol. B Microelectron. Nanom. Struct.* **2013**, *31* (2), 02B101, DOI: 10.1116/1.4765088.

(254) Choueib, M.; Martel, R.; Cojocaru, C. S.; Ayari, A.; Vincent, P.; Purcell, S. T. Current Saturation in Field Emission from H-Passivated Si Nanowires. *ACS Nano* **2012**, *6* (8), 7463–7471, DOI: 10.1021/nn302744e.

(255) Vila, L.; Vincent, P.; Dauginet-De Pra, L.; Pirio, G.; Minoux, E.; Gangloff, L.; Demoustier-Champagne, S.; Sarazin, N.; Ferain, E.; Legras, R.; et al. Growth and Field-Emission Properties of Vertically Aligned Cobalt Nanowire Arrays. *Nano Lett.* **2004**, *4* (3), 521–524, DOI: 10.1021/nl0499239.

(256) Maurer, F.; Dangwal, A.; Lysenkov, D.; Müller, G.; Toimil-Molares, M. E.; Trautmann, C.; Brötz, J.; Fuess, H. Field Emission of Copper Nanowires Grown in Polymer Ion-Track Membranes. In *Nuclear Instruments and Methods in Physics Research, Section B: Beam Interactions with Materials and Atoms*; **2006**; Vol. 245, pp 337–341.

(257) Chakraborty, I.; Ayyub, P. Controlled Clustering in Metal Nanorod Arrays Leads to Strongly Enhanced Field Emission Characteristics. *Nanotechnology* **2011**, *23* (1), 015704, DOI: 10.1088/0957-4484/23/1/015704.

(258) Dangwal, A.; Müller, G.; Maurer, F.; Brötz, J.; Fuess, H. Field Emission Properties of Bare and Gold-Coated Nickel Nanowires Grown in Polymer Ion-Track Membranes. *J. Vac. Sci. Technol. B Microelectron. Nanom. Struct.* **2007**, *25* (2), 586, DOI: 10.1116/1.2709888.

(259) Joo, J.; Lee, S. J.; Park, D. H.; Kim, Y. S.; Lee, Y.; Lee, C. J.; Lee, S.-R. Field Emission Characteristics of Electrochemically Synthesized Nickel Nanowires with Oxygen Plasma Post-Treatment. *Nanotechnology* **2006**, *17* (14), 3506–3511, DOI: 10.1088/0957-4484/17/14/024.

(260) Dangwal, a.; Pandey, C. S.; Müller, G.; Karim, S.; Cornelius, T. W.; Trautmann, C.; Müller, G.; Karim, S.; Cornelius, T. W.; Trautmann, C. Field Emission Properties of Electrochemically Deposited Gold Nanowires. *Appl. Phys. Lett.* **2008**, *92* (6), 063115, DOI: 10.1063/1.2844853.

(261) Geng-Min, Z.; Roy, E.; Hong-Wen, L.; Wei-Min, L.; Shi-Min, H.; Yu-Zhang, K.; Zeng-Quan, X. Field Emission from an Array of Free-Standing Metallic Nanowires. *Chinese Phys. Lett.* **2002**, *19* (7), 342, DOI: 10.1088/0256-307X/19/7/342.

(262) Navitski, A.; Serbun, P.; Muller, G.; Alber, I.; Toimil-Molares, M. E.; Trautmann, C. Correlation between Field Emission Current Limits and Morphology Changes of Gold Nanowire Patches. In *International Vacuum Nanoelectronics Conference*; IEEE, **2010**; pp 163–164.

(263) Serbun, P.; Jordan, F.; Navitski, A.; Müller, G.; Alber, I.; Toimil-Molares, M. E.; Trautmann, C. Copper Nanocones Grown in Polymer Ion-Track Membranes as Field Emitters. *Eur. Phys. J. Appl. Phys.* **2012**, *58* (1), 10402, DOI: 10.1051/epjap/2012110473.

(264) Lysenkov, D.; Muller, G. Field Emission Measurement Techniques for the Optimisation of Carbon Nanotube Cathodes. *Int. J. Nanotechnol.* **2005**, *2* (3), 239–254, DOI: 10.1504/IJNT.2005.008062.

(265) Navitski, A.; Müller, G.; Sakharuk, V.; Cornelius, T. W.; Trautmann, C.; Karim, S. Efficient Field Emission from Structured Gold Nanowire Cathodes. *Eur. Phys. J. Appl. Phys.* **2009**, *48* (3), 30502, DOI: 10.1051/epjap/2009167.

(266) Michaelson, H. B. The Work Function of the Elements and Its Periodicity. *J. Appl. Phys.* **1977**, *48* (11), 4729–4733, DOI: 10.1063/1.323539.

(267) Duan, J. L.; Lei, D. Y.; Chen, F.; Lau, S. P.; Milne, W. I.; Toimil-Molares, M. E.; Trautmann, C.; Liu, J. Vertically-Aligned Single-Crystal Nanocone Arrays: Controlled Fabrication and Enhanced Field Emission. *ACS Appl. Mater. Interfaces* **2016**, *8* (1), 472–479, DOI: 10.1021/acsami.5b09374.